Vibrational and Anion Photoelectron Spectroscopy of Transition Metal Clusters

vorgelegt von
M. Sc.
David Yubero Valdivielso

an der Fakultät II - Mathematik und Naturwissenschaften
der Technischen Universität Berlin
zur Erlangung des akademischen Grades

Doktor der Naturwissenschaften
Dr. rer. nat.

genehmigte Dissertation

Promotionsausschuss:

Vorsitzender: Prof. Dr. Mario Dähne
Gutachter: Prof. Dr. Otto Dopfer
Gutachter: Prof. Dr. Gerard Meijer
Gutachter: Prof. Dr. Knut R. Asmis

Tag der wissenschaftlichen Aussprache: 18. Januar 2022

Berlin 2022

Abstract

David Yubero Valdivielso

Vibrational and Anion Photoelectron Spectroscopy of Transition Metal Clusters

The understanding of chemical bonding and of the resulting atomic arrangements is a central topic in molecular physics. The bonding mechanisms of transition metal atoms still constitute a challenge in their theoretical description due to the massive number of valence electrons. Moreover, small transition metal clusters and their complexes may serve as models for catalytic systems of interest for science and technology. The goal of this thesis is the characterization of the geometric and electronic structures of isolated transition metal clusters in the gas phase and, consequently, a better understanding of their bonding nature.

The first part of the thesis encompasses experimental results and conclusions for the anionic platinum trimer (Pt_3^-) and the tantalum nitride anion (TaN^-). The data is obtained through anion photoelectron spectroscopy via velocity map imaging (VMI), which permits the simultaneous measurement of photoelectron spectra and photoelectron angular distributions (PADs). The study on TaN^- reports the first photoelectron spectra of this diatomic molecule. The spectroscopic assignments, carried out with the support of previous theoretical and experimental works, provide measurements of the adiabatic electron affinity (EA_{ad}) and of the vibrational frequencies of the anion and the neutral molecule. In addition, the analysis of the PADs reveals the existence of two core excited shape resonances and disentangles the hybridization of a key molecular orbital. In the study of Pt_3^-, the experiment is

performed in the slow electron velocity map imaging (SEVI) mode to resolve the low-frequency vibrational structure, characteristic of metal clusters. A plethora of information is obtained with the support of density functional theory (DFT) calculations, which includes the presence of two isomeric forms (triangular and linear) and hints at pseudo Jahn-Teller and Jahn-Teller effects. Some of the PADs reveal an oscillatory energetic dependence that, according to the quantum analogy established by Fano with the Young's double slit experiment, is interpreted as interferometric effects in the linear isomer.

In the second part of the thesis, the characterizations of $CoAr_n^+$ (n=3 to 6), $Co_{n-m}Mn_mAr_x^+$ (n=3 to 14; m=0 to 2) and saturated cationic Ru cluster carbonyls $Ru_n(CO)_m^+$ (n=1 to 8) via (far-)infrared multiple photon dissociation (IRMPD) spectroscopy, more suitable to obtain structural information on the studied complexes, are reported. The investigation on $CoAr_n^+$ readdresses the question on the nature of the interaction between the metal cation and the rare gas atom by proposing some amount of covalency in the bonding. Motivated by the role of ruthenium as catalyst for CO methanation in the Fischer-Tropsch process, the composition and structures of saturated cationic ruthenium carbonyls are studied. Their IR spectra are obtained in the range of the C-O stretches, Ru-CO stretches and deformation modes. Structural assignment is achieved with the aim of DFT calculations and the results corroborate former predictions. Finally, IR spectra of $Co_{n-m}Mn_mAr_x^+$ are presented and discussed in comparison to those of pure cobalt clusters with the purpose of motivating future theoretical studies that may solve the puzzling structures of these binary metal clusters.

Zusammenfassung

David Yubero Valdivielso

Vibrational and Anion Photoelectron Spectroscopy of Transition Metal Clusters

Das Verständnis der chemischen Bindung und der daraus folgenden räumlichen Anordnungen von Atomen ist ein zentrales Thema der Molekülphysik. Die große Zahl der Valenzelektronen von Übergangsmetall-Atomen stellt auch heute noch eine Herausforderung für die theoretische Beschreibung ihrer Bindungsmechanismen dar. Gleichwohl können kleine Übergangsmetallcluster und ihre Komplexe als Modelle für katalytische Systeme von Relevanz in Wissenschaft und Technik dienen. Das Ziel dieser Arbeit ist die Charakterisierung der geometrischen und elektronischen Strukturen von isolierten Übergangsmetallclustern in der Gasphase und damit ein besseres Verständnis für das Wesen ihrer chemischen Bindung.

Der erste Teil dieser Arbeit beinhaltet experimentelle Ergebnisse und darauf beruhende Schlussfolgerungen für das Anion des Platintrimers (Pt_3^-) und das Tantalnitrid-Anion (TaN^-). Die Daten basieren auf Anionen-Photoelektronenspektroskopie mittels velocity map imaging (VMI), einer Technik, die die gleichzeitige Messung der Photoelektronenspektren und der Winkelverteilung der Photoelektronen ermöglicht. Für das zweiatomige Molekül TaN^- wurde das Photoelektronenspektrum erstmalig bestimmt. Die spektroskopische Zuordnung gelang unter Zuhilfenahme vorhergehender theoretischer und experimenteller Arbeiten und liefert Werte für die adiabatische Elektronenaffinität (EA_{ad}) sowie die Schwingungsfrequenzen des Anions und des neutralen Moleküls. Weiterhin lässt die Untersuchung der Winkelverteilung

auf das Vorliegen von zwei rumpfangeregten Formresonanzen (engl. core excited shape resonances) schließen und erlaubt die Analyse der Hybridisierung eines wichtigen Molekülorbitals. Die experimentelle Untersuchung von Pt_3^- erfolgte im SEVI-Modus (von engl. slow electron velocity map imaging), um die Schwingungsstruktur bei den für Metallclustern charakteristischen niedrigen Frequenzen aufzulösen. Die große Menge an experimentellen Daten erlaubt, unterstützt durch Dichtefunktionaltheorie(DFT)-Rechnungen, den Nachweis von zwei isomeren Formen (linear und gewinkelt) und liefert Hinweise auf den Einfluss von Jahn-Teller- und Pseudo-Jahn-Teller-Effekten. Einige Winkelverteilungen zeigen eine oszillierende Energieabhängigkeit, die, entsprechend der von Fano beschriebenen Quanten-Analogie zu Youngs Doppelspaltexperiment, als Interferenzeffekt im linearen Isomer gedeutet werden kann.

Der zweite Teil der Arbeit widmet sich der Charakterisierung von $CoAr_n^+$ (n=3 to 6), $Co_{n-m}Mn_mAr_x^+$ (n=3 to 14; m=0 to 2) und gesättigten kationischen Rutheniumcluster-Carbonylen $Ru_n(CO)_m^+$ (n=1 to 8) mittels (Fern-)Infrarot Mehrphotonendissoziations-(IRMPD)-Spektroskopie, welche besonders geeignet ist, Strukturinfomationen für diese Komplexe zu erlangen. Die Untersuchung von $CoAr_n^+$ widmet sich der Frage nach der Art der Wechselwirkung zwischen Metallkation und Edelgasatom und lässt auf einen kovalenten Anteil an der Bindung schließen. Motiviert durch die Funktion von Ruthenium als Katalysator bei der CO-Methanisierung in der Fischer-Tropsch-Synthese wurden Zusammensetzung und Struktur von gesättigten kationischen Rutheniumcarbonylen untersucht. Deren IR-Spektren wurden im Bereich der C-O Streckschwingung sowie der Ru-CO Streck- und Deformationsmoden bestimmt. Die Zuordnung der Strukturen gelang mit Hilfe von DFT-Rechnungen und bestätigt frühere Vorhersagen. Schließlich werden die IR-Spektren von $Co_{n-m}Mn_mAr_x^+$ vorgestellt und, im Vergleich zu denen der reinen Cobaltcluster, diskutiert. Diese Daten stehen als Motivation für zukünftige theoretische Untersuchungen, die das Rätsel um die Strukturen dieser binären Metallcluster lösen könnten.

Common abbreviations	
EA_{ad}	Adiabatic electron affinity
DE_{vert}	Vertical detachment energy
AO	Atomic orbital
BE	Binding energy
BH	Born-Huang
BO	Born-Oppenheimer
CA	Crude adiabatic
CCD	Charge-coupled device
CNPI	Complete Nuclear Permutation Inversion
DFT	Density functional theory
FEL	Free-electron laser
FC	Franck-Condon
FWHM	Full width at half maximum
HF	Hartree-Fock
IR	Infrared
IRMPD	Infrared multiple photon dissociation
IVR	Internal vibrational redistribution
JT	Jahn-Teller
KE	Kinetic energy
LCAO	Linear combination of atomic orbitals
LFR	Laboratory frame of reference
MCSCF	Multi-configurational-self-consistent-field
MCP	Microchannel plate detector
MFR	Molecular frame of reference
MO	Molecular orbital
MS	Molecular Symmetry
PAD	Photoelectron angular distribution
PES	Photoelectron spectroscopy
POP	Polar onion-peeling
PSEPT	Polyhedral skeletal electron pair theory
PJT	Pseudo Jahn-Teller
ReToF	Reflectron time-of-flight
SEVI	Slow electron velocity-map imaging
SOC	Spin-orbit coupling
TDDFT	Time-dependent density functional theory
T-M	Transition-Metals
ToF	Time-of-flight
VB	Valence bond
VMI	Velocity map imaging

Contents

Chapter 1

Introduction

History

The chemical bond is a conceptual cornerstone in the field of chemistry that encompasses the understanding of the atomic world in terms of interatomic interactions. The development of qualitative and quantitative models for the description of chemical bonds and the prediction of molecular properties is up until now a highly active field in physical chemistry. Despite the many new developed methods in quantum chemistry to calculate approximate solutions to the Schrödinger equation, it does not often exist an aprioristic theoretical tool to check their reliability upon describing real physical systems. Experimental data are therefore necessary and desirable to provide starting points that facilitate reliable theoretical predictions. The understanding of the chemical bonding and the development of models to rationalize it date back to the beginning of the 19th century when John Dalton and Jöns Jakob Berzelius began to denote elements by atomic symbols instead of alchemic ones. At that time, the term chemical affinity was used to describe the tendency to form new compounds from the combination of different original substances[1] and significant efforts were being made to disentangle the cumbersome conceptual relation between chemical affinity and valence since Edward Frankland identified multiple valences in some elements in 1852[2]. Furthermore, the key relationship between atomic valence and the

three-dimensional distribution of atoms in the molecules was not accepted by the scientific community until August Kekulé proposed by 1865 a hexagonal structure for benzene and Jacobus Henricus van't Hoff demonstrated a decade later that a tetrahedrally coordinated atom was needed to explain certain aspects of stereochemistry [3].

The transition to the 20th century brought two breakthroughs (and perhaps the most important ones) which underpin our current vision of the chemical bonding: the discovery of the electron in 1897 by Joseph John Thomson and the birth of quantum theory. Thus, the proposition of an ionic bonding can be traced back in the works of Thomson as early as 1904 suggesting that the atoms in HCl are joined by an electromagnetic force [4], and the concept of covalent bonding in terms of two-electron two-center bonds between atoms was originally formulated by Gilbert N. Lewis in 1916 [1,5]. Two early approaches for describing the chemical bonding in the diatomic hydrogen molecule within the theoretical framework of quantum mechanics were developed by Walter Heitler and Fritz London in 1927 [6] and, almost simultaneously, by Robert S. Mulliken and Friedrich Hund [7–9]. The Heitler-London approach describes the bonding in terms of localized atomic bonds and led to the development of the valence bond (VB) approach. Linus Pauling then in the "The Nature of the Chemical Bond" [10] not only builds bridges between the VB theory and the Lewis model, but also with the crystal field theory. The Mulliken-Hund approach considers that the molecular orbitals are delocalized over several atomic centers and formed by linear combinations of atomic orbitals (LCAO).

Despite the complementary visions and explanations to diverse chemical phenomena that VB and LCAO theories offer, the former was originally better accepted by the chemical community due to its easier handling. The emergence of digital computers in the 1950s enhanced the use of the LCAO theory, since its coding was much easier to implement in the newly born technological world. This success increased in the next decades when Roald Hoffmann and Kenichi Fukui were awarded with the Nobel Prize in 1981 for the development of the Woodward-Hoffmann rules [11] and the VB theory was increasingly relegated to a residual role. Nevertheless, VB and LCAO

theories are still complementarily used, e.g., in coordination chemistry for a more qualitative, pictorial explanation of the structures and properties of metal complexes.

Nowadays, computational chemistry can provide fundamental and very detailed insights helping the understanding of chemical bonds. Density functional theory (DFT), Hartree-Fock (HF) and post-Hartree-Fock, or the multi-configurational-self-consistent-field (MCSCF) methods are some of the many methods that have been computationally implemented in quantum chemistry. Among all of them, DFT is currently the most frequently used since it provides approximate solutions to the Schrödinger equation with a mostly good accuracy at a reasonable computational cost. DFT calculations have successfully predicted ground states of a great variety of molecular systems. The current challenges that it confronts are the calculation of excited, intermediate and virtual states, as the developments in time-dependent density functional theory (TDDFT) have shown [1,11,12], in addition to the design of new exchange correlation functionals that provide a more accurate description of relativistic effects. Beyond and despite their higher computational cost compared to DFT, the implementation of the different post-Hartree-Fock methods allows the inclusion of electronic correlation effects as well as the presence of quasi-degeneracies in regions with high density of electronic states or bond-breaking processes requires the use of, for example, the aforementioned MCSCF.

Chemical bonding in transition metals

At the beginning of the 20th century concepts for ionic and covalent bonding existed, the latter in terms of two-electron two-center bonds. In the sixties, the state of the art in inorganic chemistry considered bonding between transition metal atoms with different extents of ionic and covalent mixed character leading to either single, double or triple bonds. This situation was revolutionized in 1964 with the discovery of short Re-Re distances in the crystal structure of $K_2[Re_2Cl_8]H_2O$ that have been explained by the presence of quadruple bonds [13]. Metal-metal quintuple bonds were reported [14–16] less

than twenty years ago, and even metal-metal sextuple bonds have been found in Mo_2 and W_2 [17–20], what turns this field into a hot topic of research.

Chemical bonds within and to metal clusters

In nanoscience, a cluster is a single cohesive particle that can be formed from 2 to few thousands of atoms or molecules. Such small and well defined systems are attractive as idealized models to gain insights into the nature of the chemical bond or the understanding of quantum effects in their own right. Clusters range from the strictly quantum regime at very small sizes, where "each atom counts" and the addition or removal of a single atom can provoke drastic changes in their physical and chemical properties, to the emergence of the bulk state, where their properties scale somehow more smoothly with size. Therefore, cluster properties are not only individually characterized (specially at very small sizes), but also allow to bridge the broad gap between atomic systems and the bulk state in order to track the emergence of macroscopic physical and chemical properties.

Clusters are as well suitable systems to study the mechanisms of catalytic processes. Isolated clusters in gas phase provide a large surface-atom / volume-atom ratio and, consequently, many low coordinated surface atoms and a large variety of binding sites. Indeed, the adsorption mechanisms of ligands on transition metal clusters and their characterization is a vivid research topic since the 1980s [21–26], within which part of the investigation in this thesis has been carried out.

Conceptually and historically, the origin of cluster science may be linked to the concept of "active sites", which was firstly coined by Taylor in 1928 [27]. With the aim of characterizing certain heterogeneous catalytic processes, experiments under (ultra-) high vacuum began to be carried out in the late 50's by depositing ligands on single crystal surfaces. In some cases, it was found a different catalytic behavior between the real catalyst and the single crystal surface, thus suggesting that the catalytic activity is rather performed in "active sites" of the surface (defects, edges, etc.). These sites

are characterized by a different coordination from those of the perfect surface, which gives them special geometric and electronic properties.

Furthermore, the specificity and small size of "active sites" and the development in the early 80's of new molecular beam technologies were the factors that triggered the explosion of cluster science with the goal of understanding the behavior of complex heterogeneous catalysts by investigating their separated parts (substrates, active (metal) particles, uncovered or reacted with ligands) through tailored cluster systems. In the last 40 years, clusters have shown to be interesting models for active sites and for the development of new catalysts. This motivation as well as the characterization of the specific binding mechanisms guides the study along this thesis of mono- and bimetallic transition metal clusters that range from 2 to 20 atoms to which few ligands are added.

Many different experimental methods have been developed to explore the properties of clusters in the gas phase. Flow tube reactors [28] are employed in reactivity studies and the magnetic properties are characterized by Stern-Gerlach type experiments and x-ray magnetic circular dichroism spectroscopy [29,30]. Information about the electronic structure can be obtained by photoelectron spectroscopy [31] and, furthermore, ion mobility spectrometry (IMS) [32], trapped ion electron diffraction (TIED) [33] and infrared multiple photon photodissociation spectroscopy (IRMPD) [34] constitute powerful tools to gain insight into geometric structure of the clusters. In this thesis, the two performed methods are anion photoelectron spectroscopy via velocity map imaging (VMI) and IRMPD.

Anion photoelectron spectroscopy probes the electronic structures of the clusters and, when using high resolution variants of VMI, even low-frequency vibrational structure can be resolved. The combination of the measured spectra with Franck-Condon simulations and anisotropy parameter analysis, gives insights into the geometric structures and chemical bonding of the anionic and neutral states of the clusters. IRMPD spectroscopy often can provide sufficient information to characterize the binding geometry of ligands (CO, Ar, etc.) to the clusters. Together with DFT calculations, it provides

not only structural information for the small bare clusters and their ligands, but also into the nature of their bonding.

Furthermore, the predictive capabilities of DFT calculations can often be improved upon the inclusion of electronic correlations or relativistic effects. In addition, the development of theoretical methods that are focused on reproducing the accurate wavefunctions of the molecular orbitals in the cluster rather than their energies would require the availability of new experimental results as a basis for future theoretical developments. As it will be later shown, this is also one of the goals pursued by this thesis.

Outline of this thesis

In this thesis, clusters and small molecules containing transition metal atoms are characterized by means of anion photoelectron spectroscopy and IRMPD spectroscopy. Both techniques provide experimental data on gas-phase species that, in conjunction with theoretical considerations originating, e.g., in group theory and quantum chemical calculations, allow for detailed insights into their complex electronic and geometrical structures.

The experimental methods and their theoretical background are described in **Chapter 2**. First, the basics of molecular photoelectron spectroscopy are introduced, explaining the information contained in the photoelectron angular distribution about molecular orbital structure and the role of resonances during photodetachment. The experimental realization of the measurements using VMI of electrons that are photodetached from mass-selected anions is described and the energy resolution of the VMI spectrometer is discussed. The second part of the chapter introduces IRMPD as a technique to obtain mass-selected vibrational spectra from highly dilute media, like molecular beams. These experiments rely on Free Electron Lasers as very intense and widely tunable infrared sources, FELIX at the Radboud University Nijmegen, The Netherlands, and the FHI-FEL at the Fritz-Haber Institute in Berlin, Germany. Their working principle and the implementation of the lasers with the molecular beam setup for the spectroscopy of gas-phase clusters is shown.

The chapter ends with presenting the very first data measured in a user experiment with the FHI-FEL.

Chapter 3 introduces the principles of group theory focusing on aspects that will become relevant, in particular, for the two following chapters. The description follows the spirit of Philip Bunker and Per Jensen [35] and briefly comments on three different mathematical approaches to the Born-Oppenheimer (BO) approximation. Lastly, the breakdown of the BO approximation in the Jahn-Teller (JT) and pseudo Jahn-Teller (PJT) effects is covered.

Chapters 4 and 5 present the results obtained using anion photoelectron spectroscopy for the tantalum nitride anion, TaN^-, and the anionic platinum trimer, Pt_3^-. For both systems, the vibronic structure and the photoelectron angular distributions are analyzed by comparison of the experimental data with predictions from quantum chemical calculations. The potential of photoelectron spectroscopy for in-detail characterizations of isolated molecules will be demonstrated for the diatomic molecule TaN^-. All features in its spectrum can be unequivocally assigned and yield molecular constants as the vibrational frequencies in the anionic and neutral states, the electron affinity of TaN, relative energies of different low-lying electronic states, as well as the spin orbit splitting in the $^3\Delta$ state. In addition, it will be shown how the photoelectron angular distributions of species containing transition metal atoms that include *spd* hybridization can be modelled through Sanov's "sequential mixing model" [36,37].

The seemingly simple Pt_3^-, a prototype system for cluster catalysis presents very complex photoelectron spectra that were measured with photon energies between 1.887 eV (657 nm) and 4.769 eV (260 nm), i.e. to obtain both, overview spectra and those covering different parts with high (vibrational) resolution. Contributions from linear and triangular isomers of Pt_3^- can be clearly distinguished. More detailed assignments are proposed based on predictions from density functional theory calculations (J. Jellinek, Argonne National Laboratory, USA and A. Sumer, University of Health Sciences, Turkey). The presence of PJT and Renner-Teller effects as well as the coalescence of JT effect and spin-orbit coupling (SOC) are suggested to

understand the observed vibronic structures. The measured photoelectron angular distributions for the triangular isomers are successfully modelled within the "central atom approximation", while for the linear ones strong deviations of the anisotropy parameter from the atomic Wigner-Bethe-Cooper-Zare like behavior suggest the presence of interferometric effects for the outgoing photoelectron.

Chapters 6 to 8 include the results obtained based on IRMPD. In **chapter 6** it is shown how the interaction of Ar atoms with cobalt cations can be probed through the far-infrared spectra of $CoAr_n^+$ complexes (n=4 to 6). In conjunction with the results of density functional theory calculations the structures of these complexes are assigned and further insights into the Co^+-Ar bonding nature are obtained. **Chapter 7** presents vibrational spectra of bimetallic $Co_{n-m}Mn_m^+$ clusters, starting with the pure Co_n^+ clusters (m=0) that are discussed in comparison to earlier experimental data and theoretical predictions. The far-IR spectra of the $Co_{n-m}Mn_m^+$ clusters are obtained by IRMPD of their complexes with Ar atoms, thus contributions of M-Ar vibrations as studied in the preceding chapter can be expected to be of relevance. Finally, in **chapter 8** the infrared spectra of a series of saturated cationic ruthenium carbonyls clusters $Ru_n(CO)_m^+$ (n=1 to 8) are presented, covering not only the C-O stretching modes (1900-2150 cm^{-1}) but also the range of C-M stretches and deformation modes in the far-infrared (400-600 cm^{-1}). The structures are assigned by comparison with results from density functional theory calculations. The resulting structures (of the metal cluster skeleton) agree well with the predictions from the polyhedral skeletal electron pair theory (PSEPT).

Chapter 2

Experimental methods

2.1 Photoelectron spectroscopy via velocity map imaging (VMI)

2.1.1 Photodetachment principles

In photoelectron spectroscopy (PES), electrons are ejected from atoms or molecules upon absorption of monochromatic light [38], and the amount and the energy of the released electrons (called photoelectrons) is recorded. For a negligible recoil of the remaining atom or molecule, the conservation of energy in the photoelectron process is given by the relation:

$$E_k = h\nu - E_B \tag{2.1}$$

where E_k is the kinetic energy (KE) of the emitted photoelectron, $h\nu$ is the energy of the incident photon and E_B is the binding energy (BE) of the electron in the target atom or molecule. The process is called photodetachment spectroscopy or anion PES when the target atom or molecule is negatively charged and photoionization spectroscopy when the target is neutral or positively charged. In most photodetachment cases (and in all cases discussed in this thesis) the atom or molecule has one extra electron, but there have been photodetachment studies on multiply charged anionic molecules as well [39,40].

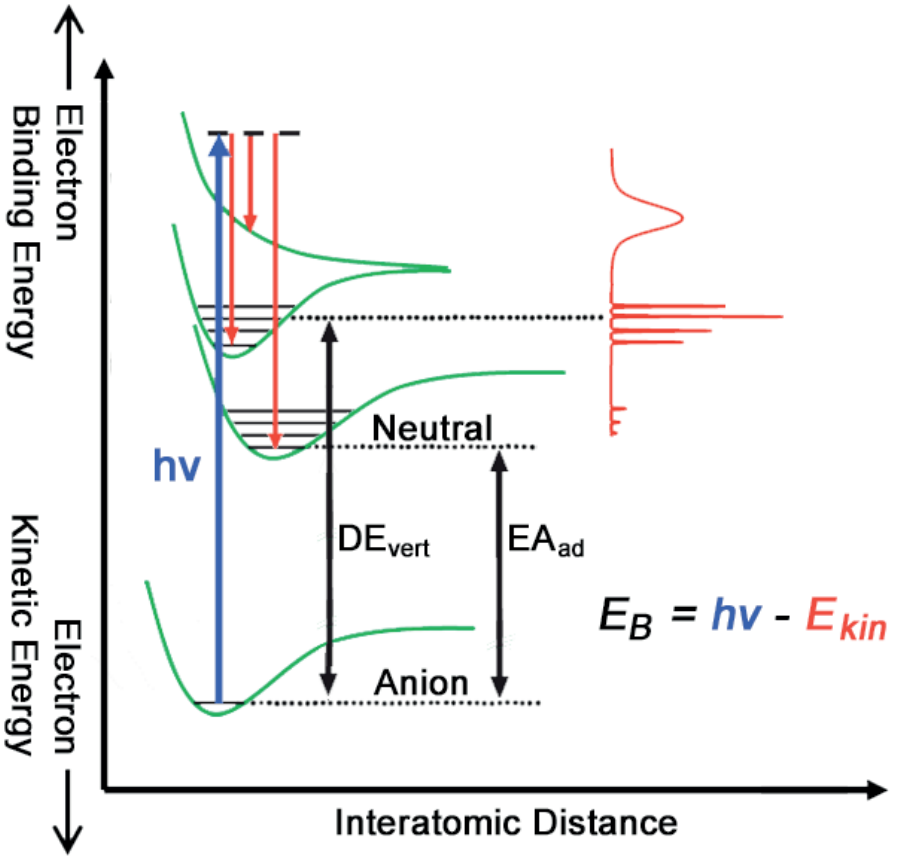

Figure 2.1: Schematic diagram summarizing the fundamental magnitudes of a general molecular photodetachment process. The equation 2.1 is depicted through colour-coded arrows. In the diagram, a ground or excited anionic state absorbs photons with an energy bigger than the $\mathrm{EA_{ad}}$ of the molecule and, therefore, electrons are detached. The neutral vibronic states that can be accessed through photodetachment are energetically below the discrete continuum level reached by the photon energy. The excess energy in the photodetachment process is carried by the emitted photoelectrons in form of KE. The detection of these photoelectrons as a function of their KE allows for the mapping of the vibronic structures in anionic and neutral states. For direct photodetachment processes, the probability of each transition is given by the Franck-Condon factors, which in coalescence with the KEs of the detected photoelectrons, allow the reconstruction of a photoelectron spectrum characteristic of the molecule as it shown in the right side of the diagram. Magnitudes as $\mathrm{EA_{ad}}$ or $\mathrm{DE_{vert}}$ are discussed in the text.

Anion PES on atoms and molecules in the gas phase offers several technical advantages over neutral PES in the gas phase and PES on surfaces.

Anionic atoms and molecules can be mass-selected, which is fundamental in size-selective investigations. Instead of using synchrotron light sources, anion PES experiments can be carried out with easily manageable table-top lasers due to the generally low photon energy that is needed to detach photoelectrons. As the photon absorption process goes into the continuum, the selection rules are less restrictive than in rovibronic spectroscopic methods which do not release photoelectrons. Therefore, insights over broad energy ranges into the vibronic structure of the neutral species can be gained.

Prior to further discussing the process of photodetachment of electrons from anionic metal clusters, it is worthwhile to discuss the stability of atomic or molecular anions, following the approach presented in the work of Simons[41]. An anion is thermodynamically stable when it fulfills conditions of electronic and geometric stability and when the energy of its lowest-energy structure lies below that of any molecular or atomic fragments into which it can dissociate. An anion is electronically stable if at a fixed molecular geometry the anion's electronic energy is lower than that of the neutral molecule at this same geometry. If at a specific local geometry, Q_0, the anion is electronically stable, it is geometrically stable if the anion's electronic energy $E(Q_i)$ as a function of nuclear displacements $E(Q_i)$ away from Q_{i_0} obeys $\frac{\partial E}{\partial Q_i} = 0$, for all i and if all the vibrational frequencies are real.

As it is shown in Figure 2.1, the adiabatic electron affinity (EA_{ad}) of a molecule is defined as the difference in energy between the neutral molecule, A, and the anionic one, A^-, in their ground states[42]. Consequently, the molecule is defined to have a positive EA_{ad} if the ground state of A^- lies below the ground state of A, and a negative EA_{ad} if the ground state of A^- lies above the ground state of A. Thus, a thermodynamically stable anion exists when the atom or molecule has a positive EA_{ad}[43]. The vertical detachment energy (DE_{vert}) is the energy needed to eject an electron from the negative ion in its ground (electronic and vibrational) state in a transition to a neutral electronic (ground or excited) state without changing the internuclear distance[42] (in case of a diatomic molecule) or, more generally, without changing the geometry of the neutral core. The corresponding adiabatic detachment energy, DE_{ad}, for the same transition is the minimum energy needed to reach the ground

state of the neutral atom or molecule from the ground state of the anion, i.e. when the final neutral state has adiabatically relaxed to a stable geometry. The values of DE_{vert} and DE_{ad} for any anion-to-neutral state transition are identified respectively via the most intense and the lowest energy transitions in the Franck-Condon vibrational progression that is normally observed.

The photoelectron spectroscopic process studied in this thesis consists of the absorption of a single photon by a singly charged anion with enough energy to detach one photoelectron. This process can be written as:

$$A^- + h\nu \rightarrow A + e^- \tag{2.2}$$

Generally, the detachment process is faster than structural rearrangements of the nuclei in the remaining neutral cluster. It is thus commonly stated that anion PES probes the electronic structure of the neutral molecule in the ground-state geometry of its anion [44]. More specifically, the ejection of the electron from the anion can be caused by various mechanisms. The most commonly observed one is the electronic excitation of the anion to a final state in which an electron exists in a continuum rather than in a bound orbital, without electronic configuration changes in the neutral core. The electron ejection may also be accompanied by small electron reorganizations in the neutral core. Alternatively, the photon may first cause excitation to a metastable, electronically excited state of the anion whose rovibrational levels lie energetically above one or more levels of the neutral molecule [41]. This can then result in the ejection of the extra electron from the anion through a process called autodetachment, a process that will be treated in more detail below. As well, thermionic emission can provoke the ejection of electrons from the anion.

The anionic potential

The effective potential (V_{eff}) that binds the extra electron to the neutral core in the anion is the combined effect of a repulsive (V_{rep}) and an attractive potential (V_{att}). In the absence of a permanent electric dipole moment, the dominant contribution to V_{att} is the charged-induced dipole interaction

between the detached electron and the remaining neutral (molecular or atomic) core[45]. This Coulombic attraction scales as $\propto\frac{1}{r^4}$, where r is the electron-molecule distance. The centrifugal potential V_{rep} arises from the relative motion of two bodies (electron and neutral core)[42]. It varies as $\propto\frac{l(l+1)}{r^2}$, where l is the angular momentum quantum number. The total effective long-range electron-molecule potential is given by:

$$V_{eff} = V_{att} + V_{rep} = -\frac{\alpha}{r^4} + \frac{\hbar^2}{2\mu^2}\frac{l(l+1)}{r^2} \tag{2.3}$$

where μ is the reduced mass of the electron-molecule system and α is the polarizability of the neutral core. V_{eff} is shown in Figure 2.2 for different values of l. If l>0 the repulsive potential is non-zero and produces a centrifugal barrier in V_{eff}, increasing in height with increasing l. This centrifugal potential barrier is important in autodetachment processes, as will be discussed below.

The cross section for photodetachment, σ, is zero at threshold, in contrast to the finite value that is characteristic for photoionization cross sections[47]. Its functional behavior at energies just above threshold for ejection of an outgoing electron with angular momentum l and kinetic energy KE was calculated by Wigner as[48]:

$$\sigma = Ak^{2l+1} = B(KE)^{l+\frac{1}{2}} \tag{2.4}$$

where k is the wavenumber of the detached electron[47], A and B are normalizing constants, and l is the lowest value of the free electron quantum number. Its energy dependence is shown in the lower part of Figure 2.2.

For completeness, and although not relevant for the systems studied in this thesis, it is mentioned that the ejected electron in a photodetachment process can experience long-range potentials proportional to $\propto\frac{-\mu e}{r^2}$ (for a molecule with a dipole moment μ) or $\propto\frac{-Qe}{r^3}$ (for a molecule with a quadrupole moment Q)[41]. The functional dependence of the Wigner threshold law on the KE of the photoelectron is more complicated in these situations. For practical applications, it suffices to mention that the kinetic energy dependence of the

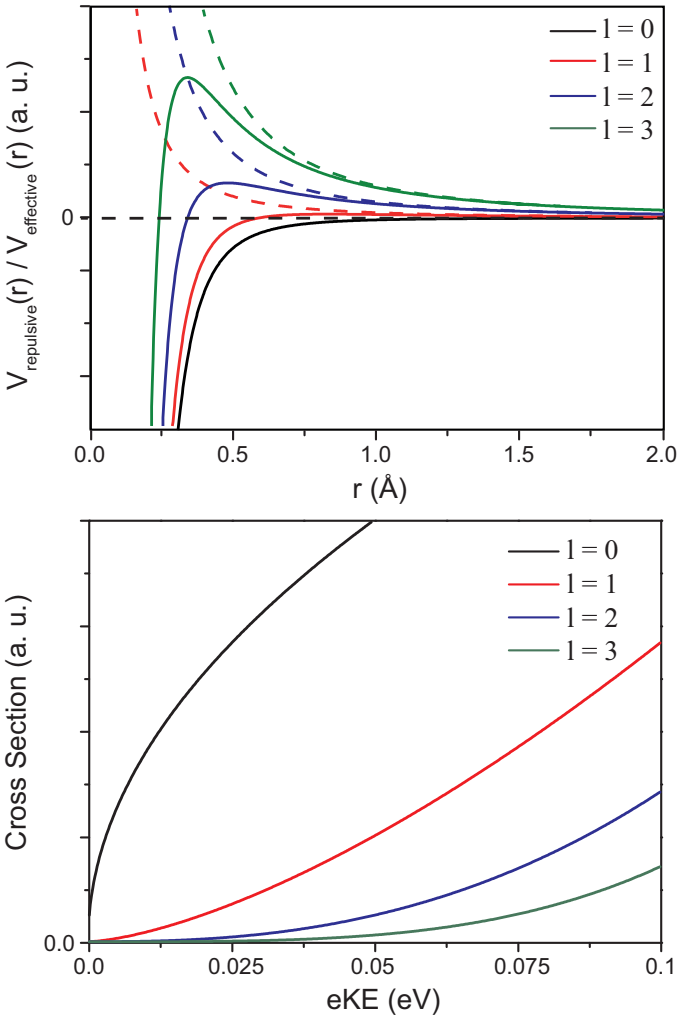

Figure 2.2: (Upper) Plot of the interaction between the outgoing electron and the remaining neutral core as a function of the distance, r, in a photodetachment process for different values of l according to equation 2.3. V_{rep} and V_{eff} are depicted respectively by the dashed and solid curves. (Lower) Visualization of the Wigner threshold law for different values of l.

cross-section can be expressed in this case as[41]:

$$\sigma = \sigma_0 (KE)^{l+\frac{1}{2}} \{1 + a(KE) + b(KE)^2 + c(KE)^3 ...\} \tag{2.5}$$

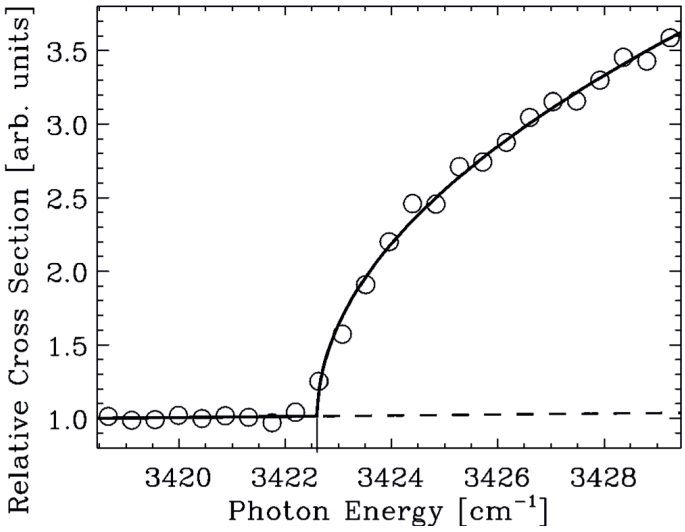

Figure 2.3: High-resolution photoelectron spectrum in the threshold region of the $^3P_2 \rightarrow {}^2P_{1/2}$ transition in Al^-. The solid line, that represents a fitted s wave, has a clear resemblance to the function given by the Wigner threshold law for l=0 (equation 2.4), as shown in the lower plot of Figure 2.2. The figure is taken from the work of Scheer et al. [46].

2.1.2 Shape and Feshbach resonances

The general phenomenon of a resonance is observable by changes in the scattering cross section of the photodetachment process that can increase its value even more than one order of magnitude. These changes are measured either as a function of the photon energy or as a function of the kinetic energy of the released electron. Generally, resonances have either Breit-Wigner [49] or Cohen-Fano [50] profiles. The Wigner profile corresponds to a Lorentzian curve while the asymmetric Fano profile is the result of the interference between a continuum background and a resonant scattering process [51]. These resonances correspond to metastable states of the anion in which the electron and the neutral core are transiently associated, forming a transient negative ion (TNI) [43]. We will refer to these metastable anionic states as resonant states, and the process in which a resonant state decays into a neutral electronic state by emitting a photoelectron as resonances or autodetachment processes.

The reaction that defines this process is:

$$A^- + h\nu \rightarrow A^{-*} \rightarrow A + e^- \tag{2.6}$$

As the lifetime of the resonant state, τ, is finite and often very short, it can be observed in the photoelectron spectra by a certain width given by the full width at half maximum (FWHM), Γ. It is governed by the Heisenberg's uncertainty principle:

$$\tau = \frac{h}{2\pi\Gamma} \tag{2.7}$$

Autodetachment resonances were first observed by Lineberger et al. in atomic and small molecular anions[52,53]. The resonances are classified as Feshbach resonances[52] or shape resonances[54] depending on their energy position relative to the corresponding electronic state in the neutral core that has the same geometry, similar to the way this is done in electron attachment studies[42,43]. Feshbach resonances lie below the neutral parent state while shape resonances lie above it. Shape resonances have received their name because the extra electron in the resonant state is trapped by the "shape" of the potential[43], i.e. by the centrifugal potential barrier[55]. Since this potential barrier does not exist for l=0, shape resonances cannot occur for outgoing electrons with l=0; in this case, only Feshbach resonances can occur. The resonances are additionally classified depending on whether the neutral parent state is the ground state or if the remaining neutral core is electronically excited. The resulting four types of resonances that can occur are schematically depicted in Figure 2.4.

Single-Particle Shape resonances can occur if the resonant state is above the ground electronic state of the parent neutral. It is also often called a $1p$ shape resonance as the excitation process to the resonant state involves the promotion of one electron to a, normally, unoccupied valence orbital[57]. A single-particle resonance involves no change in the configuration of the other electrons[43]. Since the energy lies above that of the neutral molecule, the decay process results in a neutral molecule in its ground state plus a free

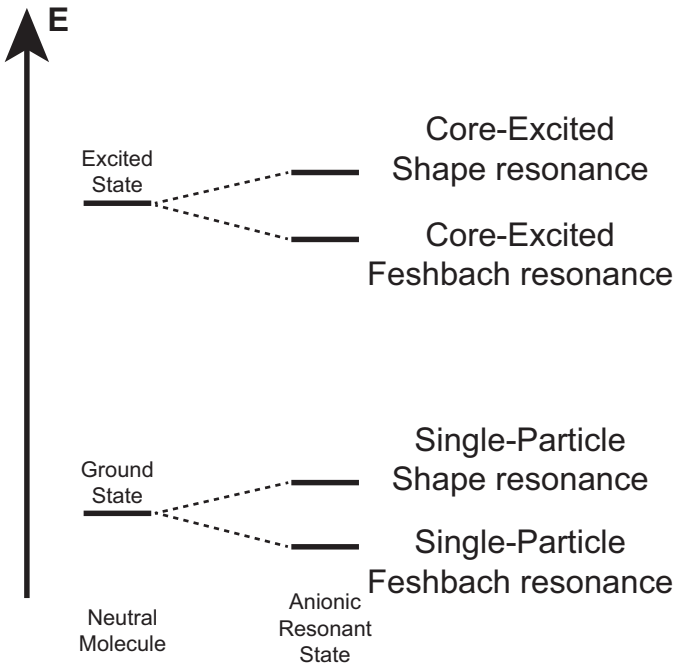

Figure 2.4: Schematic overview of the four types of resonances that can occur in photodetachment [43,56].

electron. The neutral molecule can also be left with some vibrational and/or rotational energy. The decay, resulting from electron penetration through the potential barrier, is analogous to the α-particle decay of radioactive nuclei. The excited states typically have very short lifetimes (10^{-15} to 10^{-10} s) [42], resulting in relatively broad spectral features ($\approx$1 eV to several 10^{-6} eV). Shape resonances are associated with almost all unoccupied orbitals of almost all small molecules at their respective equilibrium structures (N_2, CO_2) [58].

Core-Excited Shape resonances can occur if the resonant state is above an electronically excited state of the parent neutral. This resonance is also called core-excited Type II resonance or $2p-1h$ shape resonance, since after the photon absorption the resonant state has two electrons that occupy previously empty molecular orbitals (mostly valence ones). The electron that can undergo autodetachment is trapped, as in the previous case, by the shape of the centrifugal barrier. The decay process can occur similarly to that for

a single-particle shape resonance, but after the autodetachment process the extra excited electron remains in the orbital to which it was promoted. These resonances also appear with so strong features as the single-particle shape ones.

Single-Particle Feshbach resonances can occur if the resonant state is below the ground electronic state of the parent neutral. They are sometimes also called nuclear-excited Feshbach resonances. As the resonant state lies below the electronic ground state of the neutral molecule, direct emission of the excess electron is not possible and these states cannot be observed in photodetachment studies. These resonances can be observed in low-energy electron collisions with molecules and clusters, for instance [59], and then decay to produce the anion in its electronic ground state. The lifetimes of the excited states are relatively long (often $>10^{-6}$ s), resulting in well-resolved spectral features, like in spectroscopic investigations of excited states of neutral species.

Core-Excited Feshbach resonances can occur if the resonant state is below an electronically excited state of the parent neutral but above its electronic ground state. They are also called core-excited Type I resonances, $2p-1h$ Feshbach resonances or closed channel resonances. The resonant state can decay into the electronic ground state of the neutral via a two-electron process. The electron ejection rate for this process is governed by the strength of the coupling between the electronic configurations of the resonant state of the anion and the ground state of the neutral molecule. As these differ in two orbitals, the lifetime of these resonances can be rather long (around 10^{-5} s). The photodetachment process competes with the electronic relaxation within the anion, which takes place on somewhat shorter time scales (10^{-8} to 10^{-6} s). The electron ejection rates from the core-excited Feshbach resonances are therefore small compared to those from the core-excited shape resonances. A very instructive example on Au_2^- was studied by Lai-Sheng Wang et al. [60].

Scattering studies on NO [61–63] and N_2 [64,65] have shown that even diatomic molecules can show a myriad of different resonances over broad energy ranges (up to 10 eV). Photoelectron studies with VMI have shown the richness of the resonance structures in bigger molecules [66]. It should be noted that the classification of resonances found in autodetachment is not yet complete

with the four types mentioned above and shown in Figure 2.4. In anions that have a large enough dipole moment in their neutral core (larger than 2-2.5 Debye), dipole-bound states can be stabilized. Since the dipole orbital is essentially non-bonding, the potential surfaces of the neutral molecule and the dipole-bound states of the anion run almost parallel in a substantial region around their virtually identical equilibrium structures [57]. Autodetachment from excited dipole-bound states therefore has the propensity rule $\Delta\nu$=-1. Although the first studies on autodetachment from dipole-bound states of anions were dominated by rotational effects [67,68], pure vibrational autodetachment from dipole-bound states has been found for $C_6H_5O^-$ [69] and AgF^- [70]. Photoelectron studies on CuF^- and AgF^- have shown dipole-stabilized shape resonances [71], while on $(CQ_0)_2^-$ (π-stacked coenzyme Q_0 (benzoquinone) dimer radical anion) multiple resonances with hybrid shape and Feshbach character have been observed [72].

2.1.3 Photoelectron angular distributions

A VMI spectrometer allows to measure simultaneously KE distributions and photoelectron angular distributions (PADs). The study of the PADs gives insights into the experimental character of the photodetachment process providing information about the quantum nature of the parent bound orbitals from which the outgoing electrons are ejected.

Some assumptions are done in order to establish the theoretical frame to study the PADs: the initial and final states are usually calculated with the same potential V and the molecular orbital (MO) description of the electronic structure in the molecule is adopted. It is assumed as well that the initial and the final states are written as products of N one-electron wavefunctions, where the incoming photon affects only the wavefunction of the photodetached electron, leaving the other $(N-1)$ wavefunctions unchanged. These assumptions imply that the residual neutral core is completely unrelaxed [73] and, therefore, the photodetachment process is studied in the Koopmans' theorem [74] spirit. Consequently, configuration interaction, vibronic coupling and relaxation effects are avoided [36]. Additionally, spherical symmetry is

assumed. In the case of atomic species, the initial state of the electron can usually be described as a bound state with a definite value of the orbital angular momentum quantum number, l, resulting from the solution to the Schrödinger equation with the unperturbed Hamiltonian. The wavefunction can be written as:

$$\phi_{nml}(r,\theta,\phi) = R^i_{nl}(r)Y_{lm}(\theta,\phi) \tag{2.8}$$

with n, l and m the initial quantum numbers of the electron in the bound orbital. The free-electron wavefunction is given in terms of spherical harmonic partial waves with definite values of the orbital angular momentum, l' [75]. The final state is characterized by the direction, (θ,ϕ), of the outgoing electron that escapes to infinity at time t=0 after the ionization:

$$\psi_{kf}(r,\theta,\phi) = k^{-1/2}\sum_{l'm'} C_{kl'm'}e^{i\delta_{l'}}R^f_{kl'}(r)Y_{l'm'}(\theta,\phi) = \sum_{l'm'} c_{kl'm'}e^{i\delta_{l'}}Y_{l'm'}(\theta,\phi) \tag{2.9}$$

where the coefficients $C_{kl'm'}$ and $c_{kl'm'}$ contain radial and angular information about the state from which the photodetachment takes place and about the continuum state of the photoelectron [76]. The quantum numbers of the final state are l' and m', the energy is given by the wave vector k, $k^{-1/2}$ is a normalization factor and $\delta_{l'}$ is the phase shift of the l'-th partial wave. The PAD is calculated as the coherent square of the wavefunction given by equation 2.9:

$$\begin{aligned} I(\theta,\phi) \propto \psi^*_{kf}(r,\theta,\phi)\psi_{kf}(r,\theta,\phi) &= \sum_{lm}\sum_{l'm'} c^*_{l'm'}c_{lm}e^{i(\delta_l-\delta_{l'})}Y^*_{l'm'}(\theta,\phi)Y_{lm}(\theta,\phi) \\ &= \sum_{LM} B_{LM}Y_{LM}(\theta,\phi) \end{aligned} \tag{2.10}$$

where the B_{LM} coefficients contain information about contributions of individual partial waves and interferences between them [76]. The vector combination of the angular momenta in equation 2.10 fulfills l–$l' \leq L \leq l$+l' and M=m+m'. Therefore, orbital and azimuthal quantum numbers in one-photon ionization

are linked in the electric dipole approximation by the selection rules:

$$\Delta l = l' - l = \pm 1 \tag{2.11}$$

$$\Delta m = m' - m = 0 \tag{2.12}$$

If the molecules are randomly oriented all m sublevels of a given state (n, l) are equally populated, so the angular distribution of photoelectrons for this state must be averaged over all values of m:

$$I_{nl}(\theta, \phi) = \sum_{m=-l}^{+l} I_{nlm}(\theta, \phi) \tag{2.13}$$

The general formula of the PAD in a multiple photon absorption process with linearly polarized light is[77]:

$$I(\theta) = a[1 + \beta_2 P_2 \cos(\theta) + \beta_4 P_4 \cos(\theta) + \beta_6 P_6 \cos(\theta) + ...] \tag{2.14}$$

The Legendre polynomial is determined in each case by the subscript $2m$, where m is the number of absorbed photons. For a single photon absorption the formula is reduced to[77]:

$$I(\theta) = a[1 + \beta_2 P_2 \cos(\theta)] \tag{2.15}$$

where a is normalization constant proportional to the total photodetachment cross section, θ is the angle between the photoelectron velocity vector and the laser polarization direction, $I(\theta)$ the probability of emission at a particular angle θ, $P_2(x)$ is the second-order Legendre polynomial, $P_2(x) = \frac{1}{2}(3x^2 - 1)$, and β_2 is the commonly named anisotropy parameter, or simply β parameter. The β parameter ranges between two extreme values, $\beta = -1$ for $I(\theta) \sim \cos^2(\theta)$ when the PAD appears as fully perpendicular to the laser polarization axis and $\beta = 2$ for $I(\theta) \sim \sin^2(\theta)$ when the PAD appears as fully parallel to the laser polarization axis. $\beta = 0$ corresponds to a fully isotropic PAD. The β parameter fully characterizes a one-photon PAD in atomic photodetachment.

Its equation was initially derived by Bethe[78] and generalized by Zare and Cooper[79], commonly referred to as the Cooper-Zare central-potential formula:

$$\beta_l = \frac{l(l-1)\chi^2_{l,l-1} + (l+1)(l+2)\chi^2_{l,l+1} - 6l(l+1)\chi_{l,l+1}\chi_{l,l-1}\cos\delta_{l+1,l-1}}{(2l+1)[l\chi^2_{l,l-1} + (l+1)\chi^2_{l,l+1}]} \tag{2.16}$$

Here l is the angular momentum of the orbital from which the photoelectron is detached, $\delta_{l\pm1}$ are the phase shifts of the dipole-allowed outgoing wavefunctions and $\chi_{l,l\pm1}$ are the radial dipole transition matrix elements for these partial waves, which are given by:

$$\chi^{\varepsilon}_{l,l\pm1} = \langle R_{free,l\pm1}|\, r\, |R_{n,l}\rangle = \int_0^\infty R_{k,l\pm1} r R_{n,l} r^2 dr \tag{2.17}$$

where $R_{n,l}$ and $R_{free,l\pm1}$ are the radial components of the electronic wavefunction in the bound and the free states. The superscript ε indicates the normalization scale in the energy space in atomic units.

Beta parameter modelling

The Cooper-Zare formulation of β offers a powerful frame by reducing the photoionization process to the **LS** coupling scheme. It is based on the existence of a total orbital angular momentum **L** and a total spin **S**, and it allows to reduce the number of parameters necessary to describe the subshell photoionisation of both closed-shell and open-shell atoms to three: two transition matrix elements ($\chi_{l,l+1}$, $\chi_{l,l-1}$) and one relative phase shift ($\cos\delta_{l+1,l-1}$). Even if this approximation has shown limitations to provide deep quantitative acceptable results[80], it is normally considered in the literature as a first step to reach a complete quantitative description of photoionization. An evaluation of equation 2.16 following the steps described in the work of Bartels[75] allows to extract some information about the values of the two possible radial dipole transition matrices relative to each other which, consequently, can give some understanding of the free wavefunction behavior as a function of the outgoing electron energy. If the lower channel ($l \to l-1$)

is dominant, then $|\frac{\chi_{l,l+1}}{\chi_{l,l-1}}| \to 0$. The resulting β parameter depends only on the angular momentum l of the initial state and is given by:

$$\beta \to \frac{l-1}{2l+1} \tag{2.18}$$

If the upper channel ($l \to l+1$) is dominant, then $|\frac{\chi_{l,l-1}}{\chi_{l,l+1}}| \to 0$, and the resulting β parameter is given by:

$$\beta \to \frac{l+2}{2l+1} \tag{2.19}$$

Therefore, only the "interference term" $(-6l(l+1)\chi_{l,l+1}\chi_{l,l-1}\cos\delta_{l+1,l-1})$ can mathematically contribute, according to equation 2.16, to obtain negative values for β. Thus, if one of the matrix elements is so dominant that the other can be considered zero, the "interference term" is also zero and the β parameter does not depend on $\delta_{l+1,l-1}$, but only on l, as equations 2.18 and 2.19 show.

Besides that, $\delta_{l+1,l-1}$ plays a role if there is a significant contribution from both channels, $\chi_{l,l+1}$ and $\chi_{l,l-1}$, and this can be quantified by the factor x[75]:

$$x = \frac{|\chi_{l,l+1}| - |\chi_{l,l-1}|}{|\chi_{l,l+1}| + |\chi_{l,l-1}|} \tag{2.20}$$

Normally, the interaction between the outgoing electron and the remaining neutral core in photodetachment processes is small and the values that $\cos\delta_{l+1,l-1}$ reaches are mostly in the numeric interval that goes from 1 to 0.9[81–83]. Under these conditions, the evaluation of equation 2.16 for l=1 and l=2 is:

Figure 2.5 reveals that the maximum is independent of l and it is reached when $|\chi_{l,l+1}| = |\chi_{l,l-1}|$, while the minimum depends on l in the form of $|\chi_{l,l+1}| = \frac{l}{(l+1)}|\chi_{l,l-1}|$. As well, the effect of a phase distinct from 0 does not change the dependence of β on x but it reduces the maximum and minimum values that β reaches. This reduction is bigger the smaller the value of $\cos\delta_{l+1,l-1}$ is and it does not affect the anisotropy values at x=1 and

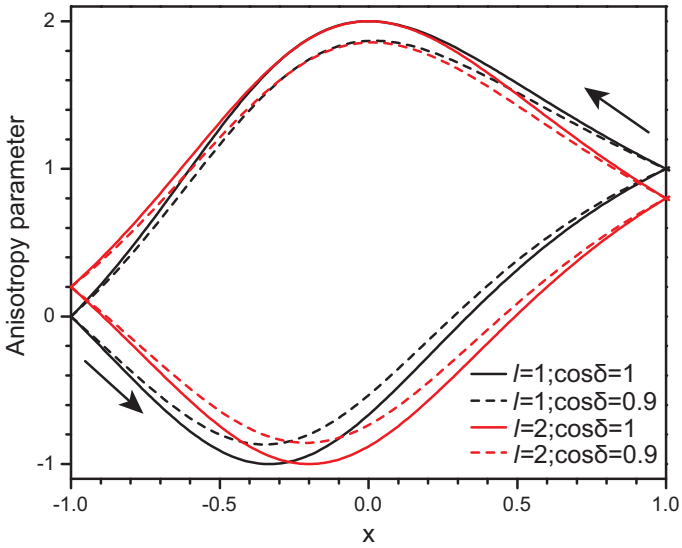

Figure 2.5: Evolution of β_2 as a function of the ratio between both radial dipole transition matrix elements, x. The black lines plot the anisotropy for l=1 and the red ones for l=2. The solid lines are obtained when $\cos\delta_{l+1,l-1} = 1$ and the dashed ones when $\cos\delta_{l+1,l-1} = 0.9$. The arrows indicate the direction followed in the analysis of the curves throughout the text.

x=–1 because they are given respectively by equations 2.18 and 2.19. The radial part of the wavefunctions that represent the outgoing photoelectrons in photodetachment are spherical Bessel functions[36,75,84], $R_{k,l\pm1} = j_{l\pm1}(kr)$, and their visualization in Figure 2.6 allows a more detailed interpretation of Figure 2.5. This interpretation is done for all the curves plotted in Figure 2.5 by starting at x=–1 and following the directions marked by the arrows.

At KEs close to threshold, the repulsive term of the effective potential, $V_{rep} = \frac{l(l+1)}{2r^2}$ (see equation 2.3), provokes that the lower channel wavefunction, $R_{k,l-1} = j_{l-1}(kr)$, has a bigger amplitude than the upper channel one, $R_{k,l+1} = j_{l+1}(kr)$, because a bigger part of the latter falls in a region that is classically forbidden. The clear dominance of the lower channel, $|\frac{\chi_{l,l+1}}{\chi_{l,l-1}}| \to 0$, gives the energy independent anisotropy value, $\beta = \frac{l-1}{2l+1}$, that is shown in Figure 2.5 when x=1.

As it will be discussed later in this section, we will use hydrogenic functions to describe the bound states, $R_{n,l}$, upon the evaluation of the

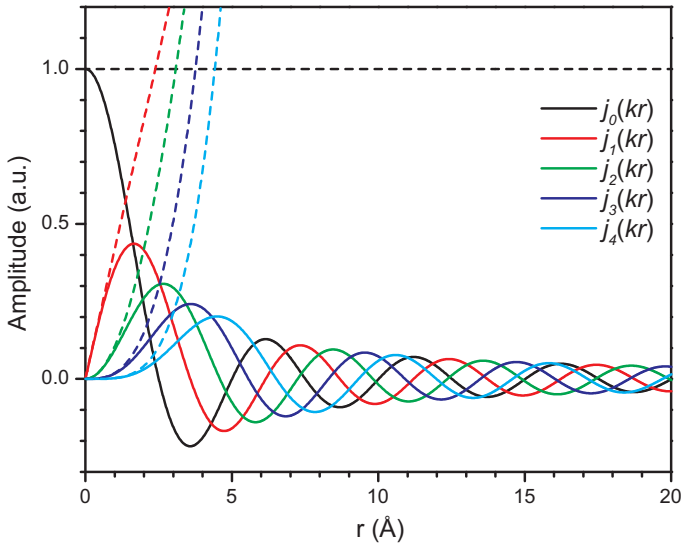

Figure 2.6: Bessel functions, $j_l(kr)$, of the first kind to visualize the spatial evolution of the wavefunctions of the photodetached electron as a function of its angular quantum number, l. The dashed lines represent the first term of the McLaurin expansion for each Bessel function, approximation that is taken at very low KEs. All curves are plotted for a KE, ε=5 eV.

transition dipole matrix elements in equations 2.16 and 2.17. The tails of these wavefunctions in the spatial region where they overlap with the free spherical wavefunctions are positive when n is odd and negative when n is even[75,85]. Additionally, if we move from the threshold to small KEs, we observe in Figure 2.6 that the wavefunctions of both outgoing channels are positive. Consequently, both transition matrix elements are positive (for n=odd) or negative (for n=even) at low KEs, so their product is positive and the "interference term" $(-6l(l+1)\chi_{l,l+1}\chi_{l,l-1}\cos\delta_{l+1,l-1})$ contributes to obtain negative values of β. This is the case observed in Figure 2.5 when all curves move to negative anisotropy values.

The higher the KE is, the bigger is the part of the free wavefunction that falls in the region where it overlaps with the wavefunction of the bound state and, as it is observed in Figure 2.6, there will be an energy at which the lower channel is 0 so, consequently, $|\frac{\chi_{l,l-1}}{\chi_{l,l+1}}| \to 0$. This situation is shown in Figure 2.5 by $\beta = \frac{l+2}{2l+1}$ at x=1.

At higher KEs, we begin to follow the curves in Figure 2.5 from right (x=1) to left (x=-1). Here the Bessel function of the lower channel becomes negative and the transition dipole matrix elements have opposite sign, being their product negative. Therefore, the "interference term" contributes to obtain positive anisotropy values, and this trend is maintained until β reaches its maximum at $x = 0$. Once the Bessel functions of the lower and upper channel have reached respectively their minimum and maximum in Figure 2.6, the anisotropy decreases again as the energy of the outgoing photoelectron increases from the maximum of β (at x=0) to x=-1. The wavefunctions of the upper and lower channels overlap at decreasing amplitudes with the wavefunction of the bound state, thus the interference term decreases until the starting point of this path is reached, i.e., $\beta = \frac{l-1}{2l+1}$ at x=-1. In principle, the understanding of the β evolution in this theoretical frame is valid for KEs $<$ 2eV.

General mixed model

The expansion of a MO as a linear combination of atomic orbitals (LCAO) is the fundament of the LCAO-MO theory [36] and it is given by:

$$\psi_{MO} = \sum c_{nlm}\psi_{nlm} = \sum \langle \psi_{MO} \,|\, \psi_{nlm} \rangle \, \psi_{nlm} \tag{2.21}$$

where ψ_{MO} is the wavefunction of the MO, c_{nlm} are the expansion coefficients and ψ_{nlm} are the wavefunctions of the AOs or basis functions. The bound molecular orbitals that are expanded are normally linked to the spatial localization of a particular atom or distributed over several centers. Nevertheless, this method holds as long as the mathematically calculated MO resembles to the physically existent one and regardless the physical insights that the AOs used in the expansion can bring. However, a wise election of the AOs in the studied molecule within Molecular Frame of Reference (MFR), has proven to be extremely useful in the understanding of the PADs. As an example, the center of mass of O_2^-, which does not spatially coincide with any of both oxygen nuclei, was chosen to expand the molecular HOMO in terms of AOs. This was possible thanks to the geometric resemblance between the HOMO

and d-like atomic orbitals with origin in the center of mass of O_2^-, as it was experimentally demonstrated [36,81,86,87].

The Cooper-Zare formula has been further developed in the last decade to describe the photodetachment from hybridized MOs with mixed l character [36,37,88–91]. This developement was initially proposed by Grumbling [90] to study hybridized sp MOs and, also, has been applied to polarized orbitals in cluster-solvation processes [36,89]. This model was further extended to mixed pd MOs and, more generally, to any other "sequential $l, l+1$" hybridization, but it showed limitations for $l \geq 1$ when it was experimentally tested [36,37]. Lastly, the model was successfully used to gain insights into spd hybridizations [92]. Here we are going to introduce firstly the general formulas for any "sequential $l, l+1$" hybridization to, afterwards, describe more in detail the mixed sp case since it is the one that manifests its usefulness the most straightforward. As it was mentioned, this model considers the detachment from a MO expressed as a linear combination of atomic orbitals that form a complete basis set and are localized on a single center, the best adapted one to the studied system [37]:

$$|\psi_{MO}\rangle = \sum_l \sqrt{\gamma_l}\,|l\rangle \tag{2.22}$$

where γ_l are the fractional characters of the AOs whose wavefunctions, $|l\rangle$, satisfy the normalization condition $\sum_l \gamma_l = 1$. The phase factors of each wavefunction are absorbed into the kets. Additionally, the Cooper-Zare formula can be expressed by the ratio:

$$\beta_l = \frac{v_l}{w_l} \tag{2.23}$$

where v_l and w_l are respectively named as the Cooper-Zare numerator and denominator:

$$\begin{aligned} v_l &= \frac{l(l-1)\chi^2_{l,l-1} + (l+1)(l+2)\chi^2_{l,l+1} - 6l(l+1)\chi_{l,l+1}\chi_{l,l-1}\cos\delta_{l+1,l-1}}{(2l+1)} \\ w_l &= l\chi^2_{l,l-1} + (l+1)\chi^2_{l,l+1} \end{aligned} \tag{2.24}$$

Therefore, the inclusion of equation 2.22 in equation 2.23 leads us to the general mixing formula. It must be remarked that the Cooper-Zare formula expressed in this manner includes the degeneracy factor, $2l+1$, as part of the numerator[37]:

$$\beta_l = \frac{\sum_l \gamma_l v_l}{\sum_l \gamma_l w_l} \tag{2.25}$$

In the application of equation 2.25 to a particular *sp* hybridization, the *s* and *p* wavefunctions have to share the same center in the MFR. The expansion of the MO wavefunctions in the fashion of equation 2.22 is:

$$|\psi_{sp}\rangle = \sqrt{1-\gamma_p}\,|\psi_s\rangle + \sqrt{\gamma_p}\,|\psi_p\rangle \tag{2.26}$$

where γ_p is the fractional *p* character ($0 \leq \gamma_p \leq 1$) and any phase factor is absorbed into the kets[37]. Consequently, equation 2.25 for a *sp* hybridized MO is:

$$\beta_{sp} = \frac{2(1-\gamma_p)\chi_{0,1}^2 + \gamma_p(2\chi_{1,2}^2 - 4\chi_{1,0}\chi_{1,2}\cos\delta_{2,0})}{(1-\gamma_p)\chi_{0,1}^2 + \gamma_p(\chi_{1,0}^2 + 2\chi_{1,2}^2)} \tag{2.27}$$

Hanstorp formulation and low KEs approximation

The Cooper-Zare equation (2.16) for a single l as well as for any other hybridized orbital (equation 2.25) can be rearranged following Hanstorp ideas[93] to show that β does not depend on the radial dipole transition matrix elements themselves, but on their ratios. This simplification is derived from the Wigner law[48] for near-threshold photodetachment (equation 2.5). As the partial cross-sections are proportional to the squares of the corresponding radial transition matrix elements, $\sigma_{l,l\pm1} \propto \chi_{l,l\pm1}^2$, the assumption of $\frac{\sigma_{l,l+1}}{\sigma_{l,l-1}} \propto \varepsilon^2$ leads us to the following ratio:

$$\frac{\sigma_{l+1}}{\sigma_{l-1}} = \frac{\chi_{l+1}^2}{\chi_{l-1}^2} = A_l^2\varepsilon^2 \quad \text{and} \quad \frac{\chi_{l+1}}{\chi_{l-1}} = A_l\varepsilon \tag{2.28}$$

where ε is KE of the photoelectron and A_l is a proportionality coefficient with units of reciprocal energy that is called Hanstorp coefficient. The division

of all radial transition matrix elements in 2.16 by $\chi^2_{1,0}$ (for $l = 1$) allows to express the Cooper-Zare equation in the following manner (red curve in Figure 2.7):

$$\beta_p = \frac{6A_1^2\varepsilon^2 - 12A_1\varepsilon\cos\delta_{2,0}}{3 + 6A_1^2\varepsilon^2} \tag{2.29}$$

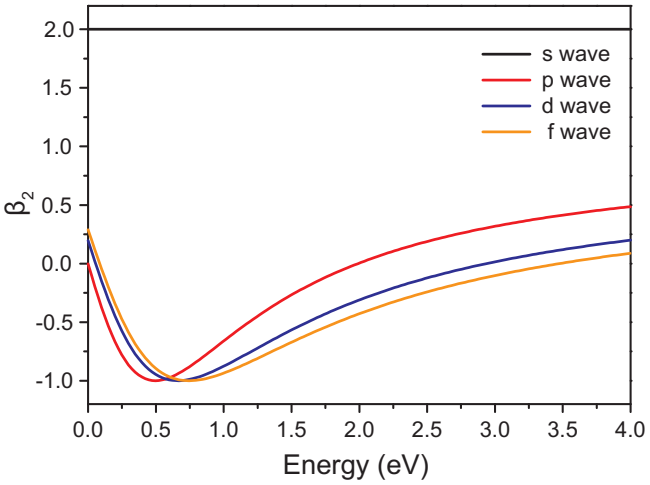

Figure 2.7: Plot of the β parameter for different initial integer l values in the Hanstorp's approximation at low KEs for an arbitrary coefficient, $A_l = 1eV^{-1}$. $l = 1, 2, 3...$ show a minimum as result of the interference between the two possible outgoing wavefunctions in the dipole approximation. Contrary, the selection rule for $l_i = 0$ gives a single final value without any interference, $l_f = 1$, which is shown by the horizontal black line.

In the same vein, the division of all radial transition matrix elements in equation 2.27 (for a *sp* hybridization) by $\chi^2_{1,0}$ gives β_2 as a function of ε:

$$\beta_{sp} = \frac{2(1-\gamma_p)B_1\varepsilon + \gamma_p(2A_1^2\varepsilon^2 - 4B_1A_1\varepsilon\cos\delta_{2,0})}{(1-\gamma_p)B_1\varepsilon + \gamma_p(A_1^2\varepsilon^2 + 2)} \tag{2.30}$$

where A_1 is the aforementioned Hanstorp coefficient and B_1 is a new defined Hanstorp parameter that is given by $B_1\varepsilon = \frac{\chi^2_{0,1}}{\chi^2_{1,0}}$. A visualization of equation 2.30 for different fractional p characters, γ_p, is shown in Figure 2.8.

The introduction of the parameter B_1 in equation 2.30 has, as the presence of A_1, an easy physical interpretation. The detachment from a hybrid sp orbital has in the electric-dipole approximation three possible detachment channels: $s \to p$, $p \to s$ and $p \to d$. A_1 describes the relative intensity of two detachment channels from the same AO, but the $s \to p$ channel is related with $p \to s$ through an "intercrossing" constant called B_1. These results are referred to as Hanstorp formulation of the Cooper-Zare equation, as well as the Wigner-Bethe-Cooper-Zare equation [93].

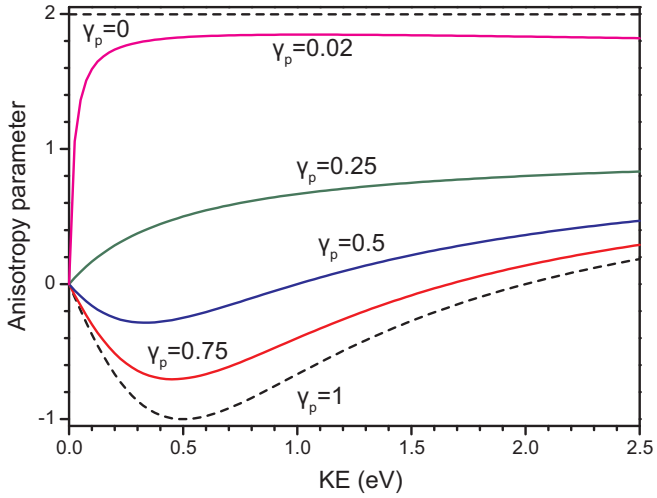

Figure 2.8: Plot of the mixed sp model in the Hanstorp formulation for arbitrarily chosen A_1 and $B_1 = 1eV^{-1}$ values and $\cos\delta_{2,0} = 1$ (see equation 2.30). Each curve represents the anisotropy parameter for different fractional p charaacters γ_p. Even a very small p component in the molecular orbital, $\gamma_p = 0.02$, modifies strongly the anisotropy parameter at low KEs towards β=0.

The explicit evaluation of A_1 and B_1, as well as any other possible parameter introduced in the general mixing formula (2.25), is done in the low-eKE approximation, originally assumed by Hanstorp et al. [93]. This approximation is defined by $kr \ll 1$ in the region where the wavefunctions of the bound state and the free-electron significantly overlap [88]. As a consequence of the Wigner threshold law, it is in principle strictly valid at vanishing small KEs [88], $\varepsilon \ll 1$ eV. However, since the prediction of Wigner law is applied to ratios that

involve cross sections in numerator and denominator this approximation is valid in a broader KE range, ≈2 eV, as several works have already proven.

Figure 2.6 depicts the spherical Bessel functions (straight curves) in the Wigner limit ($kr \to 0$), i.e., when they are given by the first terms of their McLaurin series expansions[75,88] (dashed curves):

$$j_l(kr) \cong \frac{(kr)^l}{(2l+1)!!} \tag{2.31}$$

where l is the angular quantum momentum of the outgoing photoelectron wavefunction. Therefore, the expressions for the A_1 and B_1 coefficients are:

$$\begin{aligned} A_1\varepsilon &= \frac{\chi_{1,2}}{\chi_{1,0}} = \frac{\int_0^\infty j_2(kr) r^3 R_{np}(r) dr}{\int_0^\infty j_0(kr) r^3 R_{np}(r) dr} \\ B_1\varepsilon &= \frac{\chi_{0,1}^2}{\chi_{1,0}^2} = \frac{(\int_0^\infty j_1(kr) r^3 R_{ns}(r) dr)^2}{(\int_0^\infty j_0(kr) r^3 R_{np}(r) dr)^2} \end{aligned} \tag{2.32}$$

and since $\varepsilon = \frac{k^2}{2}$ (in atomic units):

$$\begin{aligned} A_1 &= \frac{\chi_{1,2}}{\chi_{1,0}} = \frac{2\int_0^\infty r^5 R_{np}(r) dr}{15\int_0^\infty r^3 R_{np}(r) dr} \\ B_1 &= \frac{\chi_{0,1}^2}{\chi_{1,0}^2} = \frac{2(\int_0^\infty r^4 R_{ns}(r) dr)^2}{9(\int_0^\infty r^3 R_{np}(r) dr)^2} \end{aligned} \tag{2.33}$$

The final values of the Hanstorp parameters will depend on the elections of the radial parts of the bound states (in this particular case, $R_{ns}(r)$ and $R_{np}(r)$). Provided that in the central atom approximation the molecular orbital is analyzed through its resemblance with atomic orbitals, Sanov's model chooses hydrogenic wavefunctions[36,37,88] as the radial parts of bound states to evaluate the parameters. More details will appear in the studies of TaN^- and Pt_3^-.

2.1.4 Photoelectron VMI setup

Our experimental setup consists of a single-target laser ablation cluster source, a linear Time-of-Flight (ToF) mass spectrometer with a Wiley-McLaren design[94] and a velocity map imaging (VMI) unit[95]. The setup is schematically shown in Figure 2.9.

Various laser-vaporization flow-condensation sources have been developed in the early eighties in the Smalley group[96–98]. The design of our cluster source is inspired by the one used in another apparatus that is installed at the FHI and that is used for far-infrared (FIR) spectroscopic studies on metal clusters[99,100]. The source block (20 x 20 x 60 mm) is made out of stainless steel. Three channels are drilled through this block along mutually orthogonal axes. There is a vertical channel with a 6.5 mm diameter opening for the target rod (6 mm diameter rods as well as 1/4-inch rods can be used) and there are two horizontal channels with 1 mm and 3 mm diameter openings for the incoming laser pulse and for the mix of ablated material with the carrier gas, respectively. The target rod is turned by a vacuum-compatible stepper motor (Phytron VSS42-HV), mounted inside the source chamber. The motor motion is translated to a four-corner shaft by two gearwheels. The shaft slides over another one that has an inner thread, thus inducing translation and rotation of the target rod. The whole source is mounted on the back flange of the source chamber, which can be slided backwards on a motion system for easy accessibility.

Clusters are produced upon laser ablation with the second harmonic output (532 nm) of a BRIO compact Q-switched Nd:YAG laser manufactured by Quantel. The light is focused onto the rotating target rod with typical energies ranging from 1–12 mJ/pulse. The ablation laser can cause significant structural changes of the surface of the target rod[101]. The carrier gas is released from a pulsed solenoid valve (Parker, general valve series 9), mounted directly onto the 3 mm diameter, 20 mm long, horizontal channel in the source block, referred to as the cluster formation chamber. Cluster formation is strongly influenced by the pressure in this cluster formation chamber, which controls the collision rates and the heat transfer[102]. Directly in front of

the stainless steel source block, a temperature-controlled, 3 mm diameter copper channel can be mounted. The mix of gas and ablated material flows and reacts in this elongated channel and then expands through a conical converging-diverging nozzle with an opening of ≈0.7 mm into the source chamber, where there is a base pressure of 10^{-6} mbar. The temperature of the copper channel can be set to any value between -180 °C and +100 °C, using a flow of cold gas-phase or liquid nitrogen, post-heated by an electrical heating cartridge. To form cluster complexes, a second pulsed reaction valve (Parker, general valve series 9) can be mounted on the copper channel 20 mm downstream of the target rod. In this work, metal cluster anions are produced by slowly rotating the target rod with 1.2 revolutions per hour and by expanding the ablated material with a backing pressure of 15 bar of pure He into the source chamber.

About 20 mm downstream from the nozzle, a skimmer is installed to separate the source chamber from the chamber in which the mass spectrometers are mounted. This allows for the required differential pumping and restricts the ion beam to be about 10 mm in diameter at the center of the extraction region of the linear ToF mass spectrometer. Optionally, a second skimmer can be installed some 70 mm downstream from the first one to further restrict the size of the ion beam that, accordingly, reduces the cluster signal and increases the resolution. For the systems studied in this thesis, this reduction drastically hindered the photoelectron signal and, consequently, it has been removed. About 130 mm downstream from the nozzle, the charged particles in the molecular beam (in our case the anions) are perpendicularly extracted into the linear ToF mass spectrometer. For this, the electrodes of the ToF spectrometer are switched to the appropriate high voltages using fast-rising MOSFET switches (Behlke). The total flight distance of the ions from the extraction region to the multi-channel plate (MCP) detector at the other end of the horizontally mounted ToF chamber is about 830 mm. The accelerated ions are steered onto the MCP detector using electrostatic deflectors, to compensate for the initial forward velocity of the anions in the molecular beam as well as for any non-perfect alignment of the ToF electrodes. The linear ToF mass spectrometer has a resolution $\frac{M}{\Delta M}$ of about 500.

Photoelectron spectra are measured via velocity map imaging. The VMI spectrometer is coupled perpendicularly to the linear ToF mass spectrometer, and is also positioned in the horizontal plane. The center of the extraction lens of the VMI spectrometer is located at approximately 80% of the total distance along the field free drift region of the linear ToF mass spectrometer, i.e. about 17 cm in front of the MCP detector. The mass-selected ion package passes through a vertical slit with a 4 mm opening which is installed directly in front of the VMI extraction region to establish a differential pumping between the ToF chamber (with a base pressure of 10^{-6} mbar) and the chamber where the VMI spectrometer is installed (with a base pressure of 10^{-9} mbar).

The laser pulses that are used to induce the electron photodetachment of the anions are produced by a Panther EX optical parametric oscillator pumped by a Surelite II Nd:YAG laser, both manufactured by Continuum. This system delivers pulsed radiation that is tunable throughout the 205–2500 nm region. The detachment laser beam enters the experimental apparatus from the top and crosses the ion beam perpendicularly. To define the optical path of the detachment laser beam and to reduce the amount of background electrons caused by scattered light, a stack of light baffles is installed. These light baffles consist of small apertures and skimmers with 4 mm diameter openings. The voltages on the VMI electrodes are applied some 200 ns before the detachment laser is fired; this is short enough for the incoming ions not to be significantly deflected between the VMI electrodes and it is long enough that there are stable voltages on the extraction electrodes when the photoelectrons are created. After a field-free drift over about 250 mm the detached photoelectrons are amplified by a MCP detector (Chevron assembly, imaging quality, 38 mm diameter active size) and accelerated onto a phosphor screen. In order to minimize the background noise, both the imaging MCP and the CCD camera that records the images from the fast phosphor screen (P43 phosphor) are gated. The imaging MCP is operated with an offset voltage of 1200 V that is increased to a value in the 1500–1800 V range during the temporal window (50-100 ns) when the photoelectrons arrive.

The whole experiment is triggered and controlled by four 4-channel delay generators (BU 3008 delay generators made by the ELAB of the FHI Berlin).

The four cards are interconnected in series to minimize timing-jitter. The set of delay generators is controlled by the so-called KouDa software, developed by the MP department, in collaboration with the PP&B group, at the FHI Berlin. This software makes it possible to sequentially interlink all device timings in order to obtain a more robust control of the experiment "as a block" from an initial stable clock. KouDa also provides options for real-time visualization of the mass spectrum or to digitally control power supplies for more stable voltages. All voltages of the setup can be computer controlled. This is done by 16-bit digital-to-analog converters (16+8 channel Acromac IP231). The voltages for the extraction plates of the linear ToF and the VMI lens are stabilized by 0.5 μF capacitors.

The images taken by the CCD camera (Basler A102f, 1392 x 1040 pixel, 15 frames/s) are added together using a Labview computer program. Typically, a few hundred thousand laser shots are added for a single image. The repetition rate of the experiment is limited by the repetition rates of the lasers, which is in our case 10 Hz. For some systems up to 300.000 laser shots (around 8 hours acquisition time) were necessary. This sets high requirements for the stability of the experiment, as reference spectra also have to be measured for energy calibration of the imaging detector. The detected photoelectrons are converted into light flashes on the phosphor screen and digitally visualized as spots of several pixels in the recorded image, in the so-called "integration mode". Sometimes the size of the individual spots is too big to resolve sharp structures, and simply reducing the voltage on the imaging MCP does not cure this. This limitation can be overcome in the so-called "event counting mode"[103], an option that has been implemented in our program. In this mode, use is made of the fact that each event covers many pixels on the CCD chip, and that it is possible to determine its position much more accurately by centroiding every event as a single pixel using a fast computer algorithm.

The perpendicular arrangement of the linear ToF mass spectrometer and the VMI setup has the advantage that one can simultaneously monitor the anionic cluster mass spectra and the photoelectron images. Furthermore, the MCP that is used at the end of the ToF mass spectrometer has a grid in front that can be put at -5000 Volts in order to fully prevent any anionic clusters to

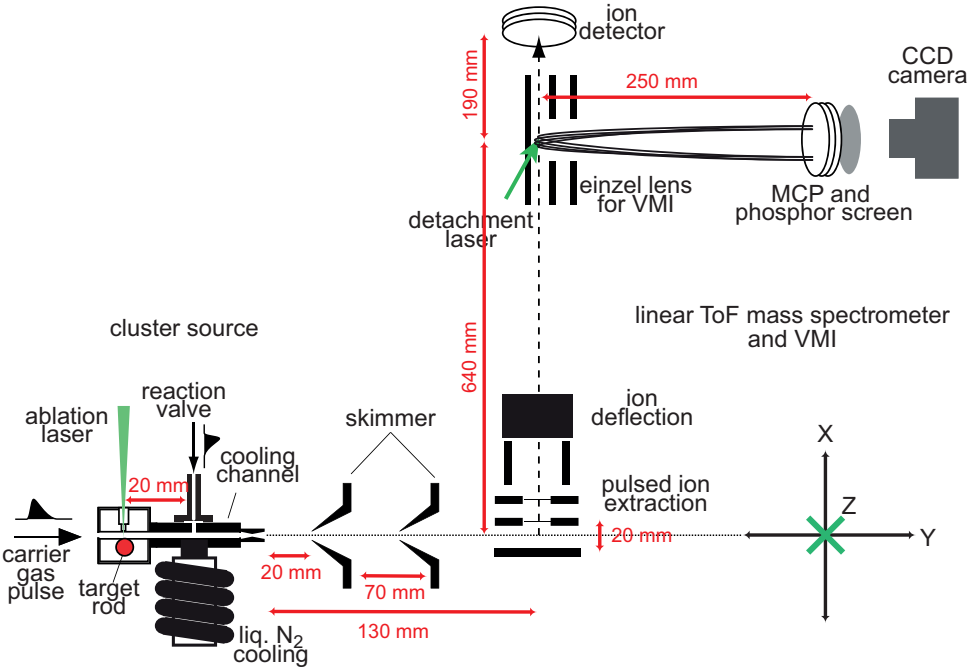

Figure 2.9: Scheme of the experimental setup. The molecular beam, the linear ToF mass spectrometer and the VMI setup are all in the horizontal plane, i.e. this is a schematic top-view of the apparatus. The detachment laser beam comes from the top, along the vertical axis.

reach the detector. The neutral clusters, produced after the photodetachment process, can pass through this grid and are energetic enough to release electrons when they impinge on the MCP detector. This allows for a real-time detection of the photodetached, neutral clusters and can be used to optimize the spatial and temporal overlap of the anions with the photodetachment laser beam. A disadvantage of this geometry, however, is that the photoelectrons have an initial velocity perpendicular to the axis of the VMI setup, given by the speed of the anionic clusters at the moment of photodetachment. This initial off-axis velocity component introduces a spatial offset of the photoelectron cloud on the VMI detector that depends on the drift-time of the cloud along the VMI axis, i.e. on the voltages that are applied to the electrodes of the VMI setup.

In the following, we wish to quantify the influence of the chosen experimental geometry on the resolution that can be obtained in the photoelectron images. For this, we first define the axis system as indicated in Figure 2.9, i.e. with X along the axis of the linear ToF mass spectrometer and with Y along the axis of the VMI setup. The repeller (lower) and extractor (center) electrodes of the linear ToF mass spectrometer are spaced by 20 mm, and are typically switched to -4000 V and -3500 V, respectively. The voltages in the linear ToF are set such that ions that originate from different positions in the extraction region arrive at the detector at the same time, i.e. space-focusing conditions are used. If we assume static voltages and an initial cluster anion packet with a width (along X) of 10 mm, there will be a spread in potential energy of the anions (and therefore in their kinetic energy later on) of 250 eV. The repeller and extractor electrodes are switched to high voltage by two independent high voltage switches, however, and the exact energy spread that the anions will have critically depends on the relative timing of these high voltage switches. The extractor is switched to high voltage slightly before the repeller is switched on, causing the anions to start-off in the "wrong" direction and to then turn around in the extraction region, resulting in some energy focusing, like in a reflectron. For the analysis below, we will nevertheless assume an original spread in kinetic energy around the mean value of $\pm$125 eV. The spatial distribution of the cluster cations along the X-axis at the point of photodetachment can be directly inferred from the observed arrival time distribution of the anions on the MCP detector. The typical width of the ion signal of about 20 ns after a total flight time of about 10 μs corresponds to a length of the packet of anions in the photodetachment region of about 1.5 mm.

For an anion of mass 600 u (close to the actual mass of the Pt_3^- system studied in this thesis) with a kinetic energy of 3750 eV, the velocity in the X-direction is about 3.5 x 10^4 m/s. This velocity displaces the center of the projected image on the phosphor screen over a distance X_{offset}, given by the product of this velocity with the time of flight of the photoelectrons over the 25 cm distance in the VMI setup. The latter is determined by the voltages applied to the VMI electrodes, and is typically around 50 ns, resulting in

value for X_{offset} of 1.75 mm. The non-negligible value for X_{offset} (that will be larger when anions with lighter masses are studied or when lower voltages are used in the VMI setup) can make it problematic to collect the whole photoelectron cloud on the MCP detector and phosphorscreen. For this reason, the VMI electrode stack can be tilted slightly away (a few degrees) from the perpendicular arrangement when high resolution experiments are performed. The initial kinetic energy spread of $\pm$125 eV, i.e. of about $\pm$3.3 % of the total kinetic energy, results in a relative velocity spread of the anions in the X-direction of about $\pm$1.7 %, and thereby causes a blurring of the image with this percentage. In the example that the value for X_{offset} is given by 1.75 mm, this blurring is about $\pm$30 μm. This is somewhat larger than the center-to-center channel resolution of the MCP (12 μm) and the grain size of the phosphorscreen (6-7 μm), so some slight smearing of the image will result from the chosen experimental arrangement.

The finite size of the region in which the photodetachment process takes place, also limits the attainable resolution in the photoelectron images. As is clearly visualized in the PhD thesis of C. Bartels[75], velocity map imaging is based on the transverse inhomogeneities of the electric field that compensate the spread of the cluster packet along the X- and Z-axes better than along the Y-axis. The size of the packet of cluster ions along the Y-axis is lastly limited by the size of the OPO laser light-beam, with a diameter of $\approx$4 mm. Therefore, some reduction in resolution resulting from the spread along the Y-axis is still expected, but it is difficult to quantify this *a priori*.

Energy resolution in the VMI setup

From the observed radial distributions in the photoelectron images, the energies can be extracted using the proportionality between the kinetic energy of the photoelectrons, KE, and the square of the distance, r, to the center of the image, via:

$$KE = k \cdot r^2 \tag{2.34}$$

Here, k is a proportionality factor that depends on the geometry of the VMI setup and on the voltages applied to the repeller, U_R, and extractor, U_E, electrodes. Differentiating the equation 2.34 we obtain for the relative energy resolution resolution, $\frac{\Delta KE}{KE}$, of the VMI:

$$\frac{\Delta KE}{KE} = 2 \cdot \frac{\Delta r}{r} \tag{2.35}$$

The voltages on the VMI electrodes are supplied by three different voltage sources. This allows us to cover variable windows of kinetic energy and to change the spectral resolution depending on the experimental requirements. The description of these voltage sources with information about the resolution reached in each case is demonstrated through calibration measurements performed on anionic atoms, the data of which are shown in Figure 2.10.

Lower resolution: The power supply NHQ215M (made by ISEG Spezialelektronik GmbH) allows to fix a maximum voltage of 5 kV with a day-to-day reproducibility of better than 1 V. This source can be controlled either manually or digitally with KouDa. The resolution is tested with the transitions:

Voltages U_R/U_E	**Wavelength (nm)**	**System**	**Transition**
4000/2671	300	Pt^-	$^3P_2$ ($[Xe]5d^86s^2$) $\leftarrow$ $^2D_{5/2}$ ($[Xe]5d^96s^2$)
3000/2027	355	Au^-	$^2S_{1/2}$ ($[Xe]5d^{10}6s^1$) $\leftarrow$ $^1S_0$ ($[Xe]5d^{10}6s^2$)

Intermediate resolution: The power supply NHQ222M 2 kV 2-channel allows to fix a maximum voltage of 2 kV with a stability of ≈50 mV. It

is controlled by a Labview program and its digital RS232 interface. The resolution is tested with the electronic transitions:

Voltages U_R/U_E	**Wavelength (nm)**	**System**	**Transition**
300/205.2	565	Pt^-	$^3D_3$ ($[Xe]5d^96s^1$) ← $^2D_{5/2}$ ($[Xe]5d^96s^2$)
280/189.3	355	Au^-	$^2D_{5/2}$ ($[Xe]5d^96s^2$) ← $^1S_0$ ($[Xe]5d^{10}6s^2$)
100/68.7	630	Rh^-	$^2F_{7/2}$ ($[Kr]4d^85s^1$) ← $^3F_4$ ($[Kr]4d^85s^2$)

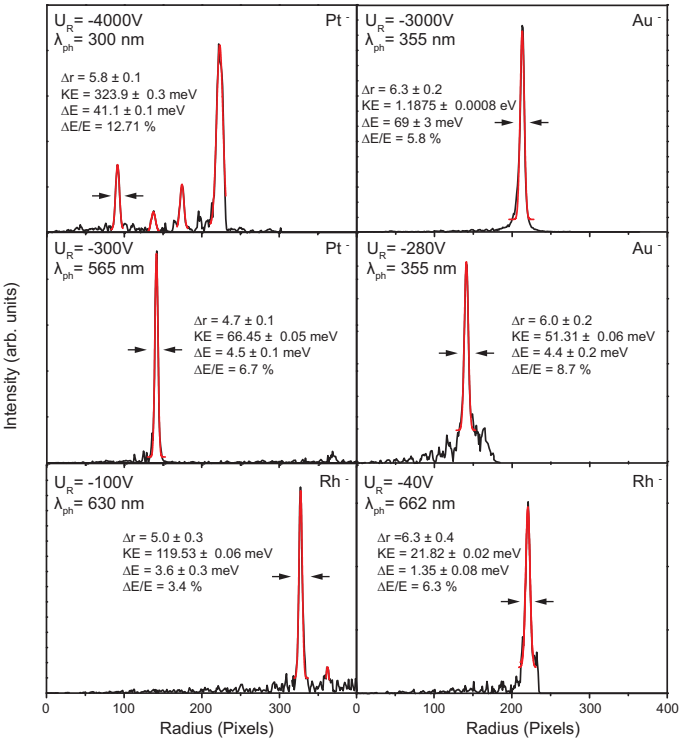

Figure 2.10: Comparison of the resolution obtained for different atomic electronic transitions with the three available power supplies for the VMI spectrometer. The lower row shows the best resolved transitions at U_R=-100 V and the one obtained in the slow electron mode at U_R=-40 V, both for anionic Rh^- atoms.

Higher resolution: In the third case we work in the slow electron mode[104] with two sources that can supply a maximum voltage of -100 V with a stability of ≈5 mV. A Labview program controls them via a Data Acquisition Device 6211 (National Instruments) and a DAQ-Link. The slow

electron mode as defined by D. Neumark[105] allows to obtain series of high-resolution photoelectron spectra, each over a restricted energy range (in our case a minimum of ≈45 meV), that can be pieced together to generate a complete spectrum. Here we used the transition:

Voltages U_R/U_E	**Wavelength (nm)**	**System**	**Transition**
40/27.6	662	Rh^-	$^2F_{7/2}$ ($[Kr]4d^85s^1$) ← $^3F_4$ ($[Kr]4d^85s^2$)

In the data shown in Figure 2.10, we observe that the resolution obtained at U_R=-4000 V is far away from the 3% mentioned in the work of Eppink et al.[95] and, moreover, it does not remain constant over the spectrum. This can well be due to the low precision of the NHQ215M power supply. The resolution is certainly improved when we use lower voltages with Au^-. The best resolution that we obtained was 3.4% with the NHQ222M power supply at U_R=-100 V, only slightly above the 2.9% energy resolution obtained on this same system in a previous work[44]. The slow electron mode at U_R=-40 V yields a lower relative energy resolution than obtained at U_R=-100 V, even though the power supply that is used for this is much more precise. Nevertheless, it yields the best absolute energies and the smallest absolute error bar of 1.35±0.08 meV (10.8 cm^{-1}), close to the 6 cm^{-1} limit given by the bandwidth of the OPO photodetachment laser. In this case, extra broadenings resulting from distortions in the circularity of the image due to spurious, weak electric or magnetic fields, cannot be excluded.

Image processing

In general, some information is lost when mapping a 3D-distribution on a 2D surface. The extraction of the velocity-map needs the original 3D distribution, which can be retrieved via an Abel inversion. As mentioned in previous works[45,106], a linearly polarized laser is used with the polarization direction parallel to the photoelectron detector surface for the photodetachment. For a given 3D distribution, $F(x, y, z)$, the projection on the detector, $f(x, y)$, is given in cartesian coordinates by:

$$f(x,y) = \int_{-\infty}^{\infty} F(x,y,z)dz = 2\int_{0}^{\infty} F(x,y,z)dz \tag{2.36}$$

and due to the cylindrical geometry of the VMI, $r^2 = x^2 + z^2$, we obtain:

$$dz = \frac{r}{\sqrt{r^2 - x^2}}dr \tag{2.37}$$

Substituting in 2.36 we obtain the Abel-transform, that relates the projection on the detector $f(x, y)$ with the 3D distribution:

$$f(x,y) = 2\int_{|x|}^{\infty} \frac{F(y,r)r}{\sqrt{r^2 - x^2}}dr \tag{2.38}$$

Therefore, given a certain 2D measurement $f(x, y)$ we can reconstruct the 3D velocity-map distribution by performing the inverse-Abel transform:

$$F(y,r) = -\frac{1}{\pi}\int_{|r|}^{\infty} \frac{\partial f(x,y)}{\partial x}\frac{1}{\sqrt{x^2 - r^2}}dx \tag{2.39}$$

However, it is extremely complex to calculate $F(y, r)$ in this way as several numerical problems will appear in this reconstruction from the experimental data. For example, $f(x, y)$ is not numerically differentiable because of the finite number of pixels on the CCD-camera. Therefore, the reconstruction problem is approached via the onion-peeling method in polar coordinates[103], also called the polar onion-peeling (POP) method.

As described in the work of Roberts et al.[107], if we consider that the 3D radial distribution is cylindrically symmetric around the Y-axis we can

express it in polar coordinates, $F(r, \theta, \phi)$, and when it is mapped onto the 2D detector we obtain the distribution $f(R, \alpha)$. The 2D projection, $f(R, \alpha)$, can be expressed as the sum of the individual 2D projections, $g(r; R, \alpha)$, for all r components of the full 3D distribution, $F(r, \theta, \phi)$:

$$f(R, \alpha) = \int_0^{r_{max}} g(r; R, \alpha) dr \tag{2.40}$$

where $R \leq r$ and the semicolon in $g(r; R, \alpha)$ is used to indicate that the 2D projections are given at specific radii r. The only circumference of this 2D projection where there is no contribution from inner Newton spheres is the one with the maximum radius, $r = r_{max}$, the outermost one, while those with $R < r$ will have multiple extra contributions from the ϕ-dependence of the electron cloud. If we subtract the most external ring (defined by the function $g(r_{max}; R, \alpha)$) from the 2D projection ($f(R, \alpha)$), we obtain for this ring a 2D distribution equivalent to a slice through the 3D distribution, $F(r, \theta, 0)$ [107]. The cylindrical symmetry of the system allows us to finally reconstruct $F(r, \theta, \phi)$ for this ring. The iterative reproduction of this process (at each r, $g(r; R, \alpha)$ is subtracted from $f(R, \alpha)$) allows to fully reconstruct the 3D image, and this is the reason why it is called "onion-peeling".

The POP method was originally developed by Zhao et al. [108]. First, the image is recorded by the CCD camera in cartesian coordinates which are converted and mapped onto a polar array. The differential area of polar and cartesian pixels remains nearly unchanged in the conversion, so the number of angles α at which pixels can be defined and, therefore, the number of polar pixels needed to define a ring will scale linearly with r. For this reason, any polar image (raw or deconvoluted) is a triangular array and looks like the window "Deconvoluted Polar Image" in Figure 2.11. After the polar conversion, the image is "peeled" in an iterative process by fitting the experimental function $g_{exp}(r; R, \alpha)$ to the angular distribution expression:

$$I(\theta) = N(r) \sum_n \beta_n(r) P_n[\cos(\theta)] \tag{2.41}$$

where the fit provides an intensity factor, $N(r)$, and the anisotropy factors, $\beta_n(r)$. This is precisely the routine followed to extract the anisotropy parameter for a desired region of the spectrum as function of the radius, which is shown in Figure 2.11. From $N(r)$ and $\beta_n(r)$, the distribution $g_{fit}(r; R, \alpha)$ may be calculated, which is then subtracted from $f(R, \alpha)$ for all $R \leq r_{max}$ in the aforementioned iterative process. As explained in the work of Roberts et al.[107], the direct numerical calculation of $g_{fit}(r; R, \alpha)$ from $N(r)$ and $\beta_n(r)$ is avoided as it is time-consuming, so we make use of idealized radial distribution functions $b_r(R)$ that form a basis set $B(R, r)$ in order to fit the experimental 2D data and to speed up the process. An idealized perfectly isotropic polar image $g_{ideal}(r; R, \alpha)$ is constructed from $b_r(R)$ using:

$$g_{ideal}(r; R, \alpha) = \rho(r, R) b_r(R) \tag{2.42}$$

where $\rho(r, R)$ introduces in $g_{ideal}(r; R, \alpha)$ the number of polar pixels at each r along with their associated intensities. Numerically, $\rho(r, R)b_r(R)$ is defined as the ratio of the number of polar pixels at r to R and accounts for the fact that in the polar image, the number of polar pixels changes to R, i.e., the polar image is a 2D triangular array. Finally, we can obtain $g_{fit}(r; R, \alpha)$ with the expression:

$$g_{fit}(r; R, \alpha) = g_{ideal}(r; R, \alpha) N(r) \sum_n \beta_n(r) P_n[\frac{R}{r} \cos(\theta)] \tag{2.43}$$

Analysis of the images

A screenshot of the Labview program used to extract the information of the spectra is shown in Figure 2.11. The program analyses the spectra following a certain protocol as described in the following:

1. VMI images are imported by the program. As a first step, the center of the image is visually fixed by introducing some approximate central coordinates and the radius of a red circumference ("Draw Mode" option) that defines the "area of interest" that will be analyzed from the whole 2D image. In case the imported image has been obtained via "Even Count mode", we can smooth the image using a subroutine ("Smooth") that assigns to

every pixel a squared matrix of pixels, the so-called Gaussian convolution (the further a pixel is away from the central one, the lower is the intensity), whose dimensions we can choose. There is also the option ("Add Images") of superimposing two different measurements in order to obtain better statistics.

2. The option "Delete Ring" allows to delete the rest of the image once the "area of interest" is fixed. This option speeds up the analysis of the image and avoids artifacts.

3. The definitive centroiding of the image is done via a trial-and-error method in which the central coordinates are slightly changed and the resultant spectra are compared, retaining the one with the best resolution. Once the central coordinates are fixed, the 2D image is symmetrized by folding its four quadrants on top of each other, as can be observed in Figure 2.11. Then, the reconstruction of the 3D velocity distribution is performed using the POP algorithm, discussed in the previous section. Additionally, one can subtract some background noise and one can select which quadrants are added up before the image is deconvoluted.

4. This reconstruction method performs the deconvolution in polar coordinates and confines the noise to the center of the image. Basis functions are used to speed up the deconvolution. The integration over all angles gives the radial photoelectron spectrum, which is calculated by the program. The program includes a visualization of the deconvoluted image in cartesian and polar coordinates.

5. The radial photoelectron spectrum can be simultaneously visualized with its corresponding β_2 parameter as function of the radius.

6. A more detailed analysis of the β_2 parameter is integrated in the subroutine "Beta Analysis" (Figure 2.12). It imports the deconvoluted image in polar coordinates and allows to select a radial region of the spectrum over which β_2 and β_4 are calculated.

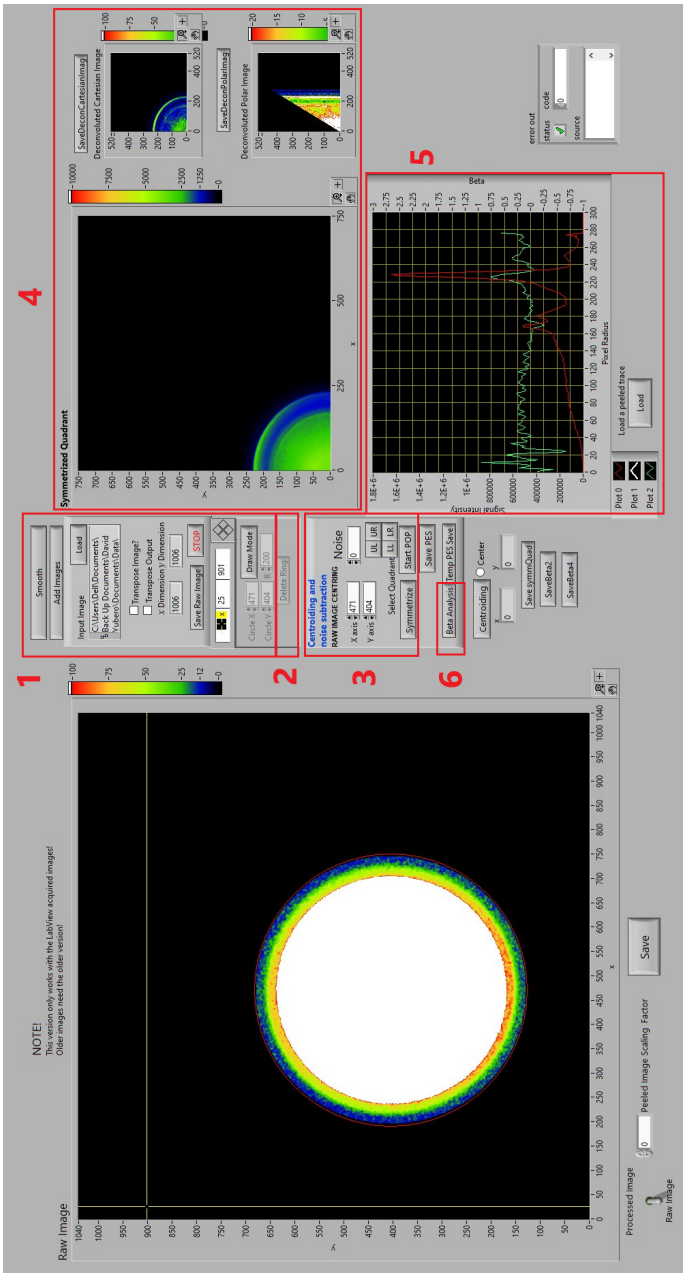

Figure 2.11: Screenshot of the Labview program interface used to analyze the images measured with the VMI. Each numbered red rectangle is explained in the text.

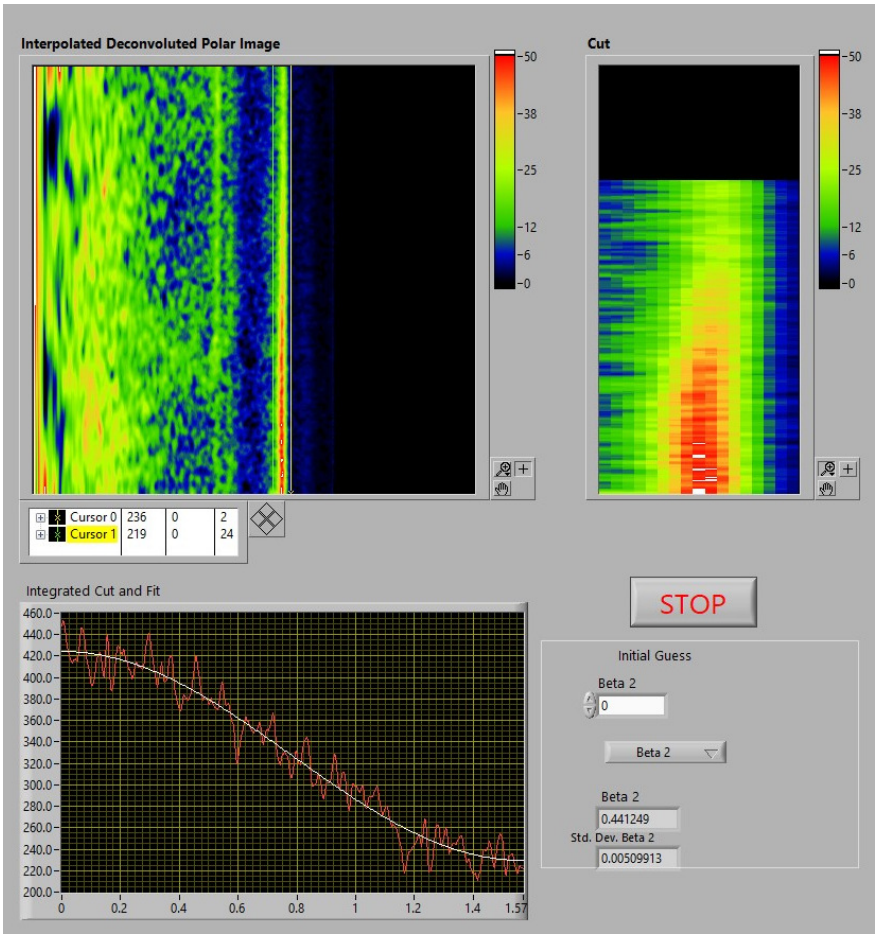

Figure 2.12: Screenshot of the Labview program interface used to analyze the β parameter. This window appears when clicking "Beta Parameter Analysis", marked with 6 in Figure 2.11.

2.2 Infrared multiple photon dissociation (IRMPD)

2.2.1 Vibrational spectroscopy

The spatial description of a molecule with N atoms requires $3N$ coordinates (x, y and z) and, therefore, it has $3N$ degrees of freedom. Three of them correspond to the movement of the center of mass in the molecule along axis X, Y and Z, the so called, translational movement, and other three to its rotations (2 in case of linear molecules). The remaining $3N - 6$ degrees of freedom ($3N - 5$ for linear molecules) are vibrational. Vibrational degrees of freedom can often be approximated by orthogonal motions called normal modes[109] in which all atoms in the molecule vary their positions sinusoidally with the same frequency and the same or opposite phase[110]. The normal modes in a molecule can be considered as "fingerprints" of its geometrical structure as they depend on the mass of the atoms involved in the motion and the nature of the chemical bonds.

Molecular vibrations can be described in the harmonic oscillator approximation, that obeys the Hooke's law, for small displacements. The potential of a one-dimensional harmonic oscillator is $V(x) = \frac{1}{2}kx^2$, where k is the force constant associated to the molecular vibration and x is the displacement from the equilibrium position. The quantum mechanical Hamiltonian harmonic oscillator is:

$$H = -\frac{\hbar^2}{2\mu}\frac{d^2}{dx^2} + V(x) \tag{2.44}$$

and the eigenvalues of the Hamiltonian, E_υ, are given by:

$$E_\upsilon = \hbar\omega(\upsilon + \frac{1}{2}) \quad \text{and} \quad \omega = \sqrt{\frac{k}{\mu}} \tag{2.45}$$

where $\hbar$ is the reduced Planck constant, μ is the reduced mass of the atoms involved in the oscillation, υ is the quantum number of the oscillator and ω is the angular frequency. Only one photon is allowed to be absorbed at a time by the molecule according to the selection rules[111] (as discussed below) and it increases υ by one.

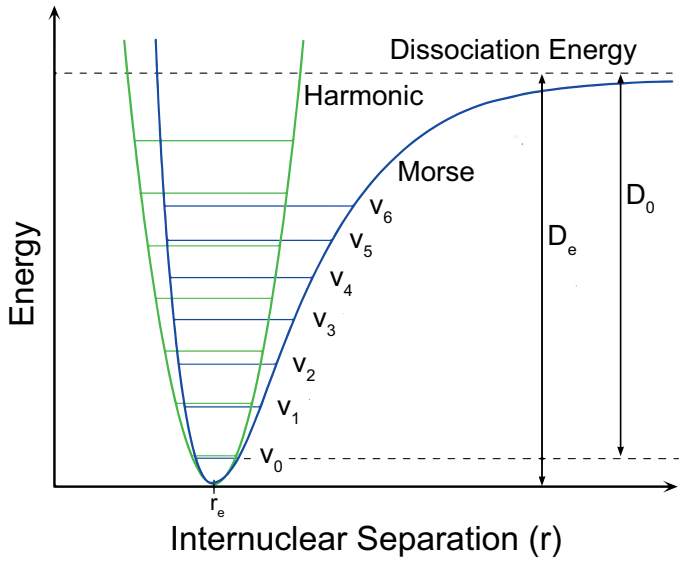

Figure 2.13: Comparison between the harmonic and Morse potentials. The energy levels in the harmonic potential are equally spaced and the potential is symmetric around r_e. The Morse potential is not symmetric around r_e and the energy levels are more closely the higher is the energy. The figure is adapted from [113].

Nevertheless, this assumption is only valid when the displacement from the equilibrium position, x, is small. At large values of x, when excited with enough quanta of vibrational energy, the molecule shows mechanical anharmonicities and it ultimately can dissociate. The real behavior of a molecule is better modeled via the Morse potential [112]:

$$V(x) = D_e(1 - e^{ax})^2 \quad \text{and} \quad a = \sqrt{\frac{k_e}{2D_e}} \tag{2.46}$$

where D_e is the depth of the potential well at the equilibrium internuclear separation, k_e is the force constant at this separation and x is the instantaneous internuclear separation. A comparison between pure harmonic and Morse potentials is shown in Figure 2.13.

By substituting the Morse potential in 2.44, the resulting Schrödinger equation can be analytically solved and its energy levels are given by:

$$E_\upsilon = \hbar\omega(\upsilon + \frac{1}{2}) - \hbar\omega x_e(\upsilon + \frac{1}{2})^2 \quad \text{and} \quad \omega = \sqrt{\frac{k}{\mu}} \tag{2.47}$$

where the anharmonicity constant is $x_e = \frac{\hbar\omega}{4D_e}$.

Some consequences of the anharmonicities in the Morse potential are that the energy levels are not equidistant because they become closer the higher the energy is and that the strict orthogonality in the vibrational modes "relaxes" since they couple via anharmonic terms, what allows the appearance of overtones and combination bands. This intercoupling between normal modes is very important in the mechanism of internal vibrational redistribution (IVR). Moreover, the Morse oscillator is only an approximation to the real model for the molecular vibrations. Indeed, perturbation theory permits to write the vibrational energy levels in a Taylor series of the form:

$$E_\upsilon = \hbar\omega(\upsilon + \frac{1}{2}) - \hbar\omega x_e(\upsilon + \frac{1}{2})^2 + \hbar\omega y_e(\upsilon + \frac{1}{2})^3 ... \tag{2.48}$$

where x_e and y_e are the first and second anharmonicity constants, respectively.

In the IRMPD experiments, the dissociation occurs after the absorption of several photons in the infrared (IR) region. Such interaction between molecules and light leads to vibrational transitions within the cluster when the frequency of the incoming radiation coincides with the vibrational frequency of a normal mode in the molecule. As the nuclei do not have a fixed position, the charge distribution undergoes a change during the vibrational motion of the molecule along the n vibrational nuclear normal coordinates, Q_i, so the dipole moment of the molecule changes periodically. The molecular wavefunction can be expressed in the adiabatic Born-Oppenheimer (BO) approximation:

$$\Psi(\boldsymbol{r}, \boldsymbol{Q}) \approx \psi(\boldsymbol{r}; Q)\chi(\boldsymbol{Q}) \tag{2.49}$$

where $\psi(\boldsymbol{r}; Q)$ and $\chi(\boldsymbol{Q})$ are the electronic and nuclear wavefunctions, whilst rotation has been neglected, that is, the motions of electrons and nuclei are

referred to a molecule-fixed coordinate system [111]. Let us suppose a transition between two molecular states, Ψ^i and Ψ^f, in a polyatomic molecule, where the electronic state does not change, $\psi^i = \psi^f = \psi$, the transition moment is given by:

$$\boldsymbol{R} = \langle \Psi^f | \boldsymbol{\mu} | \Psi^i \rangle = \iint \psi^{f*} \chi^{f*} \boldsymbol{\mu} \psi^i \chi^i d\tau_e d\tau_N = \int \chi^{f*} [\int \psi^* \boldsymbol{\mu} \psi d\tau_e] \chi^i d\tau_N \tag{2.50}$$

where the dipole moment operator for n nuclei with atomic numbers Z_n is:

$$\boldsymbol{\mu} = -\sum_m e\boldsymbol{r_m} + \sum_n Z_n e\boldsymbol{r_n} \tag{2.51}$$

The integral within brackets, $[\int \psi^* \boldsymbol{\mu} \psi d\tau_e]$, is the expected value of the dipole moment operator in the electronic state ψ, also called the electric dipole moment of the molecule, $\boldsymbol{\mu_e}$, so the transition moment is expressed as:

$$\boldsymbol{R} = \int \chi^{f*} \boldsymbol{\mu_e} \chi^i d\tau_N = \langle \chi^f | \boldsymbol{\mu_e} | \chi^i \rangle \tag{2.52}$$

As the integration in $\boldsymbol{\mu_e}$ is done over the electronic coordinates, it is only function of the nuclear ones. $\boldsymbol{\mu_e}$ and its periodical changes can be expressed for small displacements around its value at the equilibrium position, $\boldsymbol{\mu_e}(Q_0)$, as [114]:

$$\boldsymbol{\mu_e} = \boldsymbol{\mu_e}(Q_0) + \sum_j^n \left(\frac{d\boldsymbol{\mu_e}}{dQ_j} \right)_0 Q_j + \frac{1}{2!} \sum_j^n \left(\frac{d^2\boldsymbol{\mu_e}}{dQ_j^2} \right)_0 {Q_j}^2 ... \tag{2.53}$$

where $\boldsymbol{\mu_e}(Q_0)$ is the permanent dipole moment and $\frac{d\boldsymbol{\mu_e}}{dQ_j}$ are the changes induced in $\boldsymbol{\mu_e}$ when the molecule vibrates [38]. Considering the linear approximation for the electric dipole moment, the transition moment can be written as:

$$\begin{aligned} R_{\Psi'\Psi''} &= \langle \chi^f | [\boldsymbol{\mu_e}(Q_0) + \sum_j^n \left(\frac{d\boldsymbol{\mu_e}}{dQ_j} \right)_0 Q_j] ... | \chi^i \rangle = \\ &= \boldsymbol{\mu_e}(Q_0) \langle \chi^f | \chi^i \rangle + \sum_j^n \left(\frac{d\boldsymbol{\mu_e}}{dQ_j} \right)_0 \langle \chi^f | Q_j | \chi^i \rangle + ... \end{aligned} \tag{2.54}$$

The orthogonality condition in the vibrational wavefunctions results in the selection rule $\Delta\upsilon$=0, giving rise to the pure rotational spectrum of the molecule. Additionally, the IR selection rules can be deduced by only taking the first order added term for the k vibrational normal mode and by writing χ^f and χ^i in terms of their quantum numbers υ[114]:

$$\left(\frac{d\boldsymbol{\mu_e}}{dQ_k}\right)_0 \langle\chi^f|\, Q_k\, |\chi^i\rangle = \left(\frac{d\boldsymbol{\mu_e}}{dQ_k}\right)_0 \langle\upsilon_k^f|\, Q_k\, |\upsilon_k^i\rangle \prod_{j\neq k}^{n} \langle\upsilon_j^f|\upsilon_j^i\rangle \tag{2.55}$$

The right side of equation 2.55 is non-zero when three conditions are fullfilled: $\left(\frac{d\boldsymbol{\mu_e}}{dQ_k}\right)_0 \neq 0$ means that the displacement along the normal vibration k is associated with a change in the electric dipole moment and, therefore, k is IR active. If υ_k^f and υ_i^f are harmonic oscillator wavefunctions, $\langle\upsilon_k^f|\, Q_k\, |\upsilon_k^i\rangle \neq 0$ is only possible for transitions with $\Delta\upsilon$=$\pm$1 in mode k. $\langle\chi_j^f|\chi_j^i\rangle \neq$0 implies that the population quantum numbers in the modes $j \neq k$ do not change during the vibrational transition and, therefore, combination bands in the transitions are forbidden. Furthermore, the presence of electrical and mechanical anharmonicities relaxes the selection rule $\Delta\upsilon$=$\pm$1 and allows the appearance of overtones ($\Delta\upsilon$=$\pm$2,$\pm$3).

2.2.2 IR spectroscopy and IVR phenomenon

The most common technique in vibrational spectroscopy is IR absorption spectroscopy, in which the attenuation of incoming light trough a sample is measured. The Beer-Lambert law[109] gives the relationship between the incoming and outgoing light intensities, I_0 and I:

$$\frac{I(\nu)}{I_0(\nu)} = e^{-\sigma(\nu)nl} \tag{2.56}$$

where $\sigma(\nu)$ is the absorption cross-section, n is the particle number density and l the path length trough the sample. Performing spectroscopy by the direct measurement of the absorbed light works for condensed samples and for certain pure gas samples, but the latter (gas samples) impose several limitations. In case there are many different species present in the sample,

the assignment of the observed absorptions to each of the species turns out to be very difficult. As well, the sensitivity of this technique in the gas phase is limited by low densities. Since the absorption cross-section of gas-phase molecules varies from $\sim 10^{-12}$ cm^2 to $\sim 10^{-25}$ cm^2, the product nl in the lowest cross-section situation must be $\geq 10^{16}$ molecules/cm^2 to obtain an absorption spectrum. In some cases, these limitations can be overcome by using cavity-ring down spectroscopy (CRDS) [115–117], where very long path lengths, l, are established to reach the desired nl value. Even so, certain limits become insuperable since, for example, the densities for ionic species in the gas phase are limited to around 10^6 ions/cm^3 due to Coulomb repulsion [118].

For very low densities in the gas phase, it is preferable to approach experimentally the system via action spectroscopy where, instead of measuring the changes induced in the light by crossing the sample, the changes in the sample by interacting with the light are investigated. The light-matter interaction in a two level system is modeled similarly to the Beer-Lambert law by:

$$\frac{N(\nu)}{N_0} = e^{-\sigma(\nu)F(\nu)} \tag{2.57}$$

where $\sigma(\nu)$ is the absorption cross-section, N_0 and $N(\nu)$ are the populations before and after the interaction with the light and $F(\nu)$ is the photon fluence. The comparison of 2.56 with 2.57 brings up the suitability of action spectroscopy for low cross-sections since it is much easier to obtain $F(\nu)$=10^{16} photons/cm^2 rather than nl=10^{16} molecules/cm^2. Among the different action techniques (fluorescence, ionization, etc.), infrared photodissociation (IRPD) spectroscopy, where the studied molecules are dissociated, is the method employed along this thesis.

IRPD relies on mass spectrometry, as it allows the separation of the sampled species, by monitoring the photodissociation yield in the species of interest as a function of the laser frequency. Metal clusters are strongly bound systems with bond dissociation energies (BDEs) on the order of >1 eV. However, the energies of IR photons range from few meV to several hundred meV and their dissociation requires the absorption of several photons, recalling

this spectroscopy as IR multiple photon dissociation (IRMPD). The IRMPD technique allows to obtain spectra for some systems, such as metal complexes (being the ligand CO[119,120], O_2[121,122], CO_2[123]etc.) in the mid-IR, probing the geometric structure of the complex upon dissociation of the bare cluster from the ligand. The equation that defines this process is:

$$AB^{+/0/-} \xrightarrow[nh\nu(MIR-PD)]{} (AB^{+/0/-})^* \rightarrow A^{+/0/-} + B \tag{2.58}$$

where $AB^{+/0/-}$ is the complex, $A^{+/0/-}$ is the metal cluster and B is the ligand dissociated from the cluster upon absorption of photons that excite the vibrational frequency of the adsorbed ligand on the cluster or other modes.

Nevertheless, even the use of IR sources with high photon fluence (as the FELs used in this thesis) for strongly bound systems might not be sufficient to produce dissociation of transition metal or semiconductor clusters via IRMPD spectroscopy. Their high BDEs, low absorption cross-sections or the low energy inherent to a single photon in the far-IR (where the vibrational modes of the bare cluster are accessed) constitute experimental impediments. In these cases, the "messenger tagging" technique[124] is required.

The aim of the "messenger tagging" technique is to reduce the number of absorbed photons necessary to dissociate the complex to a minimum without changing the original cluster properties, but sometimes perturbations in the IR absorption cross-section[121,125] and structure[126] of the bare cluster have been found. More concretely, it consists on the formation of a weakly bound messenger complex by using rare gas atoms (Ar in our experiments) as messenger ligands. Some difficulties arise when producing the messenger-cluster complexes due to the low binding energies between both of them. They can be overcome by the use of highly polarizable messengers and low temperatures. As well, the net charge of the cluster has a big influence: For neutral clusters the interaction with the messenger is via van-der-Waals forces, whilst for ionic ones it is stronger, as it is mainly dominated by charge-induced dipole interaction. Afterwards, the dissociation of the physisorbed messenger is possible (even in the far-IR) as the BDEs are quite low. The reaction that

defines this process is:

$$AB^{+/0/-}.M \xrightarrow[h\nu]{} (AB^{+/0/-})^*.M \xrightarrow[IVR]{} AB^{+/0/-} + M \tag{2.59}$$

where the complex $(AB^{+/0/-}.M)$ is formed by the bare cluster $(AB^{+/0/-})$ and the messenger (M). The binding energies of rare-gas messengers that are adsorbed on cationic clusters can reach 0.1–0.3 eV, while for neutral clusters a single IR photon absorption can be enough to dissociate the messenger from the cluster.

As deduced from subsection 2.2.1, the anharmonicity of the vibrational energy ladders makes the absorption of many monochromatic photons by a completely coherent process impossible[124–126]. The energy spacing between consecutive vibrational levels becomes gradually smaller until the laser frequency is not in resonance with the vibrational transition and no photons are absorbed anymore. This phenomenon is called "anharmonic bottleneck" and in has been normally circumvented by the description of the multiple photon absorption mechanism as divided in three overlapping regions: the resonant regime, the quasi-continuum and the true continuum[99,127,128].

The resonant regime is characterized by a sequential and resonant absorption of photons until the "anharmonic bottleneck" is reached. For the first photons this effect is, somehow, compensated by broadenings coming from the bandwidth of the laser, temperature effects and rotational levels that can be populated. As well, the internal energy of the system increases, so does the density of its accessible rovibronic states and the "anharmonic bottleneck" relaxes the strict orthogonality in the vibrational modes via anharmonic effects. Consequently, the energy can be redistributed in the dark vibrational degrees of freedom through a process known as IVR, whose rate depends on the density of vibrational-rotational states and so, increases with the size of the system. In this model, the true continuum region is reached when the internal energy of the system is very high and the dissociative channel opens up. The huge density of states and the strong anharmonic coupling between many vibrational-rotational states allow the absorption of photons with any

frequency and, therefore, the IVR rates are so fast that the internal energy is statistically distributed over all vibrational degrees of freedom [129].

Nevertheless, the model adopted in this thesis at very high internal energies is not the one described the latter paragraph, but the one guided by the theoretical explanations of infrared-resonance-enhanced multiple multiphoton ionization (IR-REMPI) experiments with superhot (1970 K≈18 eV) C_{60} molecules [130,131]. Despite the high density of vibrational states at such high internal energies (>10^{100} states/cm^{-1}), the broadening and shift of the spectroscopic lines remain small enough to observe a clear resemblance to the spectra on C_{60} at 875 K or at room temperature, nearly regardless of the cluster temperature. Therefore, the whole dissociation process is here rationalized by a sequential absorption of single IR photons followed by fast energy redistribution [130], rather than the existence of a "continuum regime" at high internal energies.

2.2.3 Ar-tagging of bare transition metal clusters

The noble gases are a group of chemical elements with very low chemical reactivity. Their inertness is explained by an electronic configuration with a full valence shell. Comparatively, the lighter ones are the most inert due to the higher stability of their valence shell as it is less screened from the nucleus by a smaller number of core shell electrons. Among the noble gases, argon is the most abundant noble gas on Earth [132] and its name comes from the Greek term that means "lazy" or "inert" [133]. Bare ArH^+ has been the first molecule containing a noble gas detected in outer space [134,135]. Despite its inertness, a plethora of complexes with argon have been detected via inert gas matrix isolation, cold gases and plasmas through different spectroscopic methods as visible and UV spectroscopy, IR spectroscopy or microwave and far-IR spectroscopy in order to elucidate their electronic, vibrational and rotational structures.

The formation of Ar-complexes with cationic species is energetically favored with respect to neutral or anionic ones due to the negative electron affinity of Ar [136]. Binding between Ar and a negative complex ($[B_{12}(CN)_{11}]^-$)

at room temperature was very recently observed for the first time by using $[B_{12}(CN)_{12}]^{2-}$ (the electronically most stable dianion ever found) as a precursor[137]. Among the neutral complexes, HArF is up to date the only neutral and stable compound containing Ar. It was experimentally isolated at low temperatures[138] with calculations on its bonding nature indicating that the H-Ar bond is covalent, whilst the Ar-F is mainly of electrostatic nature[139]. Furthermore, many neutral complexes (van der Waals molecules bound by London dispersion forces) have been produced in the laboratory by binding neutral Ar with neutral atoms and molecules in their ground state (Ag_2Ar[140], NaAr[141,142], KAr[143], RbAr[144], etc.). Further excited state complexes, such as ArF^*, can be covalently bound. Indeed, the example of ArF^* constitutes the cornerstone of the fluorescence mechanisms in the excimer (193 nm) lasers.

As mentioned in the work of Jin et al.[137], argon can act as a Lewis base that is able to coordinate to positively charged metal centers in neutral and cationic complexes. For example, some neutral molecules are given by ArMX (with M = Cu, Ag, Au, etc. and X = F, Cl, Br or O[145–147]) or, also, by the reaction of the pentacarbonyls $M(CO)_5$ (with M = Cr, Mo, W) and Ar. The latter (carbonyl compounds) were discovered in 1975[148] and their bonding nature has been theoretically studied[149,150] concluding that the stabilizing interactions between the pentacarbonyl fragment and the noble gas are mainly dominated by the orbital interactions between equatorial carbonyl groups and noble gas p orbitals (whose p_z orbitals are stabilized) added to some dipole-induced dipole interactions[150].

The strongest bond to Ar appears in complexes with cationic species[152–154]. In complexes with cationic transition metals, the comparatively strong bond of Ar with the metallic species is rationalized by Grills et al.[148] by a process where the positive charge of the metal fragment's molecular orbitals contracts the metal d orbitals provoking two effects: on one hand and to a smaller extent, a lowering of their energy that decreases a possible π-backbonding and that increases the overlap with the p orbitals of the Ar upon the electron donation to the metal orbitals and, on the other hand and much more relevant,

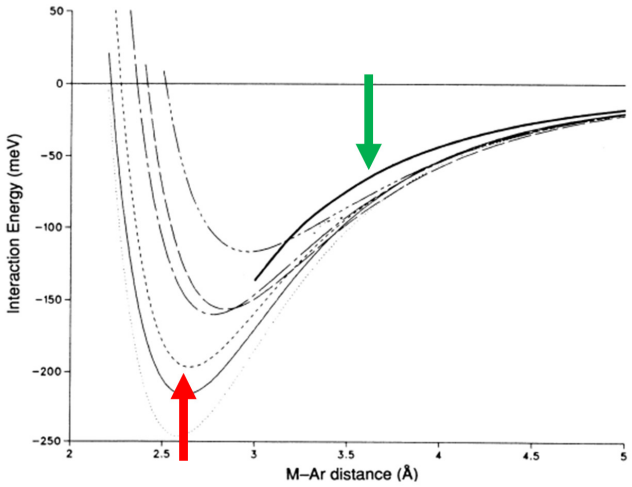

Figure 2.14: Shape of the interaction potentials for the $4s^0 3d^{n-1}$ M^+-Ar series as calculated by Hammond et al.[151], where the Figure is adapted from. The red arrow tags the Co^+-Ar curve and the green one the $V(r) = -\frac{1}{2}\frac{\alpha q^2}{r^4}$ potential.

an enhancement of the electrostatic charge-polarizability attraction between the metal center and the Ar atom[148].

The easiest way to investigate the interaction between transition metal cations and Ar atoms are the diatomic Metal-Ng complexes. Many experimental[155,156] and theoretical[151] studies have pursued this goal and according to the work of Hammond et al.[151] such interaction is divided into three different regions: at long distances dominates an attractive charge induced-dipole interaction, at intermediate distances a molecular-orbital overlap of covalent origin materialized in a partial electron transfer from Ar to the cation and, finally, a Pauli repulsive interaction at short distances. For the purposes of this thesis, the attractive interaction between the cationic metal atom (or metal cluster) and the attached Ar atom(s) can be described by the point charge-induced dipole interaction, $V(r) = -\frac{1}{2}\frac{\alpha q^2}{r^4}$, where the metal is considered the point charge with q=+1 and α is the dipole polarizability of the Ar[151]. Plots of calculated potentials are shown in 2.14.

Furthermore, many more other Ar compounds as polyatomic van der Waals molecules[157,158], cluster argon cations[159],etc. have been subjects of research, but these topics are beyond the scope of this thesis.

2.2.4 IR-FEL principles

Common commercial lasers use as gain medium atomic and molecular transitions in solids, liquids or gases, which is limiting their frequency range. Alternatively, free-electron lasers (FELs) use free electrons at relativistic velocities as gain medium [160,161], allowing in principle for a wider tunability, compared to table top systems. The IRMPD results presented in this thesis were obtained using two different IR-FELs: the Free Electron Laser for Infrared eXperiments FELIX in Nijmegen [162,163] and the FHI-FEL in Berlin [164].

The general mechanism to produce light via FELs is shown in Figure 2.15. An electron gun produces free electrons that are accelerated to relativistic velocities with a linear accelerator. These electrons are then injected into an undulator, an array of alternating poled magnets that generate an alternating static magnetic field with periodicity λ_u, where they take oscillatory trajectories due to the Lorentz force. The electrons then emit spontaneously synchrotron radiation with a laboratory frame wavelength of:

$$\lambda_{FEL} = \frac{\lambda_u}{2\gamma^2}(1 + K^2) \tag{2.60}$$

where λ_u is the period of the undulator, γ is the Lorentz factor, $\gamma = \frac{1}{\sqrt{1-\frac{v^2}{c^2}}}$, and K is a dimensionless parameter related to the strength of the magnetic field in the undulator. K, usually close to 1, accounts for the reduction of the effective forward velocity of the electron and hence, the Doppler shift caused by the induced transverse motion [165]:

$$K = \frac{8B_0\lambda_u}{\sqrt{8}\pi m_e c} \tag{2.61}$$

where B_0 is the magnetic field strength, m_e the mass of the electron in the rest frame and c the speed of light.

Due to the relativistic nature of the beam, this spontaneous radiation comes in a monochromatic cone around the forward direction. Nevertheless, as

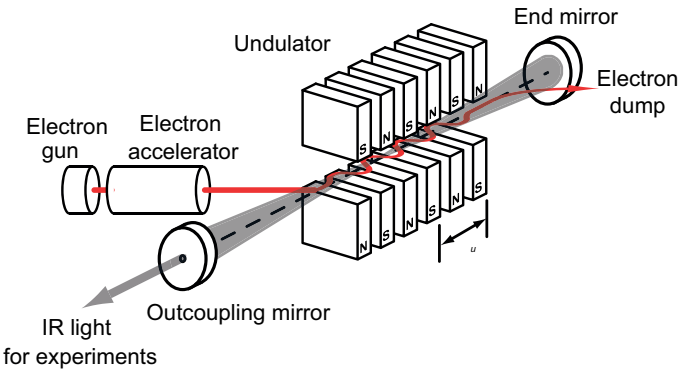

Figure 2.15: General scheme of a free electron laser. An electron beam is produced by an electron gun, accelerated to relativistic velocities and injected into a magnetic undulator. The Lorentz force experienced by the beam curves the trajectories and results in spontaneous emission of radiation. This radiation is coherently enhanced by an optical cavity in which the undulator is placed. The original picture belongs to [166].

the spatial spread of the electron bunches is larger than λ_u, this spontaneous radiation originates at different points in space and is initially incoherent and weak. The light is captured in a cavity and the interaction of the initially weak light with fresh electron bunches causes a spatial modulation of the electrons in a bunch (microbunching) with a period equal to the optical wavelength. Those microbunches can emit light coherently, causing an increase in light, which in turn causes more effective microbunching. The power of the light field can increase many orders or magnitude via this mechanism until saturation is reached. A part of the radiation is coupled out of the cavity via a small hole in one of the cavity end mirrors and is then brought to the different experiments.

FELIX & FHI-FEL

At FELIX a thermionic triode electron gun produces at 1 GHz repetition rate electron pulses which are bunched and accelerated to 3.8 MeV. As shown in Figure 2.16, the electron beam is first injected into a first 3 GHz travelling-wave radio-frequency linear accelerator (Linac 1) which accelerates to energies between 15 and 25 MeV. After Linac 1, the electron beam can be deflected and steered into the long wavelength FEL-1. Alternatively, the electrons

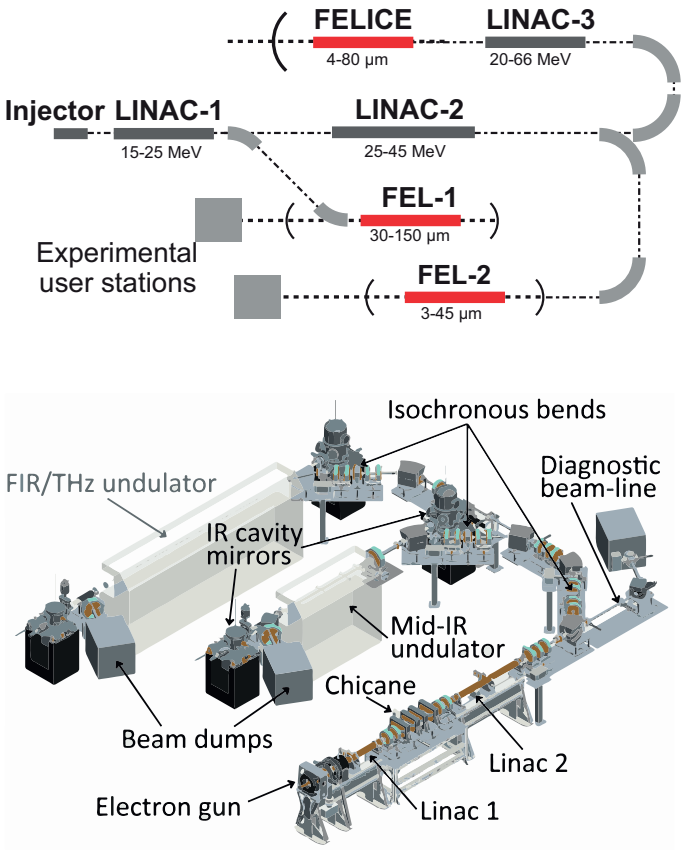

Figure 2.16: (Upper) Scheme of the FELIX installation at the Radboud University, Nijmegen. FELICE is here also shown but not used in this thesis. This picture has been adapted from [166]. (Lower) Scheme of the FHI-FEL installation. Only the MIR-FEL in the center has been present and in operation since 2013. Currently, an upgrade is taking place involving a far-IR arm and the possibility of two color operation that shall be operational from 2022. The picture was taken from [164].

can be further accelerated to 25–45 MeV in a second accelerator (Linac 2) and introduced into either FEL-2 or FELICE. The undulators in FEL-1 and FEL-2 contain permanent magnets in 38 field periods of 65 mm period length. The wavelength range covered by FEL-1 is 30–150 μm while that of FEL-2 is 3–45 μm [167].

The FHI-FEL is similar and described in detail elsewhere [164], and only a brief outline is given here. A thermionic electron gun produces pulses of

electrons with a repetition rate of 1 GHz in macro pulses with a length of typically 15 μs. The temporal length of the micro pulses of initially a few picoseconds is too long for an efficient capture in the linac and a buncher cavity is used to compress the pulse length. The electron beam is then accelerated by a first linac to a constant energy of 20 MeV, while the second linac accelerates or decelerates the electrons to a final energy between 15 and 50 MeV. The electrons are then steered into the MIR undulator. The undulator is 2 m long and contains 50 magnetic periods of 40 mm length and it is located in a 5.4 m long cavity formed by two gold-plated copper mirrors. The outcoupling side of the cavity is motorized with an in-vacuum mirror changer that allows to exchange between five out-coupling mirrors with different outcoupling-hole diameters in order to optimize the performance at different wavelengths. As

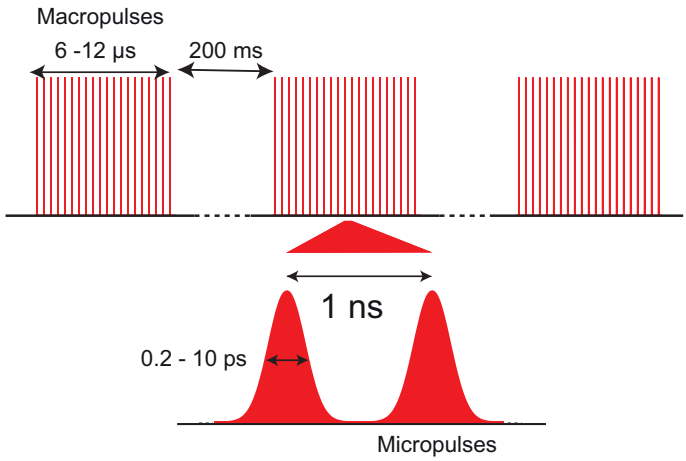

Figure 2.17: Schematic picture of the FEL pulse structure at FELIX as well as FHI-FEL. The picture was adapted from[168].

in the case of FELIX, tuning is performed by changing the undulator gap and the accessible spectral range is 200–3000 cm^{-1} with a FWHM bandwidth between 0.3 and 1% of the central wavelength. Macro pulse energies in excess of 150 mJ can be obtained. See also the references[169–171] for more examples of the application of FELs in cluster research.

2.2.5 IRMPD setup

The IRMPD experiments were performed in two different setups. One is located at the Radboud University Nijmegen and coupled to the free electron laser FELIX while the other machine is located at the FHI in Berlin and coupled to the FHI-FEL. The experimental setups are designed to allow for spectroscopic experiments on anionic, neutral and cationic clusters and cluster-ligand complexes. Both are described in detail elsewhere[44], and only a brief outline will be given here. The setups are very similar in design and construction and, if not noted otherwise, descriptions apply to both machines.

A scheme of the experiment is shown in Figure 2.18. Clusters are produced in a laser ablation cluster source. The cluster beam then passes a skimmer and can interact with light from the IR-FEL. Neutral clusters can be ionized using VUV radiation while charged clusters can directly be analyzed with a reflectron time-of-flight mass spectrometer (ReToF)[172] manufactured by Jordan TOF Products Inc. The clusters source is a Smalley-type[96] laser

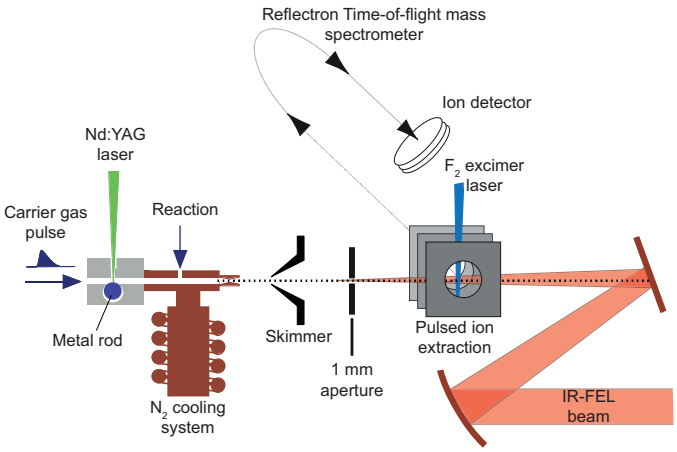

Figure 2.18: Scheme of the IMPRD experiment placed at the Fritz Haber Institute in Berlin. Currently, the experiment has been further developed by adding a dual target source and a VUV 4-wave mixing generator.

vaporization cluster source similar to the one described in 2.1.4. The source block is made out of stainless steel with three intercrossed channels. In a vertical channel, the target rod (6 mm or $\frac{1}{4}$ in) is translated and rotated.

The 2nd harmonic light from a pulsed Nd:YAG laser enters through a second channel to generate a plasma of ablated material. Carrier gas is introduced through the third channel via a pulsed gas valve (either pure He or He mixed with low percentage or Ar) to cool down and quench the ablation plasma. Cooling and clustering occurs while traveling through a temperature controlled reaction copper channel, whose temperature can be controlled between -180°C and +100°C by means of a liquid nitrogen flow and a heating cartridge. Additionally, a second pulsed valve can be mounted on this channel downstream of the target rod to supply gases such as, for example, CO or CH_4 to form cluster complexes. The gas pulse then leaves the copper channel via a nozzle and expands supersonically into the vacuum to afterward pass a skimmer that separates the cluster source region from the spectroscopy region.

Before the clusters are deflected into the ReToF by plates to which high voltage can be applied, they pass through a small aperture with a diameter of 1 mm. As shown in Figure 2.18, the aperture limits the cluster beam diameter to ensure that all clusters which are extracted into the ReToF are illuminated by the FEL light. Additionally, when studying neutral clusters, a moderate voltage (100–200 V) is applied to the aperture in order to get rid of charged clusters in the molecular beam. In those experiments on neutral clusters, 157 nm light from a pulsed F_2 excimer laser crosses the cluster beam perpendicular to the propagation direction to ionize the clusters prior to deflection into the ReToF. The power of this laser must remain low to avoid double ionization or cluster fragmentation. Then, the high voltage deflection plates, previously set to a positive or negative voltage to either study cationic or anionic clusters, extract them into the ReToF region and finally detect them on the MCP detector. The mass resolution of the ReToF is $\frac{M}{\Delta M}$=2000. Experimental timings, display of mass spectra or visualization of current cluster fragmentations, as well as data acquisition are controlled in the Berlin setup via a software called KouDa, which has been developed by the FHI. The experiment in Nijmegen is controlled with self-developed LabView routines.

To enable experiments with the FEL, two gold coated mirrors are placed in the extraction region to focus the incoming FEL light counter propagating

to the molecular beam (see Figure 2.18). In order to maximize the spatial overlap with the molecular beam, the focal point of the light beam is set slightly behind the 1 mm aperture, so the whole aperture area is illuminated with IR light. Temporal overlap between clusters and IR light is sought by changing the delay between the cluster source and the FEL to obtain maximum depletion in the mass spectrum.

Extraction of experimental data

The repetition rate of the experiment is 10 Hz while the FEL operates at 5 Hz. This allows to record at each selected FEL frequency alternating mass spectra of irradiated as well as non-irradiated ionic clusters, which are then subtracted from each other to obtain depletion spectra. During the data recording process, at every wavelength point, typically 500 mass spectra must be averaged in order to have a sufficiently good signal/noise ratio. If the vibrational frequency of one of the modes in the parent cluster, ν, is resonant with the light from the FEL one or more photons can be absorbed which in turn can cause the cluster to dissociate. The consequence is a depletion in the population of the parent ionic cluster in the mass spectra of the irradiated species, $I(\nu)$, with respect to the population in the non-irradiated clusters, I_0, and an associated enhancement in the population of the ionic fragments formed. The depletion spectrum for each mass channel is calculated by the ratio $\frac{I(\nu)}{I_0}$ which is plotted versus the photon frequency. This procedure is shown in Figure 2.19.

Absorption spectra are obtained from the depletion ratio by calculating the absorption cross-section as:

$$\sigma(\nu) = \frac{1}{F(\nu)} \ln(\frac{I_0}{I(\nu)}) \tag{2.62}$$

where $F(\nu)$ is the photon fluence. This normalization assumes that the photodissociation of cold rare gas complexes in the far-IR (where the pulse energy, the spectral width and the shape and size of the focused beam can change importantly) is the result of a sequential multiple photon absorption [100].

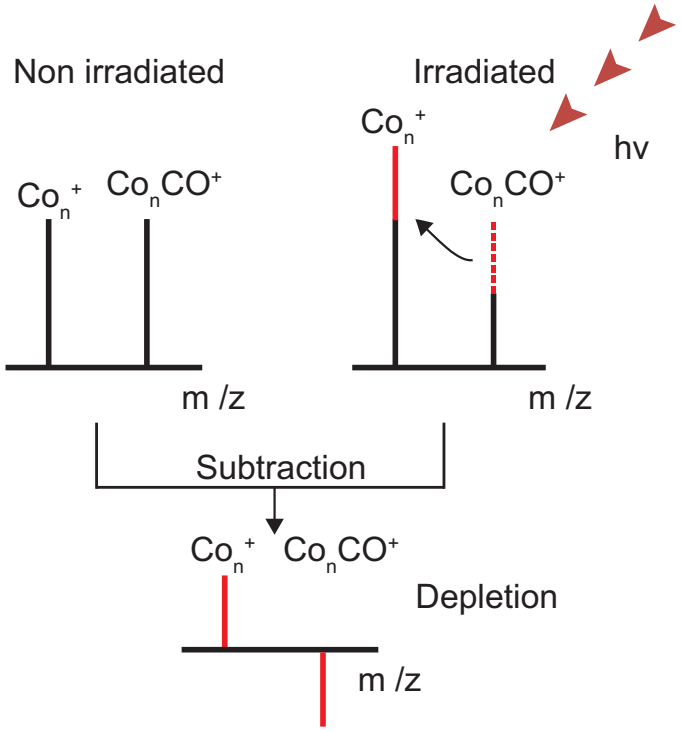

Figure 2.19: The scheme shows the procedure to obtain depletion spectra. The irradiation of the cluster ions with IR light causes fragmentation of some clusters (in this example the CO desorption from Co_n^+ clusters) changing their relative intensities with respect to the intensities of the non-irradiated clusters. A subtraction generates then the depletion spectrum.

2.2.6 Co_nCO^+ First experimental measurement with FHI-FEL in Berlin

The first experimental results using the FHI-FEL were obtained with this setup on the 6th of November 2013. Clusters of Co_nCO^+ were chosen to be compared with results previously obtained at FELIX in the Netherlands. Figure 2.20 shows a comparison between the measured band positions of the CO stretching mode ν(CO) in cationic Co_nCO clusters at the FHI-FEL and at FELIX as a function of the number of cobalt atoms in the corresponding cluster. Free CO in the gas phase has a stretching frequency of 2143 cm^{-1}. When absorbed on cationic cobalt clusters, the data shows that this value is asymptotically reduced with an increasing number of metal atoms in the

cluster towards a value of around 1960 cm^{-1}. Details concerning charge and size dependence of ν(CO) and its modeling are given elsewhere[173]. There is a very good agreement between both sets of data and only a small shift of $\approx$20 cm^{-1} to higher values for the data obtained with the FHI-FEL Berlin is observed. As it is explained in the work of Fielicke et al.[173], Co_nCO^+ measurements in FELIX were carried out under a previous FEL frequency calibration in the ν(CO) stretching region by recording the infrared absorption spectra of ethylene and CO in a photoacustic cell. At the early days of FHI-FEL, a so accurate calibration had not yet been carried out. Therefore, FELIX values are most likely more accurate and the shift of $\approx$20 cm^{-1}, i.e. of $\approx$1%, is attributed to a not yet perfect calibration of the FHI-FEL.

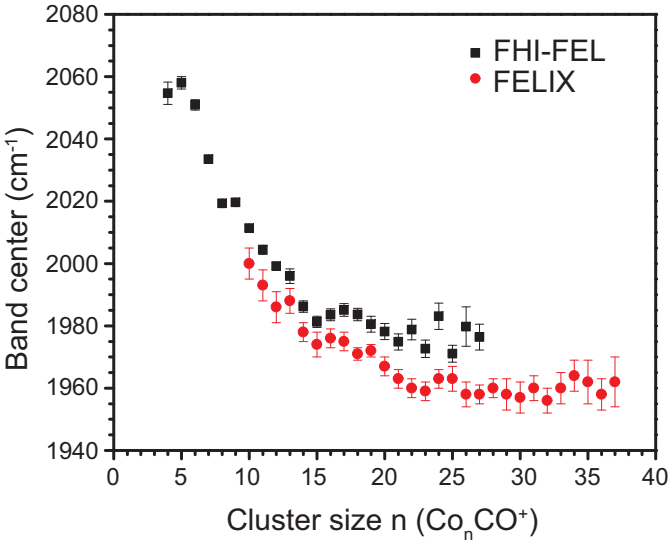

Figure 2.20: Comparison between the experimental band positions for the ν(CO) vibrational mode in Co_nCO^+ as a function of the number of cobalt atoms clusters measured at FELIX (Nijmegen, the Netherlands) and the FHI-FEL (Berlin). The peak positions are determined by a least-squares fit to a Gaussian peak shape. The error bars represent the standard deviation of the fit.

Chapter 3

Theoretical methods

3.1 Group theory principles

Group theory provides very useful mathematical tools that allow to predict physical phenomena without resorting to very complex calculations, as it will be shown in the interpretation of the photoelectron spectrum of Pt_3^- and in the assigment of its vibronic structure. In quantum mechanics, a symmetry operation is defined as a transformation that leaves the Hamiltonian for the system invariant, or equivalently, as a transformation that commutes with the Hamiltonian[35]. Nevertheless, some ambiguities appear when explaining the relationship between the geometrical symmetry of a molecule, which is expressed using the point group symmetry of its equilibrium structure, and the true symmetry of a molecule, which is expressed using the Complete Nuclear Permutation Inversion (CNPI) group and Molecular Symmetry (MS) group. In order to provide an easy walkthrough on these concepts, this subsection firmly follows the book of Phil Bunker and Per Jensen[35], and the work of Wolfgang Domcke et al.[174].

The point group describes all the symmetry operations that can be performed in a molecule that result in a conformation indistinguishable from the original[13]. Each of these operations are generated by the geometrical symmetry elements of the rigid geometrical object. If one thinks of a molecule as being a rigid object of fixed structure then its symmetry can be described

in terms of a point group. As explained few lines after, a point group is useful to describe molecules with small amplitude vibrations in isolated electronic states. However, since point group symmetry cannot deal with other problems such as conformational change, extreme nonrigidity, electronic state mixing and the effect of molecular rotation, the more general definition of symmetry in the beginning is needed.

It is fundamental to distinguish in group theory between the CNPI group and a MS group. As defined in the work of Bunker et al.[35], CNPI group for a molecule is a symmetry group that consists of all permutations of identical nuclei, the inversion E*, and the product of E* with all the permutations of identical nuclei, so the numbers of operations in a CNPI group is given by:

$$h_{CNPI} = 2 \times n_1! \times n_2! \times n_3! ... \times n_r! \tag{3.1}$$

where $1, 2, 3...r$ are the different types of nuclei in the molecule (nuclei of the same element with the same isotopic composition), and n_i the number of each of these nuclei. The factor 2 allows for the presence of the E* operation and all the permutation-inversion operations. Nevertheless, as the number of operations in a CNPI group turns to be easily very large, one defines a subgroup of the CNPI group (the MS group) that gives the useful symmetry labeling, selection rules and nuclear spin statistical weights information that the CNPI group provides.

Prior to any prediction derived from group theory, it is of capital importance to define "rigid" and "non-rigid" molecules. A rigid molecule is one for which there are no observable tunneling splittings caused by the wavefunction penetration between minima on the potential (only one minimum of the potential energy surface has to be considered in the description of the rotation and vibration of the molecule because the barrier between the minima is insuperable) while in a non-rigid molecule such splittings would be experimentally observable, as the potential energy surface of the molecular system has many minima and, therefore, it can have many different conformers with different structures.

Those permutation-inversion operations that accompany the aforementioned tunneling through the potential barrier and whose effects are not experimentally observed are called "unfeasible", while those operations that are not associated with such tunneling are called "feasible", so only feasible symmetry operations are needed when studying rigid molecules. By deleting unfeasible operations from the CNPI group of a rigid molecule it is obtained a subgroup that acts within a single minimum and does not interconvert the molecule in different potential minima; this subgroup is the MS group.

In nonlinear molecules

Furthermore, the MS group is isomorphic to the point group for a rigid nonlinear molecule and the same irreducible representations labels are used for both. Moreover, it is named as G(M), where G is the name of the point group. Each operation R of the MS group can be written as the product:

$$R = R_{ns} R_{rot} R_{ve} \tag{3.2}$$

where R_{ve} transforms vibronic coordinates, R_{rot} transforms the rotational coordinates and R_{ns} transforms the nuclear spins. The set of operations R_{ve} is the molecular point group of the rigid nonlinear molecule and it defines the operations of the molecular point group. These operations only transform the vibronic variables (i.e., vibrational displacements and electronic coordinates), because the molecular point group is not a symmetry group of the complete Hamiltonian, but it is a symmetry group of the vibronic Hamiltonian. Consequently, the point group cannot be used to classify the rovibronic or nuclear spin states. It is the MS group, as it is the symmetry group of the complete Hamiltonian, the one used to classify rovibronic, vibronic and nuclear spin states. The operations of the point group in nonlinear rigid molecules have the same effect on the electronic and vibrational coordinates as the corresponding MS group operations. Thus, either group could be used for classifying the electronic states, and the same results would be obtained. However, it is simpler to use the point group since the orientation of the

molecule-fixed axes is not affected by point group operations and it gives a simpler theoretical description.

As an example, let us see the CH_3F molecule. CH_3F has three types of nucleus (n_H=3, n_C=1 and n_F=1), so the total of permutation-inversion operations in the CNPI group is: $h_{CNPI} = 2 \times 3! \times 1! \times 1! = 12$. The unfeasible symmetry operations in the group are those that interconvert the clockwise and anticlockwise forms and they are[35]:

$$[(12), (23), (31), E^*, (123)^*, (132)^*] \tag{3.3}$$

If one removes these operations (3.3) from the CNPI group, with the remaining feasible symmetry operations (3.4):

$$[E, (12)^*, (23)^*, (31)^*, (123), (132)] \tag{3.4}$$

it is obtained the subgroup $C_{3v}(M)$, which is the MS group for CH_3F and is isomorphic to the C_{3v} point group.

In linear molecules

The point group of a linear molecule is $D_{\infty h}$ if the molecule is centrosymmetric, and it is $C_{\infty v}$ if it is not. Both groups have an infinite number of operations in them and, like any point group, they only transform the vibronic variables. The MS group for a point group $C_{\infty v}$ linear molecule is $C_{\infty v}(M)=\{E, E^*\}$, and that for a $D_{\infty h}$ linear molecule is $D_{\infty h}(M)=\{E, p, E^*, p^*\}$, where p is the permutation operation that interchanges all pairs of identical nuclei symmetrically located about the molecular midpoint, so in rigid molecules that have a linear equilibrium coniguration MS groups and point groups are not isomorphic.

Using the isomorphic Hamiltonian of a linear molecule, the Euler angle χ is introduced as a variable and we can develop Extended Molecular Symmetry (EMS) groups, $C_{\infty v}(EM)$ and $D_{\infty h}(EM)$, that are isomorphic with the point groups, but which transform the three Euler angles (and the nuclear spins). These groups can be used to classify rovibronic, vibronic and nuclear spin

states of a linear rigid molecule just like the MS groups are used for nonlinear rigid molecules.

Selection rules via group theory

Any kind of selection rule via group theory is given by the vanishing integral rule, where the quantum mechanical integral:

$$I = \int \psi_f^* \hat{\mathrm{O}} \psi_i d\tau \tag{3.5}$$

must vanish unless the integrand, $\psi_{\mathrm{f}}^* \hat{\mathrm{O}} \psi_{\mathrm{i}}$, contains a totally symmetric component, A_1, in the symmetry group of the Hamiltonian. Resorting on the irreducible representations of both wavefunctions, $\Gamma_{\psi_{\mathrm{f}}}$ and $\Gamma_{\psi_{\mathrm{i}}}$, and of the operator, $\Gamma_{\hat{\mathrm{O}}}$, it is translated in the selection rule:

$$\Gamma_{A_1} \in \Gamma_{\psi_f} \otimes \Gamma_{\hat{\mathrm{O}}} \otimes \Gamma_{\psi_i} \tag{3.6}$$

As the probability amplitude of a vibronic transition in the Franck-Condon (FC) approximation is factorized in the transition dipole moment integral, $|\langle \psi_{\mathrm{e}}^{\mathrm{f}} | \mu_{\mathrm{e}} | \psi_{\mathrm{e}}^{\mathrm{i}} \rangle|^2$ and the FC factors, $|\langle \psi_{\mathrm{v}}^{\mathrm{f}} | \psi_{\mathrm{v}}^{\mathrm{i}} \rangle|^2$, the selection rules are expressed by:

$$\Gamma_{A_1} \in \Gamma_e^f \otimes \Gamma_{\mu_e} \otimes \Gamma_e^i \quad \text{and} \quad \Gamma_{A_1} \in \Gamma_v^f \otimes \Gamma_v^i \tag{3.7}$$

where μ_{e} is in equation 3.7 the electric dipole moment and it transforms as μ_{x}, μ_{y} and μ_{z}.

The FC factor symmetry condition implies that allowed transitions can exhibit a change in vibrational quantum number of $\Delta\nu$=0,±1,±2... for totally symmetric vibrational modes and $\Delta\nu$=0,±2,±4... for non-totally symmetric modes. Moreover, the condition in the left side of equation 3.7 is reformulated for a photodetachment transition because one can assume that the outgoing electron is independent from and orthogonal to the remaining occupied molecular orbitals[114], and its electronic symmetry can be consequently factored

out. It is therefore expressed as:

$$\Gamma_{A_1} \in \Gamma_e^{neutral} \otimes \Gamma_e^{photoelectron} \otimes \Gamma_\mu \otimes \Gamma_e^{anion} \tag{3.8}$$

For each symmetry of the product $\Gamma_e^{neutral} \otimes \Gamma_e^{anion}$ at each molecular orientation along the three main axis in the Laboratory Frame Reference (LFR) (Γ_{μ_x}, Γ_{μ_y}, Γ_{μ_z}), one can predict the symmetry of the outgoing photoelectron wavefunction.

Possible breakdowns of the BO and FC approximation (JT, RT or PJT effects) are described more in detail in subsection 3.3. The PJT vibronic coupling occurs between the electronic states with the same spin multiplicity through a vibrational mode v which must fulfill the selection rule $\Gamma_{A_1} \in \Gamma_v^{m,n} \otimes \Gamma_e^m \otimes \Gamma_e^n$ [175], where m and n are the vibronically coupled electronic states. In case the vibrational modes in both electronic states have a different irreducible representation, the mix is produced via:

$$\Gamma_{A_1} \in \Gamma_e^m \otimes \Gamma_{v_1}^m \otimes \Gamma_e^n \otimes \Gamma_{v_2}^n \tag{3.9}$$

where $\Gamma_e^{m,n}$ are the irreducible representations of the electronic states m or n, and $\Gamma_{v_1}^m$ and $\Gamma_{v_2}^n$ are those of the vibrational modes involved. A sign of PJT effect in photoelectron spectroscopy in case of a weak vibronic coupling (aka Herzberg-Teller coupling) is the appearance of a vibronic transition that involves a non-totally symmetric vibrational mode that borrows intensity from a totally symmetric vibrational mode in a different electronic state [38]. In cases of stronger coupling the geometry of the involved electronic states can suffer small changes, and so the vibrational modes involved provoking shifts in the vibronic structure.

JT and RT effects are first-order vibronic couplings within the same degenerate electronic state. The selection rule for both effects is:

$$\Gamma_{A_1} \in \Gamma_e^m \otimes \Gamma_{v_1}^m \otimes \Gamma_e^m \otimes \Gamma_{v_2}^m \tag{3.10}$$

where is the Γ_e^m is the electronic state and Γ_{v_1,v_2}^m are the vibrational modes involved. In some cases, only one mode is needed, so the direct product

in equation 3.10 is reduced to three terms. In photoelectron spectroscopy, JT and RT effects provoke complex shiftings and splittings in the vibronic structure within a degenerate electronic state.

Further applications [111,174]

Several qualitative predictions about spin-orbit coupling (SOC) and possible splittings derived from it can be done via group theory through the symmetric product of the orbital, $\Gamma_e^{orbital}$, and the spin, Γ_e^{spin}, irreducible representations in an electronic state. The splitting appears as the direct sum of irreducible representations resulting from the product:

$$\Gamma_e^{orbital} \otimes \Gamma_e^{spin} = \Gamma_e^{SO1} \oplus \Gamma_e^{SO2} \oplus \Gamma_e^{SO3} \tag{3.11}$$

If the electronic state has an even unpaired number of electrons (odd multiplicity) the spin function transforms as a one-valued irreducible representation and, therefore, so will do the irreducible representations resulting from the SOC. If the electronic state has an odd number of electrons (even multiplicity), the spin function transforms as a two-valued irreducible representation that can be nondegenerate (e.g. $B_{g1/2}$) or degenerate (e.g. $E_{1/2}$, $E_{3/2}$, $G_{3/2}$) due to the Kramers degeneracy [176,177].

If an electronic state with odd multiplicity shows coalescence of relativistic and vibronic effects, the JT instability theorem remains unchanged: any state with a degenerate irreducible representation resulting from SOC is unstable in the symmetrical conformation since there is always a non-totally symmetric normal coordinate on which potential energy depends linearly [178]. Nevertheless, for even multiplicity the instability theorem changes as the electron spin is not directly affected by an electric field, and the coupling of electronic and vibrational motion (non-relativistic JT effect of electrostatic origin) cannot remove the degeneracy caused by a single spin (the Kramers degeneracy). In other words, the antisymmetrized product of the two-valued degenerate representation, $E_{1/2}$, does not contain any non-totally symmetric irreducible representation that can be relativistically JT active, $\left\{E_{1/2}^2\right\}=A_1'$ [179]. Moreover, if one of the irreducible representations resulting from the zeroth-order

SO coupling is a two-valued irreducible representation with a dimension higher than 2, relativistic first-order JT modes can appear. This is shown in the following general example taken from the work of Domcke et al. [174], where simultaneous vibronic and relativistic couplings in a tetrahedral system with T_d symmetry are studied via group theory. Here, the spin-free JT selection rules for the degenerate electronic states E, T_1 and T_2 are:

$$[E^2] = A + E \quad \text{and} \quad [T_{1,2}^2] = A + E + T_2 \tag{3.12}$$

The inclusion of SO coupling in these electronic states with multiplicity = 2 implies the use of the double-valued group, T_d'. The $^2T_1$, $^2T_2$ and ^2E states are predicted to split via group theory as follows:

$$\begin{aligned} {}^2T_1 &= T_1 \times E_{1/2} = G_{3/2} + E_{1/2} \\ {}^2T_2 &= T_2 \times E_{1/2} = G_{3/2} + E_{5/2} \\ {}^2E &= E \times E_{1/2} = G_{3/2} \end{aligned} \tag{3.13}$$

The selection rules to deduce the first-order relativistic JT active modes from the calculated states with zeroth-order SO coupling are given by:

$$\begin{aligned} G_{3/2} \times E_{1/2} &= E + T_1 + T_2 \\ G_{3/2} \times E_{5/2} &= E + T_1 + T_2 \\ \left\{G_{3/2}^2\right\} &= A_1 + E + T_2 \end{aligned} \tag{3.14}$$

One can conclude that the four-fold degeneracy in $G_{3/2}$ can be lifted in first order by vibrational modes with E or T_2 symmetry. For a ^2E state, which transforms as $G_{3/2}$ in the symmetry group T_d', the T_2 mode is not JT active in the nonrelativistic limit. Therefore, the JT activity of the T_2 mode must arise from the SO operator, i.e., it is a JT active mode of relativistic origin as well as T_1 is for $^2T_1$ and $^2T_2$.

3.2 Born-Oppenheimer approximation

The Born-Oppenheimer approximation in quantum mechanics assumes that the total wavefunction of a molecule can be expressed by the product of the electronic and vibrational wavefunctions, since the movements of nuclei and electrons can be treated separately. Despite the mathematical approaches to the different approximations based on the Born-Oppenheimer principle have been clearly calculated, there is not yet an agreement on the names they receive. A very didactic summary from 1976 [180] identifies three main adiabatic approximations that are named as Crude Adiabatic (CA) (also called diabatic), Born-Oppenheimer (BO) and Born-Huang (BH). The analysis of the photoelectron spectrum of Pt_3^- in the next chapter proposes the presence of different vibronic coupling effects within the neutral Pt_3 cluster and, therefore, it is recommended a brief overview on these phenomena.

As starting point, the Hamiltonian in a molecular system is given by:

$$\begin{aligned} H_{total}(r,Q) &= T_e(r) + T_N(Q) + V_{ee}(r) + V_{Ne}(r,Q) + V_{NN}(Q) \\ &= T_e(r) + T_N(Q) + U(r,Q) + V(Q) \end{aligned} \quad (3.15)$$

where Q and r denote, respectively, the mass weighted nuclear and electronic coordinates. $V(Q)$ is the potential energy of the nuclei, $V_{NN}(Q)$, and $U(r,Q) = V_{ee}(r) + V_{Ne}(r,Q)$ is the total coulombic potential energy that includes the interelectronic repulsion and the electronic-nuclei interaction. No relativistic potential energies are included. $T_e(r)$ and $T_N(Q)$ are the electronic and nuclear kinetic energy operators, where m is the mass of the electron:

$$T_e(r) = -\frac{\hbar^2}{2m}\sum_i \frac{\partial^2}{\partial r_i^2} \quad \text{and} \quad T_N(Q) = -\frac{\hbar^2}{2}\sum_n \frac{\partial^2}{\partial Q_n^2} \quad (3.16)$$

Since the Hamiltonian of equation 3.15 does not allow a separation of variables, we separate those terms that contain electronic coordinates and

rename them as the electronic Hamiltonian, $H_{elec}(r,Q)$:

$$\begin{aligned} H_{elec}(r,Q) = T_e(r) + U(r,Q) &= T_e(r) + U(r,Q_0) + \Delta U(r,Q) \\ &= H_{elec}(r,Q_0) + \Delta U(r,Q) \end{aligned} \quad (3.17)$$

where Q_0 is a reference nuclear configuration, $H_{elec}(r,Q_0)$ is the energy of the electrons in the field of the fixed nuclei at Q_0 and $H_{elec}(r,Q)$ is the energy of the electrons in the field of dynamic nuclei. Therefore, the static and the dynamic electronic Schrödinger equations are defined to calculate the static wavefunction, $\psi_i^0(r,Q_0)$, and the dynamic one, $\psi_i(r,Q)$:

$$\begin{aligned} [T_e(r) + U(r,Q_0) - \epsilon_i^0(Q_0)]\psi_i^0(r,Q_0) = 0 \\ [T_e(r) + U(r,Q) - \epsilon_i(Q)]\psi_i(r,Q) = 0 \end{aligned} \quad (3.18)$$

As both electronic wavefunctions form a complete set, the eigenstate of the total vibronic Hamiltonian, $\Psi_t(r,Q)$, is expanded as a linear combination of either $\psi_i^0(r,Q_0)$ or $\psi_i(r,Q)$ where $\chi_{kt}(Q)$ is just a expansion coefficient which is function of Q:

$$\begin{aligned} \Psi_t(r,Q) = \sum_k \psi_k^0(r,Q_0)\chi_{kt}(Q) \\ \Psi_t(r,Q) = \sum_k \psi_k(r,Q)\chi_{kt}(Q) \end{aligned} \quad (3.19)$$

We must emphasize that the nuclear wavefunctions in equation 3.19, $\chi_{kt}(Q)$, are not identical. Their calculation is intrinsically linked to the chosen approximation (CA, BO or BH) and it is explained in the following in parallel with some introductory details to each approach. The crudest approach is the CA approximation and it assumes fixed nuclei in a high symmetry configuration given by Q_0. The eigenstate of the total vibronic Hamiltonian is $\Psi_t(r,Q) = \sum_k \psi_k^0(r,Q_0)\chi_{kt}(Q)$ and its expansion coefficients,

$\chi_{kt}(Q)$, are obtained from the following coupled differential equations:

$$[T_N(Q) + V(Q) + \epsilon_j^0(Q) + \langle\psi_j^0(r,Q_0)|\,\Delta U(r,Q)\,|\psi_j^0(r,Q_0)\rangle - E_t]\chi_{jt}(Q) + \sum_{k\neq j}\langle\psi_j^0(r,Q_0)|\,\Delta U(r,Q)\,|\psi_k^0(r,Q_0)\rangle\,\chi_{kt}(Q) = 0 \quad (3.20)$$

If the vibronic mixing between different electronic states is ignored, the coupling terms in equation 3.20 are neglected ($\langle\psi_j^0(r,Q_0)|\,\Delta U(Q,r)\,|\psi_k^0(r,Q_0)\rangle = 0$ for $k\neq j$) and the adiabatic wavefunction is written as:

$$\Psi_{jt}^{CA}(r,Q) = \psi_j^0(r,Q_0)\chi_{jt}^{CA}(Q) \quad (3.21)$$

The BO and BH approximations assume the electrons in a dynamic nuclei field and the coupled differential equations that provide the expansion coefficients, $\chi_{kt}(Q)$, for the eigenstate of the total vibronic Hamiltonian, $\Psi_t(r,Q) = \sum_k \psi_k(r,Q)\chi_{kt}(Q)$, are:

$$[T_N(Q) + V(Q) + \epsilon_j(Q) + \langle\psi_j(r,Q)|\,T_N(Q)\,|\psi_j(r,Q)\rangle - E_t]\chi_{jt}(Q) + \sum_{k\neq j}\hbar^2[\langle\psi_j(r,Q)|\,T_N(Q)\,|\psi_k(r,Q)\rangle - \sum_n \langle\psi_j(r,Q)|\,\frac{\partial}{\partial Q_n}\,|\psi_j(r,Q)\rangle\,\frac{\partial}{\partial Q_n}]\chi_{kt}(Q) = 0 \quad (3.22)$$

If the non-diagonal elements of the coupling terms are neglected ($\langle\psi_j(r,Q)|\,\frac{\partial}{\partial Q_n}\,|\psi_k(r,Q)\rangle = 0$ and $\langle\psi_j(r,Q)|\,T_N(Q)\,|\psi_k(r,Q)\rangle = 0$ for $k\neq j$), the BH approximation is reached:

$$\Psi_{jt}^{BH}(r,Q) = \psi_j(r,Q)\chi_{jt}^{BH}(Q) \quad (3.23)$$

Furthermore, the assumption of the BO approximation is based in the BH one, but it is even more restrictive because not only the nondiagonal elements in the operator of nonadiabaticity are approximated to zero, but also the diagonal ones ($\langle\psi_j(r,Q)|\,T_N(Q)\,|\psi_j(r,Q)\rangle = 0$). The adiabatic wavefunction

in this approximation is given by:

$$\Psi_{jt}^{BO}(r,Q) = \psi_j(r,Q)\chi_{jt}^{BO}(Q) \tag{3.24}$$

It is necessary to mention that the three approaches followed in this discussion are different from the original work of Born and Oppenheimer [181], who carried out the separation between electronic and nuclear wavefunctions by employing the singular perturbation method with the perturbation parameter $m/M^{1/4}$ [180].

3.3 Breakdown of the Born-Oppenheimer approximation

Jahn-Teller coupling

Jahn and Teller showed in their pioneering study [178] that for any orbitally degenerate electronic term in a molecular system described by a symmetry point group there are non-totally symmetric displacements for which the adiabatic potential curve of the electronic term has no minimum [182]. This is stated by the JT theorem as: the nuclear configuration (geometry) of a nonlinear molecule in an orbitally degenerate electronic state (except twofold spin degeneracy-Kramers degeneracy) is unstable with respect to nuclear displacements that remove the degeneracy [183].

Moreover, Bersuker [184] gave a more recent and rigorous definition that also encompasses PJT and Renner-Teller effects: for any polyatomic system with two or more branches of the adiabatic potential energy surface that intersect at the point of degeneracy or are tangential and interact sufficiently strongly at this point, there is at least one branch that has no minimum, the case of twofold spin degeneracy being an exception.

Consequently, this introduction to the JT and PJT effects is based on the reviews of Bersuker [183,184], who approaches both vibronic interactions from the CA approximation. Therefore, the vibrational wavefunctions are determined by equation 3.20 where the initial nuclear configuration for a JT

coupling, Q_0, is chosen at the point where the electronic state is degenerate or nearly degenerate, i.e., at the molecular geometry with highest symmetry [183]. Firstly, the $U(r,Q)$ potential in the harmonic approximation is described by:

$$U(r,Q) = U(r,Q_0) + \sum_n \left(\frac{\partial U}{\partial Q_n}\right)_0 + \frac{1}{2}\sum_{n,m}\left(\frac{\partial^2 U}{\partial Q_n \partial Q_m}\right)_0 Q_n Q_m + ... \quad (3.25)$$

Considering equations 3.18 (the upper one), 3.20 and 3.25, the $\Delta U(r,Q)$ potential can be rewritten as:

$$\begin{aligned}\Delta U(r,Q) &= U(r,Q) - U(r,Q_0) = \\ &= \sum_n \left(\frac{\partial U}{\partial Q_n}\right)_0 + \frac{1}{2}\sum_{n,m}\left(\frac{\partial^2 U}{\partial Q_n \partial Q_m}\right)_0 Q_n Q_m + ...\end{aligned} \quad (3.26)$$

The analysis of the matrix elements in the coupling term with $\Delta U(r,Q)$ as it was expanded in equation 3.26, $\langle \psi_j^0(r,Q_0)| \Delta U(Q,r) |\psi_k^0(r,Q_0)\rangle$, allows to obtain a comprehensive approximation to the JT effect. If the involved electronic states are denoted by their irreducible representations (Γ, Γ',...), the irreducible representation of the nuclear displacement is Γ^* and the states Γ and Γ' can be degenerate or non-degenerate, the linear vibronic constant is:

$$F_{\Gamma^*}^{\Gamma\Gamma'} = \left\langle \Gamma \left| \left(\frac{\partial U}{\partial Q_{\Gamma^*}}\right)_0 \right| \Gamma' \right\rangle \quad (3.27)$$

$F_{\Gamma^*}^{\Gamma\Gamma'}$ is non zero only if $\Gamma^* = \Gamma \times \Gamma'$. The diagonal elements of the linear coupling, $F_{\Gamma^*}^{\Gamma\Gamma}$, are understood as the force with which the electrons in the state Γ affect the nuclei in the Q_{Γ^*} displacements. For non-degenerate electronic states it follows that $\Gamma \times \Gamma = A_1$ in the diagonal elements, and the electrons can only distort the nuclear configuration in the direction of the totally symmetric displacements, so the symmetry of the system does not change. For degenerate electronic states, $\Gamma \times \Gamma$ contains also non-totally symmetric irreducible representations that are understood as the distortions that the nuclei undergo under the influence of the electrons by reducing the symmetry of the system (JT active representations). In addition, the

quadratic vibronic constant is given by:

$$K^{\Gamma\Gamma'}_{\Gamma^*\in\Gamma_1\times\Gamma_2} = \left\langle \Gamma \left| \left(\frac{\partial^2 U}{\partial Q_{\Gamma_1} \partial Q_{\Gamma_2}} \right)_0 \right| \Gamma' \right\rangle \tag{3.28}$$

As in the linear case, Q_{Γ^*} can only be totally symmetric in the diagonal elements of the quadratic coupling ($K^{\Gamma\Gamma}_{\Gamma^*}$) for nondegenerate states and it only includes non-totally symmetric components for degenerate states (JT active). The curvature of the adiabatic potential in the displacement Q_{Γ^*} is formed by the totally symmetric part of the diagonal matrix elements and the nondiagonal elements of the linear vibronic coupling, $F^{\Gamma\Gamma'}_{\Gamma^*}$:

$$K^{\Gamma} = K_0 + K_v = K^{\Gamma\Gamma}_{\Gamma^*} - \sum_{\Gamma'} \frac{|F^{\Gamma\Gamma'}_{\Gamma^*}|^2}{\Delta_{\Gamma'\Gamma}} = \left\langle \Gamma \left| \left(\frac{\partial^2 U}{\partial Q^2_{\Gamma^*}} \right)_0 \right| \Gamma \right\rangle - 2 \sum_{\Gamma'} \frac{|\left\langle \Gamma \left| \left(\frac{\partial U}{\partial Q_{\Gamma^*}} \right)_0 \right| \Gamma' \right\rangle|^2}{\epsilon_{\Gamma'} - \epsilon_{\Gamma}} \tag{3.29}$$

where $\Delta_{\Gamma\Gamma'} = \frac{1}{2}(\epsilon_{\Gamma'} - \epsilon_{\Gamma})$ is the energy semidifference between the states Γ and Γ'. While the totally symmetric diagonal elements of the quadratic coupling constitute the basic component (harmonic) of the adiabatic potential, the non-totally symmetric ones are identified as the diagonal quadratic vibronic constants. Moreover, the nondiagonal matrix elements of the quadratic coupling, $G^{\Gamma\Gamma'}_{\Gamma^*}$, are the nondiagonal quadratic vibronic constants[183].

Pseudo Jahn-Teller coupling

As it was shown in equation 3.29, the curve of the adiabatic potential is formed by K_0 (the essential component of the adiabatic potential curvature, i.e., the force constant that is given by the totally symmetric diagonal elements of the quadratic vibronic constant) and K_v. While the JT effect is basically considered as the vibronic coupling within a degenerate electronic state, K_v is the responsible of the vibronic mixing between different electronic states and thus of the vibronic anharmonicity. Indeed, the anharmonicity in the adiabatic potential curve has two different main sources: one due to the

diagonal elements of those terms that in the Taylor expansion of $U(r, Q)$ are higher than the quadratic one (see equation 3.25), and the vibronic anharmonicity, already manifested in the nondiagonal elements of the $U(r, Q)$ linear terms. Therefore, the negative implicit sign in K_v is understood as a softening in the force constants that the electrons suffer by following the electron displacements.

As it was proved that $K_0 > 0$ for a polyatomic system in the high symmetry configuration[185,186], K_v is the only source of instability in nondegenerate states[184]. It follows from this formulation of the PJT effect that if a polyatomic system shows a negative curvature, $K < 0$, then $|K_v| > K_0$, and the distorted nuclear displacements occur due to a vibronic coupling[184]. A more

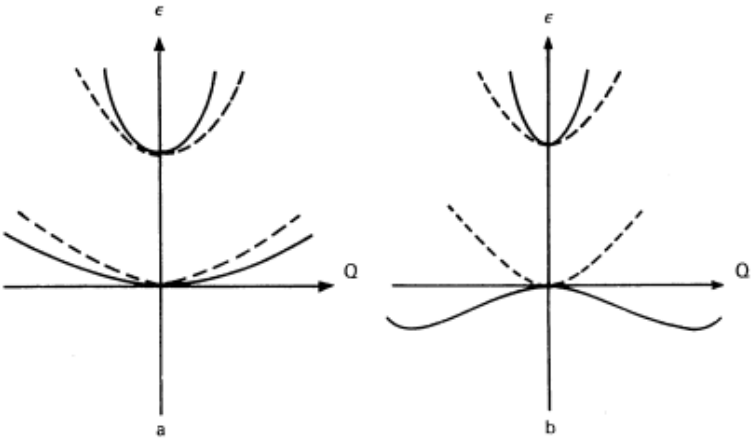

Figure 3.1: Adiabatic potential curves that interact vibronically via PJT. Dashed and solid lines represent respectively the states without and with vibronic coupling. In (a), the ground state is stable but softened (weak PJT). In (b), the ground state is unstable at Q_0 (strong PJT). The Figure is taken from[184].

detailed introduction to the PJT coupling would require the resolution of the two-level problem (and its secular determinant) for a two-(nondegenerate)state paradigm[184,185] to show that the PJT vibronic interaction between a ground and an excited nondegenerate electronic state provokes the softening of the former (destabilization with lowering of its vibrational frequencies) and the hardening of the latter (stabilization with increasing of its vibrational frequencies). This is visually summarized in Figure 3.1. Further details are left to the

interest of the reader. The works of Bersuker[183,184] that have been followed in section 3.3 are highly recommended to obtain a deeper understanding on the JT, PJT and RT effects.

Chapter 4

Photoelectron spectroscopy on Pt_3^-

4.1 Introduction

The metals of the platinum group (Ru, Rh, Pd (4d); Os, Ir, Pt (5d)), are widely used in heterogeneous catalysis for a range of economically and environmentally important processes. Nevertheless, the understanding of their structural and electronic properties is still limited and in several cases there exist discrepancies between experimental findings and theoretical predictions [21,100]. One reason for this may be that, in particular for the 5d metals, relativistic effects become significant and need to be considered appropriately in the calculations. In-depth experimental characterization of gas-phase clusters can provide detailed insights and allows for testing the suitability of the theoretical approaches. Photoelectron spectroscopy via VMI has become a powerful tool in gas-phase spectroscopy [21,36,105,187]. Simultaneously obtaining information about the energies of vibronic transitions and the PADs upon photodetachment can

All the DFT calculations in this chapter have been carried out by Julius Jellinek and Aslihan Sumer. Both collaborated actively in the scientific discussion and development of this investigation.

give a deep and detailed understanding of small sized molecules and clusters. Anion PES probes the electronic structures of the clusters and when using high resolution variants even low-frequency vibrational structure, characteristic for metal clusters, can be resolved.

This work focusses on the exemplary case of the anionic platinum trimer. There has been a long history of theoretical and experimental investigations trying to understand the physical and chemical properties of small Pt clusters in the gas phase. Anion photoelectron spectra of the Pt_3^- cluster have been published by two groups[188–192] and PES has been used to analyze the changes of its electronic structure upon binding of carbon monoxide[189–193]. Experimentally, the reactivity with CO[194], N_2O[195] and CH_4[196] has been investigated. In the latter, it could be shown that Pt_3^- is present in two isomeric forms, one reactive towards CH_4 and one unreactive[196]. The presence of two isomeric forms was also predicted by photoemission experiments on Pt_3[197]. In earlier experimental studies no conclusive assignment of the PES spectrum has been obtained[188,189]. For small cationic Pt clusters their structures in complexes with Ar atoms have been determined from the far-infrared spectra[198].

The electronic, energetic and structural properties of small platinum clusters, as well as the bond nature and its degree of orbital hybridization were subject of early theoretical studies[199–202]. First DFT calculations in the LDA approximation[203,204] on neutral Pt_3 have shown a triangular singlet ground state with D_{3h} symmetry followed by a triplet first excited isosceles triangle less than 0.1 eV higher. Similar results were obtained with the hybrid B3PW91 functional[205,206], concluding a bond distance in the singlet ground state of d=2.50 Å and a gap to the first excited triplet state of ΔE=0.24 eV[205]. Further on, spin polarized DFT calculations with the PW91 functional and scalar relativistic corrections on Pt_3 have been numerous[207–212]. Some of these works calculate a triplet D_{3h} ground state close in energy to a singlet D_{3h} first excited state[207,209,212], while others predict a triangular singlet ground state with C_{2v}[208,210] or D_{3h} symmetry[211]. In the latter case a first excited D_{3h} triplet state is found at ΔE=0.05 eV. The question about the multiplicity and geometry of Pt_3 neutral electronic ground and close-lying

first excited states remains unanswered in other works using, e.g., molecular dynamics simulations[213] or other DFT non-relativistic studies[214–217].

Fully relativistic calculations[207,208,218–221] shed new light on these questions as comparisons between not fully relativistic calculations and those accounting for SOC reach different conclusions. While upon inclusion of relativistic effects Fortunelli[207] does not observe any change in the energy order of the triplet and singlet states of the neutral, being either ground or first excited states, Balasubramanian[222] and Huda[211] find changes in the ordering of low lying electronic states. In their works, without SOC, the ground state is a singlet and the first excited a triplet but when SO coupling is included, the mixing of so close states inverts their order and the triplet becomes the ground state. Huda also observes that with SOC the triplet distorts away from the equilateral triangle lowering its energy by 20 meV, enough to become the ground neutral state. This JT distortion in the ground neutral Pt_3 by SOC is also obtained in more recent works[220,221].

Neutral isomers with linear geometry have been calculated in some of the aforementioned studies[201,203–205,207,208,218]. All conclude that they are clearly higher in energy than the triangular one and do not constitute in any case the ground state of Pt_3. However, the predictions on the linear species differ between them. While Wang et al.[201] predict $^5\Delta_g$ to be the energetically lowest linear Pt_3, Grönbeck et al.[204] obtain a triplet. A local minimum with linear structure at 0.24 eV/atom higher than the ground triangular is mentioned in the work of Yang et al.[203] and Xiao et al.[208] calculated two states resembling linear geometry: a most stable linear trimer with BE=2.18 eV/atom followed by a bent state at 2.14 eV/atom higher in energy with a bond angle of 141.6°. Finally, the DFT calculations of Fortunelli[207] on Pt_3 predict a local minimum quintet with an atomization energy of 6.20 eV and R_e=2.422 Å.

Interestingly, charged species have been considered in only very few theoretical studies[204,207,208], agreeing that for the anion Pt_3^- the ground state has linear geometry, unlike the neutral case. Fortunelli[207] also found a triangular anion at ≈0.1 eV higher than the linear one but judged that to be below the theoretical accuracy, opening the question of the real geometry in

the anionic trimer. Grönbeck and Andreoni[204] shortly later suggested the coexistence of both anionic species in the experimental studies and implicitly assigned parts of the photoelectron spectra to either the triangular or the linear one.

Nevertheless, certain questions still remain unanswered, as the spin multiplicity and geometry of the neutral and anionic ground states, the hybrid character of the metal-metal bonding, or the impact of spin-orbit coupling. Further, there has been no conclusive assignment yet of the anion photoelectron spectra connecting theoretical predictions with experimental observations. In the following we will address these points during the assignment of our experimental anion photoelectron spectra and will highlight the differences in our theoretical predictions when applying scalar-relativistic corrections via effective core potentials versus explicitly considering the effects of SOC in the triangular isomer.

We carried out DFT calculations using the PW91 functional, the cc-pVDZ-PP basis set and the scalar relativistic effective core potential "Stuttgart pseudopotental". A summary of the computational results, i.e. the relative energies of the different states, their structural parameters and vibrational frequencies is given in Figure 4.1 and in Table 4.1.

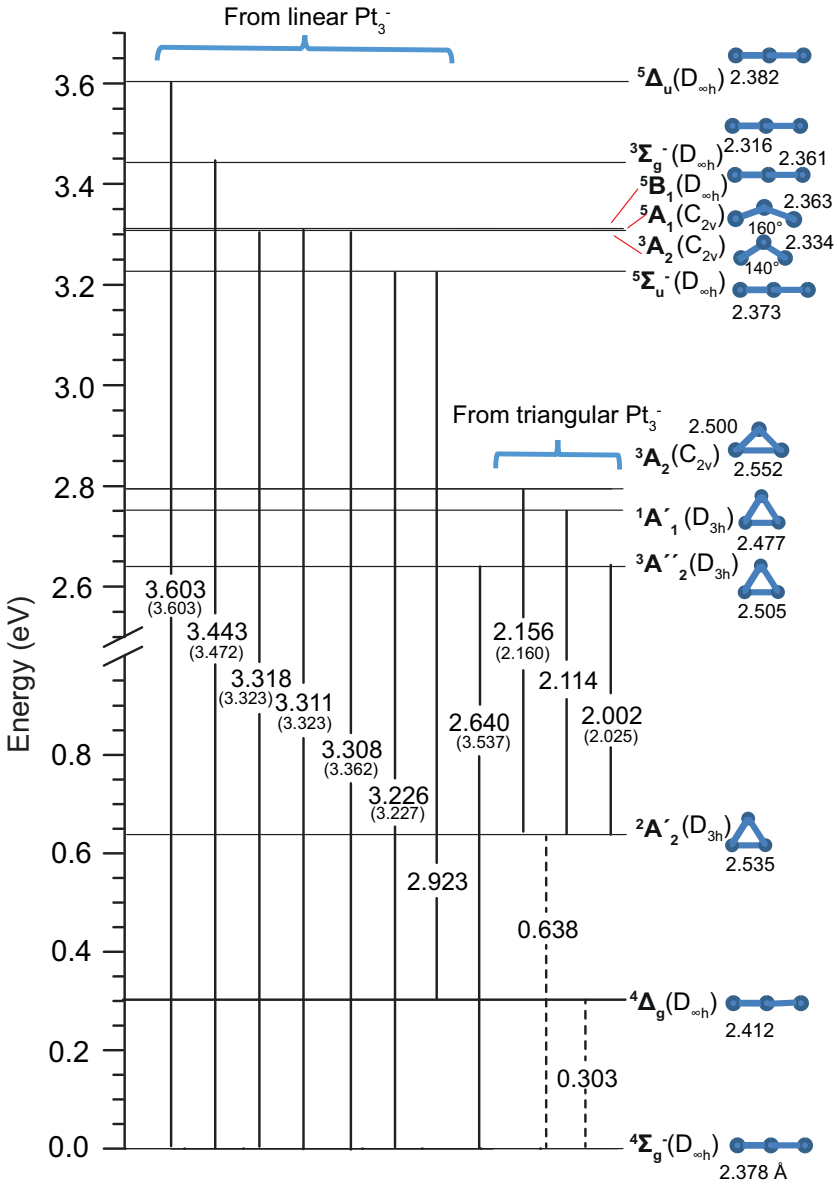

Figure 4.1: Summary scheme with all the calculations carried out on anionic and neutral Pt_3 with PW91/cc-pVDZ-PP+Stuttgart pseudopotential. All energies are expressed in eV and all bond lenghts in Å. Each calculated transition is marked by a vertical solid line with the adiabatic detachment energy (DE_{ad}) in big characters and the vertical detachment energy (DE_{vert}) in parentheses. The dashed lines mark the energies of the excited anionic states relative to the ground state one, $^4\Sigma_g^-$.

Electronic state	Electronic configuration	BE (eV/atom)	Vibrational mode	Frequency (cm^{-1})
$^4\Sigma_g^-$	$(3\pi_g)^2(6\sigma_g^+)^1(2\delta_g)^4(1\delta_u)^4(5\sigma_u^+)^2$	2.609	σ_g^+	155
			π_u	33
			σ_u^+	260
$^4\Delta_g$	$(6\sigma_g^+)^2(3\pi_g)^2(2\delta_g)^3(1\delta_u)^4(5\sigma_u^+)^2$		σ_g^+	148
			π_u	26
			σ_u^+	240
$^2A_2'$	$(1a_1'')^2(2a_2')^1(4e'')^4$	2.396	a_1'	203
			e'	123
$^3A_2''$	$(1a_1'')^1(2a_2')^1(4e'')^4$	2.378	a_1'	219
			e'	132
$^1A_1'$	$(2a_2')^0(1a_1'')^2(4e'')^4$		a_1'	227
			e'	146
$^3E''$	$(1a_1'')^2(2a_2')^1(4e'')^3$		a_1	218
			b_1	153
			b_1	151
$^5\Sigma_u^-$	$(3\pi_g)^2(6\sigma_g^+)^1(2\delta_g)^4(1\delta_u)^4(5\sigma_u^+)^1$	2.183	σ_g^+	158
			π_u	29
			σ_u^+	244
$^3A_2(^3\Sigma_u^-)$	$(3\pi_g)^2(6\sigma_g^+)^1(2\delta_g)^4(1\delta_u)^4(5\sigma_u^+)^1$		a_1	175
			b_1	39
			b_1	258
$^5A_1(^5\Delta_g)$	$(3\pi_g)^2(6\sigma_g^+)^1(2\delta_g)^3(1\delta_u)^4(5\sigma_u^+)^2$		σ_g^+	164
			π_u	25
			σ_u^+	256
$^5B_1(^5\Delta_g)$	$(3\pi_g)^2(6\sigma_g^+)^1(2\delta_g)^3(1\delta_u)^4(5\sigma_u^+)^2$		σ_g^+	162
			π_u	72
			σ_u^+	267
$^3\Sigma_g^-$	$(6\sigma_g^+)^0(3\pi_g)^2(2\delta_g)^4(1\delta_u)^4(5\sigma_u^+)^2$		σ_g^+	172
			π_u	49
			σ_u^+	281
$^5\Delta_u$	$(3\pi_g)^2(6\sigma_g^+)^1(2\delta_g)^4(1\delta_u)^3(5\sigma_u^+)^2$		σ_g^+	158
			π_u	25
			σ_u^+	207

Table 4.1: Summary of all the calculated electronic states with the PW91/cc-pVDZ-PP+Stuttgart pseudopotential. This table is complementary to the information in Figure 4.1. The column with the electronic configurations is read from left to right since the molecular orbitals are energetically ordered as HOMO, HOMO-1, HOMO-2, etc.

4.2 Mass spectrum analysis

All measurements within this chapter were carried out with a platinum target in its natural isotopic distribution. The overall mass spectrum of anionic bare platinum clusters and their complexes was firstly obtained with the aim of maximizing the amount of produced pure platinum clusters and minimizing the presence of other complexes and contaminants that might hinder measurements on the anionic photoelectron spectra of the bare ones. This spectrum is shown in the upper plot in Figure 4.2. We observe in red the formation of $Pt_n(H_2O)^-$ complexes and, additionally, a non-neglible amount of $Pt_n(H_2O)_2^-$ complexes for n>3. The lower (left and right) plots in Figure 4.2 zoom in the mass regions centered on respectively Pt^- and Pt_3^- to have better insights into contaminants and isotopic distributions of both species. Pt_3^- clearly adsorbs H_2O and its isotopic distribution agrees with the theoretical one. The observed disagreements between the experimental and the simulated isotopic distributions in Pt_3^- come from showing individually the discrete isotopic abundances rather than the isotopic profile that would result from adding up isotopic abundances with almost identical masses. It is impossible from a so dense and unresolved isotopic distribution to determine the presence of Pt_3H^- and/or $Pt_3H_2^-$, so to elucidate this last point, the mass spectrum of Pt^- is also analyzed in detail. Pt^- barely adsorbs H_2O and its isotopic distribution clearly resembles the theoretical one, except for the measured relative high intensity of the isotope ^{192}Pt. This is interpreted as an intensity artifact generated by a not perfect voltage optimization in the linear ToF, which is further supported by the shoulder that the isotopic distribution shows at masses below 192 u as well as by the slightly higher experimental intensity of the isotope ^{194}Pt respect to the isotope ^{195}Pt (their tabulated abundances are respectively 32.85% and 33.78%). Still, this mass spectrum does not fully exclude the presence of small hidden amounts of Pt_nH^- complexes that could have a non-negligible influence in the photoelectron spectra of Pt_n^- clusters. Indeed, despite the agreement between the measured photoelectron spectrum of Pt_3^- at 300 nm that is shown in the incoming subsection and the one in

the work of Ganteför et al.[190], very small imprints from the Pt_3H^- complex cannot be fully discarded.

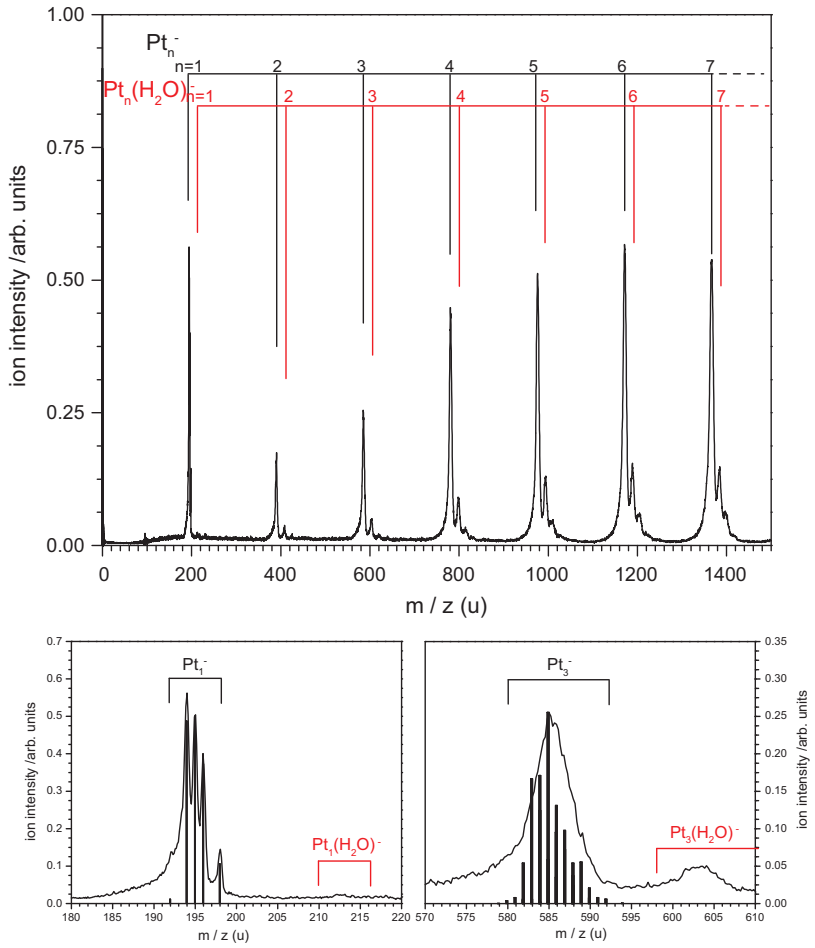

Figure 4.2: Overview of the mass spectrum of anionic Pt_n clusters (upper plot) and resolved zooms on Pt^- (lower left plot) and Pt_3^- (lower right plot) that also include their respective tabulated isotopic distributions. $Pt_n(H_2O)^-$ complexes are indicated in red in the upper plot. $Pt_n(H_2O)_2^-$ complexes are formed for n>3 but they are not explicitly indicated. The pattern observed in the lower left plot corresponds to the stable isotopic distribution of Pt: ^{192}Pt (0.78 %), ^{194}Pt (32.86 %), ^{195}Pt (33.78 %), ^{196}Pt (25.21 %) and ^{198}Pt (7.36 %). The relative high intensity of the isotope ^{192}Pt is justified by a not perfect voltage optimization in the linear ToF (see text for more details) and the intensity of $Pt(H_2O)^-$ is negligible. None of both lower spectra fully exclude the presence of small hidden amounts of Pt_nH^- complexes.

4.3 Overview

The angularly integrated VMI photoelectron spectrum of Pt_3^- for the highest photon energy used (4.133 eV, 300 nm) is shown in Figure 4.3 and it covers a range of 1.5–4.0 eV for the electron binding energy. This spectrum largely agrees with earlier results for this range[188–190]. It is worth to mention that this agreement was also found with other Pt_3^- photoelectron spectra that had been measured in the group of Lai Sheng Wang through private conversations with the author. One can identify eight main bands, X and A-G. For part of them vibrationally resolved spectra are obtained by detaching and analyzing the kinetic energy distribution of slow electrons using the appropriate photon energies. Such highly resolved spectra are measured for the bands X, A (in part), D and E (Figures 4.11 and 4.13) and will be discussed and assigned here by comparison to results from DFT calculations via Franck-Condon simulations. Additional insights into the character of the electronic transitions is obtained from the angular distribution of the detached electron.

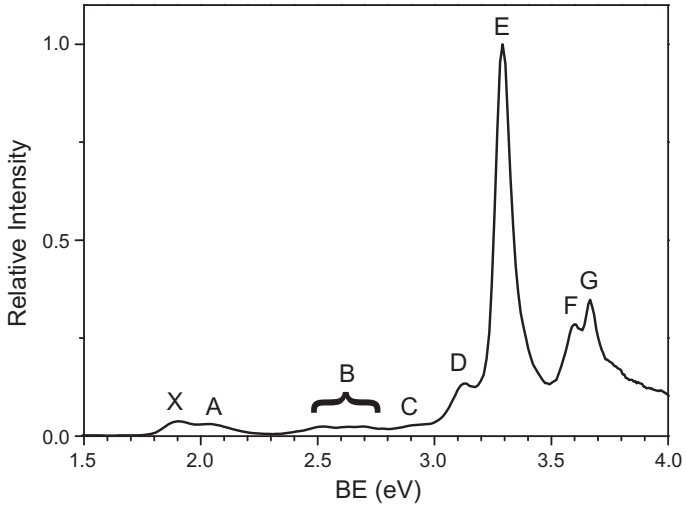

Figure 4.3: Photoelectron spectrum of Pt_3^- measured at 4.13 eV (300 nm). Eight bands are readily identified, labelled X and A to G. The bands up to a binding energy of ≈3 eV are assigned to transitions between the triangular isomers due to their low intensity. The higher energy bands are assigned to transitions between the linear isomers.

Our computational results agree with conclusions from earlier works on the contribution of two isomers, a linear and a triangular, to the anion PES[204]. The ground state is the linear isomer ($^4\Sigma_g^-$), while a triangular isomer ($^2A_2'$ with D_{3h} symmetry) is calculated to be 0.638 eV higher in energy. Their different multiplicity forbids the relaxation of $^2A_2'$ into $^4\Sigma_g^-$, so this may explain a high, non-Boltzmann, population of $^2A_2'$. This ordering is reversed in the neutral species where all transitions between linear (and bent) isomers are found at significantly higher energies (>3 eV) than the triangular ground state. Following these ideas, the adiabatic electron affinity of Pt_3 corresponds to a transition between triangular isomers (inside band X) and most transitions between triangular states are lower in energy (bands A to C), well distinguishable from those between linear and bent isomers (bands D to G). No bands were assigned to electronic transitions from linear to triangular isomers and vice versa.

In order to corroborate this assignment, we tried to quench the population of $^2A_2'$ by cooling down the cluster source to ≈77 K but no changes in the relative intensities of bands X to C with respect to bands D to G were observed. Additionally, studies on reaction kinetics between Pt_3^- and CH_4[196] demonstrated the existence of two isomeric forms; one reactive and one unreactive. Reactive gases (CH_4, N_2O, etc.) were introduced to induce relative intensity changes through isomer specific reactivities but, again, no appreciable changes were observed. As the large amount of information contained in Figure 4.1 can lead to confusion upon their application in the final assignment of the experimental results, the scheme that summarizes the information on the final assignment, Figure 4.4, is already shown here to facilitate the further discussion.

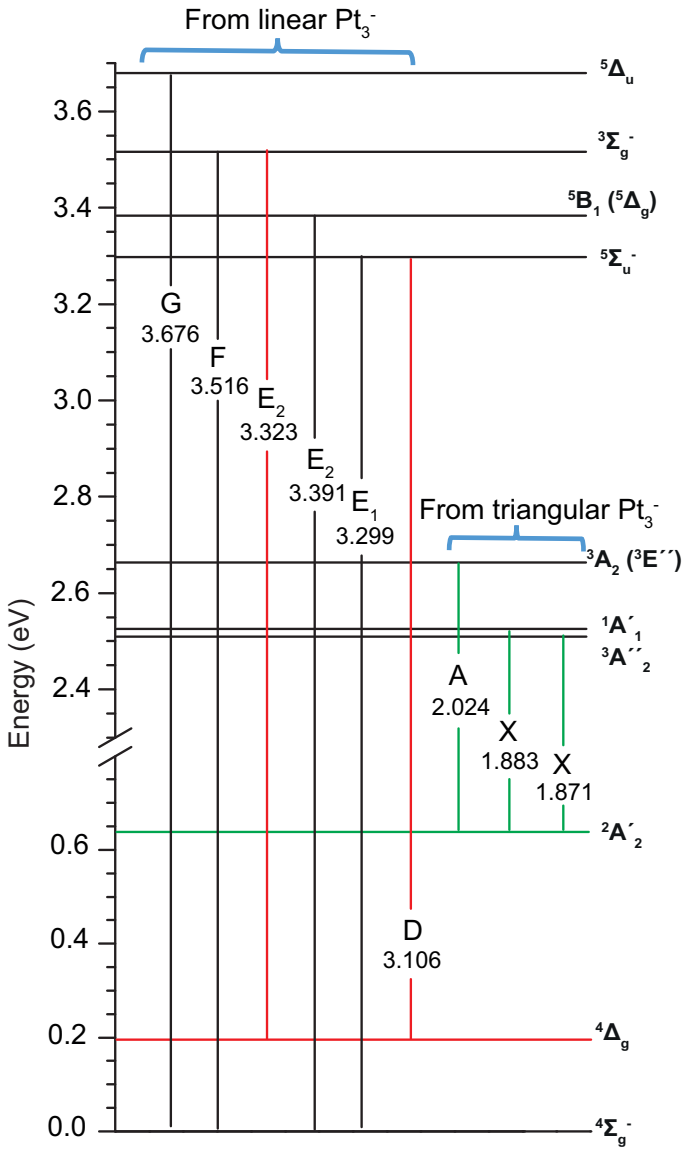

Figure 4.4: Summary scheme with all the experimentally assigned electronic transitions to the identified bands in the photoelectron spectrum of Pt_3^- where each transition shows the experimentally determined DE_{ad}. In black are the transitions from the ground anionic state with linear geometry, $^4\Sigma_g^-$, in red those from the first excited anionic state with linear geometry, $^4\Delta_g$, and in green the transitions from the ground anionic state with triangular geometry, $^2A_2'$. This scheme complements Figures 4.1 and 4.3. A more detailed discussion about the vibronic features in each band is given in this chapter. The calculated vibrational modes, as well as their electronic configurations are shown in Table 4.1.

4.4 Computational results

The calculations were carried out as follows: firstly, the ground states in the anionic and neutral Pt_3 were obtained. Secondly, the excited electronic states of the anionic and neutral trimers were obtained from their respective ground states by creating "frozen" holes in their molecular orbitals (from HOMO-1 to deeper ones) through the excitation of the corresponding electron and the subsequent relaxation of the resulting electronic structure. The obtained electronic states were tested in a third step by removing electrons in the calculated anionic states and checking the transitions that were prompted. In the anion, these calculations predict a ground state, $^4\Sigma_g^-$, with $D_{\infty h}$ symmetry, a bond length of d=2.378 Å and an electronic configuration $(3\pi_g)^2(6\sigma_g^+)^1(2\delta_g)^4(1\delta_u)^4(5\sigma_u^+)^2(1\delta_g)^4$. A linear first excited state in the anion, $^4\Delta_g$, was calculated at 0.303 eV with an electronic configuration $(6\sigma_g^+)^2(3\pi_g)^2(2\delta_g)^3(1\delta_u)^4(5\sigma_u^+)^2(1\delta_g)^4$ and a bond length of d=2.412 Å. The larger bond length of $^4\Delta_g$ is explained by the antibonding nature of $6\sigma_g^+$ which, as a consequence of a a spin-allowed electronic transition from the $2\delta_g$ to the $6\sigma_g^+$ orbital, is doubly populated. Additionally, DFT calculations predict an important energetic rearrangement of the molecular orbitals in the anion through a hypothetic $^4\Sigma_g^- \rightarrow {}^4\Delta_g$ transition, where the HOMO of $^4\Sigma_g^-$, $3\pi_g$, becomes the HOMO-1 in $^4\Delta_g$ and the HOMO-1 of $^4\Sigma_g^-$, $6\sigma_g^+$, becomes the HOMO in $^4\Delta_g$. This energy inversion in their electronic configurations is shown in Table 4.1 by a different left-to-right ordering of the orbitals. A second excited electronic state with D_{3h} symmetric structure, $^2A_2'$, is calculated at 0.638 eV as the most stable triangular anion with the configuration $(1a_1'')^2(2a_2')^1(4e'')^4$. Its different multiplicity with respect to $^4\Sigma_g^-$ reveals that a hypothetical $^4\Sigma_g^- \rightarrow {}^2A_2'$ transition would be forbidden.

The overall picture (see Figure 4.1) of the calculated states in the anionic and neutral Pt_3 corroborates the ordering proposed in the overview: while the energetically lowest states in the anion have a linear geometry, this ordering is inverted in the neutral with the triangular isomers having the lowest energies. Thus, the calculated ground state in the neutral is a triplet with D_{3h} symmetry, $^3A_2''$, and it results from the electronic detachment of the triangular anion's

$1a_1''$ orbital. It has a binding energy per atom of 2.378 eV. The calculated DE_{ad} for this triangular isomer is 2.002 eV, what corresponds to the calculated adiabatic electron affinity (EA_{ad}) for Pt_3. The first excited state of the neutral is reached when detaching the unpaired electron in the anion from the $2a_2'$ orbital, and it is an equilateral singlet, $^1A_1'$, 0.111 eV above the ground state. Vertical detachment from the $4e''$ orbital gives rise to the second excited state in the neutral, $^3E''$, which undergoes a slight Jahn-Teller distortion to an obtuse isosceles triangle, $^3A_2$, at 0.154 eV above the ground state with an apex angle of 61.4°. This adiabatically relaxed and "rigid" state is only 96 cm^{-1} lower than the vertically calculated $^3E''$ state, which means that the JT stabilization energy of the system must be even smaller. As the $^3A_2$ state corresponds to the minima of the JT distorted potential, the saddle points are a $^3B_1$ state. The degenerate e′ mode (155 cm^{-1}) in the undistorted $^3E''$ state splits in the adiabatically "rigid" $^3A_2$ state to a_1, 153 cm^{-1}, and b_1, 151 cm^{-1}, modes. Their small difference upon degeneracy breakdown of only ≈2 cm^{-1} may imply a very small JT effect. Earlier calculations of Fortunelli [207] on the triangular isomer reached the same conclusions with slightly smaller excitation energies.

The energetically lowest linear isomer calculated in the neutral is a $^5\Sigma_u^-$ state, and it is obtained by the removal of a β electron from the $5\sigma_u^+$ orbital in the $^4\Sigma_g^-$ anionic ground state. The detachment of an electron from the HOMO-4 in a hypothetical $^4\Sigma_g^- \rightarrow {}^5\Sigma_u^-$ transition is indicative, for such a small cluster in a direct photodetachment process, of a big electronic reorganization in the valence molecular orbitals. As the bond length of $^5\Sigma_u^-$, d=2.373 Å, is very similar to the 2.378 Å in $^4\Sigma_g^-$, $5\sigma_u^+$ might be a nonbonding (slightly antibonding) orbital. The next state in an increasing energy ordering is $^3\Sigma_u^-$. It appears at DE_{vert}=3.362 eV when detaching an α electron from the $5\sigma_u^+$ orbital. Contrary to the high spin state, $^5\Sigma_u^-$, the equilibrium geometry of $^3\Sigma_u^-$ is a bent structure with C_{2v} symmetry, $^3A_2$, that has an apex angle of 141° and d=2.334 Å.

Very close in energy is calculated a $^5\Delta_g$ state at DE_{vert}=3.323 eV, born from the detachment of a $2\delta_g$ electron in the $^4\Sigma_g^-$ anionic state. Its adiabatic geometrical relaxation gives a bent structure, $^5A_1$ (C_{2v}), at DE_{ad}=3.311 eV

with a bond length of d=2.363 Å and an apex angle of 160°. In this case, the Renner-Teller effect, which lifts the electronic double degeneracy of $^5\Delta_g$, is responsible for the symmetry reduction in the cluster. In addition, the adiabatic relaxation of $^5\Delta_g$ was also calculated by imposing a final linear geometry to the cluster, and a metastable linear structure was calculated at 0.007 eV higher than $^5A_1$ with d=2.361 Å. As the Renner-Teller effect predicts the splitting of Δ into the non-degenerate A_1 and B_1 states, we propose that the metastable linear state corresponds to $^5B_1$, so $^5\Delta_g$ splits into two final non-degenerate states with linear and bent geometries, i.e., $^5B_1$ and $^5A_1$ respectively. Note the proximity between $^5A_1$ and $^3A_1$, whose calculated DE_{ad} are separated by only 0.003 eV ($\approx$24 cm^{-1}).

$^3\Sigma_g^-$ and $^5\Delta_u$ are the two calculated states in the neutral with the highest energies. $^3\Sigma_g^-$ appears when the $6\sigma_g^+$ singly occupied orbital in $^4\Sigma_g^-$ is emptied, and its bond length reduction to d=2.316 Å corroborates the aforementioned antibonding character of the $6\sigma_g^+$ orbital. $^5\Delta_u$ (with d=2.382 Å) is reached by the detachment of an electron from a $1\delta_u$ orbital whose non-bonding (slightly antibonding) character is shown by the small change in the bond length of the cluster.

Additionally, a hypothetical $^4\Sigma_g^- \rightarrow {}^3A_2''$ electronic transition was calculated by the detachment of an electron from a $3\pi_g$ orbital. The big geometrical rearrangement involved in the transition would imply too small FC factors to be experimentally detected.

From the anion first excited state, $^4\Delta_g$, transitions to the neutral $^5\Sigma_u^-$, $^5A_1$ and $^3\Sigma_g^-$ states were predicted. $^4\Delta_g \rightarrow {}^5\Sigma_u^-$ can take place through two different correlated two-electron processes: either the photodetachment of an electron from $5\sigma_u^+$ and the subsequent electronic transition within the cluster from $6\sigma_g^+$ to $2\delta_g$, or the removal of an electron from $6\sigma_g^+$ accompanied by a transition from $5\sigma_u^+$ to $2\delta_g$. $^4\Delta_g \rightarrow {}^5A_1$ takes place by the detachment of an electron from the $6\sigma_g^+$ orbital (differently from the $^4\Sigma_g^- \rightarrow {}^5A_1$ transition, where the $2\delta_g$ electron is photodetached). In the $^4\Delta_g \rightarrow {}^3\Sigma_g^-$ transition the doubly occupied $6\sigma_g^+$ orbital is emptied by the detachment of one electron with the simultaneous transition of the other from $6\sigma_g^+$ to $2\delta_g$. All the transitions

that start in the predicted triangular anionic isomer, $^2A_2'$, lead only to the calculated neutral triangular isomers and do not involve any linear one.

Calculations including spin-orbit coupling were done only for the lowest energy state of the neutral and anionic triangular isomers with their structural parameters and vibrational frequencies given in Table 4.6. Resorting to group theory, the inclusion of SOC in states with even multiplicity leads to a change from D_{3h} to the D_{3h}^2 double point group for clusters with equilateral geometry. The anionic ground state in absence of SOC is $^2A_2'$. Its spin, S=$\frac{1}{2}$, transforms as $E_{\frac{1}{2}}$ in the D_{3h}^2 double group. The direct product of spin and orbital electronic parts as result of interaction of both momenta will be $E_{\frac{1}{2}} \times A_2' = E_{\frac{1}{2}}$, so the Kramers degeneracy is caused by a single unpaired electron. A JT instability will not appear in the anion because the antisymmetric product of the spin-orbit irreducible representation by itself, $E_{\frac{1}{2}} \times E_{\frac{1}{2}} = [A_1']$, does not contain the non-totally symmetric normal mode e′ [179]. The calculated ground state of the anion is an equilateral triangle with bond lengths of 2.535 Å, corroborating the predictions by group theory. The spin in the neutral ground state, $^3A_2''$, contrary to the anion, results from an even number of unpaired electrons, so the spin function and thus the spin-orbit function has only one-valued representations [111]. In the D_{3h} point group the irreducible representations for S=1 are $A_2' \bigoplus E''$ and their product with A_2'' results in the splitting in the electronic states $A_1'' \bigoplus E'$. The A_1'' state will be equilateral in the equilibrium conformation while E′, due to its degenerate spin-orbit function is expected to be unstable in the equilateral conformation upon coupling with the degenerate vibrational mode e′. However, as mentioned in Herzberg [111] the E′ component will be only slightly unstable (towards $A_1 \bigoplus B_2$) because in an orbitally non-degenerate state SO coupling is small. In principle, we see this prediction reflected in our calculations as the inclusion of relativistic effects gives rise to two different electronic states arising from the neutral ground state: an obtuse isosceles triangle (C_{2v} symmetry; short bond d=2.512 Å; apex angle α=60.13°) at DE_{ad}=2.021 eV and an equilateral triangle (D_{3h} symmetry; d=2.535 Å) at DE_{ad}=2.052 eV. An isosceles triangle as ground state was also calculated by Blonski et al. [220] as the result of a JT distortion in the D_{3h} structure favored by SOC. Other theoretical studies point to the

stabilization of a triplet relative to a singlet as neutral ground state when SOC is included; Huda et al.[211] found without SOC an equilateral singlet ground state 0.05 eV lower than the triplet, but with SOC it shifts to 0.02 eV above the triplet. Similar results appear in the work of Balasubramanian et al.[222]. Fortunelli, however, did not observe any energy order change with respect to the non-relativistic calculations. The BEs of the clusters are around 0.12 eV/atom smaller with the inclusion of relativistic effects, and this probably also relates to the slightly smaller vibrational frequencies found with SOC. Nevertheless, the calculated BE of $^3A_2''$ without SOC agrees quite well with an experimental lower bound of BE of 2.37 eV/atom obtained by collision-induced dissociation[223]. The calculated SO splitting energy between both neutral states is in our case ΔE=0.031 eV, a small value if we compare it with the 0.2 eV identified for Au_3[222].

4.5 Analysis of each band

4.5.1 Band X

The structure of band X at high resolution is presented in Figure 4.5. The experimental spectrum is constructed out of 5 single measurements at photon energies of 1.887 eV (657 nm), 1.901 eV (652 nm) 1.905 eV (651 nm), 1.922 eV (645 nm), 1.962 eV (632 nm) in the SEVI mode, detecting photoelectrons up to a kinetic energy of 0.035 eV, to get an overall good resolution. The assembly from separate highly resolved measurements leads to some discontinuities at the joining points and there are changes of the relative intensities in vibrational progressions. This lies in the fact that energy threshold effects or other VMI experimental artifacts have not been considered in the intensity scaling. Every highly resolved spectrum was normalized through multiplication by a fixed constant over all its intensities to scale the highest peak in each highly resolved spectrum to the intensity of the same peak in the 630 nm spectrum. The positions of the observed signals in this merged spectrum are listed in Table 4.3 together with their tentative assignments (page 111).

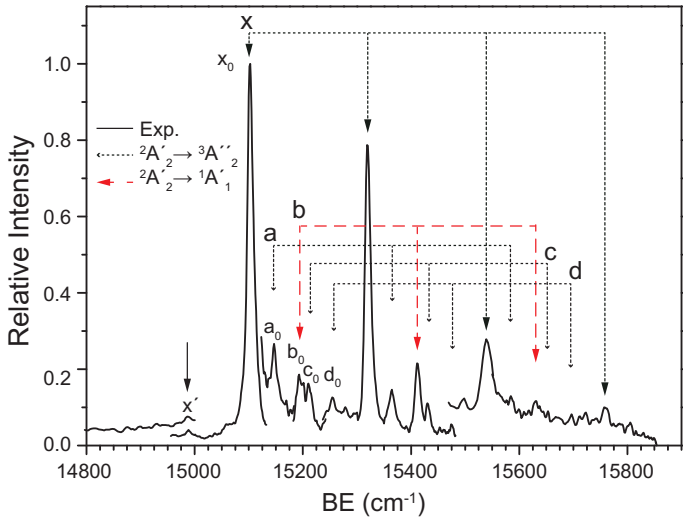

Figure 4.5: Identified vibrational progressions in band X. The arrow just below 15000 cm^{-1} marks a hot band that is discussed in the text.

For the sake of clarity, all high-resolved measurements taken over band X are shown in Figure 4.23 in the Appendix 4.A. Although the selection of data to create the merged spectrum introduces some arbitrariness, it gives in most cases a similar uncertainty for the peak positions to the single highly resolved measurements, considering their different resolution and intensity patterns. Therefore nearly always in the following only the data from the merged spectrum is used for the assignment of band X.

The most intense peak, $\mathbf{x_0}$, corresponds to a BE of 1.8716±0.0009 eV with a FWHM of 7 cm^{-1}. This gives the best absolute resolution reached here for Pt_3. $\mathbf{x_0}$ forms the origin for a distinct vibrational progression, that is visible up to the second overtone with a frequency of ω=216.9±0.5 cm^{-1} and it shows no substantial anharmonicity ($\omega_e x_e$=0.5±0.1 cm^{-1}). A progression of ≈225 cm^{-1} had been noted before by Ervin et al.[188] and its origin at 1.87±0.02 eV was used to define the EA_{ad} of Pt_3. Between the peaks of the main vibrational progression there are several features not previously resolved. All these peaks can be identified as part of four further vibrational progressions $\mathbf{a_n}$, $\mathbf{b_n}$, $\mathbf{c_n}$ and $\mathbf{d_n}$ in Figure 4.5. The progressions show a frequency of ω=217.3±0.7 cm^{-1}, the same as the main vibrational progression, and seemingly follow the intensity pattern of $\mathbf{x}$. Only $\mathbf{b}$ has a higher intensity in the second peak (even though this might be doubtful due to the possible artifacts in the intensity).

At this point, we make an *intermezzo* to tackle the vibronic structure of band X in Figure 4.5 resulting from the use of a platinum target in its natural isotropic distribution. Platinum atoms have 78 protons and there are five naturally occurring stable isotopes, whose abundance is given by

$$^{192}\mathrm{Pt} = 0.8\% \quad ^{194}\mathrm{Pt} = 32.9\% \quad ^{195}\mathrm{Pt} = 33.8\% \quad ^{196}\mathrm{Pt} = 25.2\% \quad ^{198}\mathrm{Pt} = 7.4\%$$

The nuclear spin, I, of the four isotopes with an even number of neutrons (and protons) is equal to zero. The ^{195}Pt isotope has a non-zero nuclear spin, I = 1/2.

Molecular symmetry plays an important role in the appearance of molecular spectra. Symmetry restricts the number of distinguishable vibrational

modes, for instance, and when a molecule has identical atoms in symmetry-equivalent positions this influences its rotational energy level structure. Prior to starting an analysis of the Pt_3 spectra we therefore consider the possible nuclear symmetries of the triangular and linear forms of the trimer, taking the natural abundance of the stable isotopes of Pt and their nuclear spin into account.

In all previous theoretical and experimental investigations on Pt_3, the cluster was considered either as purely formed from the most abundant isotope, ^{195}Pt, or the mass of each of the atoms in the cluster was taken as the abundance-weighted average mass of the five stable isotopes. Indeed, our calculations were carried out following the second option, with a mass of 194.9648 u for the Pt atom. In either case, all three atoms were considered to be identical and the possible influence of the nuclear spin was neglected. It is clear, however, that before interpreting the vibronic structure of the cluster based on the properties derived from the (geometrical) point group of the molecule (the point group is a subgroup of the CNPI group) we have to statistically calculate the probabilities of the various symmetries of the triangular and linear trimers, as some of the subtle vibronic effects depend purely on the nuclear symmetry of the cluster. The lack of symmetry in the cluster due to the nuclear composition has important consequences for possible physical phenomena: even if the triangular trimer in an electronic state has geometrically D_{3h} symmetry (i.e., if it is an equilateral triangle) and even if its orbital irreducible representation, according to its electronic configuration, is doubly degenerate, it can formally not undergo Jahn-Teller distortion when the three nuclei are isotopically different because, according to the CNPI group, no possible permutation operations are possible between them. As far as the symmetry properties are concerned, such a cluster has C_s symmetry and behaves as formed by three distinctly different elements.

A triangular structure in which the three nuclei have the same isotopic composition has D_{3h} symmetry. With only two identical nuclei, the symmetry is C_{2v} while the cluster will have C_s symmetry when it consists of three different isotopes. In the linear Pt_3 structure things are slightly different: if the two nuclei on the outside are isotopically the same, the symmetry of the

molecule is $D_{\infty h}$. When the central atom is isotopically identical to the two outer ones, this will not increase the symmetry further, i.e. the symmetry is $D_{\infty h}$ independent of the isotopic nature of the central atom in this case. If the linear Pt_3 cluster has two isotopically identical nuclei with one in the central atom position and the other on the outside or if all three nuclei are isotopically different, the symmetry of the molecule is $C_{\infty v}$. In the Table 4.2 the percentages of triangular and linear Pt_3 structures are given for each possible symmetry. When there are identical nuclei in symmetry-equivalent positions, the distribution of the total percentage over the two possibilities, i.e. identical nuclei with I=0 or I=1/2, is given as well.

Triangular and Linear Pt_3

CNPI Group	Total (%)	I=0 (%)	I=1/2 (%)
D_{3h}	9.063	5.202	3.861
C_{2v}	60.351	37.632	22.719
C_s	30.881		

CNPI Group	Total (%)	I=0 (%)	I=1/2 (%)
$D_{\infty h}$	28.180	17.746	11.434
$C_{\infty v}$(2 identical nuclei)	40.234		
$C_{\infty v}$(3 different nuclei)	30.881		

Table 4.2: Calculated percentages for the possible CNPI symmetries of triangular and linear Pt_3. The percentages were obtained from the isotopic abundances of Pt.

The presence of identical nuclei in symmetry-equivalent positions mainly has an effect on the rotational energy level structure of the cluster. The product of the rotational wavefunction and the nuclear spin wavefunction has to fulfill the symmetry requirements of the group to which the cluster belongs. In diatomic molecules with I=0, this leads to the disappearance of all even or of all odd rotational levels (e.g. in $^{16}O_2$) whereas in diatomic molecules with I=1/2 this leads to the existence of distinct ortho- and para-species (e.g in H_2). In the triatomic system under consideration here, the presence of identical nuclei in symmetry-equivalent positions will also lead to the existence of distinctly different nuclear spin-species (ortho-, meta- and para- for D_{3h} Pt_3; ortho- and para- for C_{2v} and $D_{\infty h}$ Pt_3). An additional comment

concerning the center of mass of the different isomers must be made: Among the triangular isomers, only those with D_{3h} symmetry will have the center of mass in the same position independently of their isotopic constituents. This situation holds for the linear isomer with $D_{\infty h}$ symmetry. For any other combination of the isotopes, the position of the center of mass would sligthly change and the structure of the rotational spectrum would gain complexity. However, as the rotational constants of the Pt_3 clusters are quite small and as the spectral resolution in the experiment is limited, it is anticipated that the effects of the nuclear spin statistics and of the positions of the centers of mass have no practical consequence for the interpretation of the experimental spectra, i.e. that their effects cannot be observed in the photoelectron spectra.

Apart from the symmetry and nuclear spin effects discussed above, there are two other effects that need to be considered. The first is the rather trivial one, that the masses of the triangular clusters that have the same symmetry will still vary depending on their exact isotopic composition. Given that the abundance of the lightest stable isotope, ^{192}Pt, is rather small and that the next least abundant isotope is the heaviest one, ^{198}Pt, the spread in mass of the various Pt_3 clusters is effectively clearly within $\pm 1\%$ of their average mass; the vibrational frequencies are thus expected to be within $\pm 0.5\%$ of their average vibrational frequency. The effect of the different isotopic compositions on the vibrational frequencies is therefore expected to be close to, but still below, the resolution obtained in the experimental photoelectron spectra.

The second effect that still needs to be considered is that the electron affinity (EA) of the triatomic clusters that contain different Pt isotopes might be slightly different. The EA isotope shift should in first order be zero and EA changes are therefore expected to be small. Nevertheless, any EA isotope shift would lead to the appearance of the photoelectron spectra at slightly different kinetic energies for clusters containing different Pt isotopes, even when these clusters would have identical vibrational and electronic structures in their anionic and neutral ground states. Several experimental[224–230] and theoretical[228,231] investigations have studied the relevance and magnitude of the isotope shift in the EAs of different atomic systems. In light elements the fractional shift of the EA appears to be slightly smaller (0.0827 cm^{-1} for

^{7}Li/^{6}Li[227] and 0.073(6) cm^{-1} for ^{13}C/^{12}C[229] on total EAs of 0.62 eV and 1.26 eV, respectively) than in heavy elements. For lead isotopes, shifts in the EA of 0.0745 cm^{-1} for ^{206}Pb/^{208}Pb and of 0.1001 cm^{-1} for ^{207}Pb/^{208}Pb[230] have been reported relative to the total EA of 0.36 eV. The latter results need to be treated with caution, however, since the reported isotope shifts appear not to be as much shifts in the EA, but rather shifts in the spin-orbit split levels of the neutral Pb isotopes. In our work, the isotope shift in a triatomic system must be considered, for which a phenomenological sum rule can be used, which dictates additivity of isotope shifts upon multiple substitution[225]. Even if we assume that the magnitude of the isotope shift scales linearly with the value of the EA, that the shift gets larger when the mass-difference between isotopes gets larger, and that the effect for a trimer is three times as large than for the atom, this would lead to an isotope shift in the EA of the Pt_3 anion that is still within the experimentally observed line-width.

The conclusion therefore is that the effect of a different EA for clusters with a different isotopic composition can be neglected in the present study, just as the effect of identical nuclei in symmetry-equivalent positions on the nuclear spin statistics and the effect of the different masses on the vibrational frequencies. The effect that remains and that cannot a priori be neglected is the formally different symmetries of the triangular and linear structures of the Pt_3 trimer.

In the low-energy photoelectron spectrum that is attributed to the transition from the triangular structure of the anion to the triangular ground state of the neutral Pt_3 cluster, five vibrational progressions (labeled **x** to **d**) are observed in a mode that has within the experimental accuracy the same frequency of 218 cm^{-1}. In all of these progressions, the first peak, labelled with the subindex 0, i.e. $\mathbf{x_0}$, $\mathbf{a_0}$, etc, is the strongest one (even though this might be doubtful for the **b** progression). Relative to the peak labelled as $\mathbf{x_0}$, the origins of the other progressions are found at +44 cm^{-1} ($\mathbf{a_0}$), at +91 cm^{-1} ($\mathbf{b_0}$), at +108 cm^{-1} ($\mathbf{c_0}$) and at +152 cm^{-1} ($\mathbf{d_0}$). These might be five distinct progressions, but as the distance $\mathbf{x_0}$–$\mathbf{c_0}$ is the same as the distance $\mathbf{a_0}$–$\mathbf{d_0}$, it might also be only three distinct progressions (**x**, **a** and **b**), with the

x and **a** progressions having a second characteristic frequency of 108 cm^{-1}. In either case, the question is where these distinct progressions originate from.

One possible explanation is that these three progressions result from the three different nuclear symmetries that are present for the triangular Pt_3. Considering the observed relative intensities of the progressions, the **x** progression would then be attributed to the most abundant species with C_{2v} symmetry, whereas the **a** and **b** progressions could be due to the less abundant species with D_{3h} or C_s, respectively. The integrated peak intensities for the **x**, **a** and **b** progressions have been calculated and their percentage values are ≈66 %, ≈20 % and ≈14 % respectively. The comparison with the calculated abundances of the three nuclear symmetries shows a certain resemblance, so this assignment should be considered in detail for future studies. Additionally, it was not possible to try the same quantitative approach for some of the bands that are assigned to transitions between linear electronic states (see bands D and E in Figures 4.11 and 4.13) since their resolution is lower than the one of band X and, therefore, the peak integration was not possible. We close here the *intermezzo* on the physical implications of the isotopic richness of Pt and we continue the explanation of the vibronic structure of band X under the assumption of an isotopically pure target.

As we mentioned just before the *intermezzo*, **b** is the only vibrational progression in band X which shows a higher intensity in the second peak. This may point to the fact that all these transitions share the same lower and upper electronic state while for **b** a different state may be involved. This interpretation is supported by the Franck-Condon simulations given below. Only a very weak feature at 1.857±0.001 eV visible in spectra taken at different photon energies and marked with an arrow in Figures 4.5 and 4.6 seems to be not related to any of these progressions because it is shifted by -208 cm^{-1} relative to $\mathbf{a_0}$, which is a significant deviation from the 218 cm^{-1} main spacing within all progressions.

For a detailed analysis of its vibrational structure, FC simulations based on the results of the non-SOC calculations included in Figure 4.1 and in Table 4.1 are performed with the PGOPHER program [232,233]. As the D_{3h}

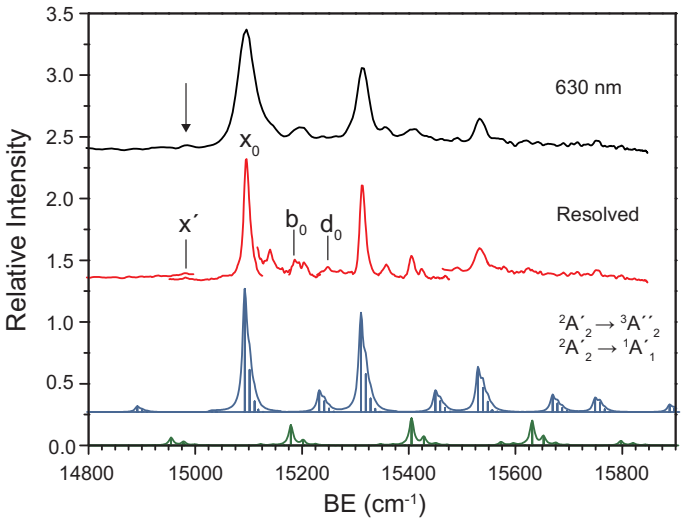

Figure 4.6: Comparison between experiment and FC simulations evidences the presence of two close low-lying electronic state in the neutral: $^1A_1'$ and $^3A_2''$. Sticks represent FC factors while their enveloping line was chosen to have a Lorentzian width of 10 cm^{-1}.

point group is not supported in PGOPHER, all the triangular isomers are treated in the following in C_{2v} symmetry. All the FC simulations are done with a vibrational temperature of 100 K because at higher temperature prominent hot bands below 1.85 eV are predicted that are not seen in the experimental spectra while at much lower temperatures progressions related to transitions starting at vibrational excited states of the anion disappear, see Figure 4.21. FC simulations for the $^2A_2'\rightarrow{}^3A_2''$ and $^2A_2'\rightarrow{}^1A_1'$ transitions are plotted in Figure 4.6. The electronic transition to the triplet reveals a perfect resemblance to the main vibrational progression, **x**, by shifting the calculated DE_{ad} by -0.131 eV. The FC simulation reveals that each peak of the experimental progression involves in fact three unresolved vibrational progressions, the two less intense are combination bands with the e′ mode, in the totally symmetric mode of the $^3A_2''$ state: $1_0^n2_0^0$, $1_0^n2_1^1$, $1_0^n2_2^2$. The simulation shows a second vibrational progression starting at +137 cm^{-1} from the one assigned to **x**. It does not perfectly coincide with any experimental feature, on one hand it is 28 cm^{-1} higher than **c** but also only 16 cm^{-1} lower than the

progression **d** so, at this point, there is no clear assignment of the combination bands $1_0^n 2_1^2$ and $1_0^n 2_2^3$ to either **c** or **d**. We observe that those combination bands do not only include transitions from excited modes in the anion but also they show a change of an odd number of quanta in ν_2. This becomes allowed only in the C_{2v} geometry considered in the simulations, but would be forbidden if both states have D_{3h} geometry. This suggests that either the real symmetry is reduced to an isosceles triangle as predicted by the SOC calculations, which would be a Jahn-Teller distortion, or the selection rules are relaxed due to vibronic effects without symmetry reduction, e.g. a pseudo Jahn-Teller effect.

Progression **b** fits from its intensity pattern well to the simulated progression for the $^2A_2' \rightarrow {}^1A_1'$ transition. Therefore, calculated vibrational frequencies in the $^1A_1'$ state were corrected by a factor of 0.96 and the whole simulation was shifted 0.257 eV to lower energies to align the most intense peaks of the progression in experimental data and simulation. The shifted origin of the simulation is then at 1.856 eV, which is close to the weak feature in the experimental spectrum at 1.857±0.001 eV discussed before. At first sight, this simulation suggests that $^1A_1'$ is the ground state of Pt_3, so triplet and singlet are energetically inverted with respect to the calculations. Nevertheless, a careful comparison of the peak positions in the FC simulation and the experimental spectrum reveals that the first peak in the simulation is shifted by about -10 cm^{-1} compared to the arrow marked peak while the positions of the other peaks fit within ±5 cm^{-1}. The shift of -10 cm^{-1} is too big to be explainable by simple experimental error, though the overall intensity pattern fits somehow. This suggests first of all that the peak marked with an arrow is not $\mathbf{b_0}$, but the progression starts as marked in Fig. 4.5 making $^3A_2''$ the neutral ground state, as predicted by theory.

The tentative assignment achieved so far gives reasonable explanations for the progressions **x**, **b**, and either **c** or **d**, but totally lacks an explanation of **a** as well as the peak **x′**. It has been discussed before that the peak **x′**, marked with an arrow in Fig. 4.5 and 4.6, does not correspond to the origin, $1_0^0 2_0^0$, of the $^2A_2' \rightarrow {}^1A_1'$ transition. If it was the case it should be at 218 cm^{-1} from peak $\mathbf{b_0}$ ($1_0^1 2_0^0$ transition), but it is only at 206 cm^{-1}. Therefore, it

is considered to be a hot band. One could assign it to a $1_1^0 2_0^0$ transition considering the totally symmetric mode of the anion at ν_1=206 cm^{-1}, but one should be able to find another hot band for peak **x$_0$** at 206 cm^{-1}. As the latter feature is not found, it is assigned instead to a $1_0^0 2_1^0$ transition to $^3A_2''$ with an anionic frequency of ν_2=115 cm^{-1}. The similar calculated value for the doubly degenerate mode in the anionic state used in the FC simulations, ν_2=123 cm^{-1}, corroborates this assignment. Furthermore, peaks **c$_0$**, **c$_1$** and **c$_2$** as shown in Figures 4.5 and 4.23 could correspond to combination bands $1_0^n 2_0^1$ with n equal to the subscript of the label for each peak. Therefore, the frequency of the doubly degenerate mode in the $^3A_2''$ state is ν_2 ≈111 cm^{-1}.

For the progressions **a** and **d** three possible explanations are proposed, but the third will be the chosen one. In the first one, the progressions **a** and **d** appear as a result of a very small SO coupling splitting in $^3A_2''$. **a** and **d** are respectively spaced from **x** and **c** by 44 cm^{-1} and **a$_0$**/**d$_0$** as well as **x$_0$**/**c$_0$** have a similar intensity ratio. This suggest that maybe **x$_0$** and **a$_0$** are the origins of the transitions to the states that result of SO splitting in $^3A_2''$, i.e. the E′ and A_1'' electronic states which are 44 cm^{-1} apart. Consequently, one can further assign **c$_0$** to the transition to E′ while **d$_0$** would correspond to A_1'', both with D_{3h} symmetry. Nevertheless, the existence of **c$_0$** and **d$_0$** as transitions with $\Delta\nu_2$=odd cannot be found in states with high symmetry configurations (D_{3h}) and, therefore, both peaks can only be explained by the presence of a small JT effect in E′ and A_1'' that reduces their symmetry to C_{2v}. This is possible in E′, but A_1'' cannot show JT distortion as a result of SOC, which limits this explanation. Additionally, the questions of how big would be the SO splitting when the electronic state (here A_2'') is orbitally non-degenerate or if E′ would interact with $^1A_1'$ via relativistc effects modifying the energy order with $^3A_2''$ as predicted by Balasubramanian et al.[218] remain opened.

A further explanation for the observed 44 cm^{-1} splitting could be that it corresponds to the hypothetical singlet excited state of $^3A_2''$, calculated to lie 0.006 eV ≈48 cm^{-1} above $^3A_2''$ by Winczewski et al.[234], so that one observes the difference between $^2A_2' \rightarrow {}^1A_2''$ and $^2A_2' \rightarrow {}^3A_2''$.

The third explanation includes a pseudo Jahn-Teller effect as result of the vibronic coupling of $^3A_2''$ via the e′ mode with an excited triplet. Interestingly,

the appearance of many additional low intensity peaks between the main progression has been observed before for other triangular systems, e.g. for BF_3, NO_3^- and Na_3 and can be a sign of pseudo JT distortion[175,235–237]. As mentioned before, already the observation of a vibrational progression with $\Delta\nu_2$=odd assigned to **c** indicates such behavior for Pt_3. In case of a small linear pseudo JT effect it can be described by the adiabatic free rotor approximation as derived by Köppel et al.[235]. For Pt_3 one can consider the coupling of the $^3A_2''$ state with the second calculated triplet, the $^3E''$ state. Such vibronic coupling can take place between states with the same spin multiplicity through a vibrational mode ν which must fulfill the selection rule, $\Gamma_\nu \bigotimes \Gamma_m \bigotimes \Gamma_n \supset \Gamma_A$ with Γ_A being the totally symmetric irreducible representation[184]. Here, the coupling is only possible through the degenerate mode e′, i.e. $e' \bigotimes A_2'' \bigotimes E'' \supset \Gamma_A$. Finally, the $^3E''$ state induces a pseudo JT effect in the $^3A_2''$ state but also undergoes a Jahn-Teller distortion as found in the DFT calculations. In such a case the energies are given by:

$$E_{nj} = (n + \frac{1}{2})\omega - \frac{\lambda^2}{\omega} + \frac{j^2\omega^3}{4\lambda^2} \tag{4.1}$$

where n=0,1,2... is the radial quantum number, j is the pseudorotational quantum number which takes integer values instead of the half-odd integer values characteristic of the JT case[235], ω is the frequency of the degenerate mode and λ the linear coupling constant. The last term of equation 4.1 gives rise to the pseudorational levels in the system theoretically spaced in the form of a geometric sequence 1,4,9... given by j^2 multiplied by $\frac{\omega^3}{4\lambda^2}$. This fits very well to shifts found between the experimentally observed progressions: starting from **x**, **a** is shifted by 44 cm^{-1} while the same shift of 44 cm^{-1} is seen between **c** and **d**. Additionally, it might be interesting in future measurements to corroborate the existence of a vibrational progression identified by **e** in Figure 4.7 (red arrows) and in Table 4.3 that, as part of the geometric sequence formed by **x** and **a**, might have the pseudorotational quantum number j=2 and might be shifted four times 44 cm^{-1}, i.e. 176 cm^{-1}, allowing to ensure the proposed pseudo JT coupling.

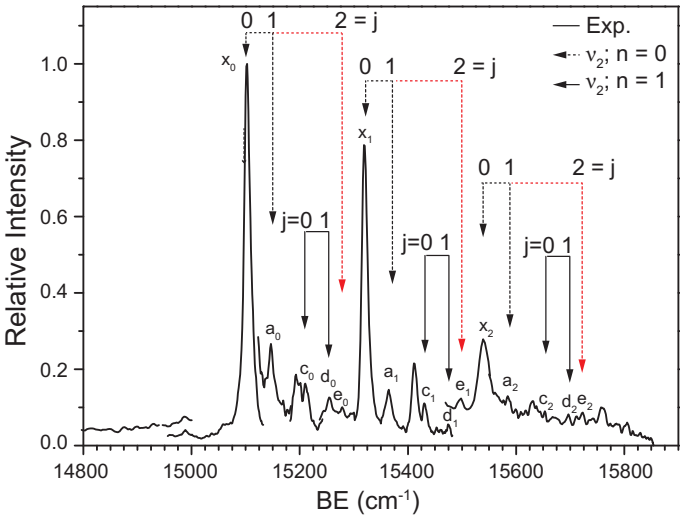

Figure 4.7: Pseudo Jahn-Teller effect observed in the transition $^2A_2' \rightarrow {}^3A_2''$ result of the vibronic coupling between $^3A_2''$ and $^3E''$ through e′. As PJT effect is weak it is treated in the AFR approximation.

A value for the linear coupling constant λ results from equation 4.1 by using as the harmonic frequency ω, the theoretically calculated value for e′ of 132 cm^{-1}. This results in λ=114 cm^{-1}, what gives a ratio of $\frac{\lambda}{\omega}$=0.86 and provides a first indication of the smallness of the pseudo JT effect and therefore, the suitability of the adiabatic free rotor approximation [235]. Consequently, the offset value $\frac{\lambda^2}{\omega}$ in equation 4.1 is 98 cm^{-1}, which now allows for conclusions about the equilibrium geometry in $^3A_2''$ that will remain D_{3h} if $\frac{\lambda^2}{\omega} \leq \frac{1}{2}(\varepsilon_{E''} - \varepsilon_{A_2''})$, as shown by Haller et al. [236]. Theoretically, half of the $^3E''$–$^3A_2''$ gap ($\frac{1}{2}(\varepsilon_{E''} - \varepsilon_{A_2''})$, see Table 4.3) is 544 cm^{-1}, while experimentally the difference between the origins of band X and A results in $\frac{1}{2}(\varepsilon_{E''} - \varepsilon_{A_2''}) \approx$ 613 cm^{-1}. Both values are clearly bigger than 98 cm^{-1} and, consistently, independently of the use of theoretical or experimental information, the conclusion is that the equilibrium geometry of $^3A_2''$ due to the pseudo JT effect has D_{3h} symmetry. A consequence of this phenomenon is a softening in the curvature of the adiabatic potential of $^3A_2''$ with the opposite effect in $^3E''$ [175]. This is the reason why the calculated harmonic frequency reduces its value

Peak	Electronic transition transition	Vibronic transition (D_{3h})	Pseudorotational number j (PJT)	Relative position to x_0 (cm^{-1})
x'	$^2A_2' \rightarrow {}^3A_2''$	$1_0^0 2_1^0$		-115
$\mathbf{x_n}$	$^2A_2' \rightarrow {}^3A_2''$	$1_0^n 2_0^0$	0	0
$\mathbf{a_n}$			1	44
$\mathbf{e_n}$			2	176
$\mathbf{c_n}$	$^2A_2' \rightarrow {}^3A_2''$	$1_0^n 2_0^1$	0	111
$\mathbf{d_n}$			1	155
$\mathbf{b_n}$	$^2A_2' \rightarrow {}^1A_1'$	$1_0^n 2_0^0$		91

Electronic state	Vibrational mode	Frequency (cm^{-1})
$^2A_2'$	a_1'	202
	e'	115
$^3A_2''$	a_1'	218
	e'	111
$^1A_1'$	a_1'	218
	e'	-

Table 4.3: Resume of the assignments in band X (upper part) and the consequently deduced modes in the three electronic states (lower part). The subscripts in the peak labels and the quanta population of the totally symmetric mode in both neutral states, $^3A_2''$ and $^1A_1'$, are designated by n since their values coincide in the assignment. More details appear in the text.

from 132 cm^{-1} till 111 cm^{-1}, as proposed before in our tentative assignment. A summary of all the assigned progressions within band X and the deduced vibrational frequencies for the states involved is included in Table 4.3.

4.5.2 Band A

The measured spectrum at 355 nm (3.49 eV) in Figure 4.8 shows a splitting of band A in three subbands, A_1, A_2 and A_3, with maxima at 2.02±0.02, 2.12±0.02 and 2.21±0.02 eV. Band A is initially assigned to the $^2A_2' \rightarrow {}^3E''$ electronic transition. The inclusion of SO coupling via group theory transforms $^2A_2'$ into $E_{1/2}$, a doubly degenerate two-valued representation which cannot be splitted by vibronic interaction (of electrostatic or relativistic origin [174]) in accordance with Kramers theorem, so no additional vibronic substructure is expected from the electronic state in the anion. The neutral electronic state, $^3E''$, splits into $E' \bigoplus A_1' \bigoplus A_2' \bigoplus E''$ with coalescence of SO coupling and JT effect. JT-SO Hamiltonians of trigonal systems were theoretically studied by Poluyanov et al. [238]. They concluded that the $^3E \times E$ Hamiltonian is formed by six adiabatic potential surfaces (V_n with n=1–6) with the lowest (V_1, V_2) and the uppermost (V_5, V_6) pairs consisting of two $^2E \times E$ JT systems where vibronic effects are quenched by SO coupling (Ham effect [183]), while the central ones (V_3, V_4) are those of a $E \times E$ JT effect without SO splitting. Applied to our system, these conclusions mean that the irreducible representations of those neutral electronic states involved in the electronic transitions that might be assigned to the subbands A_1 and A_3 are respectively E'' and E'. Thus, we will expect in both of a them a very small or fully quenched JT effect by a strong SO coupling. Additionally, subband A_2 will correspond to $A_1' \bigoplus A_2'$ with an unquenched JT effect independent of the SO coupling. The comparison of the Pt_3 spectra measured at 300 nm and at 355 nm (see Figure 4.8) reveals in the latter the splitting of band A in three subbands and enables the aforementioned explanation. In this work only subband A_1 is vibrationally resolved and assigned.

The structure of subband A_1 at high resolution is shown in Figure 4.9. This spectrum is constructed out of 4 single measurements at photon energies of 2.043 eV (607 nm), 2.070 eV (599 nm), 2.094 eV (592 nm) and 2.112 eV (587 nm) to get an overall good resolution. As for band X the assembly from separate measurements leads to some discontinuities at the joining points and changes in relative intensities. Here, the 587 nm spectrum has been taken as

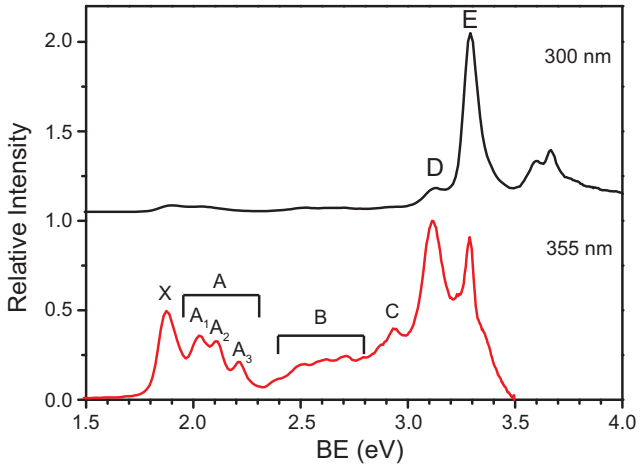

Figure 4.8: Photoelectron spectra of Pt_3^- measured at 4.13 eV (300 nm) and 3.49 eV (355 nm). The spectrum at 355 nm reveals a much better resolution with the splitting of band A in three subbands, A_1, A_2 and A_3, and an important reduction in the relative intensity of E due to threshold effects.

reference for scaling the intensities in the separate ranges. All high resolved measurements taken over band A are shown in Figure 4.22 in the Appendix 4.A.

A SO splitting from band X as the origin of subband A_1 can be discarded as its structure appears to be rather different. As well, DFT calculations without SO coupling predict a nearby $^3A_2$ state. Its calculated DE_{ad} is shifted 0.132 eV to lower energies to coincide with the peak **f**, the assumed origin of the experimental band. The $^3A_2$ state is the lower one that results from a JT splitting of $^3E''$ with D_{3h} symmetry. The lack of theoretical information about the JT stabilization energies or pseudo-potential barrier values makes any kind of a priori assumption about the nature of this JT effect (if linear or quadratic) difficult, even not considering the difficulties arising from the inclusion of relativistic effects, so important in heavy metal atoms.

Compared to band X the structure of subband A_1 appears to be very different with no obvious progression patterns. In particular, the pattern as observed in the lower resolved spectrum by Lineberger with a 180 cm^{-1} progression [188] is not retained. Peak **f** in subband A_1, considered as its origin,

appears at 2.0240±0.0009 eV (16325±7 cm^{-1}). Further peaks resolved in the 587 nm spectrum are labelled from **g** to **p**. At higher resolution most of these peaks reveal some sub-structure and more bands can be identified. The assignment of these bands is guided by the FC simulation of the $^2A_2' \rightarrow {}^3A_2$ transition with both states in C_{2v} symmetry, due to the aforementioned software limitations in PGOPHER, and the assumption of a "rigid" geometry for $^3A_2$ inside the FC approximation. As the anionic $^2A_2'$ state is considered to have C_{2v} symmetry in the FC simulations, its ν_3 mode transforms in this case as b_1. Along our tentative assignment we are going to identify the vibronic transitions in A_1 as if both states in the $^2A_2' \rightarrow {}^3A_2$ ($^3E''$) transition had also D_{3h} symmetry, considering a small JT effect in $^3E''$. The position of the bands predicted by the FC simulation, a detailed relation between the assignments in both symmetries (C_{2v} and D_{3h}), the theoretically possible JT splittings and the corresponding experimental features are listed in Table 4.4. Former works following the same procedure support our approximation [239].

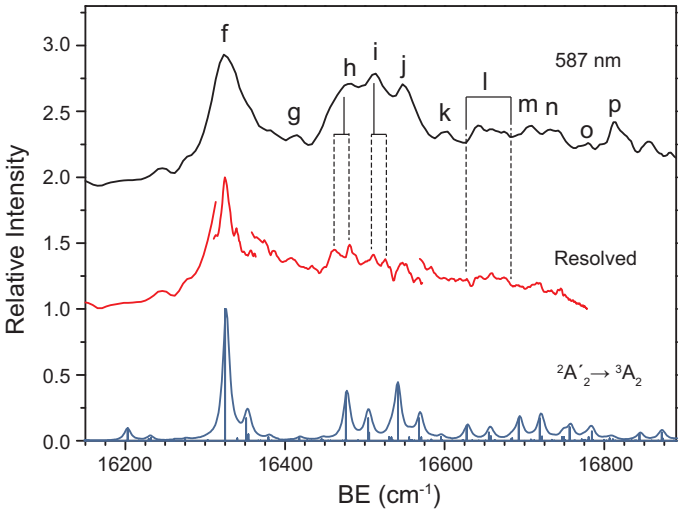

Figure 4.9: The comparison between experiment and FC simulations in subband A_1 evidences the presence of a distinct electronic state where, despite the overall resemblance, the splittings of peaks **h** and **i** are not reproduced. Sticks represent the FC factors and their enveloping line is a Lorentzian with a width of 10 cm^{-1}.

The FC simulation shows an overall good correspondence with the energy positions of the experimental features but an appreciable disagreement with their observed relative intensities. On one hand, the simulation is able to distinguish qualitatively the group of peaks formed by **h**, **i** and **j** from the one formed by **k** to **o**. On the other hand, it is neither able to reproduce exactly the relative intensities of **h**, **i** and **j**, nor to show the experimentally observed splittings in **h** and **i**. Likewise, no evidence of the peak **p** is found in the FC simulation.

The assignment is discussed in the following under the assumption of D_{3h} symmetry for $^2A_2'$ and $^3E''$. The correlation to the assignment with both states with C_{2v} symmetry is included in Table 4.4. Peak **f** is assigned to the $1_0^0 2_0^0$ transition as the origin of subband A_1. Peaks **h**, **i** and **j** in the 587 nm spectrum are assigned respectively to the $1_0^0 2_0^1$, $1_0^0 2_1^2$ and $1_0^1 2_0^0$ transitions. The transitions that are assigned to peaks **h** and **i** only involve the e' mode (JT active), and are those that in the high resolved spectrum split due to, presumably, the appearance of vibronic effects (see Figure 4.9). Oppositely, **j**, whose transition only involves the non-JT active a_1' mode, does not show any further splitting. The assignments of **f** and **j** to $1_0^0 2_0^0$ and $1_0^1 2_0^0$ lead us to the identification of the $1_0^2 2_0^0$ transition with the peak **o** and to fix $\nu_1 \approx 218$ cm^{-1}, which is in agreement with our non-relativistic calculations.

A vibrational progression involving the peaks **f**, **h** and **l**, with **l** assigned to the $1_0^0 2_0^2$ transition, is considered. As only the neutral e$'$ mode is populated in this progression, its deduced value is $\nu_2 \approx 154$ cm^{-1} (in the $^3E''$ state with high symmetry). This value is very similar to the calculated frequencies ν_2 and ν_3 in the rigid $^3A_2$ state and, therefore, a small JT effect is suggested. This assignment can be tentatively corroborated via the proposed frequency for the e$'$ mode in the anionic $^2A_2''$ state during the study of band X, ν_2=115 cm^{-1}. Under these assumptions, the peak **i** should be found at 193 cm^{-1} above **f** and, indeed, it appears in Figure 4.9 at 188 cm^{-1}.

In the case of vibronic coupling, the total angular momentum is defined by $j_2 = l_2 \pm \frac{1}{2}$, where l_2 is the angular momentum of the nuclei given by $l_2 = n_2, n_2 - 2 ... - n_2$, and $\pm\frac{1}{2}$ is the effective angular momentum of the electrons in a doubly degenerate state. According to the theoretically predicted

Peak	Experimental BE (cm^{-1})	FC simulation $C_{2v} \rightarrow C_{2v}$	Calculated BE (cm^{-1})	Correlation to $D_{3h} \rightarrow D_{3h}$	JT splittings (υ_1,υ_2,l_2) → (υ_1,υ_2,l_2,j_2)
f	16325±7	$1_0^0 2_0^0 3_0^0$	16325	$1_0^0 2_0^0$	(0,0,0)→ (1,0,0,1/2)
h	16480±10	$1_0^0 2_0^1 3_0^0$	16476	$1_0^0 2_0^1$	(0,0,0)→ (0,1,1,1/2) ~~(0,1,1,3/2)~~
i	16512±10	$1_0^0 2_0^1 3_1^1$ and $1_0^0 2_1^2 3_0^0$	16504 and 16506	$1_0^0 2_1^2$	(0,1,1)→ ~~(0,2,2,5/2)~~ (0,2,2,3/2) (0,2,0,1/2)
j	16547±9	$1_0^1 2_0^0 3_0^0$	16541	$1_0^1 2_0^0$	(0,0,0)→ (1,0,0,1/2)
o	16773±8	$1_0^2 2_0^0 3_0^0$	16757	$1_0^2 2_0^0$	(0,0,0)→ (2,0,0,1/2)

Table 4.4: Resume of the assignments proposed in subband A_1. The vibronic transitions are firstly assigned on the base of the FC simulation of the $^2A_2' \rightarrow {}^3A_2$ transition and, therefore, both states are treated in C_{2v} symmetry. The correlation to the D_{3h} symmetry, $^2A_2' \rightarrow {}^3E''$ transition, is followed by the predicted splittings for a very small JT effect in the rightmost column. In this column, the transitions that are not allowed by the $l_2 = j_2 \pm \frac{1}{2}$ selection rule are crossed out.

very small JT effect, the vibronic interaction might be weak enough to keep l_2 as a "good" quantum number and to tackle the coupling from the linear approximation. The predicted quantum numbers of the vibronic states in the neutral and the transitions that would be allowed by the $l_2 = j_2 \pm \frac{1}{2}$ selection rule [239] in the subband A_1 are included in the Table 4.4. We observe there that peak **i** would split in this approximation into two distinct vibronic transitions, as it seems to happen in the high resolved spectrum in Figure 4.9. Contrary, the observed splitting for peak **h** is not explained in the Table 4.4 since the (0,0,0)→(0,1,1,3/2) transition is not allowed by $l_2 = j_2 \pm \frac{1}{2}$. All the vibronic states in the neutral are doubly degenerate in the linear JT approximation and their irreducible representations are e′ (or e″) for regular degeneracy and $a_1' \bigoplus a_2'$ (or $a_1'' \bigoplus a_2''$) for incidental degeneracy, i.e., when $j_2 = \pm\frac{3}{2}, \pm\frac{9}{2}, \pm\frac{15}{2}...$ [183]. In this case, the energy levels obtained using second order-perturbation theory are [240]:

$$E_2 = (\upsilon_2 + 1)\omega_2 - D_2\omega_2 \mp 2D_2 j_2 \omega_2 = (\upsilon_2 + 1)\omega_2 - 2D_2\omega_2 \mp (2D_2 l_2)\omega_2 \tag{4.2}$$

with ω_2 the harmonic frequency of the υ_2 mode and D_2 a dimensionless quantity such that $D_2\omega_2$ is the stabilization energy. Under the aforementioned assumptions and taking as real the splitting of **i** (E_2=16 cm^{-1}), one can easily parametrize the predicted JT splitting through the equation 4.2. The vibronic neutral states involved in the proposed transitions for peak **i** are (0, 2, 0, 1/2) and (0, 2, 2, 3/2), so equation 4.2 simplifies to $\Delta E_2=2D_2\Delta l_2\omega_2$ and the stabilization energy is $D_2\omega_2$=4 cm^{-1}. As the proposed harmonic frequency of e$'$ is ω_2=154 cm^{-1}, it is obtained D_2=0.026 and, therefore, the chosen approximation is justified since equation 4.2 holds for $D<0.05$. The small stabilization energy is possibly due to a strong SOC quenching of the JT effect.

As a final remark, the only peak in Figure 4.9 that has no evident resemblance in the $^2A_2'\rightarrow{}^3A_2$ FC simulation is **p**. Its BE is here 16813±5 cm^{-1}=2.0884±0.0006 eV and it is, somehow, close to the maximum of subband A_2 that appears at BE=2.12±0.02 eV in Figure 4.8. Therefore, **p** is tentatively assigned to A_2 pending of future studies that vibrationally resolve subbands A_2 and A_3.

4.5.3 Bands D, E, F and G (Linear isomers)

In Figure 4.10 a resolved spectrum for the BE region between 3 and 4 eV is shown. This spectrum is constructed out of two single measurements at photon energies of 4.113 eV (300 nm) and 3.497 eV (355 nm). The most intense peak at BE=3.297±0.008 eV corresponds to band E and, therefore, it is tentatively identified with a transition from the anionic ground state, predicted linear, to the energetically lowest electronic state of the neutral with linear geometry. A feature between 3.319±0.008 and 3.469±0.007 eV that is labelled by E_2 appears in the spectrum in the form of a shoulder and it is clearly distinguished from the relatively narrow peak that constitutes the maximum of band E, E_1. Two more bands, F and G, with maxima at

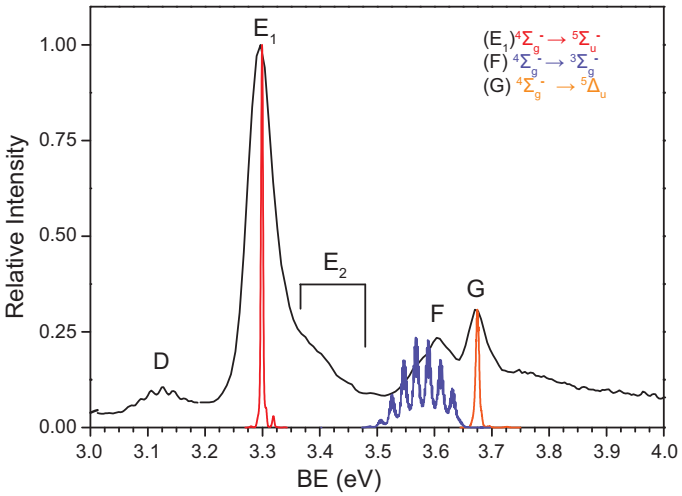

Figure 4.10: Measurement at 300 nm over bands E, F and G, and at 355 nm over band D. All these bands are assigned to electronic transitions from anionic linear isomers of Pt_3 (see text). In addition, band E shows a shoulder that is identified as subband E_2, distinct from the main peak, E_1. All the FC simulations in the figure start in the anionic ground state, $^4\Sigma_g^-$, and are carried out at a vibrational temperature of 100 K.

3.605±0.006 and 3.673±0.006 eV and with relative maximum intensities to E_1 of ≈24% and ≈31% respectively, are assigned to transitions from the anionic ground state to neutral states with linear geometry. Lastly, band D shows a vibrational progression with origin at BE=3.068±0.004 eV and a frequency

$\omega_e \approx 165$ cm^{-1}. D is also broader than E_1, which is not experimentally resolved. Additionally, the relative maximum intensity of D is clearly higher than the intensity of bands X and A, assigned to transitions in the triangular isomer, but only ≈14% of E_1. All these observations on D suggest that the band is the result of a transition from an excited anionic state with linear geometry.

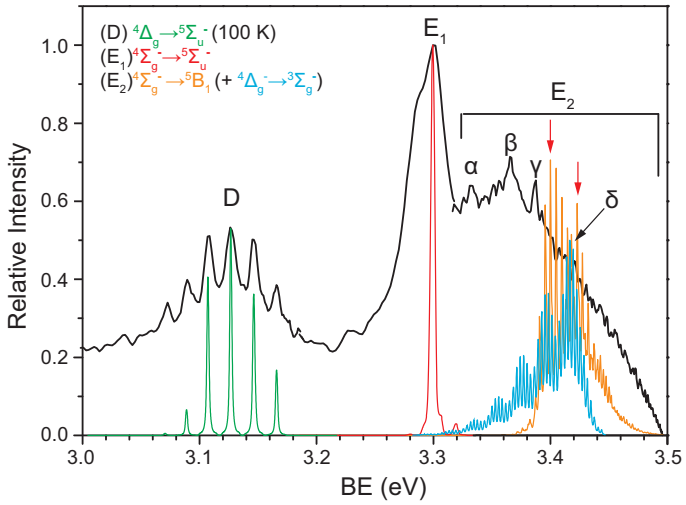

Figure 4.11: Measurements over bands D (at 386 nm) and E (at 355nm). Band E splits into subbands E_1 and E_2. E_1 corresponds to the formerly assigned $^4\Sigma_g^- \rightarrow {}^5\Sigma_u^-$ transition and subband E_2 shows a very complex substructure that is theoretically assigned to the $^4\Sigma_g^- \rightarrow {}^3A_2$, $^4\Sigma_g^- \rightarrow {}^5A_1$, $^4\Sigma_g^- \rightarrow {}^5B_1$ and $^4\Delta_g \rightarrow {}^3\Sigma_g^-$ transitions. In the figure only the FC simulations of the two latter are included. Band D is assigned to the $^4\Delta_g \rightarrow {}^5\Sigma_u^-$ transition. All the FC simulations are done at a vibrational temperature of 100 K. The peaks marked with red arrows in the FC simulation of $^4\Sigma_g^- \rightarrow {}^5B_1$ are tentatively assigned to β and γ.

The observations on band D and the appearance of a subband E_2 distinct from E_1 are further corroborated in Figures 4.11 and 4.13, which are identically constructed out of three single measurements: at 355 nm and 280 V applied on the VMI repeller in order to obtain a better resolution over E_2; at 355 nm and higher voltages (600 V) on the VMI repeller to resolve better E_1, and at 3.212 eV (386 nm) to gain a deeper insight into D. In Figures 4.11 and 4.13, subband E_2 shows a maximum at 3.366±0.001 eV with a very dense and not fully resolved substructure, D corroborates the vibrational progression in

Figure 4.10 with no further splittings and E_1 shows a shoulder at 3.291±0.002 eV that seems to be a possible splitting in the band.

Additionally, the energy dependence of the cross section in band E_1 was investigated for laser wavelengths between 260 nm and 373 nm. This dependence is plotted on the right graphic of Figure 4.12 by the ratio between the maximum intensities of bands E_1 and D (E_1/D) as function of the KE of subband E_1 for each of the investigated photon energies. Closer insights into the threshold behavior of subbands E_1 and E_2 through measurements at other energies were not possible due to experimental limitations. Despite oscillations, we observe that the relative maximum intensity ratio between E_1 and D duplicates its value for KEs from ≈1.6 to ≈0.7 eV until a maximum is reached. From 0.7 to ≈0 eV it rapidly decreases over a KE range of 0.6 eV. As it is shown in the left graphic in Figure 4.12, this drastic intensity reduction is observed in the 355 nm spectrum, where the ratio is 2, and it ends up in the 373 nm spectrum, where close to E_1's threshold it is produced an inversion in the intensity ratio.

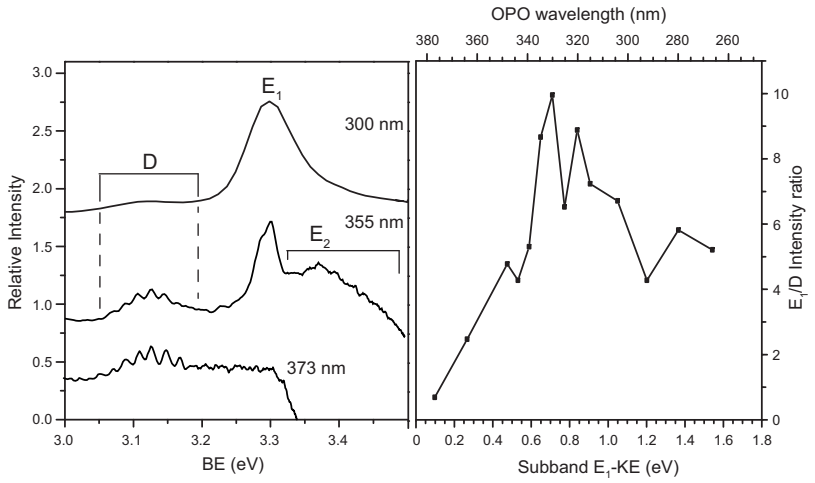

Figure 4.12: Photoelectron spectra of bands D and E at photon energies 4.133 eV (300 nm), 3.493 eV (355 nm) and 3.324 eV (373 nm) (left graphic). Ratio between the maximum relative intensities of band D and subband E_1 (E_1/D) as a function of the KE of E_1 (right graphic). A drastic reduction in the intensity of E_1 relative of D is observed close to its energy threshold. At 373 nm, the ratio E_1/D is inverted.

As it was done for bands X and A, all the simulations are going to be plotted by an enveloping Lorentzian curve with 10 cm^{-1} width. Contrary, the sticks of each vibronic transition are not included in the figures since the experimental resolution for bands D, E, F and G is lower than for X and A and their plotting do not provide extra useful information to the assignments.

In Figure 4.10 are shown the FC simulations for the assigned electronic transitions that start from $^4\Sigma_g^-$. Band E_1 is assigned to the $^4\Sigma_g^- \rightarrow ^5\Sigma_u^-$ transition. The best agreement between the maximum intensity of the FC simulation on the $^4\Sigma_g^- \rightarrow ^5\Sigma_u^-$ transition and E_1 is found by fixing DE_{ad}=3.299 eV in the simulation, 0.073 eV higher than the DFT calculated value. +0.073 eV it is therefore the offset that is going to be applied in the FC simulations to all transitions from $^4\Sigma_g^-$. The calculated small bond length change in this transition that occurs upon detachment is corroborated by the agreement between the widths of the experimental and simulated vibronic profiles. The FC simulation for the $^4\Sigma_g^- \rightarrow ^5\Sigma_u^-$ transition is formed by the $1_0^0 2_n^n 3_0^0$ vibrational sequence, where this combination band lines are separated by $\approx$5 cm^{-1}, the difference between the calculated frequencies in the bending modes of $^4\Sigma_g^-$ and $^5\Sigma_u^-$ (see Table 4.1). This agreement and the high intensity of E_1 are a confirmation of the linear geometry in the anionic ground state.

Band F is assigned to the $^4\Sigma_g^- \rightarrow ^3\Sigma_g^-$ transition after the addition of the +0.073 eV offset that fixes DE_{ad}=3.516 eV. The most intense feature in this simulation is only 0.023 eV lower than the experimental maximum of F. Its FC simulation in Figure 4.10 consists of a vibrational progression in the totally symmetric mode of $^3\Sigma_g^-$, ν_1=172 cm^{-1}, with each of its 1_0^n transitions (for n=1,2,3...) combined with a vibrational sequence in the bending mode, 2_n^n. Band G is assigned to the $^4\Sigma_g^- \rightarrow ^5\Delta_u$ transition with a perfect agreement between FC simulation and experiment for DE_{ad}=3.676 eV. The FC simulated spectrum is formed, as in the $^4\Sigma_g^- \rightarrow ^5\Sigma_u^-$ transition, by the $1_0^0 2_n^n 3_0^0$ vibrational sequence. The different experimental widths of F and G in Figure 4.10 resemble visually both FC simulations. These are signatures of a big bond length change in the $^4\Sigma_g^- \rightarrow ^3\Sigma_g^-$ transition (due to the detachment of an electron from the clearly antibonding $6\sigma_g^+$ orbital) and of a negligible bond length change in the $^4\Sigma_g^- \rightarrow ^5\Delta_u$ transition (due to the nearly non-bonding

character of the $1\delta_u$ orbital involved in the photodetachment), as predicted by our calculations.

Figures 4.11 and 4.13 show the assignments done on subband E_2 and band D, which are going to be discussed in this order. $^4\Sigma_g^- \rightarrow {}^5\Sigma_u^-$ transition is plotted as well in order to correlate visually and conceptually Figures 4.10, 4.11 and 4.13. Before explaining in detail their FC simulations and in order to avoid later confusions, we firstly justify the need to show the same experimental spectrum in Figures 4.11 and 4.13 because of the dense vibronic substructure observed in E_2 and with the aim of evidencing visually better the assignment. As we will later specify and in light of our calculations, E_2 is assigned to the

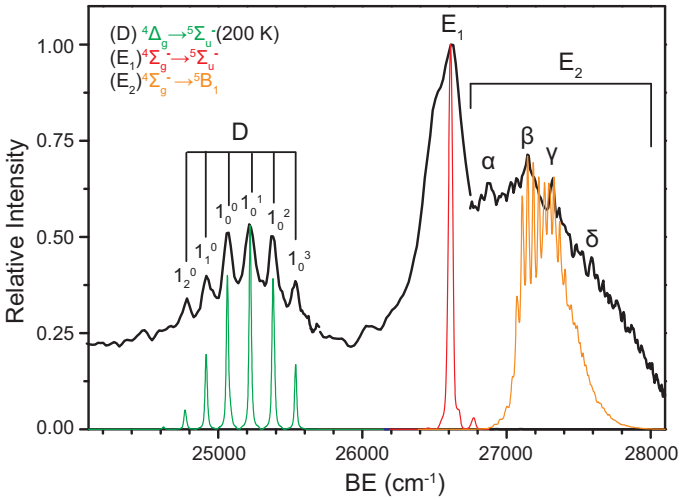

Figure 4.13: Measurement over bands D (at 386 nm) and E (at 355nm). Band E splits into subbands E_1 and E_2. E_1 corresponds to the formerly assigned $^4\Sigma_g^- \rightarrow {}^5\Sigma_u^-$ transition. In subband E_2, the FC simulation of the $^4\Sigma_g^- \rightarrow {}^5B_1$ transition is plotted with an energy offset of +0.039 eV and a Lorentzian bandwidth of 20 cm^{-1} in order to evidence more clearly than in Figure 4.12 its resemblance with the experimental data. The FC simulation of $^4\Delta_g \rightarrow {}^5\Sigma_u^-$ in band D is done at T=200 K.

$^4\Sigma_g^- \rightarrow {}^3A_2$, $^4\Sigma_g^- \rightarrow {}^5A_1$, $^4\Sigma_g^- \rightarrow {}^5B_1$ and $^4\Delta_g \rightarrow {}^3\Sigma_g^-$ transitions. The geometric changes that Pt_3 undergoes in the two latter transitions are smaller than in the two former and, therefore, their FC factors and contributions in E_2 are expected to be bigger. In addition, band D is assigned to the $^4\Delta_g \rightarrow {}^5\Sigma_u^-$ transition and its FC simulation is plotted twice to show comparatively a better

agreement to the experimental features when the vibrational temperature is fixed at 200 K rather than at the 100 K that were used in all the FC simulations of bands X, F and G, and subbands A_1 and E_1.

Among the multitude of small features in subband E_2 (see Figure 4.11) only the four small peaks named by α, β, γ and δ were experimentally reproduced in all the measurements. Their respective positions are 3.334±0.002, 3.359±0.001, 3.388±0.001 and 3.421±0.001 eV.

The FC simulations of $^4\Sigma_g^- \rightarrow {}^5B_1$ and $^4\Delta_g \rightarrow {}^3\Sigma_g^-$ with a Lorentzian width of 10 cm^{-1} appear in Figure 4.11. As it is there shown, the main contribution to E_2 comes from the $^4\Sigma_g^- \rightarrow {}^5B_1$ transition. The analysis of its FC simulation reveals that the first of group of six peaks corresponds to a combination band of 1_0^0 and the 2_n^n vibrational sequence with each peak separated by ≈39 cm^{-1}. At higher energies, a second group of four peaks with slightly lower intensity is formed by a $1_0^0 2_n^{n+2} 3_0^0$ combination band. In Figure 4.13, it is shown as well a FC simulation of the $^4\Sigma_g^- \rightarrow {}^5B_1$ transition that is plotted with a Lorentzian bandwidth of 20 cm^{-1}. It is also applied a shift of -0.034 eV (-274 cm^{-1}) to its DE_{ad} in order to evidence more clearly the possible assignment of peaks β and γ. It is remarkable the high sensitivity of this FC simulation to vibrational temperature changes and, indeed, its best agreement is obtained at 100 K, confirming the vibrational temperature chosen in Figure 4.21, in the Appendix 4.A.

In addition, $^4\Delta_g \rightarrow {}^3\Sigma_g^-$ is proposed as the second main contribution to subband E_2. Its FC simulation is formed by a combination band with a vibrational progression in the totally symmetric mode, ν_1=172 cm^{-1}, where each transition of the progression includes a 2_n^n vibrational sequence.

Lastly, we suggest the assignment of α to the $^4\Sigma_g^- \rightarrow {}^3A_2$ transition. This opens the question of a calculated linear non-degenerate state, $^3\Sigma_u^-$, that reduces its symmetry to C_{2v}, $^3A_2$. The energy difference between the calculated adiabatic DEs of $^3A_2$ and $^5A_1$ is 0.003 eV, almost exactly the frequency of the bending mode in $^3A_2$ (ν_2=25 cm^{-1}). Therefore, we propose that $^3\Sigma_u^+$ bends through a vibronic coupling, either purely electrostatic or with the inclusion of SO coupling, with the "Renner-Teller pair" formed by

$^5A_1$ and $^5B_1$. This has been studied for similar systems theoretically [241–247] and experimentally [248].

Band D shows a satisfactory agreement with the FC factors of the $^4\Delta_g \rightarrow {}^5\Sigma_u^-$ transition by fixing DE_{ad}=3.106 eV, thus 0.183 eV higher than the calculated value. It must be remarked that this offset has been also applied to the FC simulation of the $^4\Delta_g \rightarrow {}^3\Sigma_g^-$ transition in Figure 4.11. The FC simulation of $^4\Delta_g \rightarrow {}^5\Sigma_u^-$ is explained by a vibrational progression in σ_g^+ that is combined with 2_n^n vibrational sequences. Considering the calculated frequencies, the transitions in each vibrational sequence should be separated by ≈3 cm^{-1}, below our experimental resolution, and they cannot be resolved in the spectrum at 386 nm. Indeed, they are hidden in the simulations by the chosen 10 cm^{-1} Lorentzian bandwidth.

As it was mentioned, the best agreement to the experiment was obtained at a vibrational temperature of 200 K (Figure 4.13) which is able to explain all the observed features in the vibrational progression of D. The first two peaks of the progression are hot bands given by the population of the totally symmetric mode in $^4\Delta_g$ whilst the last four correspond to the aforementioned combination bands. Consequently, the experimental vibrational frequencies in the σ_g^+ modes of $^4\Delta_g$ and $^5\Sigma_u^-$ are, respectively, $\omega_e = 143 \pm 4$ and $\omega_e = 148 \pm 2$ cm^{-1} (the latter with an anharmonicity of $x_e\omega_e = 1.9 \pm 0.4$ cm^{-1}), slightly lower than the calculated values.

The unambiguous assignment of bands D and E_1 to $^4\Delta_g \rightarrow {}^5\Sigma_u^-$ and $^4\Sigma_g^- \rightarrow {}^5\Sigma_u^-$ with respectively DE_{ad}=3.106 eV and DE_{ad}=3.299 eV allows to conclude that $^4\Delta_g$ is 0.193 eV above $^4\Sigma_g^-$, so the excitation energy of $^4\Delta_g$ is 0.110 eV lower than the calculated one. The calculated Boltzmann population of $^4\Delta_g$ would be ≈1.4×10^{-5} at the vibrational temperature at which the FC simulations are carried out, 200 K. Nevertheless, we have found experimentally that the maximum relative intensity of D is around 14% the maximum of E_1 in the measured spectra at photon energies between 4.769 eV (260 nm) and 3.701 eV (335 nm). $^4\Delta_g$ is therefore a non-Boltzmann populated metastable excited state that, unlike the anionic $^2A_2'$ state, is not the result of a spin-forbidden transition. The important bond length difference between $^4\Sigma_g^-$ (2.378 Å) and $^4\Delta_g$ (2.412 Å) allows us to propose that the metastability of the latter

relies on an intercrossing between both adiabatic potentials at an energy too high for the experimental conditions to permit the relaxation into $^4\Sigma_g^-$. Moreover, group theory predicts that the vibrationally quenched $^4\Delta_g$ state might decay in $^4\Sigma_g^-$ via the vibronic coupling of both states through the π_u mode with the selection rule $\Gamma_e \otimes \Gamma_v \otimes \Gamma_e \otimes \Gamma_v = \Delta_g \otimes \pi_u \otimes \Sigma_g^- \otimes \pi_u \supset A_1$. This kind of metastability and its possible decays have been largely studied [249,250].

The presence of two excited states in the anionic cluster beam with two different isomeric forms that are non-Boltzmann populated ($^4\Delta_g$ and $^2A_2'$) raises the question of their formation process out of the initial plasma. Considering the calculated 0.638 eV of $^2A_2'$ above $^4\Sigma_g^-$ and its spin-forbidden relaxation, the atom-by-atom formation of the anionic cluster seems, for energy reasons, very unlikely. Since the ground state in the neutral trimer is a triangular isomer and therefore the initial cluster distribution is supposed to contain a high percentage of triangular neutral clusters, we propose that the state $^2A_2'$ is formed by electron attachment to these triangular neutrals. Contrary, the relaxation of $^4\Delta_g$ into $^4\Sigma_g^-$ is not spin-forbidden. In addition, the neutral electronic states in the highly energetic initial plasma from which it could be formed by electron attachment are too high in energy to represent a significant proportion. Therefore, we consider that its formation is due to a thermal electronic excitation from the $^4\Sigma_g^-$ state in the initial plasma. Once the excitation into $^4\Delta_g$ is produced, the quick cooling-down of the cluster beam quenches the relaxation into $^4\Sigma_g^-$ due to their different bond length distances.

Lastly, $^4\Sigma_g^- \rightarrow {}^3A_2''$ is the only calculated transition from a linear to a triangular isomer. The great geometric change presupposes negligible FC factors compared to any of the other proposed transitions and it hinders any possible experimental observation even if its calculated DE_{ad}=2.640 eV predicts that it might be assigned to band B, unresolved due to experimental limitations. The consequence is that the relative energies between the triangular and linear electronic states remain without experimental evidences and, therefore, triggers the measurement of bands B and C in future investigations.

4.5.4 Remarks on the calculations

Once the assignment has been finished, it is also interesting to discuss the accuracy of the DFT calculations that were carried out by Julius Jellinek and Aslihan Sumer. Given that the calculated frequencies of the electronic states have not been corrected throughout the assignment (except those of the state $^1A_1'$ by a factor of 0.96), Table 4.5 is only focused on the applied offsets to the calculated DE_{ad} and their definitive disagreements with the experimental data.

Electronic transition	Experimental Band	Calculated DE_{ad} (eV)	Applied offset (eV)	Experimental DE_{ad} (eV)	Disagreement (eV)
$^2A_2'\rightarrow{}^3A_2''$	X	2.002	-0.131	1.871	0
$^2A_2'\rightarrow{}^1A_1'$	X	2.114	-0.231	1.883	0
$^2A_2'\rightarrow{}^3A_2$	A (rather A_1)	2.156	-0.132	2.024	0
Not assigned	B				
Not assigned	C				
$^4\Delta_g\rightarrow{}^5\Sigma_u^-$	D	2.923	+0.183	3.106	0
$^4\Sigma_g^-\rightarrow{}^5\Sigma_u^-$	E_1	3.226	+0.073	3.299	0
$^4\Delta_g\rightarrow{}^3\Sigma_g^-$	E_2	3.140	+0.183	–	–
$^4\Sigma_g^-\rightarrow{}^3A_2$	E_2	3.308	–	–	–
$^4\Sigma_g^-\rightarrow{}^5A_1$	E_2	3.311	–	–	–
$^4\Sigma_g^-\rightarrow{}^5B_1$	E_2	3.318	+0.073	3.357	-0.034
$^4\Sigma_g^-\rightarrow{}^3\Sigma_g^-$	F	3.443	+0.073	3.539	+0.023
$^4\Sigma_g^-\rightarrow{}^5\Delta_u$	G	3.603	+0.073	3.676	0

Table 4.5: Summary with the assigned electronic transitions that have resulted from the DFT calculated electronic states on anionic and neutral Pt_3 with PW91/cc-pVDZ-PP+Stuttgart pseudopotential. The DE_{ad} values that are directly obtained from the DFT calculations appear in the column "Calculated DE_{ad}"; the DE_{ad} values used in the assignment of the calculated FC simulations (see Figures 4.6, 4.9, 4.10, 4.11, 4.13) are obtained by adding up the values in the columns "Calculated DE_{ad}" and "Applied offset". The column "Experimental DE_{ad}" includes the experimental DE_{ad} in each assigned electronic transition. The column "Disagreement" shows the differences between the experimental DE_{ad} values and those used in the assignment, i.e., "Disagreement" = "Experimental DE_{ad}" – ("Calculated DE_{ad}" + "Applied offset"). More information can be found in Figures 4.1, 4.4 and in the text.

The two left columns summarize the assignment of the calculated transitions to the identified experimental bands. Additionally, the two central columns in Table 4.5 show the DFT calculated DE_{ad} values (see Figure 4.1) and the offsets that were added subsequently to the latter in the assignment (see Figure 4.4). The experimental DE_{ad} values appear in the next column to the right and the column on the right side includes the disagreements between

the experimental DE_{ad} values and the corrected theoretical ones that have been applied in the assignment, i.e., "Disagreement" = "Experimental DE_{ad}" – ("Calculated DE_{ad}" + "Applied offset").

An offset of +0.073 eV has been applied to all the electronic transitions starting from $^4\Sigma_g^-$. Transitions $^4\Sigma_g^- \rightarrow {}^5\Sigma_u^-$ and $^4\Sigma_g^- \rightarrow {}^5\Delta_u$ agree exactly with the experimental data and transitions $^4\Sigma_g^- \rightarrow {}^5B_1$ and $^4\Sigma_g^- \rightarrow {}^3\Sigma_g^-$ would require for a perfect agreement respective offsets of +0.039 eV and +0.096 eV. All these different values are below 0.1 eV, which can be considered a great success since most of the transitions involve DFT calculated excited states in the neutral trimer. The transition $^4\Delta_g \rightarrow {}^5\Sigma_u^-$ has been used to establish an offset of +0.183 eV for those transitions starting from $^4\Delta_g$. Unluckily, this offset has not been further corroborated through the transition $^4\Delta_g \rightarrow {}^3\Sigma_g^-$ since it barely shows any recognizable feature within subband E_2. The bigger value of this offset compared to the aforementioned +0.073 eV reveals a lower accuracy in these of DFT calculations to obtain an anionic excited state.

The offsets of the electronic transitions involving triangular isomers have been applied individually to each case since the resolution of the experimental spectra in bands X and A is much higher than for the others and they can be modified with more certainty. The individually applied offsets to transitions $^2A_2' \rightarrow {}^3A_2''$ and $^2A_2' \rightarrow {}^3A_2$ are nearly identical. The offset of transition $^2A_2' \rightarrow {}^1A_1'$ suggests us to recalculate the $^1A_1'$ state in future studies.

4.5.5 Conclusion

A great part of the experimental Pt_3^- photoelectron spectrum between 1.5 and 4 eV was successfully assigned to several vibronic transitions between the linear and the triangular isomers. In the anion, the ground state was demonstrated to have linear geometry and, additionally, two metastable states were experimentally corroborated. In the neutral, a plethora of electronic states was calculated and assigned but there are still open questions that deserve future detailed studies. First of all, the question that arises about the general influence of the Pt_3 isotopic nature in the photoelectron spectrum was not answered.

Band by band, the proposed pseudo JT effect that explains some features in band X requires a deeper understanding of the interaction between the potential curves of different electronic states. In subband A_1, our assignment does not offer a satisfactory explanation on the intensity differences between the FC simulation and the experimental data but, at least, the presence of transitions with odd $\Delta\nu_2$ is an indication of a clear vibronic coupling in the neutral $^3E''$ state. Furthermore, better resolved measurements on the subband A_1 supported by calculations are needed to understand the coalescence of SOC and JT effects and fully elucidate the nature of the latter, either linear or quadratic, since no pseudo-potential barrier was here calculated. Moreover, our relativistic calculations on the triangular isomer do not solve the puzzling physics behind bands X and A. No theoretical prediction, so far, has been found on the SO splitting in the $^3E''$ state of the trimer and the inclusion of relativistic effects in the calculation of a second excited state in the neutral Pt_3 is briefly mentioned by Fortunelli[207]. It would be a computational challenge for future works to determine the coalescence of JT and SO coupling following the conclusions of Domcke et el.[238] in a system with around 30 valence electrons, as it is our case. In addition, the structure of subbands A_2 and A_3 has to be vibronically resolved to have a complete overview on band A.

Among the bands assigned to transitions between the linear isomers, the biggest difficulties arose in the understanding of subband E_2. Beyond better resolved measurements, not only a good modeling of the predicted Renner-Teller effect in $^5\Delta_g$ but also a characterization of the interaction between $^5\Delta_g$ and $^3\Sigma_u^-$ is needed. As well, subband E_1 shows a shoulder that was not assigned and can be the indication of a more complex substructure within E_1. The understanding of the photoelectron spectrum would be complete with the assignment of bands B and C, whose study was left out due to experimental limitations.

4.6 Analysis of β_2

The study of the beta parameter in Pt_3 is separated in two subsections corresponding to the transitions from the two isomers observed, triangular and linear, in the anionic states. First, the transitions from the triangular $^2A_2'$ anionic state are going to be discussed. In another different vein, this will be followed by an analysis of the beta parameter for the transitions from the linear $^4\Sigma_g^-$ and $^4\Delta_g$ states. Figure 4.14 has been added to aid the reader in following upcoming details about the MO structures of the $^2A_2'$ and $^4\Delta_g$ states.

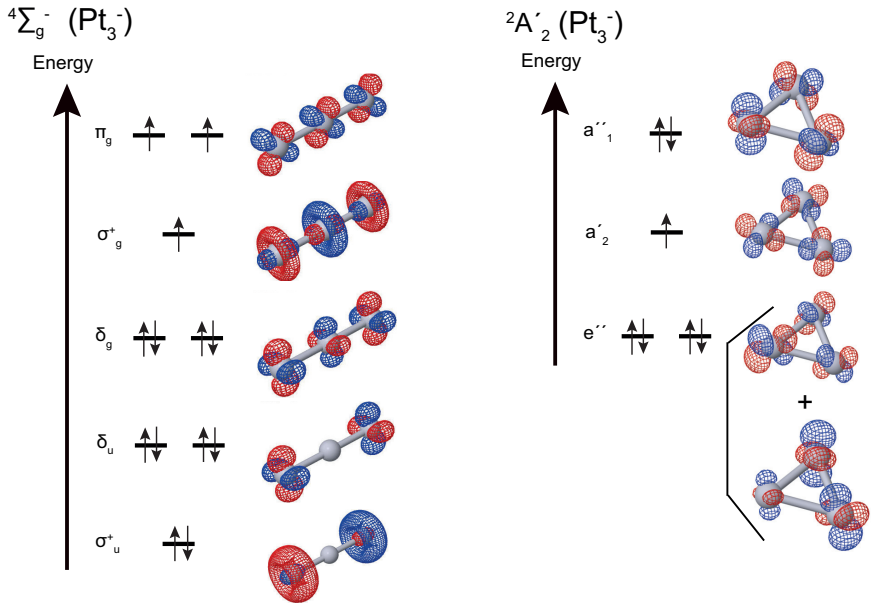

Figure 4.14: Scheme with the HF calculated molecular orbitals in the anionic ground electronic states with linear ($^4\Sigma_g^-$) and triangular geometry ($^2A_2'$). See text for more details.

4.6.1 Transitions from the triangular state $^2A_2'$

The energy dependence of β_2 in bands X and A must be analyzed under the considerations that two electronic transitions ($^2A_2' \rightarrow ^3A_2''$ and $^2A_2' \rightarrow ^1A_1'$) were assigned to X, whilst subband A_1 was considered as the result of a SO splitting with the addition of a very small JT coupling that is quenched by the relativistic effects. The β_2 values of X and A_1 in Figures 4.16 and 4.17 are subdivided in the legend, despite of belonging to the same band, because their measured values were extracted from spectra with different vibronic resolutions. Figure 4.16 shows in black (band X) and red (subband A_1) the energy dependences of β_2 that were extracted from spectra where their vibronic substructure is not resolved at all. Also, the β_2 in band X that are extracted from spectra where the main vibrational progression in the $^2A_2' \rightarrow ^3A_2''$ transition was observable but not resolved from the one in $^2A_2' \rightarrow ^1A_1'$ are also shown in blue Figure 4.16.

As in the VMI experiment the highest absolute resolutions correspond to those measured BEs close to a threshold energy fixed by the frequency of the photodetachment laser, the most reliable β_2 measurements on vibronically resolved spectra are constrained to small KEs. Figure 4.17 zooms in the low KE region of Figure 4.16 to show in orange the anisotropy of peak $\mathbf{x_0}$ ($^2A_2' \rightarrow ^3A_2''$ transition) and in green the β_2 of peak **f** in subband A_1 ($^2A_2' \rightarrow ^3A_2$ transition) since the latter is the most intense feature in A_1 that does not involve populated JT active modes.

We can observe in Figure 4.16 that X and A (A_1) follow a similar energy evolution with β_2 moving towards negative values at very low energies until a minimum, which is distinctive for each one, is reached. In the absence of better experimental results that explore in detail the energies around the β_2 minima, the minimum in X appears at KE=0.33 eV with β_2=-0.79 and in A_1 at KE=0.54 eV with β_2=-0.65. After the minima, both β_2 increase monotonically with the KE in a similar manner until they reach at energies about 2.5 eV an anisotropy of ≈1.5. The gap without data between 1.27 and 1.73 eV has its origin in experimental limitations which will be no further discussed here.

Band X

The first step to gain some understanding on β_2 implies the HF calculation of the orbitals whose photoelectron detachment gives rise to band X and subband A_1. In band X, the $^2A_2' \rightarrow {}^3A_2''$ and $^2A_2' \rightarrow {}^1A_1'$ electronic transitions appear by the detachment of electrons from the a_1'' and a_2' orbitals in the $^2A_2'$ anionic state, whilst in subband A_1 the detachment occurs from an e'' orbital.

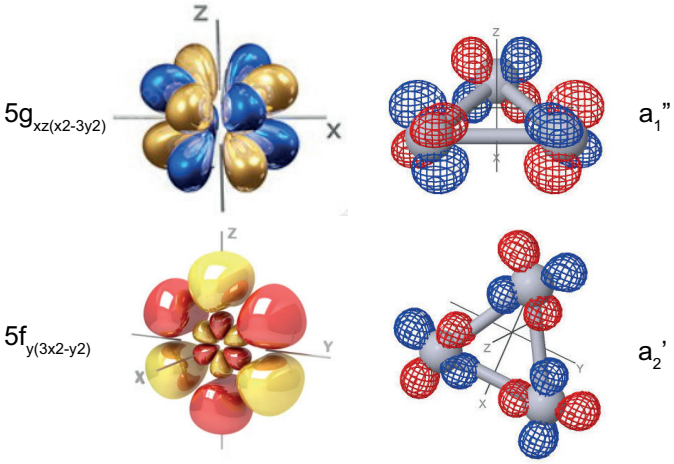

Figure 4.15: Visual comparison between the molecular orbitals a_1'' and a_2' in the triangular Pt_3^- and the hydrogenic orbitals $5g_{xz(x^2-3y^2)}$ and $5f_{y(3x^2-y^2)}$ (adapted from the work of Winter[85]).

The HF calculated orbitals are shown in Figures 4.14 and 4.15. Despite the difficulties to find any resemblance between the e'' molecular orbital with any of atomic nature, there is a clear resemblance between the a_2' molecular orbital and the $5f_{y(3x^2-y^2)}$ and $5f_{x(x^2-3y^2)}$ atomic orbitals (l=3) and, as well, between the a_1'' orbital and the $5g_{yz(3x^2-y^2)}$ and $5g_{xz(x^2-3y^2)}$ atomic orbitals (l=4). Both resemblances allow to face the modelling of β_2 in band X under the central atom approximation.

The integration of the peak areas over the high resolved spectra obtained on band X, i.e. $^2A_2' \rightarrow {}^1A_1'$ and $^2A_2' \rightarrow {}^3A_2''$ transitions in Figure 4.6, reveals respective percentage participations of a_2' and a_1'' in its β_2 of ≈10% and ≈90%. Consequently, the application of Sanov's "sequential mixing wave" model to

band X for an effective fg hybridization with γ_3=0.1 and γ_4=0.9 would be a good approximation to this system. Nevertheless, Sanov pointed out as well[37] the limitation of the "sequential mixing wave" model in reproducing β_2 minima values different from -1 for $l, l+1$ hybridizations with $l \geq 1$, since higher minima can only be reached by the inclusion of a non-negligible phase between the outgoing wavefunctions, $\delta_{l-1,l+1}$, which is physically unrealistic in photodetachment processes. As this limitation appears also when the BCZ equation is applied in the Hanstorp approximation[93] for "pure l waves" with $l \geq 1$ (see equation 2.16) and the contribution of the orbital a_2' is relatively small, we simply apply the WBCZ equation for an effective orbital with l=4 (see equation 4.3 in the Appendix 4.A). The best fitting of equation 4.3 to the PADs of band X is shown in Figure 4.16 and it is obtained for a phase shift between the outgoing wavefunctions $\cos\delta_{3,5}$=0.89 and a Hanstorp parameter A_4=2.55 eV^{-1} (see equations 4.4 to 4.6 in the Appendix 4.A for details on the theoretical calculation of A_4).

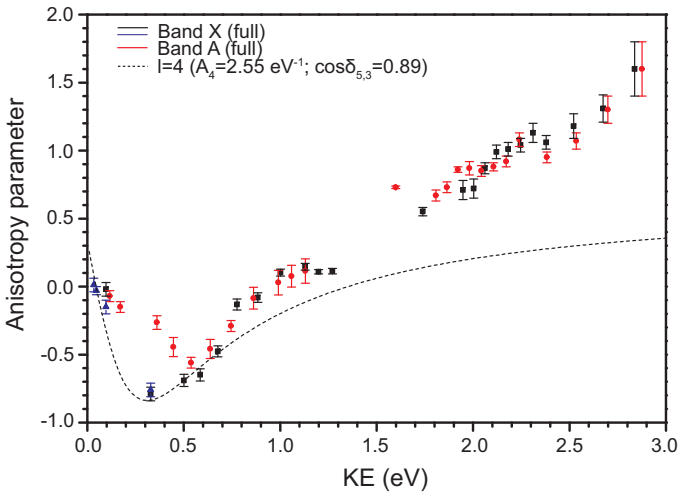

Figure 4.16: β as a function of photoelectron KE in bands X (black and blue) and A_1 (red) extracted from photoelectron spectra with very low vibronic resolution. The dashed black line is obtained by the modeling of band X with equation 4.3. The fitting parameters are A_4=2.55 eV^{-1} and $\cos\delta_{3,5}$=0.89.

Despite the satisfactory agreement in the modeling of band X between 0 and ≈0.7 eV that appears in Figure 4.16, we cannot circumvent the aforementioned problems that are associated with a phase, $\delta_{3,5}$, distinct from zero. Therefore, we consider it is necessary to check more in detail the physical suppositions under which photodetachment occurs, since many different experimental studies on atomic and molecular photodetachment [36,37] have proven the need for non-zero phases between the two outgoing wavefunctions in the dipolar approximation. Consequently, the potential barriers that the photoelectrons must overcome in the remaining neutrals might produce some phase change, as a recent study has proposed [251].

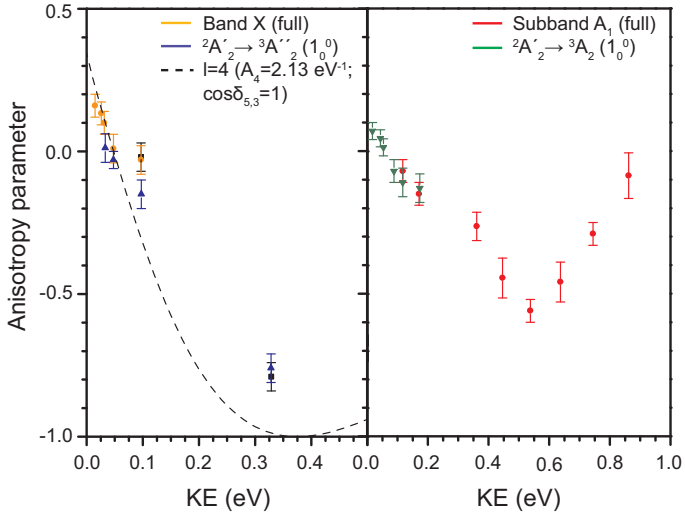

Figure 4.17: β as a function of photoelectron KE extracted from photoelectron spectra with vibronic resolution, i.e., at low photoelectron KEs. The anisotropies of the $1_0^0 2_0^0 3_0^0$ vibronic transition in $^2A'_2 \rightarrow {}^3A''_2$, peak $\mathbf{x_0}$, are plotted in orange. The data in black and blue are taken from Figure 4.16. The anisotropies of the $1_0^0 2_0^0 3_0^0$ vibronic transition in $^2A'_2 \rightarrow {}^3A_2$, peak $\mathbf{f}$, are plotted in green. The data in red are taken from Figure 4.16. The dashed black line is obtained by the modeling of the $1_0^0 2_0^0 3_0^0$ vibronic transition in $^2A'_2 \rightarrow {}^3A''_2$ with the equation 4.3. The fitting parameters are A_4=2.13 eV^{-1} and $\cos\delta_{3,5}$=1.

At very low KEs (see Figure 4.17), it is remarkable the very good agreement between the experimental anisotropy of $^2A'_2 \rightarrow {}^3A''_2$ and its modeling in the central atom approximation for A_4=2.13 eV^{-1}. The energy dependence of the first four points and their trend for KE→0 is only well reproduced

by fitting the WBCZ equation with l=4, which up until now is one of the best validations of the central atom approximation in Sanov's model since a molecular orbital with a complex shape, a_2', can be approximated to an atomic one, $5g_{yz(3x^2-y^2)}$ or $5g_{xz(x^2-3y^2)}$. In addition, the small effective charge calculated by equation 4.4, ξ_{5g}=5.59, is congruent with the supposed diffuseness of the orbital in anionic system.

The validity of the central atom approximation leads us to understand the β_2 of band X as it is detailed in pages 22 to 25 in subsection 2.1.3. Therefore, we consider that the best modeling to understand the overall energy dependence of β_2 in band X is that one shown in Figure 2.5. If the curve that shows there the β_2 dependence as a function of x is "unfolded", it almost perfectly matches with the β_2 experimental behavior between 0 and above 2 eV. A fully quantitative characterization of β_2 within this model would imply the determination of the energy dependence of x (since there is one-to-one relationship between x and β_2), which is beyond the scope of this thesis.

Band A

Under the assumption that subband A_1 appears due to a SO splitting (see subsection 4.5.2), the β_2 of this subband should show a nearly identical energy dependence to A_2 and A_3. Furthermore, it is difficult to extract any conclusion from Figures 4.16 and 4.17 because the e'' molecular orbital does not resemble any atomic orbital and the β_2 minimum at ≈0.5 eV reveals a clear influence of the predicted JT effect that would need theoretical support.

4.6.2 Transitions from the linear states $^4\Sigma_g^-$ and $^4\Delta_g$

Among the previously assigned transitions from the calculated anionic states with linear geometry, only four of them are individually resolved enough in the experimental spectra to consider their β_2 without any artifact that could come from overlappings with other electronic transitions. The transitions are: $^4\Sigma_g^- \rightarrow ^5\Sigma_u^-$ (band E_1), $^4\Sigma_g^- \rightarrow ^3\Sigma_g^-$ (band F), $^4\Sigma_g^- \rightarrow ^5\Delta_u$ (band G) and $^4\Delta_g \rightarrow ^5\Sigma_u^-$ (band D).

The energy dependence of β_2 in these transitions is shown in Figure 4.18. It is remarkable a kind of "oscillation" observed in the $^4\Sigma_g^- \rightarrow ^5\Sigma_u^-$ transition with minima at ≈0.45 and ≈1.1 eV and a maximum at ≈0.9 eV. The β_2 energy dependence in the transitions $^4\Sigma_g^- \rightarrow ^5\Sigma_u^-$ and $^4\Sigma_g^- \rightarrow ^5\Delta_u$ has a clear resemblance between 0 and ≈0.6 eV. As well, the transitions $^4\Sigma_g^- \rightarrow ^5\Sigma_u^-$ and $^4\Delta_g \rightarrow ^5\Sigma_u^-$ resemble between ≈0.8 eV and ≈1 eV since both show a similar feature (a "maximum") at ≈0.9 eV. These resemblances with a seemingly oscillatory behavior in $^4\Sigma_g^- \rightarrow ^5\Sigma_u^-$ are indications to consider the anionic states $^4\Sigma_g^-$ and $^4\Delta_g$ as sources of interferometric quantum effects, within the quantum analogy established by Fano between diatomic molecules and Young's double slit experiment. Therefore, we calculated the HF molecular orbitals in $^4\Sigma_g^-$ and $^4\Delta_g$ and we show in Figure 4.19 the dependence of β_2 with the de Broglie wavelength of the photoelectron, λ_e. The proposed observations in Figure 4.18 are corroborated by Figure 4.19, where the aforementioned similarities between the transitions are clearly evident, and the two minima and the maximum in the oscillations of β_2 are localized at respectively 18.9, 10.9 and 13 Å.

The HF calculated molecular orbitals are shown in Figures 4.14 and 4.20. The arrows represent the electrons that are photodetached in each of the studied transitions throughout this subsection and they follow the same color-code as in Figures 4.18 and 4.19. The molecular orbitals in each electronic state are energetically ordered as in the DFT calculations that have been described in subsection 4.4. The comparison of $^4\Sigma_g^-$ with $^4\Delta_g$ in Figure 4.20 shows that the transition $^4\Sigma_g^- \rightarrow ^4\Delta_g$ within the anion takes place by the promotion of an electron from the δ_g orbital to σ_g^+ and an energy

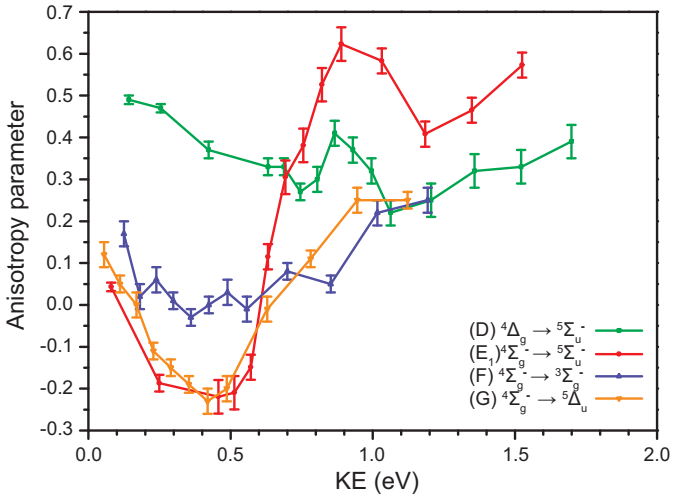

Figure 4.18: Energy dependence of the anisotropy parameter, β_2, in the transitions $^4\Sigma_g^- \rightarrow {}^5\Sigma_u^-$, $^4\Sigma_g^- \rightarrow {}^3\Sigma_g^-$, $^4\Sigma_g^- \rightarrow {}^5\Delta_u$ and $^4\Delta_g \rightarrow {}^5\Sigma_u^-$.

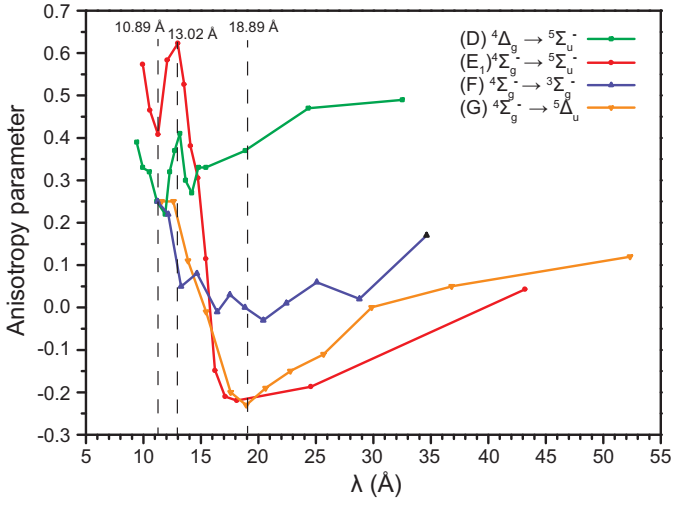

Figure 4.19: Anisotropy parameter in the transitions $^4\Sigma_g^- \rightarrow {}^5\Sigma_u^-$, $^4\Sigma_g^- \rightarrow {}^3\Sigma_g^-$, $^4\Sigma_g^- \rightarrow {}^5\Delta_u$ and $^4\Delta_g \rightarrow {}^5\Sigma_u^-$ as a function of the de Broglie wavelength, λ_e, with the aim of localizing interference patterns in the photoelectron wavefunction when the molecule is interpreted as a quantum interferometer in the analogy established by Fano. The dashed vertical lines indicate the λ_e at which it is observed a turning point in β_2 (see text).

reorganization of the molecular orbitals within the cluster where σ_g^+, the HOMO-1 in $^4\Sigma_g^-$, becomes the HOMO in $^4\Delta_g$ and σ_u^+, the HOMO-5 in $^4\Sigma_g^-$, is the HOMO-4 in $^4\Delta_g$.

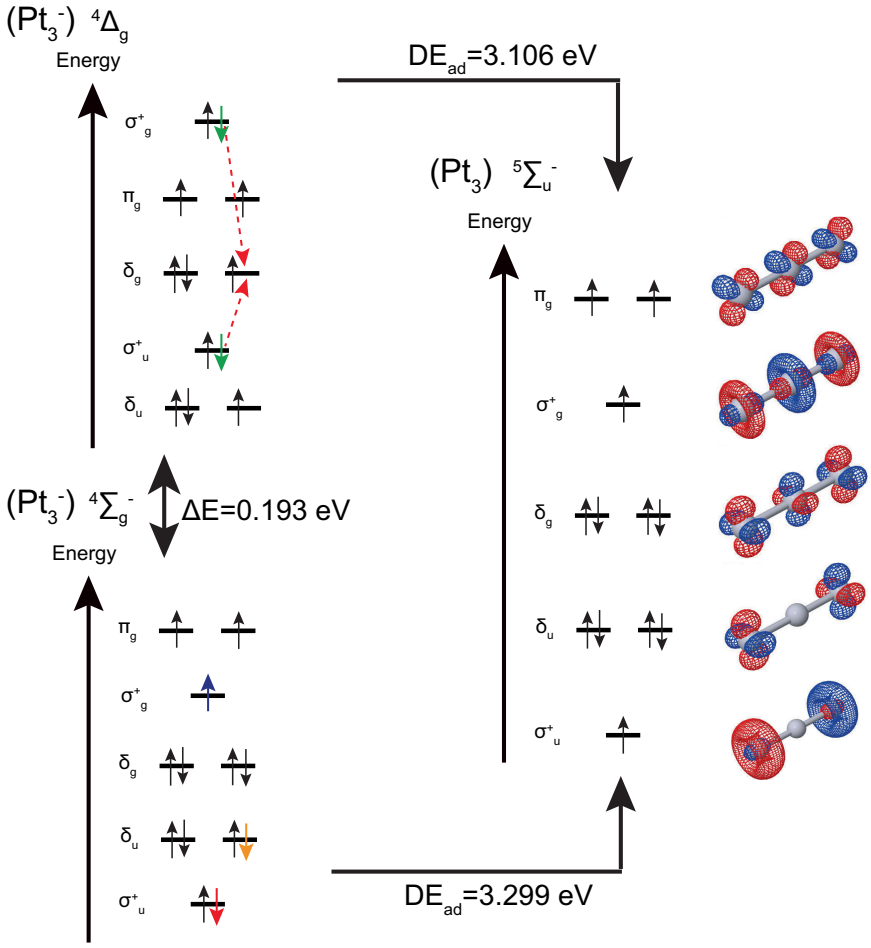

Figure 4.20: HF calculated molecular orbitals in the linear $Pt_3^{-/0}$ for the electronic states $^4\Sigma_g^-$, $^4\Delta_g$ and $^5\Sigma_u^-$. Their energy ordering is based on the DFT calculations described in subsection 4.4 and the energies between the electronic states were deduced in subsection 4.5.3. The colored arrows indicate the photoelectron detached in $^4\Sigma_g^- \rightarrow {}^5\Sigma_u^-$ (red), $^4\Sigma_g^- \rightarrow {}^3\Sigma_g^-$ (blue), $^4\Sigma_g^- \rightarrow {}^5\Delta_u$ (orange) and $^4\Delta_g \rightarrow {}^5\Sigma_u^-$ (green). There are two green arrows due to the two possible detachment pathways in the transition $^4\Delta_g \rightarrow {}^5\Sigma_u^-$. The dashed red lines indicate that when one of the "green electrons" is detached, the other one undergoes a transition to the molecular orbital δ_g.

Furthermore, the $^4\Delta_g \rightarrow {}^5\Sigma_u^-$ transition can proceed via two different correlated $2e^-$ processes that are quantically indistinguishable. As group theory reveals, the product that corresponds to the irreducible representations of the involved molecular orbitals in both pathways is $\sigma_u^+ \otimes \sigma_g^+ \otimes \delta_g = \delta_u$, i.e., either one electron is detached from σ_g^+ with the simultaneous promotion of a second electron from σ_u^+ to δ_g, or the electron is detached from σ_u^+ and an electron transition within the cluster occurs from σ_g^+ to δ_g. The photodetached electron in each pathway is indicated by a green arrow in $^4\Delta_g$ in Figure 4.20. The two possible photodetachment processes have, in principle, different quantum mechanical amplitudes that can depend on the KE of the outgoing photoelectron. Therefore, their resemblance to direct photodetachment processes according to the orbitals from which the electron is photodetached, either $^4\Sigma_g^- \rightarrow {}^5\Sigma_u^-$ (detachment from σ_u^+) or $^4\Sigma_g^- \rightarrow {}^3\Sigma_g^-$ (from σ_g^+), might be established by similarities in the cross sections or in the PADs of the transitions. Indeed, we are inclined to think that the resemblances in β_2 between 14 and 9 Å in $^4\Sigma_g^- \rightarrow {}^5\Sigma_u^-$ and in $^4\Delta_g \rightarrow {}^5\Sigma_u^-$ are due to an important amplitude for the photodetachment from σ_g^+ in these energies.

About the resemblance between $^4\Sigma_g^- \rightarrow {}^5\Sigma_u^-$ and $^4\Sigma_g^- \rightarrow {}^5\Delta_u$. It is observed in Figure 4.20 that one can take as an effective distance between the two emitting centers in the molecule (the atoms on the sides), twice the calculated bond distance in $^4\Sigma_g^-$, R_{eff}=4.746 Å. The λ_e at which both λ_e reach their minimum is four times R_{eff} and two origins are proposed. As a first hypothesis, the minimum is the imprint of a shape resonance that results from the confinement of the photoelectron wavefunction in the Pt_3 molecule, i.e., an outgoing electron that is scattered between the two side Pt atoms along the molecular axis four times (and consequently a constructive interference appears) before the electron escapes the field of the cluster [252]. As a second hypothesis, the minimum is a resonant phenomenon that appears when λ_e is small enough to probe the fine nodal structure of the density distribution in the molecular orbital [253]. The former phenomenon was found in the photoionization from N_2 [252], where the potential barriers of the remaining cation are high enough to confine the photoelectron and, therefore, we discard it in our system since the small potential barrier of the remaining neutral

could hardly confine the outgoing photoelectron. It is rather more convincing the second hypothesis, in line with the proposition of Lai Sheng Wang et al.[253]: when λ_e=$2R_{eff}$, adjacent slits (the Pt atoms on the sides) lie in spatial regions where the de Broglie wavelength of the detached electron has opposite phases, and this matches exactly the nodal structures of σ_u^+ and δ_u in our cluster. As it is observed in Figure 4.19, this matching begins to occur when λ_e=$4R_{eff}$. In addition, the wavelength at which the constructive interference begins to be observable in β_2 is bigger than the distance between the slits, in our case R_{eff}, which is a signature of the quantum nature in the "Young's double slit experiment", contrary to the classical situation[253].

Furthermore, the β_2 values at low energies are explained by the very big de Broglie wavefunctions compared to the molecular dimensions, $\lambda_e \gg R_{eff}$, through which the outgoing photoelectron "sees" the molecular orbitals in the remaining neutral molecule as if they were atomic orbitals[254]. From this standpoint, the σ_u^+ orbital ($^4\Sigma_g^- \rightarrow {}^5\Sigma_u^-$ transition) is observed by the low energy photoelectron as an atomic p_z orbital, σ_g^+ ($^4\Sigma_g^- \rightarrow {}^3\Sigma_g^-$ transition) as an atomic d_{z^2} orbital and δ_u ($^4\Sigma_g^- \rightarrow {}^5\Delta_u$ transition) as an atomic f_{zxy} orbital. Therefore, the theoretical β_2 values at KE$\rightarrow$0 for p, d and f atomic orbitals should be respectively 0, 0.2 and 0.29. The extrapolated β_2 experimental values at KE$\rightarrow$0 for $^4\Sigma_g^- \rightarrow {}^5\Sigma_u^-$, $^4\Sigma_g^- \rightarrow {}^3\Sigma_g^-$ and $^4\Sigma_g^- \rightarrow {}^5\Delta_u$ are respectively $\approx$0.1, $\approx$0.25 and $\approx$0.15. The considered approximation at very low KEs is right since extrapolated and predicted β_2 values are in the same range with a good quantitative estimation for the $^4\Sigma_g^- \rightarrow {}^5\Sigma_u^-$ transition. However, the predicted β_2 values for the other two transitions are inverted in relation to the experimental ones, and more detailed measurements at very low KEs are needed.

Other possible interferences?

The pioneering work of Fano et al.[50] explained the appearance of oscillations in the photoionization cross section of linear diatomic molecules as an interference phenomenon with quantum origin that resembles Young's double slit experiment. Several theoretical[255] and experimental works[256,257] have

added new pieces of information to these interesting physical systems as the angular photoelectron distributions in linearly photoionized and previously oriented N_2 molecules, scattering phenomena during the photoionization process due to the interaction of the outgoing electron with the columbic field of the molecule or, more simple but rather related to our system, the imprint of interferences in β_2 measured on randomly oriented molecules by the photoionization of gerade and ungerade orbitals [258].

Moreover, several theoretical studies are focused in the mathematical modelling of interferences in the photodetachment cross sections of polyatomic linear molecules illuminated with linearly polarized light [259–262]. These calculations, which are carried out on molecules oriented along the three main spatial directions (X, Y and Z) with the linearly polarized light fixed along Z, show that the interference patterns appear when the molecule is perpendicularly oriented to the direction of the light polarization. Therefore, the interferences in our randomly oriented molecules might appear when the axis of the linear Pt_3^- is perpendicular to the light polarization axis.

The turning points at ≈13 Å and ≈10.9 Å in the oscillations of $^4\Sigma_g^- \rightarrow {}^5\Sigma_u^-$ are still unexplained. In addition, the turning point at ≈18.9 Å, which was simply explained by the relation $\lambda_e = 4R_{eff}$, might provide deeper insights into the physics behind the photodetachment process. As it was mentioned in Section 2.1.3, the radial component of the outgoing wavefunctions in photodetachment are well described by Bessel wavefunctions and the wavefunction of the photoelectron is rather fully characterized by a sum of partial waves than by a single wavelength.

Only the Bessel wavefunction for $l=0$ has a wavelength identical to a sinusoidal wavefunction (see Figure 2.6). Thus, we identify the turning point at 18.9 Å with this Bessel function, $R_0(kr)=j_0(kr)$, and the condition it is fulfilled for $R_0(kr)=4R_{eff}$. Furthermore, we propose that the turning points at ≈13 Å and ≈10.9 Å in the oscillations of $^4\Sigma_g^- \rightarrow {}^5\Sigma_u^-$ have their origin in the appearance of the Bessel wavefunctions with $l>0$ that contribute to the total photoelectron wavefunction.

In the transition $^4\Sigma_g^- \rightarrow {}^5\Sigma_u^-$, the wavefunctions of the detached photoelectron are given by the selection rules $\sigma_u^+ \otimes \sigma_u^+ = \sigma_g^+$ (when the molecule is

parallel to the light polarization axis) and $\sigma_u^+ \otimes \pi_u = \pi_g$ (when the molecule is perpendicular to the light polarization axis). According to Zare et al.[262], as the transition takes place between a gerade and an ungerade electronic state, the allowed angular momenta for the photoelectron are even, i.e., l=0, 2, 4, etc. Given this, we propose that the turning points at ≈13 Å and ≈10.9 Å in the oscillations of $^4\Sigma_g^- \rightarrow {}^5\Sigma_u^-$ are due to constructive interferences between the wavelengths of the Bessel wavefunctions with l=2, 4, 6... that are derived from the molecular geometry.

There are still many unknowns in this study as the angular momentum carried by the outgoing photoelectron in the transition $^4\Delta_g \rightarrow {}^5\Sigma_u^-$ as result of correlation effects, the possible imprints in β_2 due to polarization effects between electrons of different molecular orbitals that have origin in the dense electronic structure of Pt_3^- [263] or the observation of interference effects in the simultaneous emission from three atomic centers, i.e., from the gerade orbitals in Pt_3^-. Further measurements might be of great interest.

4.A Complementary information

The Cooper-Zare formula in the Hanstorp approximation for l=4 is:

$$\beta = \frac{12 + 30A_4^2 - 120A_4 cos\delta_{3,5}}{36 + 45A_4^2} \quad \text{and} \quad A_4 = \frac{200}{3}\frac{1}{\xi_{5g}^2}(eV^{-1}) \tag{4.3}$$

The calculation of A_4 is based on the generally defined parameter in the Hanstorp approximation[93], $A_l^2\varepsilon^2 = \frac{\chi_{l,l+1}^2}{\chi_{l,l-1}^2}$, and it is calculated as follows:

$$A_4^2\varepsilon^2 = \frac{\chi_{4,5}^2}{\chi_{4,3}^2} = \frac{(\int_0^\infty j_5(kr)r^3R_{54}(r)dr)^2}{(\int_0^\infty j_3(kr)r^3R_{54}(r)dr)^2} \tag{4.4}$$

The Bessel wavefunctions in the low KE regime are $j_5(kr) = \frac{k^5r^5}{10395}$ and $j_3(kr) = \frac{k^3r^3}{105}$. If they are substited in 4.4 we have:

$$A_4^2\varepsilon^2 = \frac{(\int_0^\infty \frac{k^5r^5}{10395}r^3R_{54}(r)dr)^2}{(\int_0^\infty \frac{k^3r^3}{105}r^3R_{54}(r)dr)^2} \Rightarrow A_4 = \frac{2}{99}\frac{\int_0^\infty r^8R_{54}(r)dr}{\int_0^\infty r^6R_{54}(r)dr} = \frac{200}{3}\frac{1}{\xi_{5g}^2} \tag{4.5}$$

where the $5g$ radial hydrogenic wavefunction is:

$$\begin{gathered} R_{5g}(r) = \frac{1}{900\sqrt{70}}\rho^4\frac{Z}{a_0}^{3/2}e^{-\rho/2} \\ \text{where} \quad \rho = \frac{2Zr}{na_0} \quad \text{and} \quad \frac{Z}{a_0} = \xi_{5g} \quad \text{with} \quad n = 5 \end{gathered} \tag{4.6}$$

Charge	Point group symmetry	BE (eV/atom)	$\mathbf{DE_{ad}}$ (eV)	d (Å)	Vibrational mode	Frequency ($\mathbf{cm^{-1}}$)
Anion	$\mathbf{E_{1/2}(D_{3h}^2)}$	2.272		2.535 (×3)	a_1' e'	203 80
Neutral	**E′ (in equilibrium)** $\mathbf{(C_{2v})}$	2.253	2.021	2.517 (×1) 2.512 (×2)	a_1 b_1 b_1	212 130 125
Neutral	$\mathbf{A_1''(D_{3h})}$	2.243	2.052	2.512 (×3)	a_1' e'	218 83

Table 4.6: Summary of all the relativistic calculations with the PW91/cc-pVDZ-PP+Stuttgart pseudopotential. More details are found in subsection 4.4.

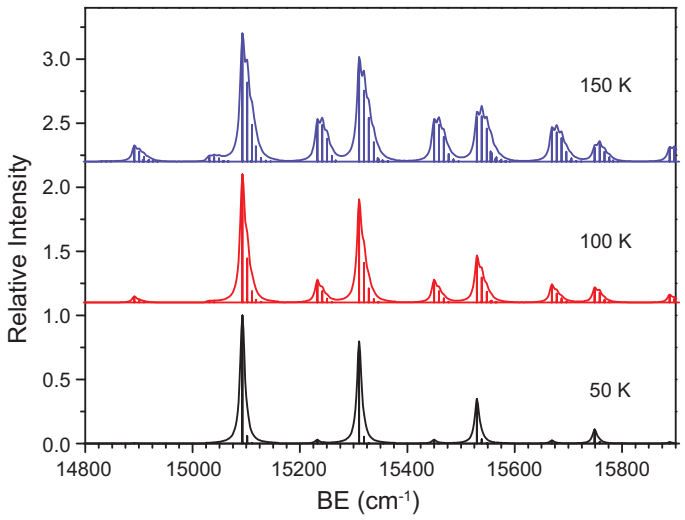

Figure 4.21: Comparison of the FC simulations done on the $^2A_2' \rightarrow {}^3A_2''$ transition at 50, 100 and 150 K with a Lorentzian width of 10 cm^{-1}. The best agreement with the experimental relative intensities is found for 100 K, the temperature at which the FC simulations are carried out.

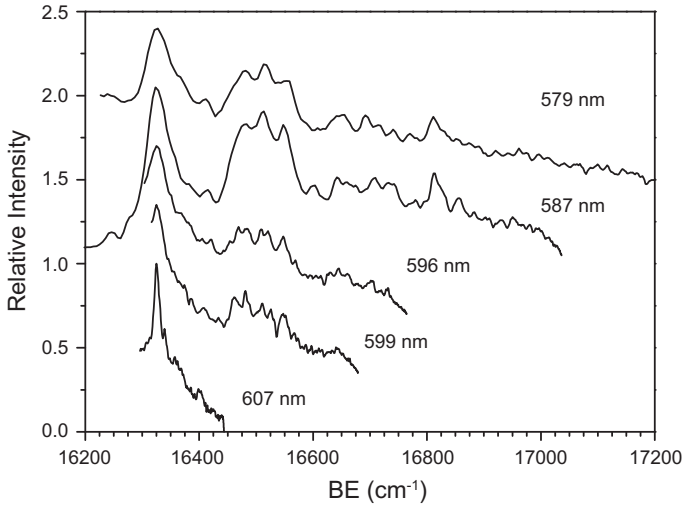

Figure 4.22: Compilation of all high resolved measurements done on band A (subband A_1). All are normalized taking their correspondent highest peak equal to 1.

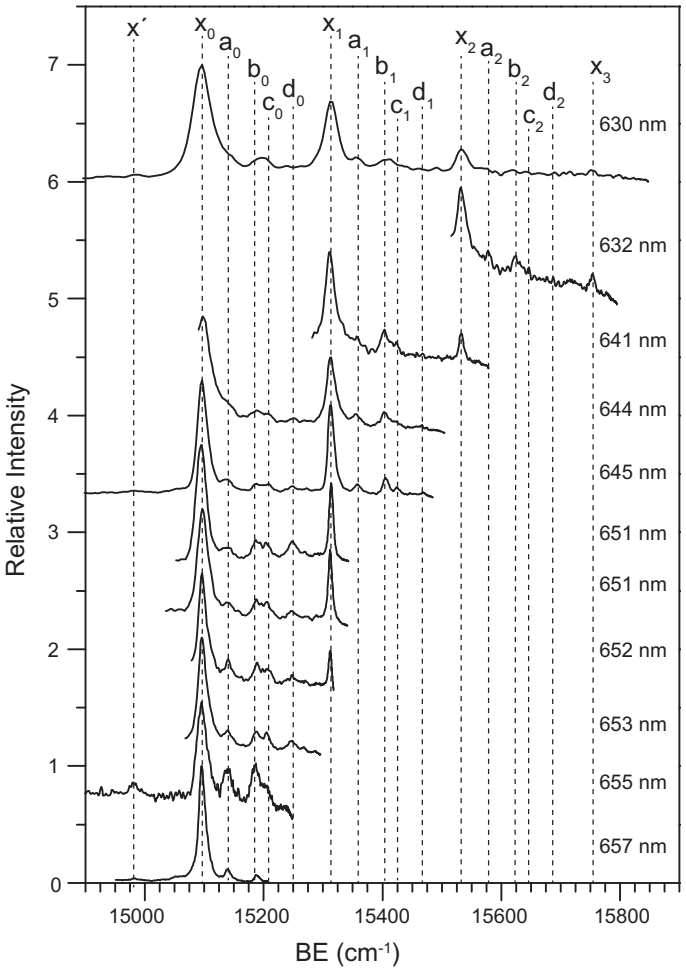

Figure 4.23: Compilation of all high resolved measurements done on band X. All are normalized taking their correspondent highest peak equal to 1. The positions of the peaks, as they were identified and discussed in Figure 4.5, are marked by vertical lines.

Chapter 5

Photoelectron spectroscopy on TaN^-

5.1 Introduction

This investigation finds its original motivation as a part of a larger study on the reactivity of $Ta_nN_m^-$ clusters. The works on $Ta_3N_2^-$ [264] and $Ta_3N_3^-$ [265] have provided fruitful outputs that are now complemented with this chapter on TaN^-. More specifically, the motivations to study the diatomic TaN molecule originate from rather distinct fields, such as physical chemistry (the use of more efficient catalysts in the Haber-Bosch process), particle physics (in search of the validity of the Standard Model) and magnetochemistry (in electron-transfer processes). The activation of N_2 in the reduction of N_2 to NH_3 (the so-called Haber-Bosch process) requires extreme temperature and pressure conditions to weaken the strong N≡N triple bond [265–269] and the large number of electrons that transition metals can provide [270] makes that tantalum nitride containing complexes constitute interesting catalyst candidates. In addition, electron attachment to neutral complexes leads to the formation of stable and transient anionic species that may be relevant in electron-transfer processes. This is why the characterization of resonant transient states in small, anionic molecules has been an important subject of study in the last years [271,272].

The Standard Model (SM) of particle physics cannot explain the matter-antimatter asymmetry nor the existence of dark matter in the Universe[273,274]. Extended models have been developed that include new interactions and particles that are asymmetric under time-reversal (**T**) or (**CP**) symmetry operations[274]; **T** and **CP** symmetry violations are equivalent since **CPT** invariance holds for all physical phenomena. The electron electric dipole moment (eEDM), an asymmetric charge distribution along the electron spin, is a plausible candidate and would be a non-negligible and measurable quantity[275,276]. The use of the $^3\Delta_1$ electronic state in ThO[274] allowed the determination of an upper limit for the value of an eEDM. The $^3\Delta_1$ state in TaN[273] has been proposed as another good system for such fundamental physics experiments.

The first study in which the vibrational properties of isolated TaN molecules in an Ar matrix were experimentally investigated was performed in 1979[277]. Zhou et al.[278] reported in 1998 vibrational results on TaN in a more general study that investigated the products of the reaction of NO with laser-ablated Ta. The work of Ram et al.[279] offers the first spectroscopic work fully centered on TaN, including a detailed study of its emission spectrum accompanied by CASSCF/CMRCI calculations that forms the basis for this section. In 2016, several laser induced fluorescence (LIF) studies on TaN, reporting on the detection of the dispersed fluorescence, enriched the knowledge about this diatomic molecule through a detailed observation, although still not complete, of the $^3\Delta$ and the $^1\Delta$ states[280]. In these studies, branching ratios of different rotational states and transition dipole moments were reported[281,282], high lying excited states above 23500 cm^{-1} were discovered[283] and the $^3\Delta_1$ state of TaN was further characterized[284]. Up to now, no anion photoelectron spectrum of TaN has been reported.

There is a comprehensive theoretical work on 4d and 5d transition metal mononitrides, in which apart from the ground electronic state of the neutral TaN molecule also the cationic and anionic species have been studied using DFT (B3LYP)[285]. The proposal to use TaN as a candidate molecule to measure an eEDM has been brought forward by Flambaum et al.[273] and Skripnikov et al.[286], substantiated by accurate calculations. Fleig et al.[287]

included calculations on the spin-orbit interaction in the first electronically excited states of TaN, whereas calculations on the triple bond of TaN are found in the large body of work of Pyykkö et al.[288].

5.2 Analysis of the photoelectron spectra

All the measurements were done with the experimental setup whose details are described in Section 2.1.4. The production of the TaN^- molecules was done at room temperature by laser ablation of a Ta rod and the addition (through the reaction valve) of a mixture of He gas at 5 bar with 0.025% of NH_3. After the mass selection of the negatively charged species in the Linear-ToF, the photoelectron spectra of the TaN^- species were obtained with the VMI spectrometer by fixing the output OPO wavelength at, nominally, the values: 650, 610, 600, 570, 525, 460 and 410 nm. Additionally, an overall spectrum of TaN^- was measured at 355 nm using the third harmonic of the Nd-YAG laser. In all the measurements of the photoelectron spectra the laser energy was fixed at a maximum of ≈1 mJ per pulse in order to avoid two-electron photodetachment processes or saturation on the CCD camera due to a too high rate of single electron photodetachment events that would obscure the final spectrum.

THEO(nm)	650	610	600	570
EXP(nm)	650.024	609.957	599.58	569.236
EXP(eV) $h\nu \pm \sigma_{h\nu}$	1.907±0.002	2.034	2.068	2.1781±0.0003
Applied offset cm^{-1}	-	-	-	+13
THEO(nm)	525	460	410	355
EXP(nm)	524.113	459.163	408.723	354.67
EXP(eV) $h\nu \pm \sigma_{h\nu}$	2.366±0.003	2.700±0.003	3.033±0.001	3.496
Applied offset cm^{-1}	+60	+56	-3	+191

Table 5.1: Comparison of the nominal (pre-set) and the experimentally deduced photodetachment laser wavelengths (second and third rows) used in the different measured photoelectron spectra of Figures 5.1a and 5.1b. The deduction of the experimental values was calculated from the photoelectron spectra on Ir^- and Rh^- used to calibrate each TaN^- spectrum. The offsets applied to each TaN^- spectrum are given in the last row.

The TaN^- photoelectron spectra in Figures 5.1a and 5.1b were individually calibrated with Ir^-, except for the spectrum recorded with 650 nm radiation, which was calibrated with Rh^-. The experimental detachment

OPO frequency was originally measured with a CCS100-Compact Spectrometer with a FWMH spectral accuracy <0.5 nm (≈26 cm^{-1}) at 435 nm, four times bigger than the linewidth of the laser (<6 cm^{-1}). Furthermore, the BEs of the electronic states in the neutral Ir and Rh atoms and the EAs of their anions have been experimentally determined with an accuracy better than 10^{-6} eV. Therefore, the laser wavelength is rather inferred from the calibrations due to their clearly higher accuracy. The presence of more than two peaks in each calibration allows their linear fit ($y = px+c$) to the equation $BE = -KE+h\nu$, where the BE values are very well known from the literature, $h\nu$ is the extracted laser wavelenght and p the calibration factor of the VMI spectrometer within $KE = p \cdot r^2$. The values of the nominal photodetachment wavelengths and the experimentally inferred ones are included in Table 5.1 for a better comparison. The errors of each wavelength in Table 5.1 are those extracted from the linear fit, and as these values are in all cases higher than the linewidth of the OPO laser in the visible (between 410 and 700 nm it is <6 cm^{-1}), the effective error bar that will be used in the analysis of the TaN photoelectron spectra is the latter. Since the peaks of the TaN spectra, calibrated by the aforementioned procedure, did not fully coincide, a small correction has been applied, consisting of individual offsets, i.e. a small overall shift of the experimental spectra. As shown in Table 5.1, the TaN spectra recorded at 650, 610 and 600 nm were taken as benchmarks when applying the offsets to the other spectra, as these have been recorded with the highest accuracy.

In total, ten peaks are identified in the measured spectra on TaN$^-$→TaN that are included in Figures 5.1a and 5.1b. These peaks are labelled by the letters X to I and, as it is explained in the following paragraphs, they resolve the vibronic structure of TaN$^-$ and TaN. No further substructure is observed nor expected; the experimental resolution does not permit to resolve the rotational structure of the complex. The BE of each peak is extracted in each individual photoelectron spectrum by checking visually the position of its maximum in the plot. Their respective errors are calculated by error propagation via the formula $BE = -KE+h\nu$. The summary of all these data appears in Table 5.4 in the supplementary material of this chapter (Appendix

5.A). The assignment of the transitions observed in Figures 5.1a and 5.1b is given in the energy level scheme shown in Figure 5.2. The experimental values of the observed transitions with their errors are given in that figure as well.

The assignment was actually preceded by DFT B3-LYP/def2-QZVP ab initio calculations (with scalar relativistic corrections) that we carried out with the aim to aid in our initial assignment and to corroborate the theoretical results on the neutral species by Ram et al.[279] and on the anion by Hong et al.[285]. However and in light of the photoelectron spectra, the lower accuracy of our theoretical predictions compared to the previous theoretical studies[287] deterred us from including them here.

In the absence of spin-orbit coupling, the proposed electronic configuration for the electronic ground state of the anion is $1\delta^1 6\sigma^2 5\sigma^2$ ($^2\Delta$). The electronic configuration of the ground state of the neutral species is $6\sigma^2 5\sigma^2$ ($^1\Sigma^+$)[279]. Detachment of the α-spin electron from the 6σ molecular orbital leads to the configuration $1\delta^1 6\sigma^1 5\sigma^2$ ($^3\Delta$) while, at yet higher energy, the detachment of the β-spin leads to a $1\delta^1 6\sigma^1 5\sigma^2$ ($^1\Delta$) electronic state. The presence of a Ta atom leads to strong spin-orbit coupling[277,279–281,283,284]. The qualitative energy order of the spin-orbit components of the aforementioned electronic states in neutral TaN is, from lower to higher energies, $^1\Sigma_0^+$, $^3\Delta_1$, $^3\Delta_2$, $^3\Delta_3$ and $^1\Delta_2$. More specifically, Ram et al.[279] identified the $^1\Sigma_0^+$ state as the electronic ground state of neutral TaN and found the $^3\Delta_1$ state some 2827 cm^{-1} higher in energy (difference between the ν=0 levels, i.e. the T_0 values, of both states). They also observed what they identified as the ν=0 level in the $^3\Delta_2$ state but they did not report its energy relative to the $^1\Sigma_0^+$ state. In a later study, Mukund et al.[280] found the ν=1 level in the $^1\Sigma_0^+$ state at 1064.3 cm^{-1} and they deduced from it the term-value for the ν=1 level in the $^3\Delta_1$ state. They also experimentally observed the ν=0 and ν=1 levels of the $^3\Delta_2$ state and the ν=0 level of the $^1\Delta_2$ state.

We are not aware of any theoretical study that has considered the influence of spin-orbit coupling in the anionic TaN species. Neutral TaO, a similar diatomic molecule whose electronic ground state shows the same valence electronic configuration as TaN^- ($\delta^1\sigma^2$)[289], has been proven to have a $^2\Delta_{3/2}$

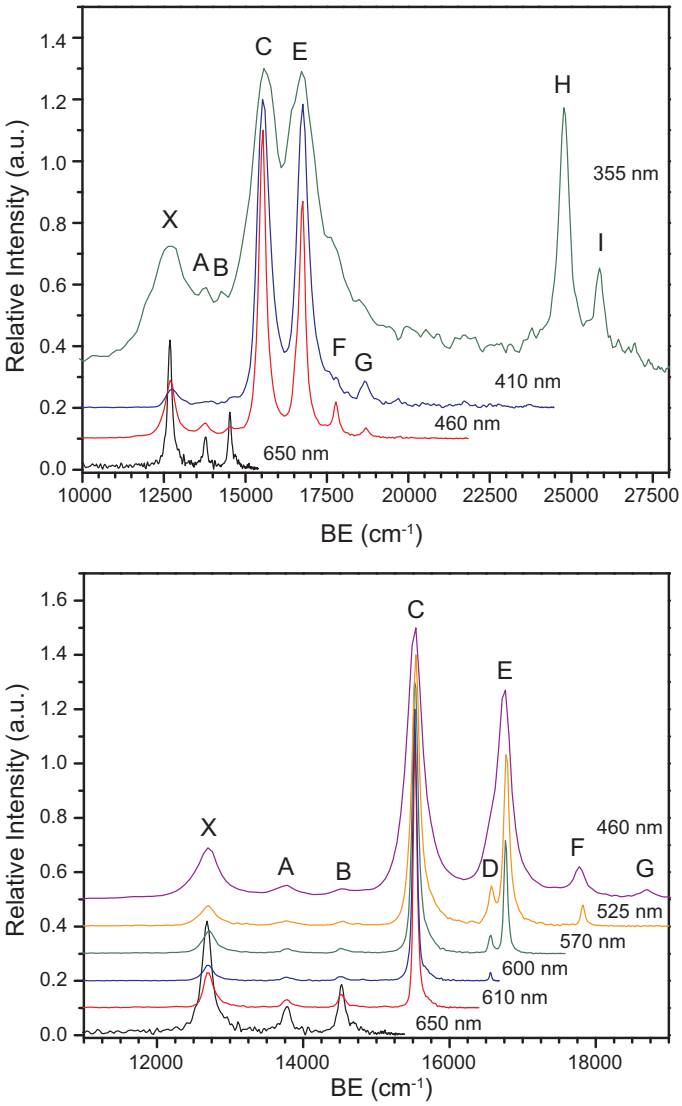

Figure 5.1: Photoelectron spectra of TaN^-. Next to each spectrum, the nominal wavelength at which the detachment laser was positioned is indicated; the more precise detachment frequencies are given in Table 5.1. The positions of the peaks in each spectrum are compiled in the Appendix 5.A, Table 5.4. While the spectra in Figure 5.1a are intended for the general overview, those of Figure 5.1b have a better resolution and are used to determine the transition frequencies.

electronic ground state with the $^2\Delta_{5/2}$ spin-orbit component 0.43 eV higher in energy[290,291]. In addition, PES on TaC^- has localized an excited electronic

state in the anionic molecule at 0.83 eV [292]. Based on this and following Hund's rules, we also assign the lowest energy spin-orbit component in TaN^- as the $^2\Delta_{3/2}$ state. The $^2\Delta_{5/2}$ component is expected to be significantly higher in energy, such that its traces in the photoelectron spectrum, if visible at all, would be very weak due to a very low Boltzmann population.

The peak indicated by X is assigned as the origin peak, i.e. it is assigned to the $^2\Delta_{3/2}(\nu"=0)\rightarrow{}^1\Sigma_0^+(\nu'=0)$ transition and, therefore, it yields the adiabatic electron affinity of TaN as EA_{ad}=12698±4 cm^{-1}. In the following, EA_{ad} is taken as the reference energy to assign peaks A to I. The similar intensities of peaks C and E in the 355, 410 and 460 nm spectra and their energies with respect to X (2836 and 4067 cm^{-1}) lead us to assign them, respectively, to the $^2\Delta_{3/2}(\nu"=0)\rightarrow{}^3\Delta_1(\nu'=0)$ and the $^2\Delta_{3/2}(\nu"=0)\rightarrow{}^3\Delta_2(\nu'=0)$ transitions. Peaks H and I only appear in the 355 nm spectrum at 12077 and 13166 cm^{-1} above the peak X. The only experimental value reported for T_0 of the $^1\Delta_2$ state is 11925(5) cm^{-1} [280]. Moreover, CASSCF/CMRCI calculations predicted $^1\Delta$ with T_0=11727 cm^{-1} [279] and relativistic calculations [280] have obtained for $^1\Delta_2$ a term value of T_e=11729 cm^{-1}; the vibrational frequencies were found as ω_e=1053 and 1123 cm^{-1}, respectively. We therefore assign peak H to the $^2\Delta_{3/2}(\nu"=0)\rightarrow{}^1\Delta_2(\nu'=0)$ transition. To date the vibrational frequency of the $^1\Delta_2$ state has not been experimentally determined and no new electronic states have been found in the region between ≈11000 and ≈18000 cm^{-1} [280,281]. As the only theoretical study that covers energies from 0 to above 25000 cm^{-1} [279] predicts the next electronically excited state at energies ≈19000 cm^{-1} above $^1\Sigma_0^+$, we assign peak I to the $^2\Delta_{3/2}(\nu"=0)\rightarrow{}^1\Delta_2(\nu'=1)$ transition. Peaks A, D and F are assigned, respectively, to the transitions $^2\Delta_{3/2}(\nu"=0)\rightarrow{}^1\Sigma_0^+(\nu'=1)$, $^2\Delta_{3/2}(\nu"=0)\rightarrow{}^3\Delta_1(\nu'=1)$ and $^2\Delta_{3/2}(\nu"=0)\rightarrow{}^3\Delta_2(\nu'=1)$. All our experimental frequencies are slightly larger than the experimental values in the work of Mukund et al. [280] (between 5 and 20 cm^{-1}) indicating that the calibration of our photoelectron spectra might have been slightly off.

The most intriguing assignments are those of peaks B and G. Peak B is localized 1014 cm^{-1} below peak C and two possible assignments were initially considered: either it is the $^2\Delta_{3/2}$ $(\nu"=1)\rightarrow{}^3\Delta_1$ $(\nu'=0)$ transition or the $^2\Delta_{3/2}(\nu"=0)\rightarrow{}^1\Sigma_0^+$ $(\nu'=2)$ transition. Peak B has a rather strong

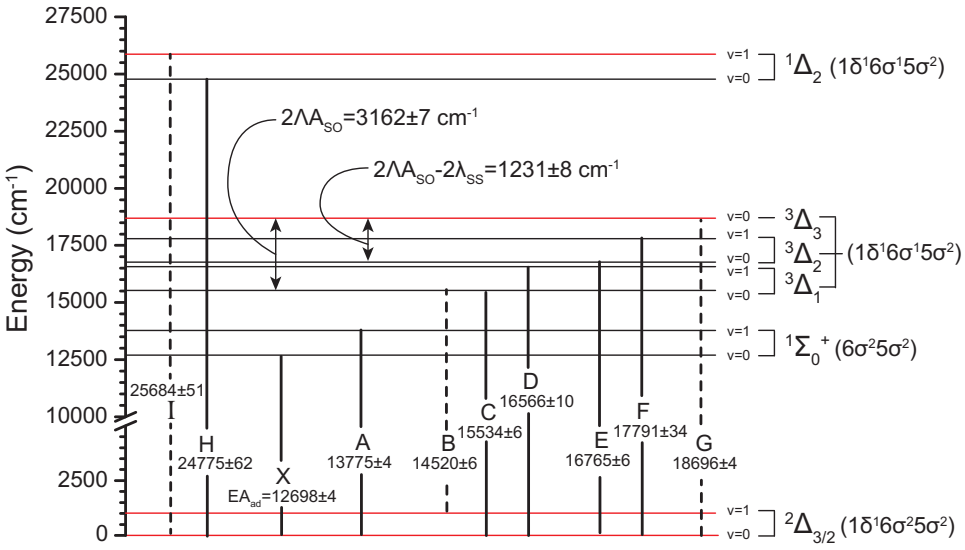

Figure 5.2: Level scheme with the vibrational transitions (labelled by X to G) observed in Figures 5.1a and 5.1b. Vibrational transitions that have been assigned in earlier works are represented by solid lines. Newly identified transitions are represented by dashed lines. The averaged experimental energies of each transition are included below their labels, all in cm^{-1}. On the right side, the vibrational levels involved in each transition are given together with their respective electronic terms and electronic configurations. The four vibronic levels that are observed in this work for the first time are shown in red. The energies that characterize the splitting due to spin-orbit interaction are explicitly indicated. A summary with the vibronic data shown in Figure 5.2 is included in Table 5.5, in Appendix 5.A. Table 5.5 is followed by Tables 5.6 and 5.7, where the experimental and theoretical data on TaN from previous studies are added for completeness.

intensity compared to peak A in the spectrum measured at 650 nm, even though B is closer to the threshold energy. According to the Wigner threshold law, different cross sections at low kinetic energies are imprints of transitions that occur by the detachment of electrons from different molecular orbitals, and this is the first reason that peak B is identified as being due to a hot band of the $^2\Delta_{3/2}\rightarrow{}^3\Delta_1$ transition rather than to the $^2\Delta_{3/2}\rightarrow{}^1\Sigma_0^+$ transition. A second reason is that an assignment of peak B to the $^2\Delta_{3/2}(\nu\text{''}=0)\rightarrow{}^1\Sigma_0^+(\nu\text{'}=2)$ transition would imply a very large, unrealistic anharmonicity in the neutral molecule. Last but not least, a T_1 value of 1014 cm^{-1} agrees quite well with

the calculated value of ω_e=1026 cm^{-1} for the $^2\Delta$ state by Hong et al.[285], corroborating further this assignment.

The assignment of peak G is based on the work of Fleig et al.[287], in which the most accurate theoretical results on TaN are reported. The MR12-CISD(18) calculation predicts the $^3\Delta_1$ state at T_e=2879 cm^{-1}. The $^3\Delta_2$ and $^3\Delta_3$ states have only been calculated at the lower MR12-CISD(10) level, which for the $^3\Delta_1$ and $^3\Delta_2$ states underestimates the equilibrium term values by ≈240 and ≈440 cm^{-1}, respectively. It appears therefore reasonable that $^3\Delta_3$ is some ≈600–700 cm^{-1} higher than at its calculated T_e value of 5276 cm^{-1}. Peak G is measured at 5998 cm^{-1} above the ν=0 level in the electronic ground state of the neutral TaN molecule, and we therefore assign it to the $^2\Delta_{3/2}(\nu"=0)\rightarrow{}^3\Delta_3(\nu'=0)$ transition.

The spin-orbit coupling constant (A_{SO}) and the spin-spin interaction term (λ_{SS}) in the $^3\Delta$ state of neutral TaN can be calculated with the information given in Figure 5.2. The splitting between the different spin-orbit components of the $^3\Delta$ state is determined by the Hamiltonian[293,294]:

$$H = A_{SO}\vec{L}\cdot\vec{S} = 2\lambda_{SS}(S_Z^2 - \frac{1}{3}S^2) \tag{5.1}$$

from which it is seen that the energy separation between the $^3\Delta_3$ and the $^3\Delta_1$ multiplet is given by $2\Lambda A_{SO}$=$4A_{SO}$ whereas the energy separation between the $^3\Delta_2$ and the $^3\Delta_1$ multiplet is given by ΛA_{SO}-$2\lambda_{SS}$=$2(A_{SO}$-$\lambda_{SS})$. Consequently, the spin-orbit coupling constant of the $^3\Delta$ state of TaN is found as A_{SO}=791 cm^{-1} whereas λ_{SS} is about 175 cm^{-1}. This new information on the spin-orbit and spin-spin interaction of the $^3\Delta$ state together with the observed vibrational frequency of the anionic ground state is expected to be useful in further studies on TaN.

5.3 Analysis of β_2

The extraction of the anisotropy parameter, β_2, was done with the self-designed program described in subsection 2.1.4 by measuring β_2 over approximately the full area of each peak. All the experimental information about β_2 as a function of the photodetached electron KE (for peaks X, A, C, E, F and G) is included in Figure 5.3a. The anisotropies of peaks B, D, H and I are not included because either their intensity in the photoelectron spectra is too small to give reliable β_2 values or because the KE range at which their β_2 values were extracted is too small to establish any kind of conclusion.

Additionally, the plot of β_2 as a function of the photodetachment photon energy, $h\nu$, is shown in Figure 5.3b and it enables a more straightforward evaluation and interpretation of the β_2 behavior than Figure 5.3a. We observe two distinct anisotropy trends, one is followed by X and A and the other by C, E, F and G. This observation further corroborates the assignment of the photoelectron spectrum as X and A have been assigned to the electronic transition $^2\Delta_{3/2}\rightarrow{}^1\Sigma_0^+$, i.e. to the detachment of an electron from a δ molecular orbital, and C, E, F and G to the $^2\Delta_{3/2}\rightarrow{}^3\Delta_{1,2}$ transitions, i.e. to the detachment from a σ orbital.

The evolution of β_2 at low KEs (until $\approx$0.5 eV) in peaks C, E, F and G is nearly identical with an increase in β_2 from a value close to 0 to a maximum at around 1.8 which, in principle, is a signature of a σ orbital that in the central atom approximation has an important "s atomic-like" component (since its maximum value is close to 2) with a smaller contribution of a "p atomic-like" wave (because β_2 tends to 0 at 0 eV). Between KE=0.5 and 1 eV β_2 shows in all the cases a sudden decrease with a minimum of β_2=0.5 at a different KE for each peak. The observation of a common minimum at $h\nu$=2.82 eV in Figure 5.3b that corresponds to the measurement at 440 nm evidences the presence of a resonance, marked by a red arrow, that will be called "Resonant state 1". At KEs higher than 1 eV β_2 does not behave identically in C and F. After the resonance, C reaches β_2=1.73 at KE=1.10 eV and then it decreases to β_2=1.36 at KE=1.57 eV, very similar to the nearly constant value reached

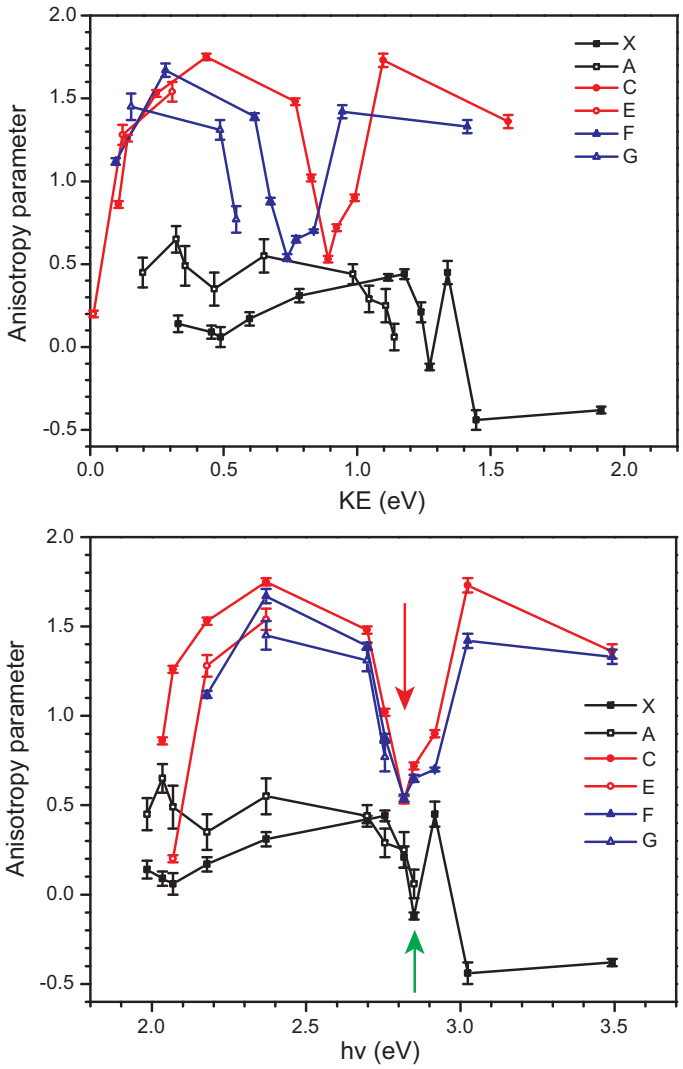

Figure 5.3: Anisotropy parameter dependence on the outgoing photoelectron KE (upper plot, Figure 5.3a) and on the photodetachment photon energy (lower plot Figure 5.3b) for vibronic transitions X, A, C, E, F and G. The two arrows in Figure 5.3b mark the positions of the two identified resonances; red for the "Resonant state 1" and green for the "Resonant state 2". Further details are discussed in the text.

by F, $\beta_2 \approx 1.40$, after the resonance. The lack of more data in this energy range does not allow to draw any further conclusion.

In spite of showing a similar trend at low KEs, the β_2 evolutions of X and A are far from identical. While the evolution of β_2 for peak A shows ups and downs, we observe in X a monotonic decrease from a value that in a linear extrapolation would reach $\beta_2 \approx 0.3$ at 0 eV until a minimum, $\beta_2 \approx 0.06$, at KE=0.49 eV. After that, it monotonically increases again. One reason could be the presence of vibronic coupling effects that modify the value of β_2 for different vibrational transitions inside the same electronic transition as was already shown in a previous work on O_2^- [81]. We cannot exclude that the low intensity of most of A peaks in the photoelectron spectra from which their β_2 was extracted is the reason for this disagreement due to the introduction of experimental artifacts. We will not speculate on this further. Figure 5.3b reveals the presence of another resonance that is marked with a green arrow, "Resonant state 2", since the sudden β_2 minima in X and A coincide at $h\nu$=2.86 eV (435 nm).

In order to gain a deeper understanding in the observed direct (one-photon, one-electron) and resonant photodetachment, we have carried out extra calculations that include the Hartree-Fock (HF) determination of the molecular orbitals in TaN^- (shown in Figure 5.4), the Mulliken population analysis of the anionic HOMO, HOMO-1 and HOMO-2 and TDDFT calculations on TaN^-. Firstly, we are going to discuss more in detail the observed resonances with the support of our calculations to model, in a second step, the contribution of the direct photodetachment to β_2 following the generalized *sp* model of Sanov [36,37,88,89].

5.3.1 Resonances

On the left side of Figure 5.4 the molecular orbitals in the ground state of TaN^-, $^2\Delta_{3/2}$, are depicted as obtained from our HF calculations in the absence of SO coupling. These plots are in agreement with those in the work of Ram et al. [279]. The central diagrams in Figure 5.4 visualize the information on the obtained resonant states via TDDFT/B3-LYP calculations and their numerical data are included in Table 5.2. Among all the calculated anionic virtual states, only those that are allowed and approximately isoenergetic

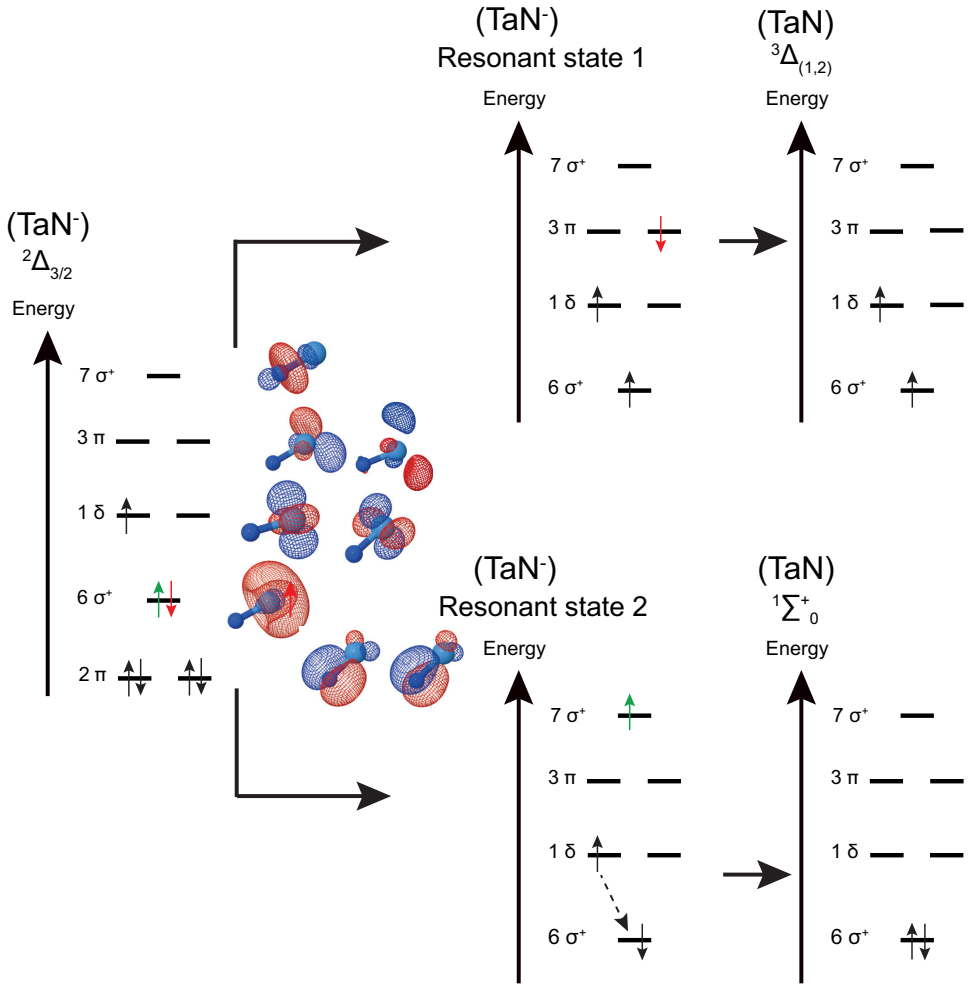

Figure 5.4: Molecular orbital diagrams of anionic and neutral TaN to visualize how the autodetachment processes and further decays to a neutral state take place. The molecular diagram of the anionic TaN is plotted on the left side as it was obtained via HF calculations. In the center of the figure are included the molecular orbital diagrams of the resonant states associated with the resonances observed in Figure 5.3b that have been calculated via TDDFT. A resume of these calculations is shown in Table 5.2. The red arrows identify the electron that is autodetached from the "Resonant state 1" in the decay to the neutral states $^3\Delta_{1,2}$, while the green ones represent the electron that is autodetached from the "Resonant state 2" to reach $^1\Sigma_0^+$. This autodetachment, as it is explained further in the text, occurs by the simultaneous transition of an electron in the 1δ molecular orbital to the 6σ.

with the resonances observed in Figure 5.3b are shown in Table 5.2. The

same color code that was established in the study of the resonances (red for the "Resonant state 1" in the $^2\Delta_{3/2}\rightarrow{}^3\Delta_{(1,2)}$ transitions and green for the "Resonant state 2" in $^2\Delta_{3/2}\rightarrow{}^1\Sigma_0^+$) is used to identify the theoretical data shown in Table 5.2.

According to this assignment, only minor disagreements coming from the calculated energies of the resonant states deserve further comments. The "Resonant state 1" is predicted at 3.09 eV but it is observed at 2.82 eV (0.27 eV lower) and the "Resonant state 2" has its center at 2.86 eV but it is calculated at 2.60 eV. This means that while "Resonant state 1" is observed experimentally 0.04 eV lower than "Resonant state 2", it is predicted theoretically 0.49 eV higher than the latter. Despite this disagreement, we are tempted to think that our assignment is correct because the stronger beta parameter change observed in the $^2\Delta_{3/2}\rightarrow{}^3\Delta_{(1,2)}$ transition may correspond to a stronger electronic transition dipole moment (μ=5.53 D). Furthermore, the molecular orientation determines a spatial selectivity in the excitation of the resonant states due to the use of linearly polarized light, and this effect must be considered to corroborate the calculated shapes of the molecular orbitals involved in the autodetachment process. This last point will be discussed further in the last part of this section.

It is also useful to quantify the lifetimes of the resonant states on the basis of the widths of the resonances in Figure 5.3b. The observed FWHMs for the "Resonant states 1 and 2" are respectively 0.1 and 0.07 eV and their estimated lifetimes would be, according to the equation $\tau = \frac{\hbar}{\Gamma}$, on the order of 5–10 fs. Since these values are orders of magnitude below the vibrational or rotational periods, we consider that we are in the axial recoil approximation[252] and, therefore, we can assume that the position of the molecule in the LFR does not change in the lapse of time during which the photon is absorbed, the resonant state is excited and the autodetachment occurs.

According to this assignment, the "Resonant state 1" in the $^2\Delta_{3/2}\rightarrow{}^3\Delta_{(1,2)}$ transitions is reached by the promotion of an electron from the 6σ to the 3π molecular orbital followed by a decay to the $^3\Delta_{(1,2)}$ state by autodetachment from the 3π orbital. The "Resonant state 2" participates in the $^2\Delta_{3/2}\rightarrow{}^1\Sigma_0^+$ transition by the promotion of an electron from 6σ to 7σ followed by the

Active μ component	$\Psi_i \rightarrow \Psi_f$	**ΔE from $^1\Sigma_0^+$ (eV)/(cm^{-1})**	**ΔE from $^2\Delta_{3/2}$ (eV)/(cm^{-1})**	$\langle\Psi_f\|\mu\|\Psi_i\rangle$ **(Debye)**
$\mathbf{\Sigma^+}$	$6\sigma(\alpha) \rightarrow 7\sigma(\alpha)$ 29.8 % $6\sigma(\beta) \rightarrow 7\sigma(\beta)$ 68.6 %	0.09563/771	2.60237/20990	1.122305
$\mathbf{\Pi}$	$6\sigma(\alpha) \rightarrow 3\pi(\alpha)$ 56 % $6\sigma(\beta) \rightarrow 3\pi(\beta)$ 35.2 %	0.11361/916	3.09153/24935	5.534522
$\mathbf{\Pi}$	$\mathbf{2\pi(\alpha) \rightarrow 1\delta(\alpha)}$ **79.3 %** $\mathbf{2\pi(\beta) \rightarrow 1\delta(\beta)}$ **19.1 %**	**0.11624/938**	**3.16298/25511**	**0.100210**

Table 5.2: TDDFT calculations carried out to interpret the observed resonances in Figure 5.3b. The theoretical data are colored in red and green as they are assigned to the experimentally observed resonances. The data in bold black are shown here, despite their low calculated electric transition dipole moment, since they are proposed as a benchmark to explain the sudden change in the β_2 evolution of X in Figures 5.3a and 5.3b.

Ψ_i	**Photodetachment laser polarization $\longleftrightarrow$ (in LFR)**	**Anion orientation (in LFR)**	**Active μ component**	Ψ_i
6σ	$\varepsilon \| \| Z_{LFR}$	$\longleftrightarrow$	$\mathbf{\Sigma^+}$	7σ
6σ	$\varepsilon \| \| Z_{LFR}$	$\updownarrow$	$\mathbf{\Pi}$	3π

Table 5.3: Scheme to visualize the spatial selectivity in the LFR, perpendicular or parallel to the light polarization axis, that the excitations to the different resonant states exhibit depending on the molecular orientation and, therefore, on which component of the electric dipole moment is active.

decay to the neutral ground state ($^1\Sigma_0^+$) that could, in principle, open two autodetachment channels that involve a 2-electron process: either autodetachment from 7σ with a $1\delta \rightarrow 6\sigma$ transition or, oppositely, autodetachment from 1δ accompanied by a $7\sigma \rightarrow 6\sigma$ transition. This is all visualized in Figure 5.4.

The linearly polarized light of the detachment laser allows an even more complete understanding of the resonant phenomena. Linearly polarized light causes a selective excitation of the molecules depending on their spatial orientation in the LFR with respect to the laser polarization axis. As it is predicted by Table 5.2 and further explained in Table 5.3, the excitation to the "Resonant state 1" only happens if the active electric dipole moment has the Π irreducible representation in the Molecular Frame of Reference (MFR) and the excitation to the "Resonant state 2" can only take place if the irreducible representation of the electric dipole moment is Σ^+. This is normally visualized through a simplified spatial plot with 3 main spatial directions along the principal axis (X, Y and Z) in MFR and LFR. In this plot, the internuclear axis coincides with the Z axis of the MFR, Z_{MFR}, and

the light polarization axis is coincident with the Z axis of the LFR, Z_{LFR}. As the point group of the TaN molecule is $C_{\infty v}$, the excitation to "Resonant state 1" will take place when Z_{MFR} is perpendicular to Z_{LFR} and the one to "Resonant state 2" when Z_{MFR} is parallel to Z_{LFR}.

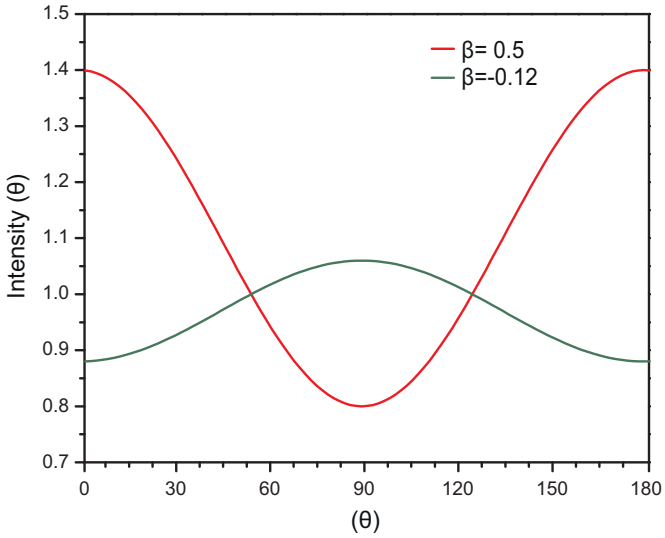

Figure 5.5: Representation of the calculated intensity distributions for the two identified resonances at their corresponding β_2 experimental minimum values (see Figure 5.3b) and as function of θ. Colors red and green correspond to the established assignment. See text for further discussion.

Under these geometrical considerations and the axial recoil approximation, we can calculate with the relation $I(\theta) = 1 + \beta_2[\frac{3}{2}\cos^2(\theta) - \frac{1}{2}]$ an approximate reconstruction of the $I(\theta)$ distribution for both autodetachment processes. This information provides a spatial printout of the electronic distribution in the molecular orbital from which autodetachment happens. Using the β_2 minima observed in the transitions $^2\Delta_{3/2} \rightarrow {}^3\Delta_{(1,2)}$ (β_2=0.5/red) and $^2\Delta_{3/2} \rightarrow {}^1\Sigma_0^+$ (β_2=-0.12/green) we calculate the angular distributions that appear in Figure 5.5. These distributions show a nice agreement only if the autodetachment in the resonance in the transitions $^2\Delta_{3/2} \rightarrow {}^3\Delta_{(1,2)}$ occurs when Z_{MFR} is perpendicular to Z_{LFR} and takes place from the 3π orbital. As well, the resonance in the transition $^2\Delta_{3/2} \rightarrow {}^1\Sigma_0^+$ happens when Z_{MFR} is

parallel to Z_{LFR} and an electron is autodetached from the 7σ orbital rather than from δ, as it is shown in Figure 5.4.

We can conclude that "Resonant state 1" is a core excited shape-resonance because it decays in an excited electronic state of the neutral molecule and it is energetically above it. In the case of "Resonant state 2", we have a Feshbach resonance whose parent neutral state is $^1\Delta_2$. The decay to $^1\Delta_2$ could hypothetically be induced through vibronic coupling or, as it is here the case, "Resonant state 2" decays electronically by a two-electron process to an electronic state lower in energy.

As a final remark, we want to justify the presence in Table 5.2 of a calculated resonant state in bold black that has not been further discussed, since it is proposed as a benchmark for future studies on TaN to explain the sudden change observed in the β_2 evolution of X in Figures 5.3a and 5.3b at, respectively, KE=1.45 eV and $h\nu$=3 eV.

5.3.2 Direct photodetachment

The study of β_2 is completed by the modelling of the direct photodetachment processes in the $^2\Delta_{3/2}\rightarrow{}^3\Delta_{(1,2)}$ and $^2\Delta_{3/2}\rightarrow{}^1\Sigma_0^+$ transitions via Sanov's "wave-mixing" model. The spatial visualization of the bound parent molecular orbitals in both transitions, orbitals 6σ and 1δ in Figure 5.4, shows that both are fully centered on the Ta atom and, therefore, we can admit the central atom approximation to model the PADs via the Wigner-Bethe-Cooper-Zare formula (equation 2.16) by choosing the Ta atom as the center of the MFR. Moreover, the photoelectron spectra in Figures 5.1a and b show that SOC in TaN is described by the Russell-Saunders coupling scheme.

$^2\Delta_{3/2}\rightarrow{}^3\Delta_{(1,2)}$ transition

Despite of illustrating 6σ in a very similar manner to our HF calculations, the pioneering work of Ram et al.[279] proposes that the orbital is formed by the hybridization of atomic s and d orbitals. However, our Mulliken population analysis reveals a non-negligible p component (76% Ta(s); 10% Ta(p); 13%

Ta(d)) in agreement with the relativistic calculations of Fleig et al.[287] (79% Ta(s); 10% Ta (p_σ); 8% Ta (d_σ)). Both populations in the predicted *spd* hybridizations do not add up to 100% since a small contribution from the N atom (3% in both cases) is neglected. In the study of Fleig et al.[287] it is not even mentioned and in our case we calculate it as 2% N(s)+1% N(p).

The introduction to the Cooper-Zare formula, its use in the approximation of Hanstorp[93] and its further adaptation to hybridized molecular orbitals (that was carried out by Sanov's group[37,88–90]) were explained in the subsection 2.1.3. On one hand, the study of the *spd* hybridization follows the same lines that Neumark et al.[92] applied in the study of ortho-pyridine, and that were calculated as a generalization of the "sequential mixing" hybridizations (*sp*, *pd* or *df*) developed by Sanov[37,88–90,92]. On the other hand, the determination of β_2 for a "non-sequential mixing" case (such as the *sd* hybridization) has not yet been reported, but its calculation is straightforward through the general mixing formula[37] by aggregating the contributions of l=0 and l=2 in the numerator and the denominator of equation 2.25. The complementary details about the calculations of the anisotropy parameters for both hybridizations, β_{spd} and β_{sd}, the mathematical derivations of each Hanstorp parameter as a function of the theoretical and empirically deduced effective nuclear charges in Ta (ξ_{5p}, ξ_{5d} and ξ_{6s}) as well as their quantitative relations are included in the Appendix 5.B. The different fittings of the $^2\Delta_{3/2}\rightarrow{}^3\Delta_{(1,2)}$ transitions to the *spd* and *sd* models are shown in Figures 5.6a and 5.6b. Figure 5.6a shows all the fittings based on the Mulliken population calculated by Fleig et al.[287] and figure 5.6b shows those based on our calculated Mulliken population. The short-dashed curves in Figures 5.6a and 5.6b are obtained by fitting the *spd* model (equation 5.3) with the effective nuclear charges theoretically calculated by Clementi et al.[295] and the long-dashed curves correspond to the best fit of the *spd* model. The parameters A_1, A_2, B_1 and B_2 that are obtained in this fitting are then used to calculate C and D (equations 5.9) in order to plot trough equation 5.8 the predictions obtained by the *sd* hybridization. As in the work of Ram et al.[279] there is no comment on the exact populations in the *sd* hybridization, we have considered two possibilities based on our knowledge about the calculated

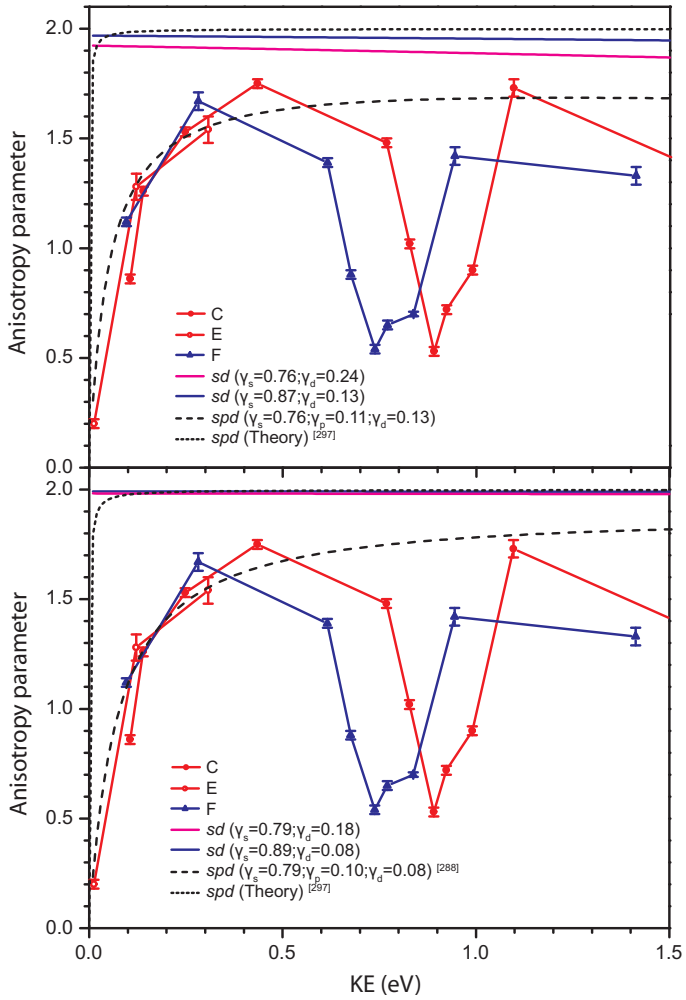

Figure 5.6: Different fittings of the experimental PADs for the $^2\Delta_{3/2} \rightarrow {}^3\Delta_{(1,2)}$ transition. The fittings in Figure 5.6a are done on the basis of the Mulliken analysis of Fleig et al.[287] and those in Figure 5.6b are based on our own calculations. In both Figures blue and pink curves are the fits to the sd model (equation 5.8) and dashed lines the fits to the spd model (equation 5.3). Short-dashed curves are obtained by using the effective nuclear charges as calculated by Clementi et al.[295] and long-dashed curves are the best fittings to the experimental data.

Mulliken populations on 6σ. Firstly, we have added the calculated percentage of the "p-like" component to the "d-like" one (pink curves) and, secondly, we have added the "p-like" percentage to the "s-like" one (blue curves). Table

5.8 in Appendix 5.B includes a compilation with all the Hanstorp parameters obtained in the *spd* fittings and the deduced effective nuclear charges.

We can conclude from figures 5.6a and 5.6b that the *spd* hybridization reproduces the β_2 energy dependence of the 6σ orbital and, therefore, the *sd* hybridization can be discarded. This conclusion can be qualitatively understood when considering the possible photodetachment channels in each hybridization: $s\rightarrow p$, $p\rightarrow s$, $p\rightarrow d$, $d\rightarrow p$ and $d\rightarrow f$ for *spd*, and $s\rightarrow p$, $d\rightarrow p$ and $d\rightarrow f$ for *sd*. *sd* hybridization does not include the "intercrossing channels" $s\rightarrow p$ vs. $p\rightarrow s$ and $p\rightarrow d$ vs. $d\rightarrow p$. Moreover, the pure $s\rightarrow p$ photodetachment channel shows a pure constant value β_2=2 and, as Sanov mentions in his studies on the *sp* hybridization[88–90], it is the existence of the additional $p\rightarrow s$ channel and, consequently, the intercrossing between $s\rightarrow p$ and $p\rightarrow s$ the reason why it is observed and increase from β_2=0 at 0 eV to positive values at higher KEs. The photodetachment from the 6σ shows the same behavior and, therefore, the *sd* hybridization can be directly discarded.

Among the plotted curves based on the *spd* hybridization, those that were obtained by taking the calculated effective nuclear charges in the work of Clementi et al.[295] do not fit with our experimental results. Despite of roughly reproducing the trend of the anisotropy parameter at low KEs (β_2=0 at KE=0 eV, with a monotonic increase towards positive β_2 values the higher the KE is), such increase is too sudden and its maximum value is too high. Furthermore, the effective nuclear charges that are deduced from the two best fittings correspond respectively to our Mulliken population analysis and to the one of Fleig et al.[287], and both have much more realistic values according to the physics behind the valence electrons in the Ta atom. Both fittings corroborate the general "sequential-mixing" model for the *spd* hybridization and predict the behavior of the β_2 parameter very well for KEs below 0.4 eV and correctly for KEs between 0.4 and 1 eV. As the discussion about the slight differences and/or similarities between the two best fittings is beyond the scope of this chapter, these extra details are included in the Appendix 5.B.

$^2\Delta_{3/2} \rightarrow {}^1\Sigma_0^+$ transition

As it is shown in Figure 5.4, the Mulliken population analysis that was carried out on the 1δ orbital reveals its non-bonding nature and its exact correspondence with a hybridization of the $5d_{xy}$ and $5d_{x^2-y^2}$ atomic orbitals in the Ta atom without any further contribution. As the detachment takes place from an orbital with l=2 that fulfills the central atom approximation, the modeling of the beta parameter for the $^2\Delta_{3/2} \rightarrow {}^1\Sigma_0^+$ transition is calculated via the Cooper-Zare formula in the Hanstorp approximation for l=2 (see Appendix 5.B for more details). As it shown in Figure 5.7, the most reasonable fitting

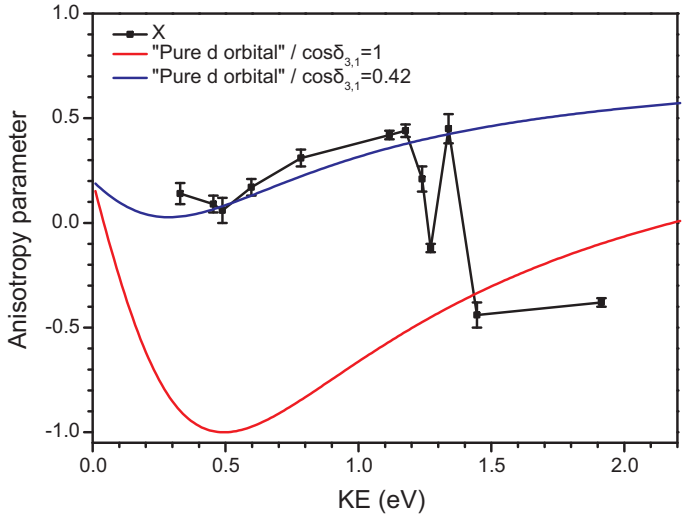

Figure 5.7: Different fittings of the experimental PADs in the $^2\Delta_{3/2} \rightarrow {}^1\Sigma_0^+$ transition by using equation 5.16. The red curve implies no phase-difference between the outgoing waves (physically realistic), but the best fit is obtained by including a phase of $\delta_{3,1} \approx \pi/3$. More details appear in the text.

to equation 5.16 is given by the blue curve for a phase factor of $\cos\delta_{3,1}$=0.42 between the two outgoing waves. Independently of the A_2 value, this phase factor is rather unrealistic because for a photodetachment process, where the interaction between the outgoing electron and remaining neutral cluster is small, it is expected to be between 1 and 0.9 [37].

However, we have previously mentioned in our study on the resonances that the decay of the Resonant State 2 in the neutral ground state, $^1\Sigma_0^+$, most probably takes place by the detachment of an electron from the 7σ orbital and the simultaneous $1\delta \rightarrow 6\sigma$ electronic transition. This autodetachment manifests a strong electronic correlation between the electrons in the orbitals 7σ, 1δ and 6σ, which could give clues to explain β_2. To date, the influence of electron correlation effects in β_2 has not been studied in detail.

5.4 Conclusion

The anion photoelectron spectrum of the TaN molecule has been studied via VMI. The measured photoelectron spectra have enabled to obtain an accurate value for EA_{ad} and the identification of new vibronic states. The PADs of several vibronic transitions have been analyzed. Together with TDDFT calculations, two resonant states have been found and the autodetachment processes have been characterized. The PADs of the direct photodetachment processes have been interpreted via the *spd* "sequential-mixing" model.

5.A Complementary information I

Peak	650nm	610nm	600nm	570nm	525nm	460nm	410nm	355nm
X	12688 ±30	12698 ±36	12698 ±38	12707 ±31	12698 ±46	12698 ±70		
A	13779 ±21	13776 ±28	13768 ±31	13777 ±28		13776 ±65		
B	14523 ±14	14519 ±23	14510 ±25	14519 ±25	14528 ±37			
C		15529 ±15	15529 ±17	15532 ±20	15540 ±31	15540 ±56		
D			16563 ±6	16563 ±14	16572 ±25			
E				16766 ±13	16772 ±24	16762 ±50	16760 ±71	
F					17826 ±17	17772 ±50	17776 ±66	
G						18698 ±38	18694 ±61	
H								24775 ±62
I								25864 ±51

Table 5.4: Position of all peak maxima extracted from each measured photoelectron spectrum. As explained in the text, the errors are calculated by propagation considering the photodetachment laser linewidth <6 cm^{-1}.

ν ($\mathbf{cm^{-1}}$)	$\mathbf{^2\Delta_{3/2}}$	$\mathbf{^1\Sigma_0^+}$	$\mathbf{^3\Delta_1}$	$\mathbf{^2\Delta_2}$	$\mathbf{^2\Delta_3}$	$\mathbf{^1\Delta_2}$
$\mathbf{T_0}$	$\mathbf{EA_{ad}}$=(-)12698	0	2836	4067	5998	12077
$\mathbf{T_0 - T_1}$	1014	1077	1032	1026		1089

Table 5.5: Summary on the identified electronic states and vibrational frequencies in TaN and TaN^- as extracted from the values included in Figure 5.2, where the definitive assignment of our experimental spectra is done. This summary allows a better comparison with the compilation of experimental data from previous investigations included in Table 5.6 in this appendix.

ν $(\mathbf{cm^{-1}})$	$^2\Delta_{3/2}$	$^1\Sigma_0^+$	$^3\Delta_1$	$^2\Delta_2$	$^2\Delta_3$	$^1\Delta_2$
$\mathbf{T_0}$		0	2830(4) [279] 2827.2917(24) [283]	4051		11925
$\mathbf{T_0 - T_1}$		1064.3(1) [279,283]	1014	1021		

Table 5.6: Measured electronic states and vibrational frequencies on TaN included in previous experimental works. The selected data have been compiled for a better comparison with our data in Table 5.5. This information is extracted from the references [279] and [283].

ν $(\mathbf{cm^{-1}})$ [287]	**Model**	$^1\Sigma_0^+$	$^3\Delta_1$	$^2\Delta_2$	$^2\Delta_3$	$^1\Delta_2$
$\mathbf{T_e}$	MR_{12}-	0	2526	3618	5276	11729
$\omega_\mathbf{e}$	CISD(10)	1061	1116	1117	1119	1123
$\mathbf{T_e}$	$\mathbf{MR_{12}}$-	0	2598			
$\omega_\mathbf{e}$	CISD(10)+T	1122	1088			
$\mathbf{T_e}$	$\mathbf{MR_{12}}$-	0	2879			
$\omega_\mathbf{e}$	CISD(18)	1084	1136			
$\mathbf{T_e}$	$\mathbf{MR_{12}}$-	0	2967			
$\omega_\mathbf{e}$	CISD(18)+T	1134	1095			
ν $(\mathbf{cm^{-1}})$ [285]	**Model**	$^2\Delta$	$^1\Sigma_0^+$			
$\omega_\mathbf{e}$	B3LYP/SSD/	1026	1098			
EA	/Stuttgart/	13712				
	/Dresden ECD					

Table 5.7: Calculations on electronic states and vibrational frequencies in $TaN^{0/-}$ included in previous theoretical works. The selected data have been compiled for better comparison with our data in Table 5.5. These data are extracted from the references [287] (upper part) and [285] (lower part).

5.B Complementary information II

$^2\Delta_{3/2} \rightarrow {}^3\Delta_{(1,2)}$ transition

The application of equation 2.22 to a molecular orbital with *spd* hybridization gives:

$$|\psi_{MO}\rangle = \sqrt{\gamma_s}\,|0\rangle + \sqrt{\gamma_p}\,|1\rangle + \sqrt{\gamma_d}\,|2\rangle \tag{5.2}$$

The determination of β_2 for the *spd* hybridization as appears in the work of Neumark et al.[92] is:

$$\beta_{spd} = \frac{\sum_l \gamma_l v_l}{\sum_l \gamma_l w_l} = \frac{\gamma_s v_s + \gamma_p v_p + \gamma_d v_d}{\gamma_s w_s + \gamma_p w_p + \gamma_d w_d} = \\ = \frac{(\gamma_s \frac{B_1}{A_1} - \gamma_p 2 + \gamma_d \frac{1}{5} \frac{A_1}{B_2}) 2A_2\varepsilon + (\gamma_p - \gamma_d \frac{18}{5} \frac{A_2}{B_2}) 2A_1 A_2 \varepsilon^2 + (\gamma_d \frac{12}{5} \frac{A_1}{B_2}) A_2^3 \varepsilon^3}{\gamma_p \frac{A_2}{A_1} + (\gamma_s \frac{B_1}{A_1} + \gamma_d \frac{A_1}{B_2}) 2A_2\varepsilon + \gamma_p 2A_1 A_2 \varepsilon^2 + (\gamma_d 3 \frac{A_1}{B_2}) A_2^3 \varepsilon^3} \tag{5.3}$$

The election of the parameters is based on the generally defined $A_l^2\varepsilon^2 = \frac{\chi^2_{l,l+1}}{\chi^2_{l,l-1}}$ and $B_l\varepsilon = \frac{\chi^2_{l-1,l}}{\chi_{l,l-1}}$ parameters in the "sequential mixing" cases[37,82,88–90] (for *sp* and *pd* hybridizations) and they are given by:

$$A_1^2\varepsilon^2 = \frac{\chi^2_{1,2}}{\chi^2_{1,0}} \quad A_2^2\varepsilon^2 = \frac{\chi^2_{2,3}}{\chi^2_{2,1}} \quad B_1\varepsilon = \frac{\chi^2_{0,1}}{\chi^2_{1,0}} \quad B_1\varepsilon = \frac{\chi^2_{1,2}}{\chi^2_{2,1}} \tag{5.4}$$

In the case of *sd* hybridization the equation 2.22 is:

$$|\psi_{MO}\rangle = \sqrt{\gamma_s}\,|0\rangle + \sqrt{\gamma_d}\,|2\rangle \tag{5.5}$$

The determination of β_2 for a "non-sequential" mixing has not been yet reported, but its calculation for the *sd* hybridization is straightforward through the general mixing formula[37] (see equation 2.25) by adding up l=0 and l=2 in the numerator and the denominator:

$$\beta_{sd} = \frac{\sum_l \gamma_l v_l}{\sum_l \gamma_l w_l} = \frac{\gamma_s v_s + \gamma_d v_d}{\gamma_s w_s + \gamma_d w_d} = \\ = \frac{\gamma_s 2\chi^2_{0,1} + \gamma_d(2\chi^2_{2,1} + 12\chi^2_{2,3} - 36\chi_{2,1}\chi_{2,3}\cos\delta 1,3)/5}{\gamma_s \chi^2_{0,1} + \gamma_d(2\chi^2_{2,1} + 3\chi^2_{2,3})} \tag{5.6}$$

The equation 5.6 is rearranged by the division of the numerator and the denominator by $\chi^2_{0,1}$ and the introduction of the Hanstorp parameters:

$$C^2 = \frac{\chi^2_{2,1}}{\chi^2_{0,1}} \quad D^2\varepsilon^2 = \frac{\chi^2_{2,3}}{\chi^2_{0,1}} \tag{5.7}$$

C and D are introduced for the first time and, therefore, they are differently named in order to distinguish them from A_l and B_l, which are used in the "sequential mixing" cases. As it was mentioned in subsection 2.1.3, the general definition of any parameter is based on the Wigner threshold law[48] and on the proportionality between the partial cross sections and their corresponding radial transition dipole matrix elements. Consequently, the introduction of any new parameter that is expressed as the ratio of the squares of two radial transition dipole matrices has to be multiplied by ε with ε, the energy, powered to the difference between the quantum angular momentum of the outgoing wavefunction that appears in the subindex of the radial transition dipole matrix in the numerator minus the one in the denominator. The equation 5.6 is expressed as:

$$\beta_{sd} = \frac{\gamma_s 2 + \gamma_d(2C^2 + 12D^2\varepsilon^2 - 36CD\varepsilon\cos\delta 1,3)/5}{\gamma_s + \gamma_d(2C^2 + 3D^2)} \tag{5.8}$$

The Hanstorp coefficients C and D can be expressed as a function of A_1, A_2, B_1 and B_2 in order to compare the results predicted by equations 5.3 and 5.8. The obtained relations are:

$$C^2 = \frac{A_1^2}{B_1 B_2} \quad D^2 = \frac{A_1^2 A_2^2}{B_1 B_2} \tag{5.9}$$

The modelling of β_2 is completed with the calculation of the theoretical expressions of A_1, A_2, B_1 and B_2 (see equations in 5.10). The atomic orbitals that hybridize in our system to form the 6σ orbital in TaN$^-$ are fully centered in the atom of Ta, whose electronic configuration in the ground state is [Xe] $4f^{14}5d^36s^2$. Therefore, the bound electronic states that are considered in this calculation are the radial parts of the $5p$, $5d$ and $6s$ hydrogenic wavefunctions -$R_{5p}(r)$, $R_{5d}(r)$ and $R_{6s}(r)$-. Additionally, the radial parts of the outgoing electron wavefunctions are Bessel functions of the first kind, which are reduced in the Hanstorp approximation to the first term of their McLaurin expansion,

$j_l(kr)$. The mathematical expressions and the results for the four parameters in Hartree^{-1} (as they are calculated) and in eV^{-1} (as they are evaluated) are:

$$\begin{aligned}
A_1^2\varepsilon^2 = \frac{\chi_{1,2}^2}{\chi_{1,0}^2} &= \frac{(\int_0^\infty j_2(kr)r^3R_{51}(r)dr)^2}{(\int_0^\infty j_0(kr)r^3R_{51}(r)dr)^2} \Rightarrow \\
&\Rightarrow A_1 = 380\frac{1}{\xi_{5p}^2}(Hartree^{-1}) = 13.96\frac{1}{\xi_{5p}^2}(eV^{-1}) \\
A_2^2\varepsilon^2 = \frac{\chi_{2,3}^2}{\chi_{2,1}^2} &= \frac{(\int_0^\infty j_3(kr)r^3R_{52}(r)dr)^2}{(\int_0^\infty j_1(kr)r^3R_{52}(r)dr)^2} \Rightarrow \\
&\Rightarrow A_2 = 171.4\frac{1}{\xi_{5d}^2}(Hartree^{-1}) = 6.30\frac{1}{\xi_{5d}^2}(eV^{-1}) \\
B_1\varepsilon = \frac{\chi_{0,1}^2}{\chi_{1,0}^2} &= \frac{(\int_0^\infty j_1(kr)r^3R_{6s}(r)dr)^2}{(\int_0^\infty j_0(kr)r^3R_{51}(r)dr)^2} \Rightarrow \\
&\Rightarrow B_1 = 6899\frac{\xi_{5p}^5}{\xi_{6s}^7}(Hartree^{-1}) = 253.53\frac{\xi_{5p}^5}{\xi_{6s}^7}(eV^{-1}) \\
B_2\varepsilon = \frac{\chi_{1,2}^2}{\chi_{2,1}^2} &= \frac{(\int_0^\infty j_2(kr)r^3R_{5p}(r)dr)^2}{(\int_0^\infty j_1(kr)r^3R_{52}(r)dr)^2} \Rightarrow \\
&\Rightarrow B_2 = 309.4\frac{\xi_{5d}^7}{\xi_{5p}^9}(Hartree^{-1}) = 11.37\frac{\xi_{5d}^7}{\xi_{5p}^9}(eV^{-1})
\end{aligned} \tag{5.10}$$

where ξ_{5p}, ξ_{5d} and ξ_{6s} are the effective nuclear charges of the orbitals involved in the hybridization. Each numerator and denominator is an integral that was calculated by Sanov et al.[88]. Only the integrals $\int_0^\infty j_3(kr)r^3R_{52}(r)dr$ and $\int_0^\infty j_1(kr)r^3R_{52}(r)dr$ have not yet been calculated (see equation 5.11) The Bessel wavefunctions in the low KE regime are $j_1 \cong \frac{kr}{3}$ and $j_3 \cong \frac{(kr)^3}{105}$. If they are substituted in the equation 5.10 that determines A_2, we have:

$$\begin{aligned}
A_2^2\varepsilon^2 &= \frac{(\int_0^\infty j_3(kr)r^3R_{52}(r)dr)^2}{(\int_0^\infty j_1(kr)r^3R_{52}(r)dr)^2} \Rightarrow \\
\Rightarrow A_2 &= \frac{2}{99}\frac{\int_0^\infty \frac{r^8}{105}r^3R_{52}(r)dr}{\int_0^\infty \frac{kr}{3}r^3R_{52}(r)dr} = \frac{k^2}{35}\frac{\int_0^\infty r^6R_{52}(r)dr}{\int_0^\infty r^4R_{52}(r)dr}
\end{aligned} \tag{5.11}$$

and in atomic units $\varepsilon = \frac{k^2}{2}$:

$$A_2\varepsilon = \frac{k^2}{2}\frac{2}{35}\frac{\int_0^\infty r^6 R_{52}(r)dr}{\int_0^\infty r^4 R_{52}(r)dr} \Rightarrow A_2 = \frac{2}{35}\frac{\int_0^\infty r^6 R_{52}(r)dr}{\int_0^\infty r^4 R_{52}(r)dr} \tag{5.12}$$

where the $5d$ radial hydrogenic wavefunction is:

$$\begin{gathered} R_{5d}(r) = \frac{1}{150\sqrt{70}}(42 - 14\rho + \rho^2)\rho^2\frac{Z}{a_0}^{3/2} e^{-\rho/2} \\ \text{where} \quad \rho = \frac{2Zr}{na_0} \quad \text{and} \quad \frac{Z}{a_0} = \xi_{5d} \quad \text{with} \quad n = 5 \end{gathered} \tag{5.13}$$

and when it is introduced in each integral their values are:

$$\int_0^\infty r^6 R_{52}(r)dr = \frac{5^5 4032000}{\sqrt{70}}\frac{1}{\xi_{5d}^{11/2}} \quad \text{and} \quad \int_0^\infty r^4 R_{52}(r)dr = \frac{5^3 33600}{\sqrt{70}}\frac{1}{\xi_{5d}^{7/2}} \tag{5.14}$$

so:

$$A_2 = 171.4\frac{1}{\xi_{5d}^2} \tag{5.15}$$

Theoretical considerations on the four equations 5.10

Similarly to what Sanov commented on the *sp* hybridization[88–90], it would be interesting to do few theoretical remarks on the calculated parameters and, specially, in the *pd* hybridization within the *spd* hybridization to gain some extra insights in the model. An interesting quantity established in the *sp* hybridization is the ratio $\frac{B_1}{A_1} = K(n)(\frac{\xi_{np}}{\xi_{ns}})^7$, which in the case of the same principal quantum numbers in numerator and denominator allows the assumption of equal effective nuclear charges, $\xi_{np} = \xi_{ns}$. Under this assumption the ratio is identical to $K(n)$, $\frac{B_1}{A_1} = K(n)$, where $K(n)$ is a numerical value that decreases monotonically from $K(2) = \frac{8}{3}$ to an asymptotic value of $\frac{5}{3}$ when $n \to \infty$ (for more information check Figure 4 and Section E in[88]).

This assumption cannot be done in our case since in the *sp* hybridization within the *spd* model the ratio between the equations of B_1 and A_1 contains effective nuclear charges with different n,

$\frac{B_1}{A_1} = \frac{6899}{380}(\frac{\xi_{5p}}{\xi_{6s}})^7$. Nevertheless, the corresponding ratio for the *pd* hybridization part in the general *spd* model fulfills such assumption because the ratio between equations B_2 and A_2 gives $\frac{B_2}{A_2} = \frac{309.4}{171.4}(\frac{\xi_{5d}}{\xi_{5p}})^7 = 1.81(\frac{\xi_{5d}}{\xi_{5p}})^7$. Therefore, we have $\frac{B_2}{A_2} \approx 1.805$ for $\xi_{5d} = \xi_{5p}$, very similar to the calculated ratio in the *sp* hybridization for n=5, i.e. $\frac{B_1}{A_1} = \frac{135}{76} \approx 1.776$. The similarity between both values constitutes a test to evaluate the validity of the calculations of A_2 and B_2 and, moreover, it can be the benchmark for an easy and a more complete study on the *pd* hybridization for the different $\frac{B_2}{A_2}$ ratios as n changes, as it was done for the *sp* hybridization [88].

Experimental deductions from the equations 5.3 and 5.10

The data shown in Table 5.8 summarize the calculated Hanstorp parameters (A_1, B_1, A_2, and B_2) and the effective nuclear charges (ξ_{5p}, ξ_{5d} and ξ_{6s}) in three different scenarios whose outputs correspond to its second, third and fourth row.

SPD MODEL	ξ_{5p}	ξ_{5d}	ξ_{6s}	A_1	B_1	A_2	B_2
Clementi-Raimondi [295] effective nuclear charges	20.47	16.37	9.53	0.033	128.488	0.006	0.023
Fleig et al. [287] γ_s**=0.79;** γ_p**=0.10;** γ_d**=0.08**	4.47	5.52	5.82	0.7	2	0.21	2.5
This work γ_s**=0.76;** γ_p**=0.11;** γ_d**=0.13**	7.47	10.36	8.40	0.25	2	0.06	2

Table 5.8: Summary of the Hanstorp parameters and the effective nuclear charges used in the fit of the experimental data through the *spd* model (equation 5.3). The second row in the table includes the effective nuclear charges calculated by Clementi et al. for Ta [295] and the Hanstorp parameters that are deduced from them. The curve using these data corresponds to the short-dashed line in Figures 5.6a and 5.6b. The third row includes the best fitting parameters to our experimental data on the basis of the Mulliken analysis carried by Fleig et al. [287] and they correspond to the long-dashed curve in Figure 5.6a. The fourth row show the best fitting data on the basis of our Mulliken analysis and it corresponds to the long-dashed curve in 5.6b.

The second row in Table 5.8 shows the effective nuclear charges calculated by Clementi et al. [295] for Ta and the Hanstorp parameters that are obtained from these charges with the equations in 5.10. The third and the fourth row include the deduced Hanstorp parameters from the fittings of the equation

5.3 to the measured PADs for the $^2\Delta_{3/2}\rightarrow{}^3\Delta_{(1,2)}$ transition. As it is shown in the first column of the third and the fourth row, these fittings were done, respectively, with the Mulliken populations that were calculated for the orbital 6σ by Fleig et al.[287] and by us. The effective nuclear charges shown in the third and fourth rows were calculated in a second stage from the corresponding deduced Hanstorp parameters with the equations in 5.10.

These three scenarios are visualized in Figures 5.6a and b and were introduced in subsection 5.3.2. The short-dashed curves in both figures correspond to the fit of the *spd* model (equation 5.3) with the Hanstorp parameters from the second row in Table 5.8. The Hanstorp parameters in the third row on the basis of the Mulliken populations analysis carried by Fleig et al.[287] and the equation 5.3 lead to the long-dashed curve in Figure 5.6a, whereas the Hanstorp parameters in the fourth row on the basis of our Mulliken population analysis and the equation 5.3 are plotted by the long-dashed curve in Figure 5.6b.

About the Clementi and Raimondi[295] effective nuclear charges: In light of Figures 5.6a and b, the comparison of Table 5.8 and the equation 5.10 that determines B_1 from the Clementi-Raimondi effective nuclear charges[295] concludes that the parameter B_1 (and, therefore, the radial transition dipole matrix $\chi^2_{0,1}$ that corresponds to the $s\rightarrow p$ photodetachment channel) is overestimated because the value calculated for the nuclear effective charge ξ_{5p} is too high. As well, one can argue that the parameters A_2 and B_2 calculated from the Clementi-Raimondi effective nuclear charges[295] are underestimated but, as we will see in the following paragraphs, their unrealistic values do not have a drastic influence in the β_2 values because the contributions of γ_p and γ_d are small in 6σ.

About the effective nuclear charges calculated from our Mulliken populations and those of Fleig et al.[287]: the parameters B_1 and B_2 (those that describe the "intercrossing" detachment channels) show in both cases very similar values, but A_1 and A_2 are deduced with nearly three times bigger values from the Mulliken populations of Fleig compared to ours. Unluckily, this model is not developed enough to give answer to these discrepancies, which are not so substantial and do not change the basic insights we

gain into TaN. Moreover, the contributions of γ_p and γ_d are, compared to the one of γ_s, so small that the sensitivity to numerical changes in A_2 and B_2 in the fit of β_2 is lower than the sensitivity to changes in A_1 and B_1. Indeed, the changes in B_2 have a clear imprint in the β_2 curves for a certain numerical range of that parameter, being unobservable out of it. In the fittings of figures in 5.6a and b, β_2 changes asymptotically to a stationary value that is reached when $B_2 \geq 4$ eV^{-1} (the closer to this stationary value we are, the smaller the observed changes in β_2 will be).

The relations between the numerical values of the effective nuclear charges that are obtained in both fittings reveal bigger pieces of information. In both cases ξ_{5p} is smaller than ξ_{5d} and ξ_{6s}, opposite to the calculations of Clementi et al.[295] where ξ_{5p} is the biggest one. Additionally, ξ_{5d} and ξ_{6s} have similar values or even, as in the fit to the Mulliken population analysis of Fleig, ξ_{6s} is bigger than ξ_{5d}. We can rationalize these changes in terms of the presence of relativistic effects in the Ta atom. The small value of ξ_{5p} is an indication of a more diffuse $5p$ atomic orbital which does not suffer so strong contractions product of the relativistic effects as the $6s$ orbital. Therefore, a bigger effective nuclear charge for $6s$ than for $5p$ indicates a more localized atomic orbital. This idea is further supported by the similar effective nuclear charges of $5d$ and $6s$ orbitals. $5d$ orbitals should theoretically "see" a higher effective nuclear charge than $6s$ orbitals, but as $5d$ orbitals are barely affected by relativistic effects compared to the $6s$ ones, they do not suffer any radial contraction and, consequently, the nuclear effective charge that is seen by the $6s$ orbitals is similar or bigger than the one of the $5d$ orbital.

$^2\Delta_{3/2} \rightarrow {}^1\Sigma_0^+$ transition

The Cooper-Zare formula in the Hanstorp approximation[93] for l=2 is:

$$\beta_d = \frac{2 + 12A_2^2\varepsilon^2 - 36A_2\varepsilon\cos\delta_{1,3}}{10 + 15A_2\varepsilon^2} \quad \text{and} \quad A_2 = 6.30\frac{1}{\xi_{5d}^2}(eV^{-1}) \qquad (5.16)$$

Problems derived from the fitting of β_2 with a minimum value distinct from -1 (blue curve in Figure 5.7) when the detachment occurs from a purely

atomic orbital with l $\geq$1 or a hybridized orbital that does not contain *s* "wave-like" contributions were discussed in more detail by Khuseynov et al.[37] in his study about the hybridized *pd* model. There, the lack of a mathematical tool different from the introduction of an unphysical phase factor to simulate these observations was considered a limitation of the "sequential-mixing" model that should be solved in the future. So far, with the exception of the work of Hanstorp et al.[251] where a non-zero phase has been proposed, no new advance has been published, so we just mention the physically unrealistic solution proposed here by introducing $\cos\delta_{1,3}$=0.42 and A_2=1.35 eV^{-1}.

Final remarks

The presence of a transition metal atom in a molecule constitutes an interesting novelty that allowed to check successfully the application of the "sequential-mixing" model developed by Sanov to systems with a big number of valence electrons. As well, some limitations were found (as a not solid explanation for the changes in the Hanstorp parameters A_1 and A_2 in the detachment from 6σ or the most likely presence of electronic correlation effects in the $^2\Delta_{3/2}\rightarrow{}^1\Sigma_0^+$ transition) that can trigger through deeper theoretical studies a more precise knowledge about PADs. Most DFT methods (also the one we used here) have been developed in order to provide the best possible estimates for energy eigenstates or electron density, but not so much for the wavefunctions of the initial and final states, crucial to interpret PADs. For anions in particular, the PADs are very sensitive to the long-range tails of the wavefunctions in the molecular orbitals, but one cannot account for electron correlation effects in the wavefunctions using a density approximation. Only wavefunction-based methods can consider in detail correlation, configuration interaction, or relaxation effects on PADs that DFT barely takes in account. Very little attention has been paid so far to PADs and how they depend on various correlation/relativistic effects. This is the reason why photodetachment studies on transition metals is so interesting.

Chapter 6

Far-IRMPD on $CoAr_6^+$

6.1 Introduction

Complexes between metal ions and weakly bound ligands are useful as simple models, e.g., for studying metal-ligand interactions or solvation processes. Such complexes can be formed isolated in the gas phase and characterized as a function of the number of ligands or solvent species. Thereby one can obtain detailed insight into the binding between metal ion and solvent, the effect of coordination of the central ion, or the occurrence of solvation shells. The binding interaction with the solvent can significantly change the ion's initial properties and its interaction with the environment. Recently, mass spectrometry in combination with size-selective infrared spectrometry has been shown to be a very useful tool to characterize such complexes between metal ions and solvent molecules in the gas phase[296].

Already in the seemingly simple model case of complexes with noble gas (Ng) atoms a number of different contributing factors for the bonding are of competing magnitude, such as covalent bonding as well as induced dipole and dispersion effects. The essential role of non-covalent interactions for the bonding in such complexes has made their description a challenge to quantum chemical methods[297]. On the other side, experimental data sensitive to the properties of the metal-Ng bond is relatively scarce, apart from a few compounds containing metal-xenon bonds that have been synthesized

in macroscopic quantities[298]. Further, there have been several, mostly mass spectrometric, studies showing the formation of rare gas solvation shells by metal ions[298–305]. Here we report on an example where infrared spectroscopy is used to directly probe the interaction between noble gas atoms and a transition metal cation.

In the past, potential energy surfaces for the interaction between transition metal ions and rare gas atoms have been reconstructed based on ion mobility measurements[155,306]. Additionally, ground and excited states of the diatomic $CoAr^+$ have been thoroughly investigated using optical photodissociation spectroscopy[156] and by theory[307,308]. Experimentally, Lessen and Brucat found that cobalt cations can be readily solvated by multiple Ar atoms, but that the $CoAr_6^+$ complex appears to be uniquely stable, something they attribute to a 'covalent interaction between an octahedral array of Ar atoms about the central d^8 ion'[309]. Later, similarly stable and saturated Ng complexes have been found for several other transition metals[301–303]. Such complexes provide the possibility for ion-molecule reactions at low temperatures[301] and, specifically the $CoAr_6^+$ complex has been used to measure absolute pressures in mass spectrometric applications[310,311]. More recently such Ar complexes of the cationic cobalt atom and dimer have been prepared by pickup of the ions into Ar clusters[305].

Based on the previous works one would expect there is little doubt about the octahedral structure of $CoAr_6^+$, but there has not been any spectroscopic characterization of such fully Ng solvated metal ion. A recently published study on the IR spectra of MAr_n^+ (n=3–5; M=Au, Ag, Pd)[312] has been directed at this aim. Infrared spectroscopy is, due to its selection rules, well suited to probe the symmetry of these solvation complexes and it directly probes the bonding via the force constants. Obviously, the comparatively low binding strengths result in a rather low frequency of the metal-Ng stretching fundamentals, which are found in the far-infrared, making them experimentally challenging to detect. Despite this challenge, such spectra are of great interest, as their sensitivity can provide valuable information on the metal-Ng interaction, which may also be useful as reference for detailed theoretical analysis of the binding.

6.2 Experiment

IR spectra of $CoAr_n^+$ complexes are obtained using infrared multiple photon dissociation (IRMPD) spectroscopy. The complexes are formed in the gas phase through laser ablation, thermalization in a He/Ar mixture at 90 K[100,313] and mass analyzed by time-of-flight mass spectrometry. When irradiated with intense monochromatic far-IR light, a complex can absorb multiple photons when the light is in resonance with an IR-active mode of the complex. This finally leads to a heating and the subsequent dissociation of the complex is observed as depletion in the mass spectrum. These intensity changes in the mass spectra are evaluated mass-selectively as a function of IR frequency. As this method does not apply explicit mass selection, fragmentation of larger complexes may disturb the spectra of the resulting fragments, as seen here for $CoAr_5^+$ and smaller. It should be noted that such far-IRMPD experiments require an intense and tunable far-IR source, in this case the FELIX Free Electron Laser at Radboud University, the Netherlands, that is here scanned through the range of 85–250 cm^{-1}. In that range a macropulse of about 10 μs duration contains an energy of 20–50 mJ. Details on the experimental and data analysis procedures can be found in subsections 2.2.4 and 2.2.5. This study is encompassed within the investigation on bimetallic $Co_{n-m}Mn_m^+$ clusters that constitutes chapter 7 and the same CoMn target was used for the production of clusters. Consequently, small traces of $MnAr_n^+$ complexes can appear in the mass spectrum in Figure 6.1, as it is discussed in subsection 6.3.

6.3 Results and discussion

The experimental mass spectra without and with IR light are shown in Figure 6.1 and the $CoAr_n^+$ peaks (n=0 to 7) are marked by red lines. The intensity for the $CoAr_n^+$ complexes in the non IR-illuminated spectrum is clearly higher for n=4, 5 and 6. This trend can be explained by a higher stabilization energy in the cluster upon adding Ar atoms that breaks down at n=7, as this peak is absent in both spectra. The spectrum of the IR-illuminated

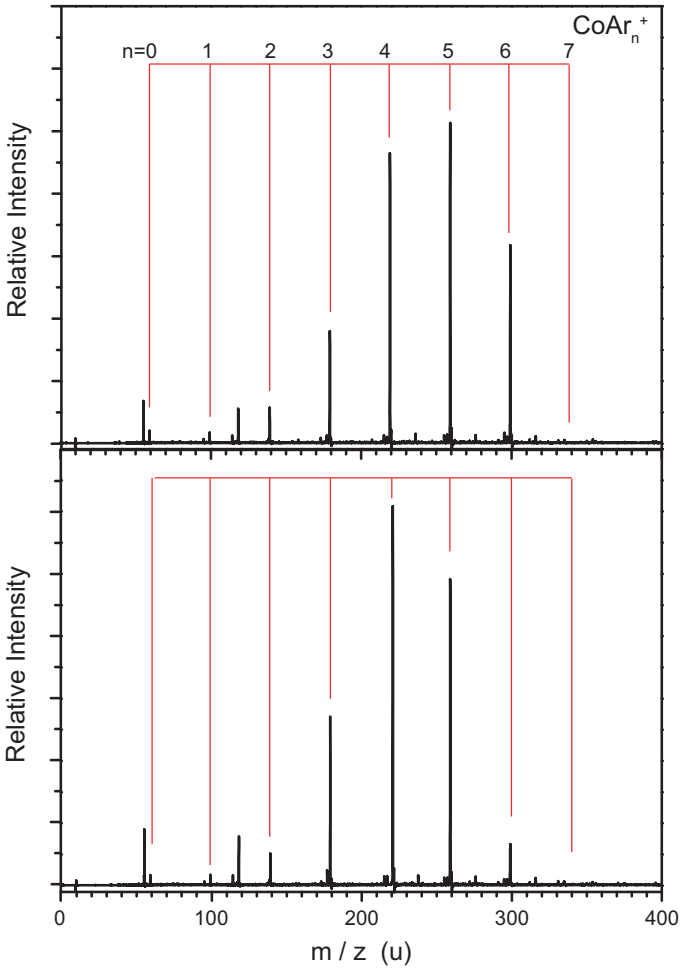

Figure 6.1: Experimental mass spectrum without (upper) and with (lower) IR light obtained by laser ablation of a CoMn bimetallic target rod. The complexes are formed by thermalization in a He/Ar mixture at 90 K. The $\mathrm{CoAr_n^+}$ (n=0–7) species investigated here are marked with read lines. The $\mathrm{CoAr_7^+}$ complex is absent in both spectra due to, presumably, its very low stabilization energy. More details in the text.

ions has a different intensity distribution as a result of the fragmentation processes occurring between the $\mathrm{CoAr_n^+}$ complexes, that will be discussed in more detail in Figure 6.2. This spectrum is further in detail commented: Complexes assigned to the formula $\mathrm{MnAr_n^+}$ have a negligible intensity. Their absence is explained by the comparison of the electronic configurations of

Mn^+, $[Ar]3d^54s^1$, and Co^+, $[Ar]3d^8$. The half-filled Mn 3d shell is more stable than the Co $3d^8$ configuration, leading to a smaller polarization toward the 3p AOs of Ar[314]. In addition, a screening effect appears in Mn due to the half-filled Mn 4s orbital that hinders the polarization of the 3d orbitals in Mn^+ towards the orbitals of Ar[314].

While metal-Ng vibrations have been detected before through infrared spectroscopy, e.g. in Ng complexes of metal clusters[315,316], here we report the first IR spectra of a single Co ion solvated by an Ar shell. The experimental far-infrared multiple photon dissociation (far-IRMPD) spectra for $CoAr_3^+$, $CoAr_4^+$, $CoAr_5^+$, and $CoAr_6^+$ are shown in Figure 6.2. For $CoAr_6^+$ a sharp and comparably narrow band at 125±1 cm^{-1} is identified. Weaker features are seen for $CoAr_5^+$, shifted to a higher frequency at 142±6 cm^{-1}, and for $CoAr_4^+$, even further shifted at 163±2 cm^{-1}. No clear peak is observed in $CoAr_3^+$. Additionally, the features with negative intensity in $CoAr_5^+$, $CoAr_4^+$ and $CoAr_3^+$ are interpreted as depletion paths from the fragmentation of the larger complexes into this species. In $CoAr_5^+$, the small dip between 114 and 126 cm^{-1} with minimum at 121 cm^{-1} comes from the fragmentation of $CoAr_6^+$ to yield $CoAr_5^+$. In $CoAr_4^+$ the region between 104 cm^{-1} and 149 cm^{-1} is a kind of continuum slope with no clear gaussian profile where the fragmentations from $CoAr_6^+$ and $CoAr_5^+$ are difficult to distinguish. Still it is possible to tentatively assign the minimum at 127 cm^{-1} as coming from $CoAr_6^+$ while the minima near 140 cm^{-1} correspond almost exactly with the peak observed in the $CoAr_5^+$ spectrum. In $CoAr_3^+$ there are two clear negative signal regions: one between 108 and 142 cm^{-1} where, as for $CoAr_4^+$, the minima at 121 and 139 cm^{-1} are assigned to depletions from $CoAr_6^+$ and $CoAr_5^+$ respectively, and another between 152 and 188 cm^{-1} clearly coming from $CoAr_4^+$. The depletion cascades from $CoAr_6^+$, $CoAr_5^+$ and $CoAr_4^+$ are marked in Figure 6.2 by black, red and blue arrows.

To assign structures for these complexes, their geometries are optimized using density functional theory calculations (Turbomole V6.6; TPSS-D3/def2-TZVP)[317–319] and harmonic infrared spectra are calculated. It appears that the calculated frequencies of the intense bands are significantly higher than for the observed bands, however, applying a scaling factor of 0.895 gives good

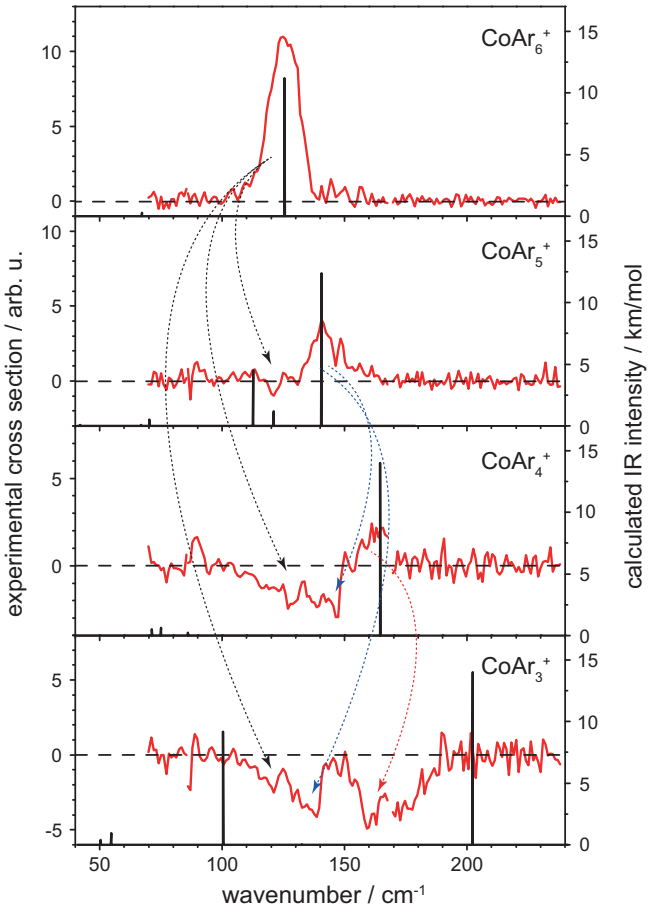

Figure 6.2: Experimental far-IRMPD spectra of $CoAr_3^+$, $CoAr_4^+$, $CoAr_5^+$, and $CoAr_6^+$ compared to the calculated spectra at the TPSS-D3/def2-TZVP level of theory. The black, blue and red arrows mark respectively the fragmentations from $CoAr_6^+$, $CoAr_5^+$ and $CoAr_4^+$ down to lower solvated complexes. In the experimental data the gap of $\sim$2 cm^{-1} at 170 cm^{-1} is due to a small uncovered spectral region between two different measured spectral ranges. The calculated IR spectra are shown by sticks without any Gaussian broadening. A horizontal dashed line marks the baseline in each spectrum.

agreement with the positions of the experimentally observed bands (Figure 6.2).

For completeness, the full row of complexes $CoAr_n^+$ (n=1–7) has been investigated theoretically. All of them possess a triplet ground state, analogous to the d^8s^0 configuration of the isolated cobalt cation leading to a ^3F electronic

state. Their structures are shown in Figure 6.3 and the binding energies for successively added Ar atoms are plotted in Figure 6.5.

The good agreement that we found in $CoAr^+$ with the results of high-level calculations[308] as well as with the experimental values[156] (bond length: exp 238.6 pm; calc. 235.0 pm. Binding energy: exp. 0.508 eV; calc. 0.559 eV) it is used as benchmark for the following calculations. In addition, the significant stronger Ar bonding (0.562 eV) in the linear $CoAr_2^+$ compared to the larger complexes explains the much shorter Co-Ar distances in $CoAr^+$ and $CoAr_2^+$. This can be understood in terms of absence of repulsive steric effects due to small coordination numbers. Successive addition of Ar atoms leads via the T-shaped $CoAr_3^+$ to the distorted square planar $CoAr_4^+$, the square pyramidal $CoAr_5^+$ and, further, the octahedral $CoAr_6^+$. The third Ar atom is relatively weakly bound by about 0.2 eV, suggesting a high stability of the $CoAr_2^+$ entity, while the binding energies for the addition of the 4^{th} to 6^{th} Ar atom are nearly constant at 0.3 eV. With the 6^{th} Ar atom the first solvation shell is closed and further Ar atoms can not directly attach anymore to the central Co cation. This is seen for $CoAr_7^+$, where the binding energy drops to only 0.05 eV. A D_{5h} symmetric pentagonal bipyramidal arrangement is significantly higher in energy (+0.72 eV). Presumably due to this lower stability, the $CoAr_7^+$ complex is not detected in our experiments.

The calculated IR spectra for the larger clusters give, after frequency scaling, good agreement to the experimental data. The O_h symmetric $CoAr_6^+$ has only two (triply degenerate) IR active modes at 66.6 and 125.3 cm^{-1} (both F_{1u}). While the first is outside the investigated spectral range it also has very low IR intensity and would probably not be observable under the experimental conditions. The second predicted band coincides with the experimental band at 125 cm^{-1}.

For $CoAr_5^+$ the predicted most intense peak at 141.6 cm^{-1} (E) is seen in the experiment (141 cm^{-1}) with an excellent agreement. There is as well a certain agreement between the predicted band at 112.4 cm^{-1} and the experimental feature at 113 cm^{-1}, although this peak is not so evident as the former. Additionally, the predicted band at 120.6 cm^{-1} is not observed. One

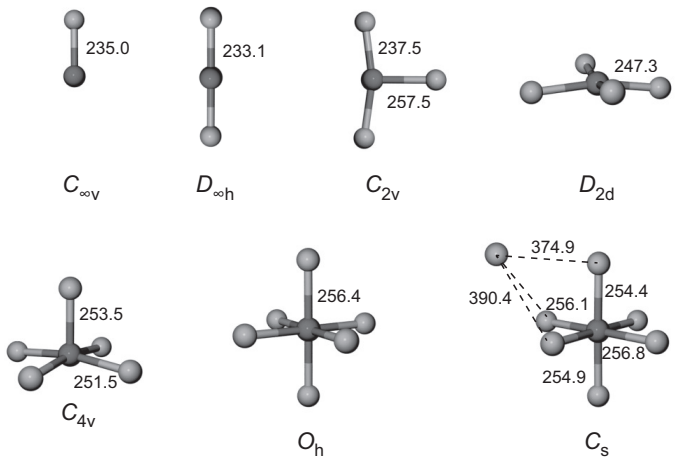

Figure 6.3: Ground state structures of the $CoAr_n^+$ (n=1–7) complexes calculated at the TPSS-D3/def2-TZVP level of theory. For these structures symmetries and bond lengths (in pm) are given. All complexes are triplet states, i.e., the electronic state of the isolated cobalt cation (^{3}F) is retained.

possible reason is its coincidence with a depletion path coming from $CoAr_6^+$, which obscures its presence in the spectrum.

For the nearly square planar $CoAr_4^+$ the predicted most intense band is at 164.8 cm^{-1} (E), and it agrees very well with the experimental one at 163 cm^{-1}. Another small peak seems to exist at 90 cm^{-1} for which there is no satisfactory theoretical explanation, despite the three tiny bands predicted at lower frequencies (85.7, 74.5 and 70.7 cm^{-1}). Finally, there is no evident agreement between theory and experiment for $CoAr_3^+$.

The experimental band intensities are less intense the smaller is their solvation shell, while the theoretical intensities are predicted to be in same range, even slightly higher in $CoAr_4^+$ and $CoAr_3^+$. This may be related to a slower intramolecular vibrational energy redistribution the smaller the molecule is.

The data shown in Figure 6.2 and, for the smaller complexes, simply given by the calculations indicate that the most intense and highest frequency vibration of the complexes suffers a red-shift with increasing number of Ar

atoms. Only $CoAr^+$ has a slightly lowered vibrational frequency compared to $CoAr_2^+$.

To relate this behavior to the properties of the Co-Ar bonds a vibrational analysis in non-redundant internal coordinates has been performed resulting in the Co-Ar stretching force constants k_e (Figure 6.4). With the exception of $CoAr^+$, k_e monotonously decreases with increasing number of Ar atoms in the complex, while $CoAr_3^+$ and $CoAr_5^+$ contain, due to their symmetry, a secondary type of Co-Ar bonds with a significantly lowered k_e. Interestingly, there appears to be an inverse proportionality between k_e and the Co-Ar distances r_e, following the empirical relationship $k_e \cdot (r_e - a)^b = const$, similar to those intensively discussed in the past [320,321]. Although these relations have some relevance even today they are sometimes criticized for not giving much direct physical insight [322,323]. Without speculating further on the reason of the relation observed here it shall be noted that, in principle, it contains information on the interaction potential. However, we could not obtain yet a conclusive explanation based, e.g., on the charge induced dipole interaction potential.

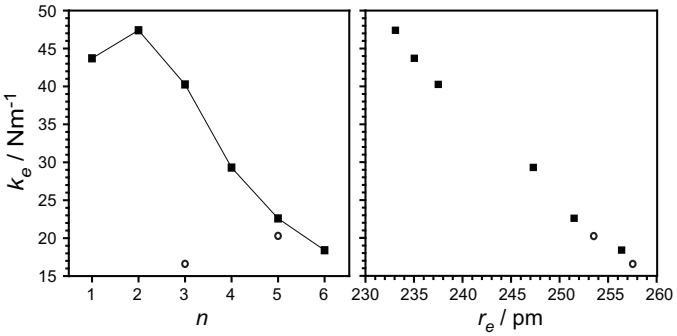

Figure 6.4: Force constants for the Co-Ar stretches obtained from the calculated and scaled vibrational frequencies, plotted as function of Ar coverage (left) and Co-Ar bond length (right). The data for the weaker bound, second type of Co-Ar bonds in $CoAr_3^+$ and $CoAr_5^+$, is indicated by hollow circles.

A natural population analysis shows that with increasing number of Ar ligands the formal charge at the metal ion decreases by a similar amount of 0.05-0.09 e per Ar, which is transferred to the Ar ligands (Figure 6.5). After filling of

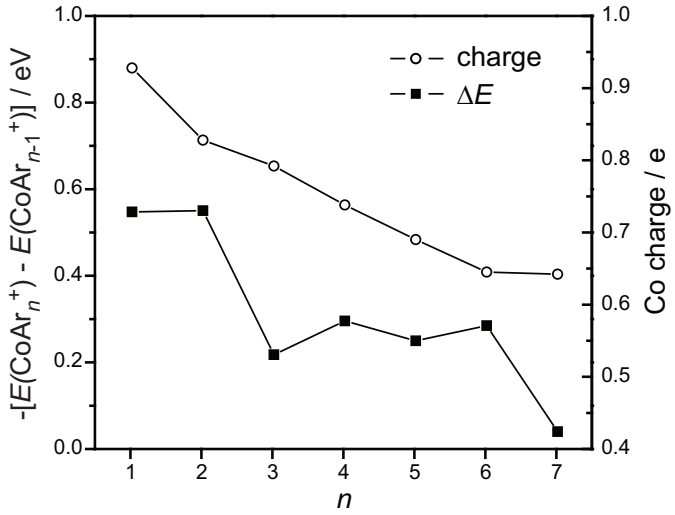

Figure 6.5: Differential binding energies for the $CoAr_n^+$ (n=1–7) complexes and charges at the Co atom from natural population analyses. Especially striking is the high stability of $CoAr^+$ and the di-argon complex as well as the drop in the binding energy after completion of the inner solvation shell at n=6.

the inner solvation shell for n=6 this charge transfer stops. The formal charge transfer may be an expression of a strong charge induced dipole interaction and indeed the here calculated binding energies are overall consistent with values from a pairwise additive model potential, describing the interaction via induced dipoles and the Ar-Ar Lennard-Jones potential[301,303,309,324]. From a detailed study of the Co-Ng dimers (Ng=Ar, Kr, Xe, Rn), comparing static dipole polarizability of the noble gas atoms with the Co^+-Ng interaction energies, it had been concluded that also for these complexes the bonding may be essentially electrostatic[308]. From a Mulliken population analysis of the atomic-like Co orbitals in $CoAr_6^+$ one can deduce a Crystal Field Stabilization Energy (CFSE) of $\Delta_0 \approx 0.8$ eV for this octahedral complex. This splitting between t_{2g} and e_g states is remarkably large despite the weak nature of the interaction between the central cation and the rare gas atoms and close to the splittings for isovalent d^8 complexes, e.g. $[Ni(NH_3)_6]^{2+}$, for which $\Delta_0 \approx 1.2$ eV[325]. The structures expected for just electrostatic interactions should be highly symmetric and do not agree, e.g., with the predictions

from quantum chemistry for $CoAr_3^+$ and $CoAr_4^+$ (Figure 6.3), where a purely electrostatic model would result in equilateral triangular or tetrahedral Ar atom arrangements. Here the structures suggest a relevant contribution of covalent interactions and all geometries can be explained within the model of an octahedral crystal field splitting, i.e., interactions of the only half-filled d_{z^2} and $d_{x^2-y^2}$ orbitals of the Co^+ with filled orbitals of the Ar atoms. For comparison, the Ar complexes of Li^+, which has an ion radius similar to Co^+ and where one would not expect involvement of d orbitals to the binding, show indeed the structures consistent with the electrostatic interaction model. While for the total interaction strength the electrostatics might be still the most important term[314,315], it appears that covalent contributions are relevant for the structural arrangement. This can be compared to the case of Ar bound to mixed Ag/Au trimers where relativistic effects lead to a higher covalency of the Ar Au bond and thus a stronger binding[316]. Also for the chemically synthesized M-Xe complexes the bonding is explained as σ-donor interaction[326].

6.4 Conclusion

Far-infrared multiple photodissociation spectra are obtained for cationic cobalt-Ar complexes via direct excitation of Co-Ar vibrational fundamentals. The agreement between the calculated and the experimental spectra suggests the presence of an octahedral complex for $CoAr_6^+$, a square pyramidal structure for $CoAr_5^+$, and a distorted square planar one for $CoAr_4^+$, but further studies must be done in order to corroborate such structures. As these structures cannot be entirely explained by barely electrostatic Co^+-Ar interactions, it is as well considered a covalent contribution to the binding. This may be a peculiarity of the Ng binding to transition metal ions, but a more detailed theoretical analysis of this binding may give further insights into the contributions of the different type of interactions and their mutual importance for binding energies and complex geometries.

Chapter 7

Far-IRMPD on cationic $Co_{n-m}Mn_mAr_x$ clusters

7.1 Introduction

A frequent motivation for the study of atomic or molecular clusters is the appearance of novel properties compared to the bulk state that are frequently associated to surface and quantum effects. In heterogeneous catalysis, active sites determine the reaction properties of the material and further, the properties of metal clusters as catalyzers has been proven to be very much dependent on cluster size. Among the transition metals, Co is one of the most important in heterogeneous catalysis, as it is used in the conversion of H_2 and CO to longer hydrocarbons[327,328]. The evolution of the magnetic properties in small Co clusters has been subject of theoretical[329] and experimental study via Stern-Gerlach experiments[330,331] and it has been shown that the changes in the magnetic properties of small Co clusters depend on their geometric and electronic structures[332–336] until the bulk regime is reached, where Co is ferromagnetic. Several studies have gained insights into their electronic structure via photoionization efficiency[337], photoelectron spectroscopy[338,339] and photodissociation spectra[340]. The elucidation of their geometries has been the goal of collision-induced dissociation studies[341] and of chemical-probe reaction studies with ammonia[342–345]. All these studies point to big changes

in magnetic and structural properties, with the beginning of a "bulk-like" regime around 19 atoms.

Furthermore, bimetallic clusters of transition metals are highly interesting since their chemical and physical properties can be "ad hoc" tailored to induce reactivity, stability or (specially in Co clusters) magnetic changes. There exists a plethora of studies on doped Co-based clusters using as dopant many different transition metals: Au[346], Rh[347], Cu[348], Cr[349], Pd[350] or Pt[351]. Bimetallic Co-based clusters with 3d transition metals as dopants have been intensely studied as well. Photoelectron experiments have been done on Co_nMn_m[352] and on Co_nV_m clusters[353,354] and also reactivity experiments were done on the latter[355–357]. Magnetism has been as well the cornerstone of different theoretical studies on both systems[358–360], concluding that V as dopant in Co-based clusters decreases their average magnetic moments, opposite to Mn, where magnetic moments are enhanced. Stern-Gerlach experiments on bimetallic Co_nMn_m clusters (with n+m=11–29)[361] showed that each substitution of a Co atom by a Mn atom increases the average magnetic moment of the cluster by 1.7 μ_B[362], contrary to the bulk state, where each substitution decreases the average magnetic moment by 6 μ_B. A comprehensive study was done on Co_nTM^+ (TM = Ti, V, Cr and Mn) clusters[363] showing an enhancement in the stability of the doped cobalt clusters compared to the bare ones by singly doping them with Ti and V. The opposite was observed for Cr and Mn as dopants, with the exception of $Co_{12}Cr^+$, which is more stable than Co_{13}^+. An interesting IRMPD study gives also a broad insight into singly Cr-doped small cationic Co_n-based clusters (n=3–5)[349]. The same experimental method is chosen here to study bimetallic $Co_nMn_mAr_x^+$ clusters in order to reach a better understanding about their geometrical structures through their vibrational fingerprints.

This section contains the far-IRMPD spectra on the $Co_nMn_mAr_x^+$ clusters measured at the Free Electron Laser FELIX in Nijmegen (The Netherlands). Some DFT theoretical calculations were carried out on the smallest measured complexes using the Gaussian16 package[364] with the PBE0 hybrid functional and the def2-TZVP basis set. Dispersion interaction was taken into account by using the Grimme-D3(BJ) method. However, the impact was observed to

be small. Additionally, the spectra of pure $Co_nAr_x^+$ clusters are described and further analyzed to address two issues that are a qualitative understanding of the possible perturbations in the vibrational spectra introduced by the Ar tagging and, furthermore, a comparison with previous results obtained on these systems, mainly with those of Gehrke et al.[315]. This is going to allow us to corroborate our experimental outputs and to deduce further possible structures that have been proposed in other theoretical[329,335,336] and theory-supported studies[338–344] done on Co clusters. Secondly, we will try to rationalize the changes induced in the spectra of the Ar-tagged clusters after the substitution of Co by Mn atoms with the help of the aforementioned calculations.

7.1.1 About the magnetic properties of bare $Co_n^{(+/0/-)}$ clusters

According to Hund's rules, the electronic configuration of atomic Co is [Ar] $3d^74s^2$ and, therefore, its magnetic moment is 3 μ_B. In the bulk regime each atom contributes with one electron to the conduction band that is formed by the delocalized 4s orbitals. The 3d orbitals remain basically localized[29] forming the valence bands. The experimental magnetic moment per Co atom in the bulk regime is 2.2 μ_B.

Theoretical studies have concluded that the average magnetic moment shows a continuous decrease in neutral Co_n clusters towards bigger sizes with alternations superimposed[365,366], with the strong 3d charge localization[329] being responsible for their spin polarization. Interesting comments were done on the relevance of the 4s electrons in Co_5 due to appearance of single bonds rather than multiple ones[329].

Small Co_n cluster cations (n=3 to 5) have been studied via photodissociation spectroscopy[340] and anions via photoelectron spectroscopy[338], revealing ferromagnetic behavior in all the cases (the 3d band with α spins is totally filled, while the 3d band with β spins is partially filled). Moreover, the experimental results for Co_n^- with n≥7 suggested a transition in the electronic structure which implies the presence of mobile electrons (the beginning of a conduction band)[353]. X-ray magnetic circular dichroism studies have given

also insights into Co_n^+ clusters (n=8 to 22)[332,367,368] disentangling the orbital and spin contributions to the magnetic moments, and concluding a weak spin-orbit coupling (Russel-Saunders) for the inner 3d electrons. Moreover, the average number of unoccupied 3d states is nearly constant and close to the bulk value[367], and a local minimum in the orbital magnetic moment of Co_{13}^+ can be a sign of a high-symmetry structure (I_h).

The calculated magnetic moment per atom in Co_3^+ is 2 μ_B and those calculated by Gehrke et al.[315] are, in order from Co_4^+ to Co_8^+, 1.75 μ_B, 2 μ_B, 2.5 μ_B, 2.29 μ_B and 2.19 μ_B. They clearly converge towards 2.2 μ_B, the bulk value, in agreement with all previous studies.

7.1.2 About the magnetic properties of $Co_nMn_m^{(+/0/-)}$ clusters

Prior to a scientific chronology on the magnetism of $Co_nMn_m^{(+/-)}$ bimetallic clusters, it is worth to briefly mention the magnetic behavior of Mn. According to Hund's rules, the electronic configuration of atomic Mn is [Ar] $3d^5 4s^2$ and, therefore, its magnetic moment is 5 μ_B. As it was mentioned above, Mn in the bulk regime is antiferromagnetic while Mn_n clusters (with n=5 to 99) show a ferromagnetic or ferrimagnetic behavior[369,370]. CoMn alloys rich in Co are antiferromagnetic with a decrease of 6 μ_B per Mn atom.

Theoretical studies[358,359] on bimetallic Co_nMn_m clusters with less than 6 atoms have calculated magnetic moments of ~2 μ_B and ~4 μ_B for Co and Mn respectively. This is translated in the aforementioned enhancement of 1.7 μ_B/atom for each Co substituted by Mn within the cluster in percentages not bigger than 40%. These results were experimentally observed[361,362] at 90 K (around our experimental temperature), 160 and 295 K. Such magnetic behavior is understood as a ferromagnetic ordering (in Co_n and $Co_{n-1}Mn_1$ clusters) due to the well localized 3d functions. In order to understand the calculated trend $E_b(Co_{n-1}V) > E_b(Co_n) > E_b(Co_{n-1}Mn)$, it is established for these bimetallic clusters a relation between a stronger atomic interaction inducing antiferromagnetic coupling and a weaker interaction that induces ferromagnetic coupling[358]. This is contradicted by the work of Jia et al.[349],

where the calculated Cr-Co bond lengths of Co_3Cr^+ and of Co_4Cr^+ for low spin states are larger than the high spin states.

The clusters Co_n^-, $Co_{n-1}V_1^-$ and $Co_{n-2}V_2^-$ (with n=4 to 14)[353] were studied by anionic photoelectron spectroscopy. The comparison of the photoelectron spectra of Co_n^- with $Co_{n-1}V_1^-$ revealed a weak electronic perturbation by the V dopant that was rationalized as small changes in the electronic structure because of similar oxidation states in Co and V. As well, the authors did not expect big geometry changes in $Co_{n-1}V_1^-$ respect to Co_n^- due to the similar Wigner-Seitz radius of Co and V. The last idea is supported by the calculations of Shen et al.[358] upon comparing the most stable structures of $Co_{n-1}V_1$ and $Co_{n-1}Mn_1$ with those of Co_n. It is difficult to propose any conclusion with our following data since our study is centered on cationic species. Moreover, the Wigner-Seitz radius of Co and Mn (125.3 pm and 145.6 pm respectively) have remarkably different values and among their most stable oxidation states they only have +2 in common ($3d^7$ for Co and $3d^5$ for Mn).

A recent study[360] calculates two $Co_{11}Mn_2$ isomers with icosahedral geometry. A ground state (25 μ_B) has one manganese atom in the center with nearly no spin polarization, and the other in the bottom position. The first excited state is found at 0.01 eV (31 μ_B) with both manganese atoms on the surface of the cluster and big spin polarization. The existence of two isomers with icosahedral structure is proposed after the photoelectron spectrum of $Co_{11}V_2^-$ [353] and, therefore, we cannot discard it for $Co_{11}Mn_2^+$.

7.2 Experimental introduction

The description of the experimental setup appears in the subsection 2.2.5 and the description of FELIX in the subsection 2.2.4. All measurements on the $Co_nMn_mAr_x^+$ systems were done at low temperature (80 K) and a single bimetallic rod composed of 85% of Co and 15% of Mn was used as a target in the laser vaporization source. The recorded mass spectra are shown in Figures 7.1 and 7.2. The Figure 7.1 shows the spectrum obtained for the pure bimetallic clusters without addition of Ar. The inset of the plot shows

the substructure of each "group of peaks", where the peak with the highest mass corresponds to the pure Co cluster followed by peaks towards smaller masses at consecutive steps of 4 u that are assigned to progressive substitution in the cluster (one by one) of Co atoms by Mn atoms. For all $Co_{n-m}Mn_m^+$ clusters with n+m≥8, the most intense one corresponds to the general formula $Co_{n-1}Mn_1^+$, while the second most intense one is either the pure Co_n^+ cluster (for n=8 or 9) or the $Co_{n-2}Mn_2^+$ one (for n+2>8 or 9). This distribution is just the result of a statistical aggregation that depends on the composition of the rod and, therefore, higher probabilities of formation leads to higher intensities.

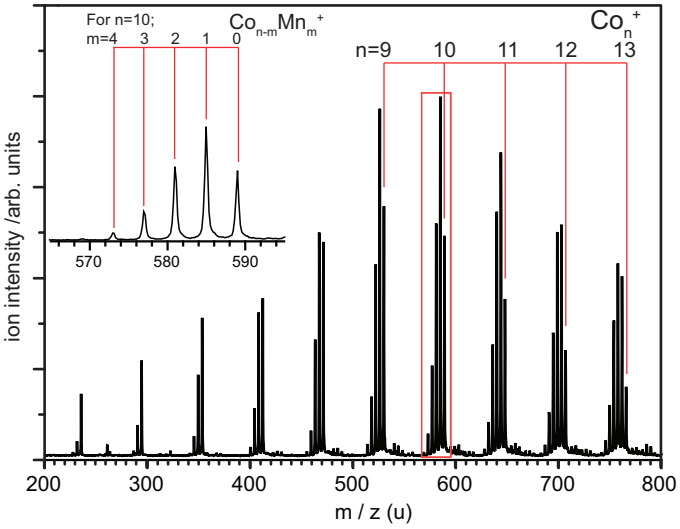

Figure 7.1: Mass spectrum of the cationic bimetallic $Co_{n-m}Mn_m$ clusters. The red lines in the main plot indicate the mass position of the bare Co_n^+ clusters in which are "based" each group of $Co_{n-m}Mn_m^+$ bimetallic clusters with the same number of atoms. The inset resolves the general substructure of each group of peaks that results from the different possible bimetallic clusters based on a certain Co_n^+ size.

Corroborating the ideas of Gehrke et al.[315], it was observed that small clusters (n+m≤5) have a much higher affinity towards Ar compared to the bigger ones (n+m>5) at low temperature conditions (80 K). More specifically, the highest affinity for Ar is shown by the bare mono- and diatomic species. Clusters with 3≤n+m≤5 initially showed an extensive complex formation with

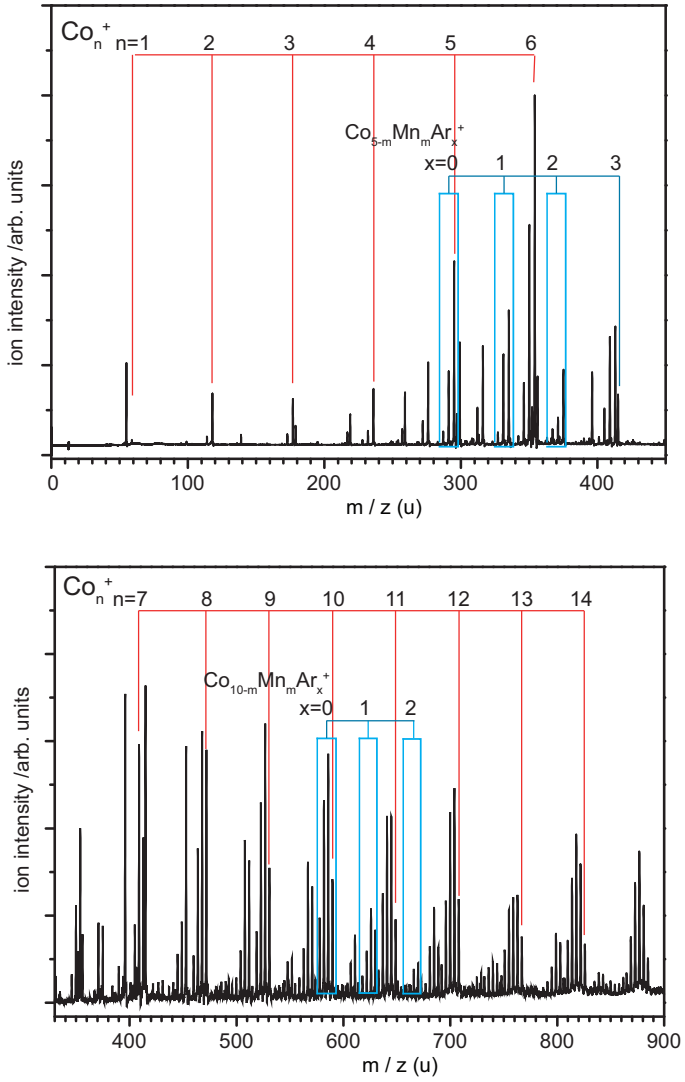

Figure 7.2: Mass spectra of the cationic Co-Mn bimetallic clusters with Ar, $\mathrm{Co_{n-m}Mn_mAr_x^+}$, at low temperatures (80 K in the reaction channel). The upper plot includes the $\mathrm{Co_{n-m}Mn_mAr_x^+}$ clusters with n<6, whilst the lower one shows those with n≥6. Both spectra appear in two different plots as they were separately measured because the experimental parameters were tuned to have the best distribution either for small or for big clusters. As in Figure 7.1, the red lines in each plot indicate the mass position of the bare $\mathrm{Co_n^+}$ clusters in which are "based" each group of $\mathrm{Co_{n-m}Mn_m^+}$ bimetallic clusters with the same number of atoms. Each blue window contains a group of bimetallic $\mathrm{Co_n^+}$-based clusters with a fixed size, n, whilst the blue lines indicate the number of Ar atoms attached to each of these groups. The blue windows in the upper plot extend until the third argon atom, corroborating the higher affinity for Ar in the smaller clusters.

up to 5 attached Ar atoms for a mix of He with 0.01% of Ar, and subsequently, the mix was diluted to 0.005% in order not to attach more than 4 Ar atoms. For bare metal clusters with n+m>5, the complexation at 80 K with a mix of He and 0.1% of Ar did not exceed 2 Ar atoms. The complexation of bare metal clusters with up to 4 Ar atoms for 3≤n+m≤5 and up to 2 Ar atoms for n+m>5 are respectively shown in the upper and lower plots in Figure 7.2 and they evidence a strong interaction between $Co_{n-m}Mn_m^+$ clusters and Ar atoms. Further evidences on such strong interaction will be observed in the Co_n^+-based vibrational spectra shown in this section, where for n<5 the frequency shifts and the relative intensity changes as function of the adsorbed Ar atoms are clearly bigger.

7.3 Analysis (Monometallic $\mathbf{Co_n^+}$ clusters)

$\mathbf{Co_3^+}$. The lowest energy structure of Co_3^+ predicted by our calculations is a distorted triangle (C_s) with S=3 ($^7A'$). The three bond lengths in the bare cluster have slightly different values (2.49, 2.47 and 2.46 Å). Our calculations on $Co_3Ar_3^+$ predict a ground state with C_1 symmetry and S=3 (^7A). The Co-Co bond lengths are nearly the same as in Co_3^+ (2.48, 2.47 and 2.46 Å) and each argon coordinates on top of each cobalt (Figure 7.3). Co-Ar distances are 2.54, 2.55 and 2.55 Å and the argon atoms are not exactly in the plane formed by Co_3^+. Previous theoretical[308] and experimental[156,307] works have given insights into the nature of the interaction in the Co^+-Ar dimer and in Co_n^+-Ar clusters. The attractive character in the Co_n^+-Ar bond is described by the polarization of the Ar atom (as a charge-induced dipole) in the electrostatic field of the cationic cluster (which can be described by a set of partial charges located on the atomic centers that interact with the Ar atoms). The strongest polarizing interaction on each adsorbed argon comes from the nearest metal center in the cluster, and its effect is expected to decrease for bigger metal clusters, as the overall charge is distributed over more atoms[315].

This interaction induces as well an electron density redistribution that was plotted (see Figure 7.4) and rationalized by Gehrke et al.[315] as the adsorption of an Ar on the top position of a metal atom of the bare cluster

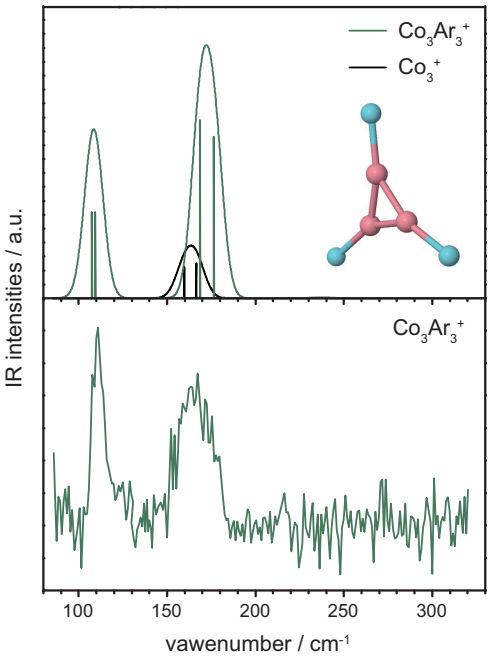

Figure 7.3: Comparison of the theoretical calculations and the far-IR experimental measurements on the $Co_3Ar_3^+$ cluster. The upper plot shows the computed vibrational spectra of Co_3^+ and the $Co_3Ar_3^+$ complex. It is observed that the three argon atoms are not exactly in the plane formed by Co_3^+. No scaling factor was applied to the vibrational frequencies, which are convoluted by a gaussian with FWHM=10 cm^{-1}.

that results in a polarization of the Ar atom and an accumulation of charge in the metal-argon region. The small shortening of the Co-Co bonds in $Co_3Ar_3^+$ can be interpreted as the transfer of electron density upon Ar attachment to some metal-metal bonding orbitals.

The experimental spectrum of $Co_3Ar_3^+$ shows two intense bands at ≈110 and ≈170 cm^{-1} and both are in good agreement with the theoretical simulations, which also predict that each band contains two modes. No scaling factor was applied to the calculated vibrational frequencies. The two calculated bands near 110 cm^{-1} are caused by an antisymmetric "in plane" Ar-Co stretching motion, while the two bands near 170 cm^{-1} result from mostly antisymmetric stretching and some bending of the Co-Co bonds. There is no experimental fingerprint of a totally symmetric "in plane" mode and "out

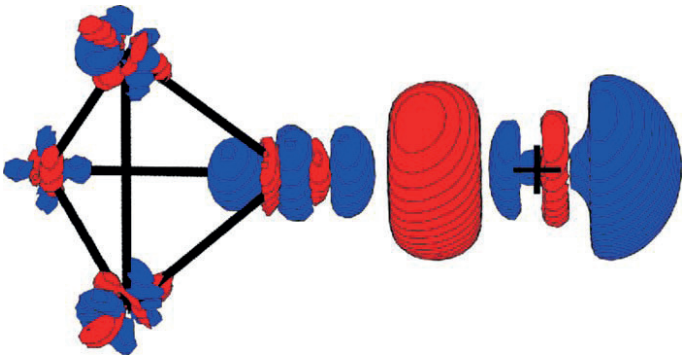

Figure 7.4: Figure taken from Gehrke et al.[315]. Changes in the electron density of the Co_4^+ upon adsorption of one Ar atom. The bonds between the Co atoms are represented by black lines and the black cross is the position of Ar. Zones in red and in blue represent electron accumulation a depletion respectively. The discussion appears in the text.

of plane" vibration since they have very low intensity. Additionally, the latter have frequencies out of the measured spectral range (<60 cm^{-1}). The comparison of the calculated IR modes in Co_3^+ and $Co_3Ar_3^+$ shows that the Ar tagging results in a blue-shift of 9 cm^{-1}, in line with the aforementioned small Co-Co bond shortening, and a huge increase in the intensities of the Co_3^+ modes.

Co_4^+. The spectrum of $Co_4Ar_3^+$ (Figure 7.5 bottom left) contains a small peak at 218 cm^{-1}, a broad band at 190 cm^{-1} and a narrow peak at 109 cm^{-1}. The spectrum of $Co_4Ar_4^+$ (orange) follows a similar pattern with bands between 160 and 230 cm^{-1}, and a maximum at ≈190 cm^{-1}. A shoulder at ≈210 cm^{-1} and the narrow peak at 108 cm^{-1} nearly coincide with the features of the $Co_4Ar_5^+$ spectrum contained in the work of Gehrke et al.[315]. There, they also include the measurements on Co_4Ar^+ and $Co_4Ar_2^+$, completing the complexation series on Co_4^+. The comparison of the five spectra reveals an increase in the intensity when going from Co_4Ar^+ to $Co_4Ar_4^+$, but it is difficult to establish if the maximum intensity corresponds to the $Co_4Ar_4^+$ or to the $Co_4Ar_5^+$ spectrum, since their relative intensities are difficult to compare. The peak near 109 cm^{-1} that appears in our spectra on $Co_4Ar_3^+$ and $Co_4Ar_4^+$ is absent in the spectra of Gruene[44] on Co_4Ar^+ and $Co_4Ar_2^+$. In the work of Gehrke et al.[315], this peak is explained by a symmetry breaking of the

bare cluster that is in turn caused by a strong binding energy in Ar-Co_4^+ of around 0.3 eV and that allows the appearance of IR-active modes in the low frequency-range. As well, its experimental absence in Co_4Ar^+ and $Co_4Ar_2^+$ is justified by a low photon energy in the far-IR which does not lead to a fragmentation for clusters smaller than $Co_4Ar_5^+$, where at least one Co atom must be coordinated to two Ar atoms. Consequently, the conclusions of Gehrke et al.[315] are only in agreement with our experimental results if we consider the possibility that a higher FEL photon fluence at low frequencies during our experiment allowed the desorption of Ar in $Co_4Ar_3^+$ and $Co_4Ar_4^+$. Contrary, the photon fluence in our case is lower and, therefore, it is recommended a repetition of the measurements at frequencies below 160 cm^{-1} to confirm better the vibrational spectra of the $Co_4Ar_x^+$ complexes. Moreover, the work of Jia et al.[349] includes a nearly identical experimental spectrum for $Co_4Ar_4^+$ and their calculations explain very nicely the region between 140 and 230 cm^{-1}. Gehrke et al.[315] predict a distorted tetrahedron with D_{2d} symmetry and Jia et al.[349] calculate, as well, a distorted tetrahedron but with C_1 symmetry, both of them with a magnetic moment of 7 μ_B. The Co_4^+ isomer by Gehrke et al.[315] at 0.32 eV with a butterfly structure (C_{2v}) can be discarded.

Co_5^+. The complexation series studied by Gruene for $Co_5Ar_x^+$ (x = 1,4 and 5) is completed here with $Co_5Ar_2^+$ and $Co_5Ar_3^+$. The comparison of our Co_5Ar^+ spectrum with the one of Gruene[44] shows a generally similar pattern, but the relative intensities of the two main peaks (at around 190 cm^{-1} and 240 cm^{-1}) are reversed. Additionally, the peak at 190 cm^{-1} is in the here presented spectra much narrower. These discrepancies can have their origin in the measuring process, since peaks at 190 cm^{-1} and 240 cm^{-1} correspond to two different experimental ranges, and a low FEL power throughout our measurements in the spectral region that contains the peak at 190 cm^{-1}, can cause these intensity differences. The comparison of $Co_5Ar_x^+$ with x=1 to 3 corroborates the ideas on the dependence of the spectra on the number of attached Ar atoms established by Gehrke et al.[315] and already introduced in the analysis of the $Co_4Ar_{3,4}^+$. These ideas entail the appearance of an absorption band at 105 cm^{-1}, frequency shifts of the peaks and the increase of the band intensities the more Ar atoms are attached. Nevertheless, the

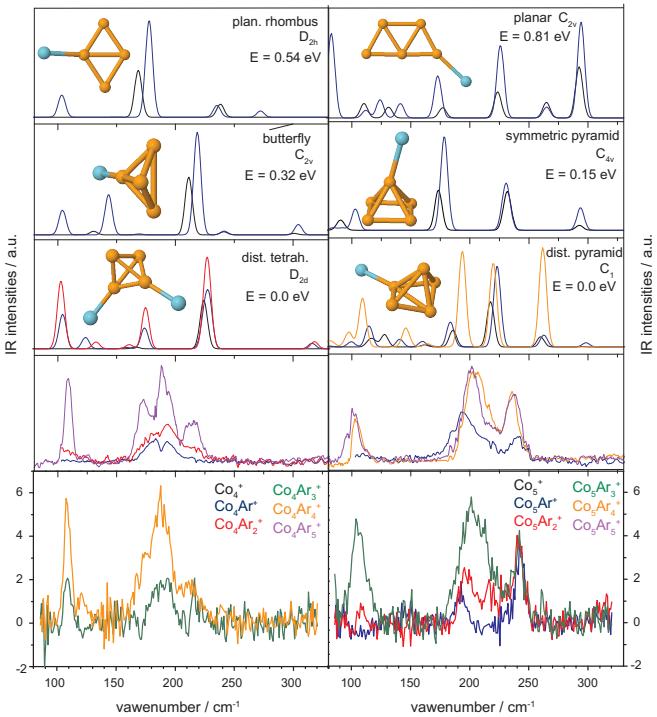

Figure 7.5: Far-IR experimental measurements and calculations on the $Co_nAr_x^+$ clusters with n=4–5. The Figure includes our own measurements and the corresponding experimental and theoretical information that has been taken and adapted from the PhD thesis of Gruene[44]. The bottom row depicts the measured spectra within the framework of this thesis. The measured spectra by Gruene et al.[44] appear immediately above. They are obtained by a three adjacent-point average on the raw data. The rest of the plots depict the calculated vibrational spectra on each isomer with information about their energies relative to the calculated ground state and a plot with their geometrical structure (with a brief description and their point group symmetry)[315].

comparison of $Co_5Ar_3^+$ with $Co_5Ar_4^+$ and $Co_5Ar_5^+$ might indicate a "saturation" of these three effects since a further blueshift of the band at 190 cm^{-1} is not observed and a clear intensity increase is not observable either (neither in the peak at 105 cm^{-1}, nor in the overall spectral intensity). One explanation for this "intensity saturation effect" can be based on the geometrical attachment of the argon on Co_5^+. If the bare cluster has a trigonal bipyramid structure, the attachment of argon atoms on the three metal atoms in the equatorial plane would change notably the symmetry of the complex, whilst the attachment

on the top or on the bottom atoms would not have such a big effect on the symmetry of the complex. Apart from that, the band at 240 cm^{-1} has the same intensity in the three measured spectra.

It is also worth to comment on the comparison between our $Co_5Ar_3^+$ spectrum and the one reported by Jia et al.[349], which does not show any peak at 105 cm^{-1} or at 240 cm^{-1}. Peaks in that range are also observed for $Co_5Ar_4^+$ and on $Co_5Ar_5^+$ in the spectra of Gruene[44]. The reason for this disagreement is not clear. The calculations carried out by Gehrke et al.[315] and Jia et al.[349] agree with previous studies on the neutral pentamer[144,335,336] that propose a three dimensional structure for the ground state. The calculations of Jia et al.[349] on $Co_5Ar_3^+$ predict a distorted trigonal bipyramid structure with three argons attached to the equatorial plane of the Co_5^+, which is in line with our aforementioned experimental prediction. Nevertheless, the agreement between our experimental IR spectrum and the calculated one by Jia et al.[349] is poor. The computed IR spectrum on $Co_5Ar_5^+$ by Gehrke et al.[315] agrees better with our experimental observations since it includes a peak at around 110 cm^{-1} and three between 175 and 275 cm^{-1} that, somehow, resemble the features of $Co_5Ar_3^+$ between 180 and 270 cm^{-1}.

Co_6^+. In the Co_6Ar^+ spectrum, a broad band at ≈240 cm^{-1} and a smaller one at 297 cm^{-1} can be observed. The agreement of the main features with the spectra in the work of Gruene[44] is very good, except for a small change in their relative intensities. Furthermore, the agreement with the spectrum of their calculated lowest energy structures (a slightly distorted tetragonal bipyramid with D_{3d} symmetry and bond lengths around 2.3 Å[315]) can be considered even better than in the original study[315], since we find an assignment for the small peak at 297 cm^{-1}.

Co_7^+. The spectra of Co_7Ar^+ and $Co_7Ar_2^+$ agree nicely with the ones measured by Gehrke et al.[315] in the region between 220 and 320 cm^{-1}, however, the here presented spectra include in addition many features at lower frequencies. The observation of new features at low frequencies or even their higher relative intensity when they are compared with those of Gruene[44] is not only particular for this cluster size, but it is a general trend. One possible reason could be the normalization method followed when extracting

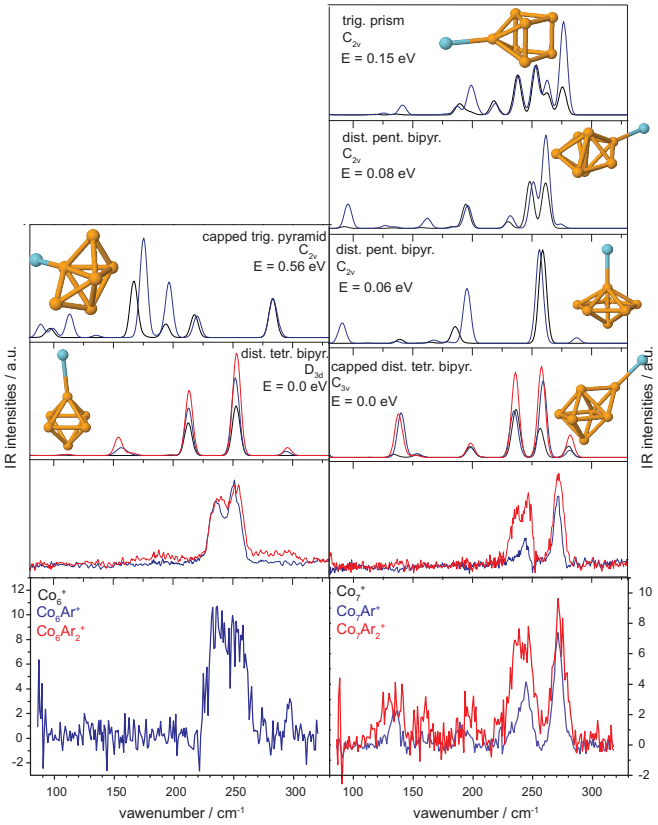

Figure 7.6: Far-IR experimental measurements and calculations on the $Co_nAr_x^+$ clusters with n=6–7. The Figure includes our own measurements and the corresponding experimental and theoretical information that has been taken and adapted from the PhD thesis of Gruene [44]. The bottom row depicts the measured spectra within the framework of this thesis. The measured spectra by Gruene et al. [44] appear immediately above. They are obtained by a three adjacent-point average on the raw data. The rest of the plots depict the calculated vibrational spectra on each isomer with information about their energies relative to the calculated ground state and a plot with their geometrical structure (with a brief description and their point group symmetry) [315].

the data since here the intensities were normalized by the photon fluence of the FEL, but in former works the FEL power was used as the normalization parameter. Another possibility already mentioned in $Co_4Ar_{1,2}^+$ and Co_5Ar^+ is that, due a lower photon fluence in the lower frequency region, dissociation of the Ar complexes has not occurred in the work of Gruene. Contrary, the photon fluence in our case is lower and this possibility can be discarded. The

higher intensity in the $Co_7Ar_2^+$ spectrum with respect to the one of Co_7Ar^+ is interpreted by Gehrke et al.[315] as being related to a lower binding energy in the second Co_n^+-Ar bond compared to the first one. Further, the addition of the second Ar can cause a broadening of some bands. Moreover, the generally much higher intensity in the spectra containing two Ar atoms, also observed in $Co_6Ar_{1,2}^+$ and in $Co_8Ar_{1,2}^+$ when compared to the smaller metal cluster sizes, is supported by the calculated decrease in the binding energy of the Co_n^+-Ar complex as n increases[315]. The calculated ground state for Co_7^+ by Gehrke et al.[315] is a capped tetragonal bipyramid with C_{3v} symmetry and magnetic moment of 16 μ_B. Almost all peaks of Co_7Ar^+ here observed are theoretically explained (at around 140, 190, 240 and 270 cm^{-1}) and just few peaks remain unassigned (a small peak at 200 cm^{-1} and a small peak theoretically predicted at 280 cm^{-1} but not found in the experiment). The agreement in $Co_7Ar_2^+$ is slightly worse but still good. Mainly, the broadenings in bands at 140, 190 and specially 240 cm^{-1} are not explained by theory. Further, we cannot discard the contribution of the calculated higher energy isomers, two spin variants of a distorted pentagonal bipyramid with C_{2v} symmetry, at 0.06 eV and 0.08 eV higher than the most stable one with respectively 14 μ_B and 16 μ_B.

Co_8^+. In the spectrum of $Co_8Ar_2^+$ several bands can be identified which are at 272, 247, 220, 204, 152, 123, 116 and 93 cm^{-1}. Further, there is also a shoulder at 138 cm^{-1}. The correspondence of these peaks with those in the spectrum of Co_8Ar^+ is nearly one-to-one with shifts in their positions smaller than 3 cm^{-1}, quite below the energy resolution of the FEL used in this experiment. At low frequencies Co_8Ar^+ and $Co_8Ar_2^+$ have nearly the same intensities, while those at higher frequencies are slightly bigger in $Co_8Ar_2^+$. The comparison with the measured spectra in the work of Gruene[44] shows a good agreement for the high frequency range and the appearance of several new features at low frequencies, which could be either caused by a higher FEL power throughout our measurements in this energy range or a different normalization procedure. Contrary to the comment of Gehrke[315], the peak at 150 cm^{-1} seems to be not an artifact but a real feature. Unfortunately, the agreement between our experimental data with those computed by Gehrke

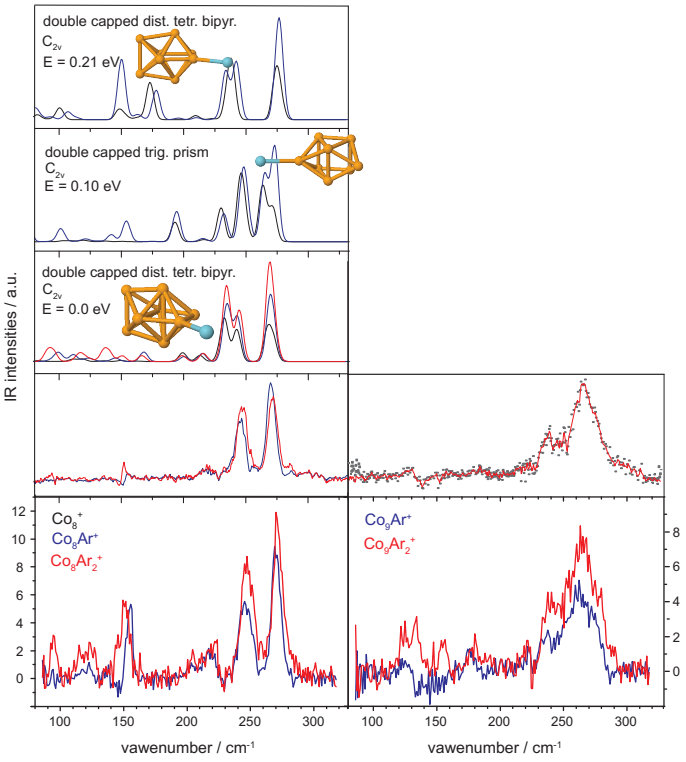

Figure 7.7: Far-IR experimental measurements and calculations on the $\mathrm{Co_nAr_x^+}$ clusters with n=8–9. The Figure includes our own measurements and the corresponding experimental and theoretical information that has been taken and adapted from the PhD thesis of Gruene[44]. The bottom row depicts the measured spectra within the framework of this thesis. The measured spectra by Gruene et al.[44] appear immediately above. They are obtained by a three adjacent-point average on the raw data. The rest of the plots depict the calculated vibrational spectra on each isomer with information about their energies relative to the calculated ground state and a plot with their geometrical structure (with a brief description and their point group symmetry)[315].

et al.[315] is not so good as for $\mathrm{Co_7Ar_{1,2}^+}$, despite the new features at low frequencies. We cannot establish a definitive assignment with their computed results[315] neither at low nor at high frequencies, since the experimentally observed band at 247 $\mathrm{cm^{-1}}$ does not seem to correspond to the two computed peaks for the lowest energy isomer at around 230 and 240 $\mathrm{cm^{-1}}$ and only the most intense peak is nicely reproduced. We tentatively take as structural candidates the two lowest isomers calculated by Gehrke et al.[315]: a double-

capped distorted tetragonal bipyramid with 7 μ_B and D_{2d} symmetry and a slightly distorted double-capped trigonal prism with 17 μ_B. More precise calculations are needed.

Co_9^+. Again, when comparing spectra of Co_9Ar^+ and $Co_9Ar_2^+$, nearly all spectral features coincide. The features that are clearly common to both of them are a broad and intense band between 229 and 289 cm^{-1} and two peaks with maxima at around 222 and 178 cm^{-1}. The slight apparent negative signal observed between 130 and 160 cm^{-1} in Co_9Ar^+ must come from the Ar fragmentation in the $Co_9Ar_2^+$ channel.

Co_{10}^+, **Co_{11}^+**, **Co_{12}^+**, **Co_{13}^+**, **Co_{14}^+** and **Co_{15}^+**. The general visual comparison of our measured spectra for pure cobalt clusters with sizes n>9 with those from Gruene in his PhD thesis[44] reveals that the quality is clearly worse in our case with a much higher noise to signal ratio, which gives rise to spiky features.

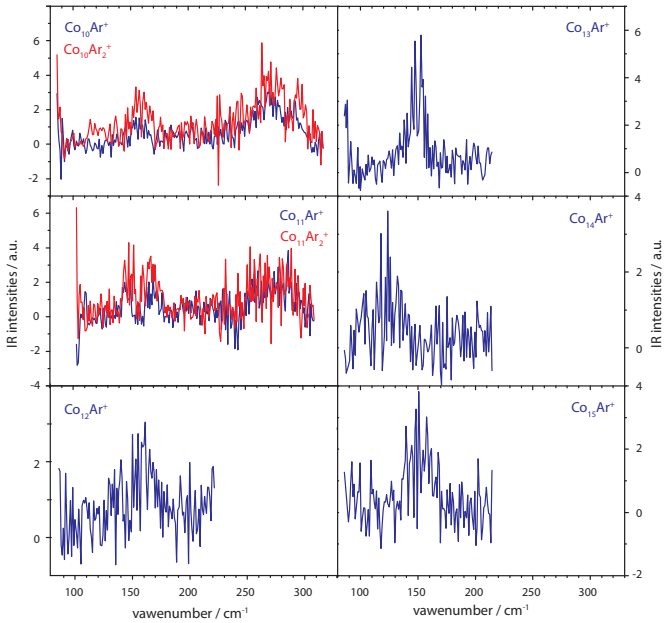

Figure 7.8: Far-IR experimental measurements on the $Co_nAr_x^+$ clusters with n=10–15. Spectra with n=12 to 15 do not include the measured spectral range between 215 and 320 cm^{-1} due to a very bad signal to noise ratio. The interpretation of the spectra is discussed in the text in comparison to the experimental results included in PhD thesis of Gruene[44], which are shown in Figure 7.9.

This is most evident in the measured frequency range between 215 and 320 cm^{-1} (see $Co_{11}Ar^+_{1,2}$ spectra in Figure 7.8), where the spectra with n>11 do only contain noise and the data are, therefore, omitted. The most important observation implies that bands at higher energies (225 to 300 cm^{-1}) reduce gradually their intensity while the peaks at lower intensities maintain or increase their intensity until a single and narrow peak at 153 cm^{-1} appears in the $Co_{13}Ar^+$ spectrum, signature of a cluster with high symmetry. For cluster

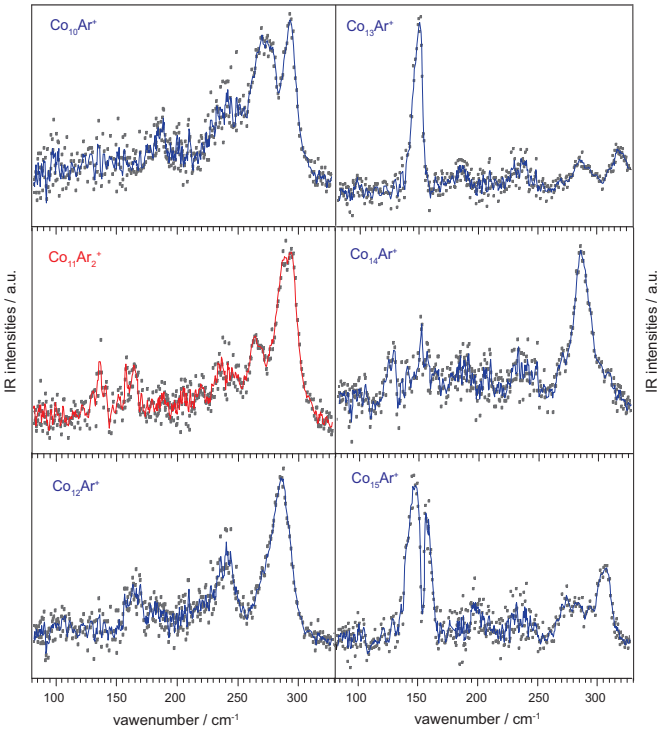

Figure 7.9: Far-IR experimental measurements on the $Co_nAr_x^+$ clusters with n=10–15. The raw experimental data are represented by grey points and the red and blue lines are obtained by a three adjacent-point average on the raw data. The spectra have been directly adapted from the PhD thesis of Philipp Gruene[44].

sizes bigger than n=9 it is difficult to find calculations on geometric structures in the literature, presumably due the high computational costs. All previous theoretical predictions[336] as well as experimental studies[343,344] on clusters in this size range base the cluster structure evolution between Co_{10}^+ and Co_{15}^+

on the geometry of Co_{13}^+ as a starting point. In these studies, icosahedral and octahedral (mainly hcp, but also fcc) geometries have been proposed for Co_{13}^+. In addition, more exotic Co_{13}^+ structures have been calculated, as hexagonal bilayer structures[371,372] or star-like icosahedral structures[373].

It is useful to establish a general overview over the $Co_nAr_x^+$ (n=7 to 15) spectra based on the evolution of their features. The most intense peaks in the $Co_7Ar_x^+$ and $Co_8Ar_x^+$ spectra can be found in the spectral region between 225 and 280 cm^{-1}, whilst the less intense and broader peaks appear at lower frequencies, mainly between 100 and 175 cm^{-1}. The most intense peaks in the $Co_9Ar_x^+$ and $Co_{10}Ar_x^+$ spectra merge in a non-resolved broad band, which is a sign for a more complex vibrational substructure, but the peaks contained between 100 and 175 cm^{-1}, although being broad, maintain distinct features with small changes in positions. The $Co_{11}Ar_x^+$ spectrum begins to show a clear change as the intense band at higher frequencies shows a much lower intensity compared to the bands at lower frequencies. This evolution continues until $Co_{13}Ar^+$ where the spectrum shows a single clear and narrow peak, a signature of a high symmetry cluster geometry. Finally, the spectra of $Co_{14}Ar_x^+$ and $Co_{15}Ar_x^+$ show the same single peak but broader, which indicates a preservation of the basic high symmetry geometry motif proposed for $Co_{13}Ar_x^+$ complemented with the addition of more cobalt atoms on its surface.

7.4 Analysis (Bimetallic $\mathbf{Co_{n-m}Mn_m^+}$ clusters)

Due to a lack of theoretical calculations, the conclusions established in previous works are going to be used as basis to interpret the spectra of bimetallic complexes. All theoretical studies on bimetallic Co-based-Mn-doped clusters[358–360] concluded that the order of bond strengths in the aggregation process is Co-Co>Co-Mn>Mn-Mn and, oppositely to the bond strength order, the metal-metal bond length in the cluster will be Co-Co<Co-Mn<Mn-Mn. A similar conclusion is also given in the work of Jia et al.[349] for $Co_{n-1}Cr^+$ (n=3–5) clusters, since the bond distances are ordered by Co-Cr>Co-Co (it is here also mentioned that the connectivity inside the cluster does not change

upon Co to Cr substitution and, furthermore, it remains unchanged upon Ar attachment). In the particular case of only one Co atom substituted by one Mn in the cluster, the predicted strength reduction in the Co-Mn bonds compared to Co-Co bonds could cause redshifts in the vibrational spectra of bimetallic clusters if the cluster symmetry is not strongly reduced and the vibrational spectrum does not suffer big modifications. Of course, after a consecutive substitution of several Co atoms by Mn atoms in the "original" pure cobalt clusters one can expect big reductions in the cluster symmetry and, therefore, even stronger modifications are supposed to happen in the vibrational spectra of bimetallic clusters as, for example, the IR activation of formerly totally symmetric modes.

Two general guidelines are going to be followed in the qualitative discussion of our experimental spectra considering either changes in the vibrational frequencies or in the relative spectral intensities:

- In the vibrational frequencies, the observed changes are going to be mainly assigned to structural, geometrical or symmetry variations in the clusters, as it was mentioned in the paragraph above.

- The relative intensities in the different $Co_nAr_x^+$ vibrational spectra will be related to the strength of the Co_n^+-Ar bonding as a function of the cluster size and how effective the argon desorption can happen. Furthermore, structural changes in the cluster (for example, substitution of Co by Mn atoms) can modify not only its total magnetic moment, but also its IR transition dipole moment. This can influence the number of absorbed photons, which in turn can influence the spectral intensities of the bimetallic clusters compared to the bare cobalt clusters, since argon atoms can be differently desorbed from them.

Co_3^+-based clusters. The spectrum of $Co_2MnAr_3^+$ just shows one band at 228 cm^{-1} and is drastically different to the spectrum of $Co_3Ar_3^+$. The calculated totally symmetric mode for $Co_3Ar_3^+$, that mainly involves the Co-Co bond stretching, is calculated at 240 cm^{-1}, but it is nearly IR inactive and experimentally not observed (Figure 7.10) due to symmetry selection rules. The substitution of one cobalt by one manganese breaks the symmetry of $Co_3Ar_3^+$ and this mode becomes more IR active, resulting in a band at around

240 cm^{-1}. The experimental redshift of 12 cm^{-1} between the calculated mode at 240 cm^{-1} and the observed spiky feature at 228 cm^{-1} could be attributed to the weakening of the Co-Mn bond respect to the Co-Co one.

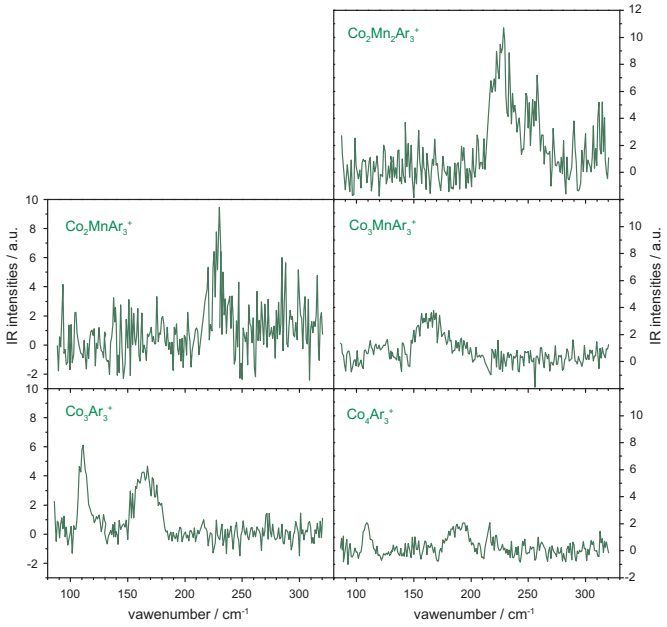

Figure 7.10: Comparison of the far-IR experimental measurements on the $Co_{n-m}Mn_mAr_x^+$ clusters with n=3 and 4.

Co_4^+-based clusters. The $Co_3MnAr_3^+$ spectrum shows one band at around 165 cm^{-1}. This spectrum can be compared to the one of $Co_4Ar_3^+$, which shows a comparable band shifted ≈35 cm^{-1} to the blue. The band of $Co_4Ar_3^+$ at 108 cm^{-1} is missing in the spectrum of $Co_3MnAr_3^+$. Two options are proposed: either it is so red-shifted that is does not appear in the investigated spectral range or it does not exist at all. The comparison of $Co_4Ar_3^+$ with our calculations on $Co_3Ar_3^+$ presumes that the observed band at 160 cm^{-1} in $Co_3MnAr_3^+$ corresponds to the bending and antisymmetric stretching Co-Co vibrations. This prediction has two implications: firstly, the substitution of one Co in the (distorted)-tetrahedron atom by one Mn should not change substantially the symmetry of the cluster, so the Mn atom may be placed at the top position in the tetrahedron; secondly, the three Ar atoms are

bound on top positions on the other three Co atoms that constitute the base of the tetrahedron. This prediction contradicts a former theoretical study that favors planar structures for neutral Co_3Mn clusters[359], but it is supported by the calculations of Jia et al.[349] on Co_3Cr^+ and recent theoretical studies on neutral bimetallic Co-Mn clusters[358,360]. Both predict three-dimensional ground state structures. Moreover, we have already shown that for $Co_4Ar_3^+$ and $Co_4Ar_4^+$ the experimental spectra agree with previous simulations[315], where the most stable structure for Co_4^+ can be a distorted tetrahedron with either D_{2d} or C_1 symmetry, with both isomers lying very close in energy. It would be reasonable to assume that a similar situation applies for Co_3Mn^+ and it has a structure in which a triangle is formed by the three Co atoms that form the base of the tetrahedron with a Mn atom on top. The redshift of ≈35 cm^{-1} observed in $Co_3MnAr_3^+$ compared to $Co_4Ar_3^+$ can be explained by weaker Co-Mn bonds.

The $Co_2Mn_2Ar_3^+$ spectrum shows two bands at 228 and 254 cm^{-1}. The changes observed in the spectrum of $Co_3Ar_3^+$ compared to the spectrum of $Co_2MnAr_3^+$ resemble the spectral changes observed between $Co_3MnAr_3^+$ and $Co_2Mn_2Ar_3^+$. Additionally, we have proposed in the former paragraph that the $Co_3MnAr_3^+$ structure is based on a distorted-tetrahedron, with the Mn atom placed on the top position and with the three argon atoms bound to the three Co atoms. The substitution of a second Co by one Mn would happen in the base of the tetrahedron and it would be geometrically and possibly spectroscopically analogous to what we observed in $Co_2MnAr_3^+$. In analogy with the $Co_2MnAr_3^+$ spectrum, we could speculate that the most intense peaks in the $Co_2Mn_2Ar_3^+$ spectrum result from metal-metal vibrational modes that have become IR active upon symmetry reduction and whose bands are redshifted relative to their values in the $Co_3MnAr_3^+$ cluster due to the higher number of Mn atoms and the comparatively weaker bonds that they form.

Co_5^+-based clusters. In the case of clusters containing one Mn atom, we observe rich spectra with distinct bands. Comparing the spectra of Co_4MnAr^+ and $Co_4MnAr_2^+$ one can see that the bands are more intense in $Co_4MnAr_2^+$ and shifted 10 cm^{-1} to the blue compared to Co_4MnAr^+. Frequency shifts and higher intensities are in line with the conclusions of Gehrke et al.[315] on

Ar coverage in small clusters and high binding energies for the Co_5^+-Ar bond. All calculations on Co_4Mn[358–360] have proposed trigonal bipyramid-based structures with slightly different final equilibrium symmetries as the most stable structures with the Mn atom placed in the equatorial plane. Jia et al.[349] calculated and investigated experimentally Co_4Cr^+ and concluded that it has a distorted trigonal bipyramid structure (^4A, C_1) with the Cr atom placed on the equatorial plane and the three argon atoms attached to the those equatorial atoms. It therefore seems reasonable that Co_4Mn^+ has a distorted trigonal bipyramid structure with the manganese occupying an equatorial atomic position. It is difficult to draw further conclusion from the data and more theory support is needed.

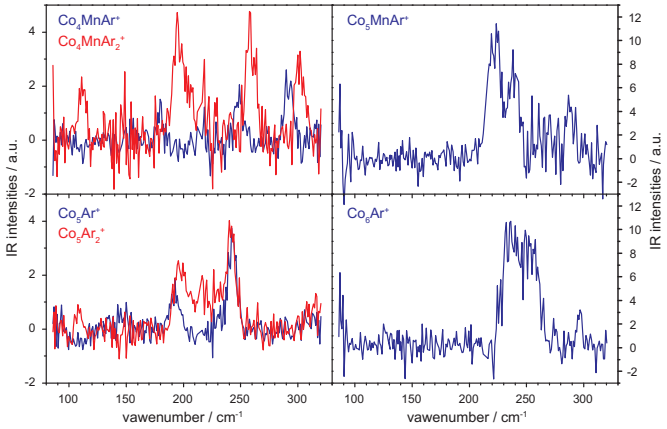

Figure 7.11: Comparison of the far-IR experimental measurements on the $Co_{n-m}Mn_mAr_x^+$ clusters with n=5 and 6.

Co_6^+-based clusters. The spectra of $Co_6Ar_2^+$ and $Co_5MnAr_2^+$ are very similar with a redshift of the main band of ∼11 cm^{-1}. Theory identified the Co_6^+ structure as a slightly distorted tetragonal bipyramid with D_{3d} symmetry and bond lengths around 2.3 Å[315]. Shen et al.[358] found that the most stable Co_5Mn isomer has the Mn atom in the equatorial plane (C_s, 16 μ_B), while the first excited sate (at only 0.061 eV) has the manganese in the top (or down) position (C_{2v}, 16 μ_B). Contrary, this second arrangement was found as the ground structure by Wu et al.[359], but the spectra shown in this work cannot answer the question of which structure is present here. However, they

can state that the structures of $Co_6Ar_2^+$ and $Co_5MnAr_2^+$ are likely to be very similar.

Co_7^+-based clusters. The conclusions established for Co_7^+ were that the ground sate is most probably a capped tetragonal bipyramid with C_{3v} symmetry and magnetic moment of 16 μ_B but we could not discard the contribution of the calculated isomers at 0.06 eV and 0.08 eV higher (two spin variants of a distorted pentagonal bipyramid with C_{2v} symmetry and respectively 14 μ_B and 16 μ_B). The comparison of the spectra of $Co_6MnAr_{1,2}^+$ relative to those of $Co_7Ar_{1,2}^+$ shows in the former a clear overall decrease of the intensity and a merging of the two high frequency bands at 245 and 272 cm^{-1} in a broad band between 230 and 280 cm^{-1}. In the frequencies below 200 cm^{-1}, one can observe a small redshift of 10 cm^{-1}. The spectrum of $Co_5Mn_2Ar^+$ does not show appreciable changes in the intensities compared to Co_6MnAr^+, but those in its vibrational structure are so big that that is impossible to propose aprioristically anything interesting.

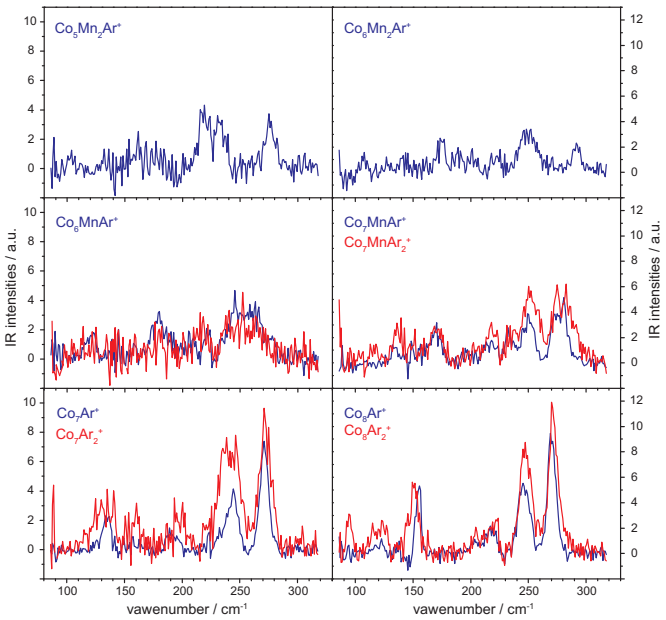

Figure 7.12: Comparison of the far-IR experimental measurements on the $Co_{n-m}Mn_mAr_x^+$ clusters with n=7 and 8.

Co_8^+-based clusters. The isomers proposed for Co_8^+ were a double-capped distorted tetragonal bipyramid with 7 μ_B and D_{2d} symmetry and a slightly distorted double-capped trigonal prism with 17 μ_B. As for the Co_7^+ based clusters, there is an overall intensity reduction by about half in $Co_7MnAr_{1,2}^+$ relative to $Co_8Ar_{1,2}^+$. With the exception of the bands below 200 cm^{-1}, there are no significant changes in the vibrational structure of $Co_7MnAr_{1,2}^+$, except a general blueshift in $Co_7MnAr_{1,2}^+$ of around 10 cm^{-1} and a slight broadening of the most intense band (at 270 cm^{-1} in $Co_8Ar_{1,2}^+$) when one Mn is included. Furthermore, the changes observed in $Co_6Mn_2Ar^+$ relative to Co_7MnAr^+ are important in the intensities (the substitution of the second Mn atom reduces the overall intensity to the half) and in the frequencies, but it is worthless to propose any explanation for the latter without any theoretical support.

It is difficult to conclude anything robust just from the qualitative observations done above on Co_7^+ and Co_8^+-based clusters, and additional calculations are needed to elucidate the geometry of the clusters. In both clusters, the inclusion of one Mn reduces the intensity of the IR spectrum compared to the bare cluster, while the intensity changes between spectra of clusters containing one and two Mn atoms are appreciable only in Co_7MnAr^+ compared to $Co_6Mn_2Ar^+$. The vibrational structures of bare cobalt and bimetallic clusters with one Mn atom maintain some similarities that become unobservable when a second Mn atom is introduced. The important intensity decrease observed in all the spectra on bimetallic clusters upon inclusion of Mn could be related to a smaller transition dipole moment. In both cases the presence of one Mn in the cluster does not change substantially the vibrational structure, so the symmetry is not really broken until the second substitution happens.

Co_9^+-based clusters. There is an apparent negative signal in the Co_9Ar^+ spectrum between 130 and 160 cm^{-1} probably coming from the depletion of one Ar atom in $Co_9Ar_2^+$. The $Co_8MnAr_{1,2}^+$ spectra compared to $Co_9Ar_{1,2}^+$ show a shift to the blue (of about 20 cm^{-1}) in the frequencies above 200 cm^{-1} with almost no intensity changes. Contrary, the bands at low frequencies show an apparent small red-shift.

Nevertheless, the changes observed when one Mn atom is included are small when they are compared to those in the $Co_7Mn_2Ar^+_{1,2}$ spectra. One can conclude that the symmetry changes induced in the Co_9^+ cluster upon substitution of one Co atom by one Mn do not modify substantially neither the overall spectral intensity, nor the vibrational spectrum, but as for Co_7^+ and Co_8^+-based clusters, the changes observed through the inclusion of a second Mn atom are too big to propose any interpretation.

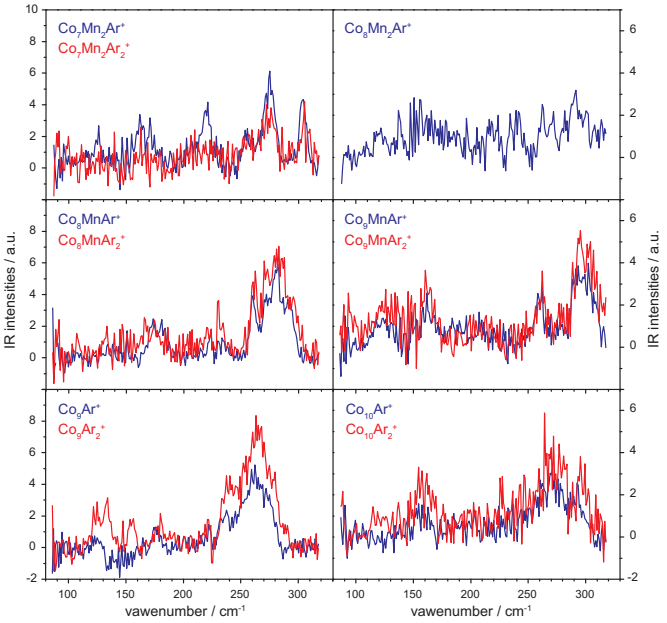

Figure 7.13: Comparison of the far-IR experimental measurements on the $Co_{n-m}Mn_mAr_x^+$ clusters with n=9 and 10.

From this point on, our spectra on the Co_n^+-based (n=10 to 14) bimetallic species are going to be discussed by comparison with the spectra on monometallic Co_n^+ clusters measured by Gruene[44] because, despite of the reasonable quality of our $Co_nAr_x^+$ (with n>10) spectra between 85 and 215 cm^{-1}, the spectra of Gruene cover a wider frequency range with a better signal to noise ratio.

Co_{10}^+-based clusters. Our $Co_{10}Ar^+$ spectrum reproduces the one of Gruene for frequencies below 200 cm^{-1}, but in our case the main feature

seems to be shifted to the red about 30 cm^{-1}. At frequencies above 200 cm^{-1}, $Co_{10}Ar^+$ shows three features: a shoulder at 235 cm^{-1} and two peaks at 265 and 290 cm^{-1}. The spectra of $Co_9MnAr_{1,2}^+$ include the features at 235 and 290 cm^{-1}, but the peak at 265 cm^{-1} is missed. Due to the limited signal to noise ratio, it is difficult to compare the spectra at low frequencies, but it its remarkable the nearly one-to-one correspondence of three maxima at 90, 120 and 160 cm^{-1} between our $Co_9MnAr_{1,2}^+$ spectra and the $Co_{10}Ar^+$ spectrum from Gruene (for the latter one must check the maxima on the grey points, because the blue line plotted as "three averaged-points" obscures them). Therefore, there are not substantial changes other than the missing peak at 265 cm^{-1}. This similarity between the $Co_{10}Ar^+$ and the $Co_9MnAr_{1,2}^+$ spectra disappears in the spectrum of $Co_8Mn_2Ar^+$.

We find again here difficulties to reach a firm conclusion from the experimental observations. Nevertheless, it is interesting to compare the spectra of Co_7^+ and Co_8^+-based clusters on one side and of Co_9^+ and Co_{10}^+-based clusters on the other, when the number of Mn atoms increases. The substitution of a Co by a Mn atom reduces in Co_7^+ and Co_8^+-based clusters the spectral intensity by half with minor frequency changes, but in Co_9^+ and Co_{10}^+-based clusters no major changes are found neither in the intensity nor in the frequencies. Furthermore, the substitution of a second Co by another Mn atom does affect the vibrational pattern of all of them strongly. The conclusion is that there may be an elementary geometrical unit that serves as a base from which Co_n^+-based clusters with n=7, 8, 9 and 10 are built. When the symmetry of this elementary unit is "destroyed" by several Co to Mn substitutions, the IR spectra show important changes. Such an elemental unit was proposed in several studies[315,336] as a (slightly distorted) tetragonal bipyramid and we proposed that the clusters Co_7^+ and larger may have structures based on this geometry. The new idea proposed here is that, also, the structure of Co_9^+ and Co_{10}^+-based clusters may be built based on a tetragonal bipyramid.

Co_{11}^+ and Co_{12}^+-based clusters. We observe in the frequency range below 200 cm^{-1} the same features in our spectra on $Co_{11}Ar_{1,2}^+$ and in the $Co_{11}Ar_2^+$ spectrum from Gruene[44], which are used in the discussion on the $Co_{10}MnAr^+$ spectrum since $Co_{10}MnAr_2^+$ is too noisy. At frequencies below

200 cm^{-1}, the bimetallic $Co_{10}MnAr^+$ cluster has a richer vibrational structure than the monometallic one and the bands at frequencies above 200 cm^{-1} seem to have a higher relative intensity in the monometallic cluster. To draw further conclusions, the quality of the spectra needs to be improved and/or theory needs to be consulted.

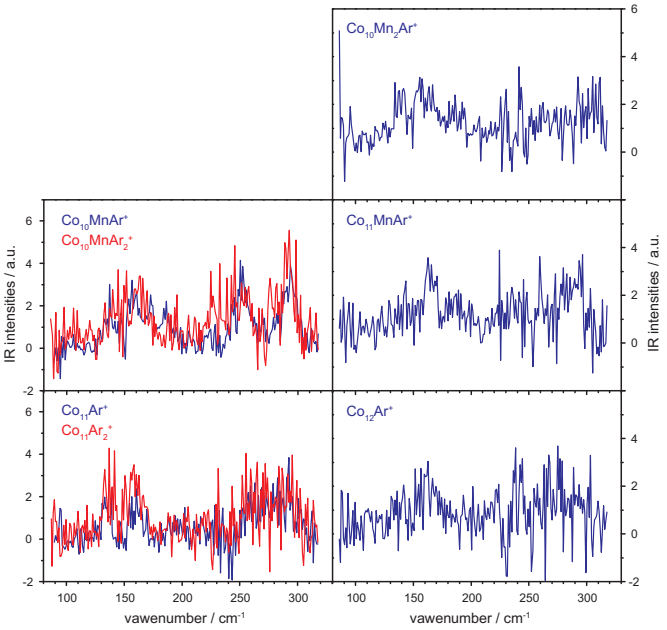

Figure 7.14: Comparison of the far-IR experimental measurements on the $Co_{n-m}Mn_mAr_x^+$ clusters with n=11 and 12.

Co_{13}^+ and Co_{14}^+-based clusters. The spectra of both groups of clusters show an increase in the intensity without addition of more vibrational substructure when one Co atom is substituted by one Mn atom. This effect is more pronounced in the $Co_{12}MnAr^+$ spectrum, which shows no shift in the vibrational pattern, while the $Co_{13}MnAr^+$ spectrum shows a blueshift of about 30 cm^{-1} compared to the spectrum of $Co_{14}Ar^+$. In the $Co_{11}Mn_2Ar^+$ spectrum, the single peak is broader and its maximum intensity is slightly lower than in the case of $Co_{12}MnAr^+$. This observation can be interpreted in the Co_{13}^+-based clusters as follows: the substitution of a first (and also a second) Co atom in the bare cluster could happen without significant de-

formations in its geometry. An important open question is the structure of the Co_{13}^+ cluster (fcc, hpc or icosahedral), but it is clear that the inclusion of manganese atoms enhances strongly the dipole transition moment of the cluster since the intensity clearly grows. These ideas can be applied to the Co_{14}^+ cluster considering that its structure is most likely based on the one of Co_{13}^+ and the observed effects can be minimized due to a general lower symmetry.

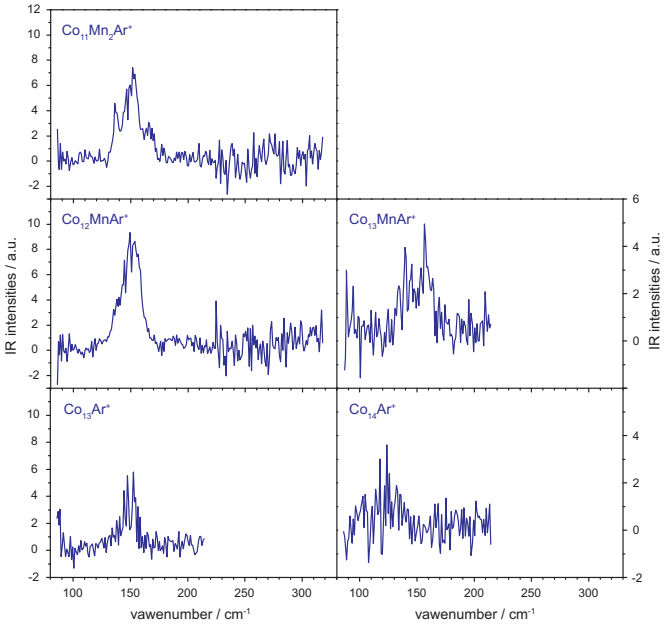

Figure 7.15: Comparison of the far-IR experimental measurements on the $Co_{n-m}Mn_mAr_x^+$ clusters with n=13 and 14.

7.5 Conclusion and outlook

This section contains the far IRMPD spectra measured on monometallic Co_n^+ clusters and bimetallic $Co_nMn_m^+$ clusters with Mn as dopant. As a first proof of the reliability of our measurements, our measured spectra on Co_n^+ (with n=4 to 8) were compared to those of Gehrke et al.[315]. They show a good agreement, except at low frequencies where new features appear in our work.

These differences are explained by either a different normalization procedure or by a higher FEL power in our case at these frequencies. In general, our measurements offer a more satisfactory agreement with the calculations of Gehrke et al.[315], but still several features remain unexplained. The newly measured $Co_3Ar_3^+$ spectrum is compared with our own DFT calculations showing a good agreement and serving as a benchmark for future calculations on these clusters. Monometallic Co_n^+ clusters (with n=9 to 15) were measured as well and they were qualitatively discussed in comparison with those collected in the PhD thesis of Gruene[44]. Despite the good quality of the Co_9^+ spectrum, our measured spectra on Co_{10}^+ to Co_{15}^+ only show a limited quality between 85 and 215 cm^{-1}, so further measurements are needed to complete them. Finally, the higher affinity of the smaller Co_n^+ clusters (with n≤5) towards Ar attachment has been observed and discussed through the measured mass spectra and the vibrational spectra.

No calculations were done, even for small sizes, on bimetallic $Co_nMn_m^+$ clusters due to the complexity of the systems and the possible correlations between a big number of unpaired 3d electrons, so all spectra were qualitatively discussed in terms of previous works. All Co_n^+-based clusters (with n≤5) show important changes upon a single Mn inclusion (Co_3^+ and Co_4^+-based clusters show a similar behavior since the totally symmetric mode becomes IR active upon such substitution, but no explanation was found for Co_5^+-based clusters). Co_6^+-based clusters are a special case since minor changes appear upon manganese doping. This is rationalized by considering Co_6^+ as a fundamental building block unit. Co_n^+-based clusters (with n>6) show again remarkable changes upon Mn inclusion, but smaller than those of n≤5. Finally, Co_{13}^+-based clusters constitute another special situation due to the big cross-section increase and simplicity in the vibrational $Co_{12}Mn^+$ spectrum. As for Co_6^+-based clusters, we identify here another basic building block on the bimetallic species, but precise calculations must be done to fully understand these systems.

Full IRMPD measurements on the cationic and neutral bimetallic clusters until n=20, both supported by powerful theoretical studies, must be done in

the future for a deeper understanding of their structures and their evolution with clusters size.

Chapter 8

IRMPD on cationic saturated Ru cluster carbonyls

8.1 Introduction

Ruthenium plays an important role in different catalytical process: ammonia synthesis at low temperatures[374,375], ammonia decomposition[376] and CO methanation reactions[377]. The Fischer-Tropsch process involves a dissociative CO adsorption on Ru, followed by a hydrogenation of the dissociated C and O to form CH_x intermediates (and furthermore long hydrocarbons) and H_2O[378]. The CO adsorption on Ru surfaces and its hydrogenation/dehydrogenation[379] or its reactivity to produce CO_2[380] have been intensively studied. Specifically, the structural and vibrational characterization of CO bound on Ru(001) surfaces via IR spectroscopy is the topic of several experimental studies[381–383] and, extended to other Ru crystalline structures, theoretical works[384–388].

A deeper understanding of these reaction mechanisms can be better achieved when focusing on small and medium size clusters. For this reason, CO adsorption on small ruthenium clusters in the gas phase was in the past treated by our group[389], which was triggered by multiple previous investigations about the structures of Ru cluster in the gas phase either experimentally[390–393] or theoretically[394–398]. The characterization of small ruthenium clusters has been linked, as well, to the study of the magnetic

properties of 4d Transition-Metals (T-M)[399,400], since it still constitutes a challenge for theoretical characterizations.

The characterization of CO adsorption on small transition metal clusters via (Far) IRMPD has been an important goal in the group of A. Fielicke that has given fruitful outputs[119,173,389,400,401]. The group V of T-M has shown to adsorb dissociatively CO with a transition to molecular CO adsorption in the group VI. Groups VII to XI show molecular adsorption of CO[402]. Among the molecularly adsorbed CO, the atop position (μ_1) is the most commonly observed, but also CO is adsorbed for some elements (preferentially 4d T-M) in bridge (μ_2) and hollow (μ_3) positions. For CO adsorbed on ruthenium it was observed, by comparison with former IR experiments on $RuCO^{\pm}$ in neon matrices[403], that cationic and anionic Ru_n clusters (n=4–19) bind the CO ligand mainly in atop positions and to a smaller extent in bridge positions[389].

Cationic saturated ruthenium cluster carbonyls are studied here. This was triggered by previous experiments of ruthenium clusters on oxide supports[404], where the former show partial positive charge[405]. The structures of some neutral ruthenium carbonyls in the condensed phase have been known for long with the remarkable examples of $Ru(CO)_5$ and $Ru_3(CO)_{12}$[406]. However, bigger neutral complexes as $Ru_4(CO)_{14}$, $Ru_5(CO)_{16}$ and $Ru_6(CO)_{18}$ have not yet been synthesized[407]. In the gas phase, the molecular structure of $Ru_2(CO)_9$ has been theoretically investigated[408], but the molecular $Ru_3(CO)_{12}$ has been by far the most studied complex with studies focused in its progressive CO de-ligation[409], its transient state upon photon excitation[410–413] or its role as catalyst[414]. So far, no study has been focused on the structural characterization of the complete set of saturated ruthenium cluster carbonyls, $Ru_n(CO)_m$, with $n \leq 20$. In this context, it is worth to mention the works of Critchley et al.[415] and Scott McIndoe[416,417] on the laser synthesis and characterization of some of these cationic and anionic complexes.

A previous study on cationic saturated rhodium cluster carbonyls via IRMPD was done by Fielicke et al.[418]. There, the structural changes induced in the complexes by the removal of an electron from the "originally" neutral metal cores were deduced from the combination of DFT calculations and the IRMPD results. The structural information via DFT on the cationic saturated

ruthenium cluster carbonyls that are studied in this chapter appeared firstly in a work by Lang et al.[407], who subsequently used it in a study on gas phase Ru_n^+ (n=4–6) clusters to elucidate their high selectivity and activity towards CO[405]. However, this information was not further experimentally corroborated and, therefore, this chapter contains the IRMPD spectra on the cationic saturated ruthenium cluster carbonyls that were measured at the FHI-FEL and supported by our DFT calculations (Turbomole 6.4 package[419]).

8.2 Mass distribution

The cationic saturated Ru cluster carbonyls are produced by laser ablation of a Ru metal rod and the simultaneous addition of CO through the reaction channel within the source chamber. The products of this reaction are mass analyzed. Further details on the experiment operation appear in the description of the setup in subsection 2.2.5. We consider that the saturation

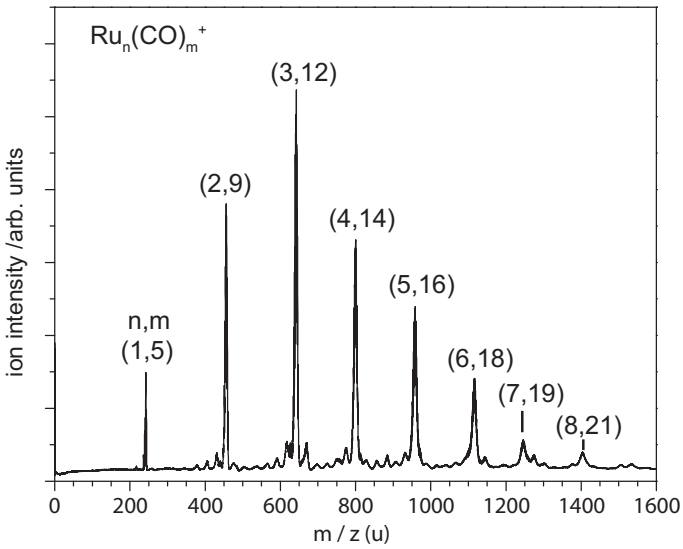

Figure 8.1: Mass spectrum of the cationic saturated Ru cluster carbonyls. The size of the cationic metal cluster and the number of carbonyls for each one is indicated in the figure by the couple of numbers (n,m). The saturation was obtained by increasing the pressure in the valve that introduces CO until a nearly-steady mass spectrum was observed. Many minor peaks appear in the spectrum resulting from less stable $Ru_n(CO)_m^+$ complexes.

Ru_n^+ clusters with CO has been obtained when, by increasing pressure in the reaction channel, a stable distribution in the mass spectrum is observed. The mass distribution of cationic saturated Ru cluster carbonyls is shown in Figure 8.1 and the obtained complexes are: $Ru(CO)_5^+$, $Ru_2(CO)_9^+$, $Ru_3(CO)_{12}^+$, $Ru_4(CO)_{14}^+$, $Ru_5(CO)_{16}^+$, $Ru_6(CO)_{18}^+$, $Ru_7(CO)_{19}^+$ and $Ru_8(CO)_{21}^+$. The last two complexes are identified for the first time here. The bigger intensity of all these complexes suggests their particularly high stability compared to several less intense peaks that appear in the spectrum with a different number of carbonyls (presumably less stable saturated species) and it will be discussed later in terms of the effective atomic number (EAN) rule[420,421]. Each peak in Figure 8.1 is the envelope of a complex mass distribution that results from the isotope distributions of Ru and C. This is shown in Figure 8.2, where

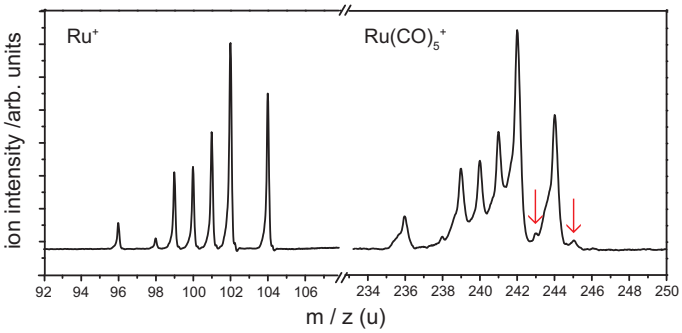

Figure 8.2: Mass spectra of the cationic Ru atom (left) and saturated with CO (right). This plot shows the utilization of Ru and C in their natural isotopic distributions. The pattern observed in the left side corresponds to the stable isotope distribution of Ru: ^{96}Ru (5.54%), ^{98}Ru (1.87 %), ^{99}Ru (12.76 %), ^{100}Ru (12.60 %), ^{101}Ru (17.06 %), ^{102}Ru (31.55 %) and ^{104}Ru (18.62 %). On the right side the saturated complexes respond to the formula $Ru(CO)_5^+$ and the mass distribution due to Ru is very similar to the left plot. The two new peaks at 243 and 245 u marked with red arrows come from the isotope distribution of C (^{12}C (98.9 %), ^{13}C (1.1 %)) and are understood as the substitution of one ^{12}C by one ^{13}C in the $Ru(CO)_5^+$ complexes with ^{102}Ru and ^{104}Ru.

the experimental mass spectra of Ru^+ and its saturated complex with CO, $Ru(CO)_5^+$, are shown. On the right side, the isotope distribution of ruthenium is reproduced (check the caption of Figure 8.2). On the left side, the two peaks marked by red arrows that appear at 241 and 245 u are the result of the ^{13}C isotope. They are respectively linked to the $Ru(CO)_5^+$ complexes at

240 and 244 u because the small natural abundance (1.1 %) of the ^{13}C isotope makes possible that among the five carbonyls bound to Ru^+ only one is ^{13}C. As well, the relative abundance of the Ru isotopes with 102 and 104 u. is big enough and the noise in the mass spectrum low enough not to obscure them.

8.3 IR spectra and structures

Figures 8.3 and 8.4 show the DFT calculated structures for the CO saturated complexes with 1–6 Ru atoms and their respective calculated vibrational spectra. All DFT theoretical calculations were carried out using the hybrid functional PBE0; the def2-TZVP basis set was used on the smaller $Ru_n(CO)_m^+$ complexes (for $n \leq 4$) and the def-SVP basis set for the bigger ones ($n > 4$). The calculated structures for $Ru_4(CO)_{14}^+$, $Ru_5(CO)_{16}^+$, $Ru_6(CO)_{18}^+$ agree with those in the work of Lang et al.[407]. The calculated Ru-Ru distances in the saturated cluster carbonyls range from 2.88 to 2.82 Å in Ru_3^+, between 2.83 and 2.78 Å in Ru_4^+, from 3.01 to 2.70 Å in Ru_5^+ and between 2.85 and 2.70 Å in Ru_6^+. The calculated Ru-Ru bond in Ru_2^+ measures 2.93 Å. The color code used in Figures 8.3 to specify the differently bound carbonyl groups is dark grey-red for atop bound ligands, orange-light grey for semi-bridging carbonyl groups and yellow-white for symmetrically bridging carbonyl ligands. The quantitative criterion employed to distinguish symmetrically bridging from semi-bridging ligands is to measure for the former a difference smaller than 0.1 Å between both M-C bonds. The C-O bond lengths in the complexes increase gradually in average from 1.12 Å in $Ru(CO)_5^+$ to 1.142 Å in $Ru_6(CO)_{18}^+$. This trend can be understood as a slight weaking of the C-O bond because the average π-backdonation done to each carbonyl group coming from the metal core increases with the size of the cluster. Precisely, the ratio "Number of CO/Number of Ru" decreases monotonically from $Ru(CO)_5^+$ to $Ru_6(CO)_{18}^+$ with the values 5, 4.5, 4, 3.5, 3.2 and 3.

The measured vibrational spectra on the saturated cluster carbonyls with 1–6 Ru atoms are shown in Figure 8.4. Both figures are divided into two regions, the M-C stretching region between 300 and 650 cm^{-1} and the C-O stretching one between 1900 and 2200 cm^{-1}. The M-C stretching region of

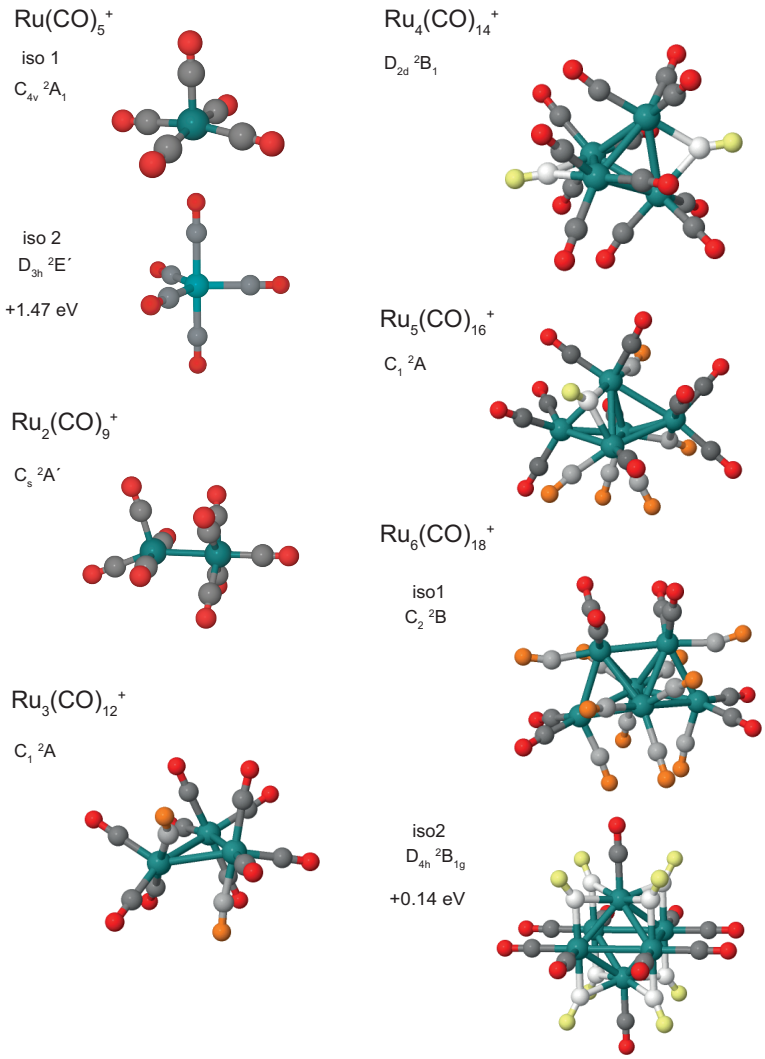

Figure 8.3: Calculated structures of the lowest energy isomers for $Ru(CO)_5^+$, $Ru_2(CO)_9^+$, $Ru_3(CO)_{12}^+$, $Ru_4(CO)_{14}^+$, $Ru_5(CO)_{16}^+$ and $Ru_6(CO)_{18}^+$. Calculated higher energy isomers for $Ru(CO)_5^+$ and $Ru_6(CO)_{18}^+$ are also included. Atop bound carbonyl groups are colored in red (O) and deep grey (C). Semi-bridging carbonyl groups are colored in orange (O) and light grey (C). Symmetrically bridging carbonyl groups are colored in yellow (O) and white (C).

$Ru_5(CO)_{16}^+$ and $Ru_6(CO)_{18}^+$ includes as well the vibrational spectra (light grey) that were measured with double IR power with the aim of having a better observation over these frequencies. The C-O stretching region is subdivided

in red, green and blue color-coded areas to distinguish the bands assigned respectively to the symmetrically bridging, semi-bridging and atop bound carbonyl groups. The calculated C-O stretching frequencies that are plotted in the simulated spectra of Figure 8.4 are compiled in detail in the Appendix 8.A. We have only included there the C-O frequencies of the calculated lowest energy isomers and identified them by the same color code as in Figure 8.4.

The intensity of the calculated and experimental vibrational spectra in the C-O stretching region is attenuated by a factor of 10 in order to have a better general overview of the whole frequency spectral range. Besides the quality of the experimental data, they are in very good agreement with the calculated frequencies in both spectral regions. Such agreement allows us to discard directly in $Ru(CO)_5^+$ contributions from the calculated higher energy isomer. In $Ru_6(CO)_{18}^+$, the overall agreement between the experimental spectrum and the contributions from the lowest energy isomer, notably the experimental absence of a band at 1950 cm^{-1} coming from the predicted higher energy isomer, concludes a lowest energy $Ru_6(CO)_{18}^+$ isomer that is not based on an octahedral metal core (see Figure 8.4). From the agreements in $Ru(CO)_5^+$ and in $Ru_2(CO)_9^+$, it can be assumed that all carbonyl ligands are atop bound. The band at ≈2130 cm^{-1} in the spectrum of $Ru(CO)_5^+$ is assigned to the a_1 mode, stretching of the top carbonyl group calculated at 2123 cm^{-1}, and to the e mode involving the four "in plane" carbonyls calculated at 2124 cm^{-1}. The dip with minimum at ≈2070 cm^{-1} is assigned to the fragmentation of $Ru_2(CO)_9^+$ into $Ru(CO)_5^+$ and $Ru(CO)_4$ by breaking the Ru-Ru bond. The low symmetry of the calculated ground state for $Ru_2(CO)_9^+$ hinders a clear assignment of the vibrational modes.

The low intensity peak at ≈2000 cm^{-1} in $Ru_3(CO)_{12}^+$ is assigned to the calculated stretching vibrations of the two semi-bridging carbonyl groups at 2001 and 2029 cm^{-1}. Consequently, the remaining ten carbonyl ligands are atop bound. In $Ru_4(CO)_{14}^+$, the band at ≈1948 cm^{-1} includes the b_2 mode of the two symmetrically bridging carbonyl ligands calculated at 1952 cm^{-1} and the bands at higher energies are assigned to modes that involve the remaining twelve atop bound carbonyl ligands. No semi-bridging carbonyl groups are identified in $Ru_4(CO)_{14}^+$. Observing the calculated lowest energy structure

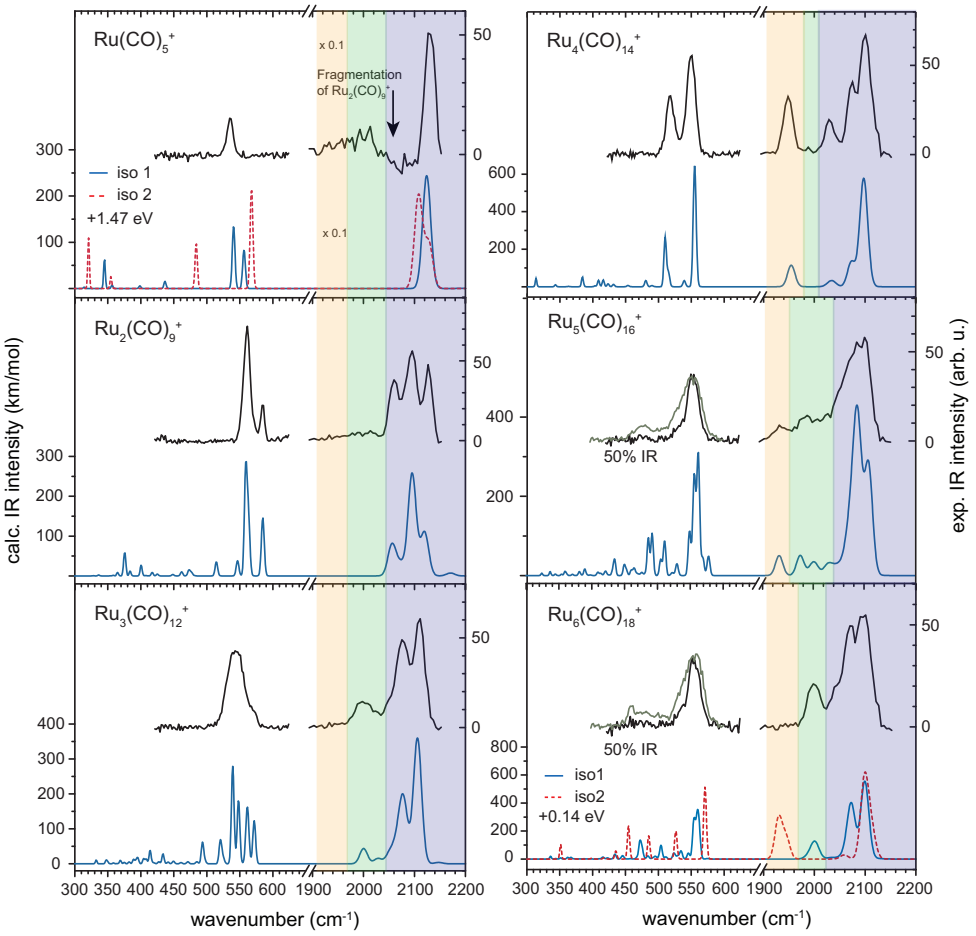

Figure 8.4: Experimental measurements (black and grey) in the far-IR (M-C bonds)/IR (C-O bonds) on the complexes $Ru(CO)_5^+$, $Ru_2(CO)_9^+$, $Ru_3(CO)_{12}^+$, $Ru_4(CO)_{14}^+$, $Ru_5(CO)_{16}^+$, $Ru_6(CO)_{18}^+$ and calculated vibrational spectra for the lowest energy isomers, and a higher energy one for $Ru(CO)_5^+$ and $Ru_6(CO)_{18}^+$ (red dotted). The calculations on the four smallest complexes were performed with def2-TZVP/PBE0 and the frequency scaling factors are 0.933/0.955. The calculations on $Ru_5(CO)_{16}^+$, $Ru_6(CO)_{18}^+$ were done with def-SVP/PBE0 with scaling factors 0.928/0.944. The spectral region between 1900 and 2200 cm^{-1} is subdivided light red (modes assigned to symmetrically bridging carbonyl ligands), light green (modes assigned to semi-bridging carbonyl ligands) and blue (atop bound ligands).

for $Ru_5(CO)_{16}^+$, only one carbonyl group is symmetrically bridging and its fingerprint in the spectrum is the feature with maximum at $\approx$1932 cm^{-1}. All those weak bands localized between 1950 and 2040 cm^{-1} are assigned to the

six carbonyl ligands that are identified in $Ru_5(CO)_{16}^+$ as semi-bridging and, therefore, the remaining nine carbonyl ligands are atop bound. The spectrum of $Ru_6(CO)_{18}^+$ shows a band at ≈2000 cm^{-1} that includes the six modes (see Appendix 8.A) assigned to the ten semi-bridging carbonyl groups. Among these ten carbonyl ligands, one can observe that the four at the bottom of the molecule (Figure 8.3) are almost atop bound, but a careful observation of the aforementioned vibrational modes clears up any possible doubts, remaining eight atop bound carbonyl ligands in $Ru_6(CO)_{18}^+$.

Once the predicted geometrical structures of the cationic Ru cluster carbonyls have been corroborated by the IR spectra, it is interesting to gain insights into their bonding by comparing them with those of the neutral Ru cluster carbonyls. All the carbonyl groups in the calculated lowest energy $Ru_2(CO)_9^+$ isomer are atop bound. A higher energy $Ru_2(CO)_9^+$ isomer was calculated with three bridging carbonyl groups (the same as the lowest energy $Fe_2(CO)_9$ isomer[422]) and a much shorter Ru-Ru bond distance than the lowest energy one. In addition, the lowest energy structures of $Ru_2(CO)_9$ and the isoelectronic $Os_2(CO)_9$[422] include one bridging carbonyl ligand. A former work on cationic Rh cluster carbonyls[418] manifests a similar phenomenon: the lowest energy $Rh_2(CO)_8$ isomer shows two bridging carbonyl groups, while all the carbonyl ligands in the lowest energy $Rh_2(CO)_8^+$ isomer are atop bound. The cationic isomer with the same structure as the lowest energy neutral one is 0.65 eV above the aforementioned lowest energy $Rh_2(CO)_8^+$ isomer. Swart et al.[418] calculate a bonding HOMO with respect to the Rh-ν_2-CO bonds that reduces its electronic population upon ionization and undergoes a charge induced structural rearrangement. The rearrangement lengthens the Rh-Rh distance and "destroys" the bridging bonds. This explanation can be satisfactorily extended to our case.

A higher energy isomer was also calculated for $Ru_3(CO)_{12}^+$. It was identified as a transition state with the same geometry (D_{3h} symmetry) as the lowest energy $Ru_3(CO)_{12}$ isomer (and the isoelectronic $Os_3(CO)_{12}$[422]) and with slightly longer Ru-Ru bonds than the calculated lowest energy cationic isomer. Based on the offered explanation in the former paragraph, we consider that the ionization of the lowest energy $Ru_3(CO)_{12}$ isomer removes an electron

from an antibonding HOMO that shortens the Ru-Ru distances and forces the turning motion of the carbonyl groups around the Ru atoms. Due to the symmetry reduction in the lowest energy $Ru_3(CO)_{12}^+$ isomer, we have to include as well the possibility of a JT effect. Finally, the removal of an electron from the lowest energy $Ru(CO)_5$ isomer results in a higher energy cationic isomer with D_{3h} symmetry whose lowest energy structure has C_{4v} symmetry (see Figure 8.3). As a previous study remarked [423,424], the square pyramidal C_{4v} structure of $Ru(CO)_5^+$ is also characteristic of the isoelectronic $Mn(CO)_5$.

8.4 Influence of the 18-electron rule on the structures of carbonyl clusters

The structure of metallorganic complexes one often tries to understand and to predict via semiempirical counting rules that rationalize the number of valence electrons which participate in the bonding. The 18-electron rule is the fundamental one. In order to reach the electronic configuration of a noble gas, the sum of the valence electrons belonging to a metal center and its associated ligands is 18. An extension of this rule to complexes where each metal center does not fulfill the 18-electron rule individually, but all the metal centers do if they are taken in average, is called the EAN rule [421]. Nevertheless, the number of skeletal M-M edges predicted by the EAN rule [421] tends to be underestimated because such rule is based on the assumption that all the metal-metal interactions consist of localized two center/two electron (2c/2e) bonds [420].

These limitations triggered the development of Wade's rules [426], which offer a more realistic prediction of the geometries of the skeletal cluster centers. Originally developed to understand the structures of boranes and carboranes, these rules are summarized, according to Dyson et al. [420], as:

- An n vertexed “closo” cluster is held together by n+1 bonding electron pairs.

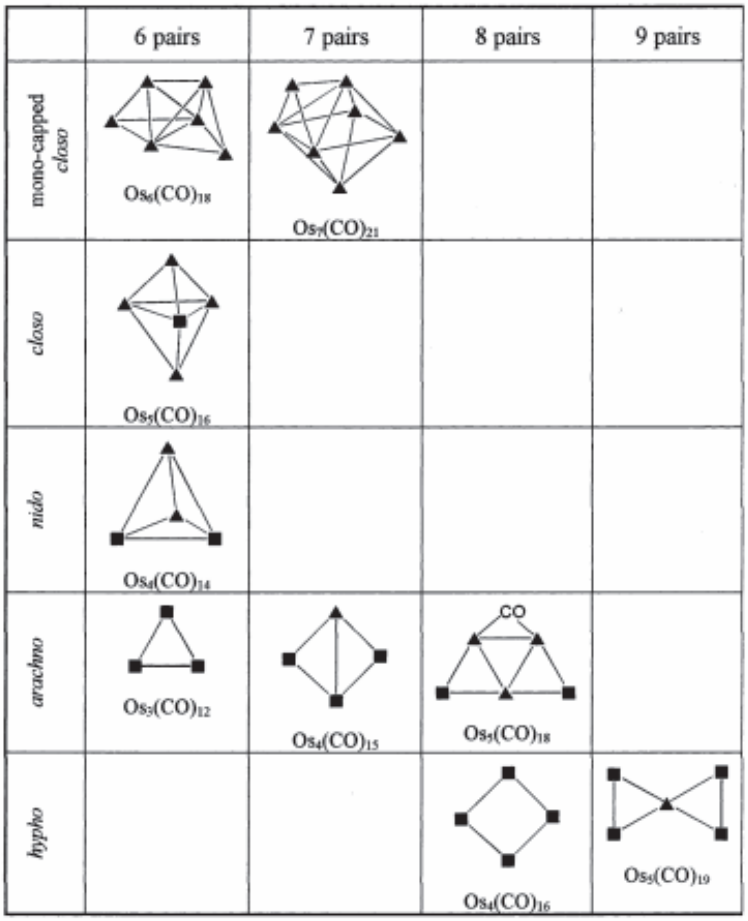

Figure 8.5: Scheme taken from the work of Hughes et al.[425] where it is shown the relation established (for the transition metal clusters in the scope of organometallic chemistry) between the nuclearity number, n, the number of the skeletal electron pairs, S, the geometric structure of the skeletal metal center and its denomination by the Wade's rules. In the scheme, the application of Wade's rules to transition metal clusters introduces the PSPET model.

- An n vertexed “nido” cluster is held together by n+2 bonding electron pairs.
- An n vertexed “arachno” cluster is held together by n+3 bonding electron pairs.

- An n vertexed “hypho” cluster is held together by n+4 bonding electron pairs.

where “closo”, “nido”, “arachno” and “hypho” are the names that receive the skeletal cluster structures (in our study the transition metal cluster in the saturated cluster carbonyl) depending on which of the aforementioned counting rules they fulfill.

Wade's rules in turn are extended to transition metal clusters by the inclusion of the “isolobal principle”. This principle considers that: two fragments are isolobal if the number, symmetry properties, approximate energy and shape of their frontier orbitals (available orbitals for cluster bonding) as well as the number of electrons occupying them are similar[420,427]. In our case, the similar bonding characteristics that have CH_2 and the $Ru(CO)_4$ unit allow through the “isolobal principle” the application of the Wade's rules[426] to transition metal clusters and, to a further extent, to introduce the polyhedral skeletal electron pair theory (PSEPT).

In the PSEPT theory, the number of skeletal electron pairs, S, available for cluster bonding in a transition metal cluster is given by[420]:

$$S = \frac{Total valence electrons - 12n}{2} \tag{8.1}$$

where n is the number of skeletal metal atoms. The number 12 appears by assuming that among the 9 atomic orbitals available in each skeletal atom, three are left for framework bonding while the other six are used in metal-ligand bonding or in the occupation of non-bonding electrons.

The visualization of the relation established for the transition metal clusters in the organometallic complexes between the nuclearity number, n, the number of the skeletal electron pairs, S, the name that it receives (“closo”, etc.) and its geometric structure is summarized in Figure 8.5. Moreover, it appears in Figure 8.5 a metal cluster with a structure named as “mono-capped closo”. This denomination as well as the terms “bicapped polyhedron”, “tricapped polyhedron”, etc. (that will appear later) are all derived from the “Capping Principle”, which is applied when the PSEPT theory is used for clusters with nuclearity higher than 6. This principle states[420]: a capped

polyhedral cluster has the same number of electron pairs for framework bonding as the uncapped cluster. In the aggregation process of a metal cluster this implies the extension of the Wade's naming rules in the following manner:

- A monocapped polyhedron with n skeletal atoms has n electron pairs available for framework bonding.
- A bicapped polyhedron with n skeletal atoms has n-1 electron pairs available for framework bonding, and so on...

The content of Figure 8.5 (first column) is explained in Table 8.1 to understand clearly how the former theoretical introduction has been used in its elaboration. Considering that the electron configuration atomic osmium is [Xe] $4f^{14}5d^{6}6s^{2}$, the application of equation 8.1 for $Os_3(CO)_{12}$, $Os_4(CO)_{14}$, $Os_5(CO)_{16}$, $Os_6(CO)_{18}$, $Os_7(CO)_{21}$ and $Os_8(CO)_{23}$ gives well known skeletal structures[422]:

$\mathbf{Os_n(CO)_m}$	**Valence e⁻s** $(\mathbf{n \cdot 8}) + (\mathbf{m \cdot 2})$	**S**	**Structure**
$Os_3(CO)_{12}$	48	6=n+3	arachno
$Os_4(CO)_{14}$	60	6=n+2	nido
$Os_5(CO)_{16}$	72	6=n+1	closo
$Os_6(CO)_{18}$	84	6=n	mono-capped closo
$Os_7(CO)_{21}$	98	7=n	mono-capped closo
$Os_8(CO)_{23}$	110	7=n-1	bi-capped closo

Table 8.1: Numerical explanation of some of the structures predicted in Figure 8.5. In the table n is the number of transition metal nuclei, m is the number of ligands (each CO contributes with 2 electrons) and S is the number of skeletal electron pairs.

Applying this model to our complexes, we observe that in the former work on $Ru_4(CO)_{14}^{+}$, $Ru_5(CO)_{16}^{+}$ and $Ru_6(CO)_{18}^{+}$ by Lang et al.[407] the cationic nature of the cluster is neglected when using Wade's rules. Nevertheless, it is going to be considered in our case. Since each Ru atom contributes with 8 electrons, each CO with 2 and all complexes are singly charged cations, the application of this formula to the bigger clusters ($Ru_3(CO)_{12}^{+}$, $Ru_4(CO)_{14}^{+}$, $Ru_5(CO)_{16}^{+}$ and $Ru_6(CO)_{18}^{+}$) gives S=5.5 for all of them as it is shown in Table 8.2. The uncommon half-integer value obtained for S is the result

of considering the positive charge of the complexes. This means that the predicted structures for each of the Ru_n^+ clusters that conform the complexes in the PSEPT model can be two: nido or arachno for Ru_3^+, closo or nido for Ru_4^+, mono-capped closo or closo for Ru_5^+ and bi-capped closo or mono-capped closo for Ru_6^+. The comparison of these predictions with our DFT calculated structures reveals that in all the cases the second option (in bold, in Table 8.2) is the correct one, i.e. S=6: arachno for Ru_3^+, nido for Ru_4^+, closo for Ru_5^+ and mono-capped closo for Ru_6^+. Consequently, a half-filled orbital counts like a full one within the PSEPT theory and, therefore, the essential element in the counting is the number of available orbitals occupied by electrons, regardless of their half or full occupation, as it was considered by Lang et al.[407].

$\mathbf{Ru_n(CO)_m^+}$	**Valence e⁻s** $(\mathbf{n \cdot 8}) + (\mathbf{m \cdot 2})$	**S**	**Possible structures**
$Ru_3(CO)_{12}^+$	47	5.5	n+2 (nido)
			$\mathbf{n+3}$ **(arachno)**
$Ru_4(CO)_{14}^+$	59	5.5	n+1 (closo)
			$\mathbf{n+2}$ **(nido)**
$Ru_5(CO)_{16}^+$	71	5.5	n (mono-capped closo)
			$\mathbf{n+1}$ **(closo)**
$Ru_6(CO)_{18}^+$	83	5.5	n-1 (bi-capped closo)
			$\mathbf{n}$ **(mono − capped closo)**
$Ru_7(CO)_{19}^+$	93	4.5	n-3 (tetra-capped closo)
			$\mathbf{n-2}$ **(tri − capped closo)**
$Ru_8(CO)_{21}^+$	105	4.5	n-4 (penta-capped closo)
			$\mathbf{n-3}$ **(tetra − capped closo)**

Table 8.2: Predicted structures by the PSEPT theory for our cationic Ru cluster carbonyls. In the table n is the number of transition metal nuclei, m is the number of ligands, where each CO contributes with 2 electrons, and S is the number of skeletal electron pairs. In bold are the correctly predicted structures. More details in the text.

Therefore, the application of the PSEPT model neglecting the cationic nature of the complexes can be used to, somehow, predict the cluster structure of $Ru_7(CO)_{19}^+$ and $Ru_8(CO)_{21}^+$. The value of S obtained in both cases is 5, which predicts for $Ru_7(CO)_{19}^+$ a tri-capped polyhedron and for $Ru_8(CO)_{21}^+$ a tetra-capped polyhedron[420,425]. Both predictions are seemingly in disagreement with the conclusions of the work of Kerpal et al.[393]. There, the assigned

structures to Ru_7^+ and to Ru_8^+ are based on a cubic motif and those that can resemble to what is proposed here lie at much higher energies. However, there is not such disagreement because Kerpal et al. [393] solely determine the structures of bare Ru_n^+ clusters and, therefore, the PSEPT considerations cannot be transposed to their investigation. IR measurements on $Ru_7(CO)_{19}^+$, $Ru_8(CO)_{21}^+$ and other metalorganic compounds that theoretically result in huge conformational spaces could be an interesting benchmark to trigger new calculations that could find with more reliability their global minimum structures.

8.5 Conclusion

The IR spectra of a complete series of cationic Ru cluster carbonyls have been measured and their geometrical structures (until n=6) have been characterized. The successful assignment of the IR spectra has allowed to fully identify the binding positions (symmetrically bridging, semi-bridging and atop bound) of the carbonyl ligands in each cationic cluster carbonyl. These structures have been correctly predicted by the semiempirical PSEPT model and, in addition, it has been shown that the essential element in the counting is the number of available orbitals occupied by electrons, regardless if they are half or fully occupied. As well, some predictions have been done on the possible structural arrangements of the skeletal transition metal clusters in $Ru_7(CO)_{19}^+$ and $Ru_8(CO)_{21}^+$ that can serve as benchmark for future studies.

8.A Complementary information

$Ru(CO)_5^+$ ($C_{4v}/^2A_1$) [C-O vibrational modes] ALL IR ACTIVE

Symmetry	Calc. freq. (x 0.955) (cm^{-1})	IR Intensity (km/mol)
a_1	2122.6	475.1
e	2124.3	987.9

$Ru_2(CO)_9^+$ ($C_s/^2A'$) [C-O vibrational modes] ALL IR ACTIVE

Symmetry	Calc. freq. (x 0.955) (cm^{-1})	IR Intensity (km/mol)
a"	2054.2	490.3
a'	2059.0	350.1
a'	2073.8	273.5
a'	2094.4	1189.9
a"	2096.3	1399.0
a'	2109.8	15.6
a"	2119.9	1083.5
a'	2170.8	72.8
a'	2109.8	15.6

$Ru_3(CO)_{12}^+$ ($C_1/^2A$) [C-O vibrational modes] ALL IR ACTIVE

Symmetry	Calc. freq. (x 0.955) (cm^{-1})	IR Intensity (km/mol)
a	2001.2	431.3
a	2029.2	149.6
a	2044.9	24.8
a	2052.5	279.8
a	2064.4	414.1
a	2072.4	372.6
a	2076.6	255.5
a	2078.1	1168.9
a	2085.7	293.2
a	2105.1	1763.8
a	2106.8	1850.8
a	2147.6	38.7

$Ru_4(CO)_{14}^+$ ($C_{2d}/^2B_1$) [C-O vibrational modes]

Symmetry	Calc. freq. (x 0.955) (cm^{-1})	IR Intensity (km/mol)	IR Active
a_1	1952.3	0	NO
b_2	1954.5	1147.3	YES
e	2029.5	63.4	YES
a_1	2034.0	0	NO
b_2	2036.4	234.6	YES
a_2	2060.6	0	NO
b_1	2066.9	0	NO
e	2073.3	664.0	YES
b_2	2096.6	1875.2	YES
e	2098.0	1957.3	YES
a_1	2134.6	0	NO

$Ru_5(CO)_{16}^+$ ($C_1/^2A$) [C-O vibrational modes] ALL IR ACTIVE

Symmetry	Calc. freq. (x 0.944) (cm^{-1})	IR Intensity (km/mol)
a	1932.4	317.5
a	1973.9	396.6
a	1996.6	89.6
a	2005.1	246.6
a	2026.8	55.1
a	2036.2	145.0
a	2041.9	86.5
a	2050.4	105.2
a	2055.1	136.3
a	2066.4	618.8
a	2068.3	17.8
a	2077.7	948.7
a	2086.2	1743.9
a	2090.0	1321.6
a	2108.9	2187.9
a	2132.5	10.7

$Ru_6(CO)_{18}^+$ ($C_2/^2B$) [C-O vibrational modes] ALL IR ACTIVE

Symmetry	Calc. freq. (x 0.944) (cm^{-1})	IR Intensity (km/mol)
a	1986.5	67.17
a	1987.1	115.6
a	1997.9	682.8
a	2000.8	14.1
a	2003.2	546.9
a	2008.1	124.5
a	2032.6	95.7
a	2036.7	0.3
a	2039.1	0.3
a	2046.8	61.5
a	2057.2	131.7
a	2060.0	98.2
a	2066.4	513.0
a	2072.2	422.3
a	2073.3	3192.9
a	2098.4	2640.7
a	2100.3	2946.1
a	2127.9	29.8

Chapter 9

Summary

The research presented in this thesis has pursued the goal of obtaining new pieces of information on the puzzling understanding of chemical bonding within transition metal clusters. In addition, the nature of the interaction with ligands adsorbed on their surface has been further characterized. Anion photoelectron spectroscopy via velocity map imaging has provided insights into the vibronic structures and the photoelectron angular distributions of Pt_3^- and TaN^- through which their bonding characteristics were in detail deduced. In a similar vein, the vibrational spectra of $CoAr_n^+$ (n=3 to 6), saturated cationic Ru cluster carbonyls and $Co_{n-m}Mn_mAr_x^+$ with a great variety of stoichiometries were obtained via (far-)infrared multiple photon dissociation spectroscopy. In both cases, the combination of DFT calculations with the experimental results was crucial for the conclusions obtained on the chemical bonding in these systems.

In this thesis, the studied clusters and cluster complexes are based on the transition metals Pt, Ta, Co, Mn and Ru. The clearly different core and valence electronic structures of these metals and, therefore, their distinct physicochemical properties make it challenging to discuss all the relevant aspects studied under a single conceptual framework. It appears therefore more appropriate to give an individual summary and outlook for each subject.

Pt_3^-

For the anionic platinum trimer, Pt_3^-, high resolution photoelectron spectra in the range of valence shell excitations illustrate the huge complexity that the electronic structure of a very small transition metal cluster with open d-shells can reach. Assignment of the photoelectron spectra has been achieved with the fundamental support of DFT calculations that were performed by Julius Jellinek and Aslihan Sumer with a remarkable very good agreement for those transitions involving excited electronic states in anion and neutral trimer. It reveals an opposite energy ordering of the two possible isomers, linear and triangular, in the anion and neutral with the more stable structures in the anion corresponding to the linear isomer while, in the neutral, they have triangular geometry. The selective detection of slow photoelectrons allows in some bands the resolution of the vibronic substructure. In these cases, Franck-Condon simulations for the calculated electronic transitions suggested the presence of pseudo Jahn-Teller, Jahn-Teller and Renner-Teller effects.

The still open questions concerning the vibronic structure of the cluster include a detailed study of the adiabatic potential surfaces for each of the calculated electronic states to fully characterize the proposed avoided intercrossing between the anionic $^4\Sigma_g^-$ and $^4\Delta_g$ states as well as the indicated pseudo Jahn-Teller, Jahn-Teller and Renner-Teller effects. This might further gain in complexity considering the importance of relativistic effects in the late transition metals and their inclusion in DFT calculations for neutral trimers of Pt, which in total have 30 valence electrons. In addition, the production of the clusters via a non-isotopically pure Pt target may call into question some of the interpretations and raises the question of isotope shifts in the photoelectron spectra.

The photoelectron angular distributions of some of the assigned electronic transitions have been experimentally characterized as a function of the photoelectron kinetic energy. These photoelectron angular distributions can be rationalized using quantitative and qualitative models for the anisotropy parameter β_2 and by spatial visualization of calculated Hartree-Fock molecular orbitals within the trimer. The success in the β_2 modelling gives insights into

the chemical bonding in terms of the Hartree-Fock molecular orbitals and corroborates further the assignment of the photoelectron spectrum. Photoelectron angular distributions have been discussed in two groups according to the geometry of the anionic electronic states from which they occur, i.e., $^2A_2'$ with a triangular geometry and $^4\Sigma_g^-$ and $^4\Delta_g$ with a linear one.

The photoelectron angular distributions of the $^2A_2' \rightarrow {}^3A_2''$ transition have been modelled with the Wigner-Bethe-Cooper-Zare approximation with a satisfactory agreement for kinetic energies below 0.7 eV. This constitutes a success of the "central atom approximation" for molecular orbitals with very complex geometrical structures that result from the hybridization of atomic d-orbitals and are characteristic of transition metals. The unexplained photoelectron angular distributions of the $^2A_2' \rightarrow {}^3A_2''$ transition for kinetic energies above 0.7 eV show β_2 values that monotonically increase until a maximum of $\approx$1.5. They provide a benchmark for future improvements in Sanov's model with regard to physical descriptions of the photoelectron wavefunction in molecular photodetachment processes that are beyond the very low KE approximation. In addition, the deviations observed at low KEs in the PADs of the $^2A_2' \rightarrow {}^3A_2$ transition might be, in comparison with those of $^2A_2' \rightarrow {}^3A_2''$, an experimental contribution to characterize the influence that vibronic effects can have on photoelectron angular distributions.

The photoelectron angular distributions of the transition from the first excited anionic state, $^4\Delta_g$, show footprints of electronic correlation effects within the trimer that are evidenced in the photodetachment process. This agrees with the previous assignment of the band system to the $^4\Delta_g \rightarrow {}^5\Sigma_u^+$ transition being a correlated two-electron process.

Lastly, the photoelectron angular distributions of transitions from the $^4\Sigma_g^-$ state show oscillations that, in the quantum analogy established by Fano to Young's double slit experiment, are interpreted as interferometric effects which are related to the emergence of the photoelectron partial waves as a function of the photoelectron KE in the photodetachment process. This opens the door for a more detailed modelling of the molecular potential barriers in anionic molecules, much less studied than those of neutral systems so far. In addition, measurements of β_2 at higher kinetic energies for Pt_3^- could provide

evidence of interferometric effects in the gerade molecular orbitals, which would be a quantum equivalent to Young's triple slit experiment.

TaN^-

In the past, the rovibronic structure of the neutral tantalum nitride molecule, TaN, had been studied. Here these studies are continued by analyzing the photoelectron spectrum of its anion, TaN^-. The newly obtained information comprises the adiabatic electron affinity of TaN along with the spin-orbit coupling constant (A_{SO}), the spin-spin interaction term constant (λ_{SS}) and vibrational terms of anionic and neutral electronic states.

The analysis of the measured photoelectron angular distributions reveals the presence of two characteristic deviations from the typically smooth dependence of β_2 on the kinetic energy for direct photodetachment processes that, with the support of TDDFT calculations, are characterized as manifestations of core excited shape and Feshbach resonances. The contributions from direct photodetachment processes are modelled within the Wigner-Bethe-Cooper-Zare approximation through Sanov's "sequential mixing model" giving insights into the chemical bonding of the molecule. The photoelectron angular distributions of the transitions $^2\Delta_{3/2} \rightarrow {}^3\Delta_{1,2}$ reveal a *spd* hybridization in the molecular orbital from which photodetachment takes place. The modeling of the photoelectron angular distributions within the Wigner-Bethe-Cooper-Zare approximation has been less successful for the $^2\Delta_{3/2} \rightarrow {}^1\Sigma_0^+$ transition due to, presumably, electronic correlation effects.

Anion photoelectron spectroscopy of transition metals- An outlook

The discrepancies between the modeling in the Wigner-Bethe-Cooper-Zare approximation of the $^2A_2' \rightarrow {}^3A_2''$ transition in Pt_3^- and the $^2\Delta_{3/2} \rightarrow {}^1\Sigma_0^+$ transition in TaN^- and the experimental results spotlight not only the need for further improvements in the models, but also for a further development of quantum chemical methods to obtain close-to-real estimates for the molecular

orbitals and photoelectron wavefunctions. Furthermore, the indications of electron correlation effects and the possible influence of relaxation effects in the photoelectron angular distributions reveal the need for a deeper theoretical understanding of these phenomena in systems that contain transition metal elements.

Typically, density-based methods are optimized to give the best possible energy estimates but they are not focused on reproducing the accurate wavefunctions, so determinant for the photoelectron angular distributions in photodetachment. Only wavefunction-based methods can do that. However, even using wavefunction based methods (CI, CCSD, etc.) one has been often limited to calculating accurate energy values, so far. The manifestation of correlation and relativistic effects in the photoelectron angular distributions might trigger future theoretical developments.

$CoAr_n^+$

Far-infrared multiple photodissociation spectra are obtained for $CoAr_n^+$ (n=3 to 6) complexes via direct excitation of Co-Ar vibrational fundamentals. The agreement obtained between the depletion spectrum of the $CoAr_4^+$ complex and its ab initio calculated IR frequencies readdresses the question of the Co^+-Ar bonding nature, since its calculated structure shows a strong directionality suggesting relevant covalent contributions to the main electrostatic interaction between the metal cation and the rare gas atom. This is backed up by a crystal field stabilization energy for the $CoAr_6^+$ molecule that is found to be close to the splittings in other isovalent d^8 complexes with a higher level of covalency as $[Ni(NH_3)_6]^{2+}$. Therefore, the predicted geometries for the $CoAr_n^+$ (n=3 to 6) complexes can be explained within the model of an octahedral crystal field splitting. This study shows the need for robust theoretical and more precise experimental quantifications of the contributions in the interactions between transition metals and rare gas atoms.

$Co_{n-m}Mn_mAr_x^+$

The vibrational spectra of $Co_{n-m}Mn_mAr_x^+$ complexes in the far-infrared are obtained for a variety of sizes and stoichiometries. The validity of the measurements is firstly corroborated by a detailed comparison of the spectra of $Co_nAr_x^+$ with those obtained in a former study [44,315] and, moreover, the structure of the $Co_3Ar_3^+$ complex is elucidated. After that, the spectra on the bimetallic $Co_{n-m}Mn_mAr_x^+$ complexes are qualitatively discussed remarking the possible high symmetry of the Co_{13}^+ and $Co_{12}Mn^+$ clusters whose structures, despite multiple previous studies, have not yet been elucidated. Beyond speculations, the support of robust DFT calculations and, maybe, even further spectroscopic studies are needed to elucidate the structures and the singularities in the metal-metal bonding of these bimetallic clusters.

Complementary infrared multiple photon dissociation measurements on the monocarbonyls of these bimetallic clusters were carried out to provide further insights into the binding and the activation of CO by binary transition metal clusters. These experiments where among the first performed with the newly installed IR-FEL at the Fritz-Haber institute and would be a useful complement to elucidate the geometric structures of the $Co_{n-m}Mn_m^+$ clusters.

Cationic ruthenium cluster carbonyls

The infrared multiple photon dissociation spectra of cationic Ru_n ruthenium cluster carbonyls $Ru_n(CO)_m^+$ with n=1-8 are obtained. For the smaller sizes with n=1 to 6 the geometric structures of the ground-state isomers and some higher energy isomers are calculated via DFT. The structures are corroborated by the agreement between their simulated vibrational spectra and the experimental data. The spectrum of the $Ru_6(CO)_{18}^+$ isomer reveals the solely contribution of the calculated lowest energy isomer, which is not based on an octahedral metal core. The geometric structures of the cationic Ru cluster carbonyls are compared with those of the ruthenium neutral species plus other isovalent/isoelectronic species to better understand the bonding nature of their highest occupied molecular orbitals.

The study continues with a brief introduction to the polyhedral skeletal electron pair theory and its application to cationic ruthenium cluster carbonyls. The theory is illustrated with some neutral isovalent carbonyls to subsequently predict the correct skeletal structures of the cationic Ru_n carbonyls with n=1 to 6. It is therefore concluded that the polyhedral skeletal electron pair theory can be successfully applied to (open-shell) cationic carbonyls since the essential element in the counting is the number of available orbitals (half or fully) occupied by electrons. Consequently, the skeletal structures of $Ru_7(CO)_{19}^+$ and $Ru_8(CO)_{21}^+$ are predicted.

This investigation triggers further applications of the polyhedral skeletal electron pair theory to charged cluster carbonyls and their corroboration via DFT calculations. These calculations might constitute a challenge since the large number of ligands in the carbonyls $Ru_7(CO)_{19}^+$ and $Ru_8(CO)_{21}^+$ results in gigantic conformational spaces where the geometry optimization to find the global minimum turns out to be quite cumbersome. Besides more accurate calculations on these carbonyls, additional experimental information could be obtained on the magnetic properties of the ruthenium clusters via X-ray magnetic circular dichroism spectroscopy or deflection experiments. In order to disentangle their electronic and geometric structures, these studies could be complemented with velocity map imaging measurements on the electronic structure of their corresponding negative species.

Bibliography

[1] E. C. Constable, C. E. Housecroft, Chemical Bonding: The Journey from Miniature Hooks to Density Functional Theory, *Molecules* **2020**, *25*, 2623.

[2] E. Frankland, B. C. Brodie, XIX. On a new series of organic bodies containing metals, *Philosophical Transactions of the Royal Society of London* **1852**, *142*, 417–444.

[3] G. M. Richardson, L. Pasteur, J. H. van't Hoff, J. A. Le Bel, J. Wislicenus, *The foundations of stereo chemistry memoirs by Pasteur, van't Hoff, Lebel and Wislicenus*, FRANKLIN CLASSICS TRADE PR., **1901**.

[4] J. J. M. F. Thomson, XL. Cathode Rays, *The London Edinburgh and Dublin Philosophical Magazine and Journal of Science* **1897**, *44*, 293–316.

[5] G. N. Lewis, The atom and the molecule, *Journal of the American Chemical Society* **1916**, *38*, 762–785.

[6] W. Heitler, F. London, Wechselwirkung neutraler Atome und homöopolare Bindung nach der Quantenmechanik, *Zeitschrift für Physik D Atoms Molecules and Clusters* **1927**, *44*, 455–472.

[7] J. C. Slater, Molecular Orbital and Heitler-London Methods, *The Journal of Chemical Physics* **1965**, *43*, S11–S17.

[8] M. J. S. Dewar, Quantum theory of molecules and solids. Volume 1, electronic structure of molecules (Slater, John C.), *Journal of Chemical Education* **1963**, *40*, 615.

[9] J. N. Murrell, The origins and later developments of molecular orbital theory, *International Journal of Quantum Chemistry* **2012**, *112*, 2875–2879.

[10] L. Pauling, *The Nature of the Chemical Bond and the Structure of Molecules and Crystals: An Introduction to Modern Structural Chemistry*, Cornell University Press, **1960**.

[11] F. Gernot, S. Sason in *The Chemical Bond* (Eds.: F. Gernot, S. Sason), Wiley-VCH, **2014**, pp. I–XXII.

[12] A. J. Cohen, P. Mori-Sánchez, W. Yang, Challenges for Density Functional Theory, *Chemical Reviews* **2012**, *112*, 289–320.

[13] F. A. Cotton, G. Wilkinson, C. A. Murillo, M. Bochmann, *Advanced inorganic chemistry, 6th Ed.*, Wiley, New York, **1999**.

[14] T. Nguyen, A. D. Sutton, M. Brynda, J. C. Fettinger, G. J. Long, P. P. Power, Synthesis of a Stable Compound with Fivefold Bonding Between Two Chromium(I) Centers, *Science* **2005**, *310*, 844–847.

[15] M. Brynda, L. Gagliardi, P.-O. Widmark, P. P. Power, B. O. Roos, A Quantum Chemical Study of the Quintuple Bond between Two Chromium Centers in [PhCrCrPh]: trans-Bent versus Linear Geometry, *Angewandte Chemie International Edition* **2006**, *45*, 3804–3807.

[16] L. Gagliardi, B. O. Roos, Quantum chemical calculations show that the uranium molecule U_2 has a quintuple bond, *Nature* **2005**, *433*, 848–851.

[17] B. Roos, A. Borin, L. Gagliardi, Reaching the Maximum Multiplicity of the Covalent Chemical Bond, *Angewandte Chemie International Edition* **2007**, *46*, 1469–1472.

[18] A. C. Borin, B. Paulo, G. O, Roos, Electronic structure and chemical bonding in W_2 molecule, *Chemical Physics Letters* **2010**, *490*, 24–28.

[19] A. C. Borin, J. P. Gobbo, B. O. Roos, A theoretical study of the binding and electronic spectrum of the Mo_2 molecule, *Chemical Physics* **2008**, *343*, 210–216.

[20] B. E. Bursten, F. A. Cotton, M. B. Hall, Dimolybdenum: nature of the sextuple bond, *Journal of the American Chemical Society* **1980**, *102*, 6348–6349.

[21] D. J. Harding, A. Fielicke, Platinum Group Metal Clusters: From Gas-Phase Structures and Reactivities towards Model Catalysts, *Chemistry – A European Journal* **2014**, *20*, 3258–3267.

[22] M. B. Knickelbein, Reactions of transition metal clusters with small molecules, *Annual Review of Physical Chemistry* **1999**, *50*, 79–115.

[23] P. S. Bechthold, E. K. Parks, B. H. Weiller, L. G. Pobo, S. J. Riley, Chemical Reactions of Small Gas Phase Metal Clusters, *Zeitschrift für Physikalische Chemie* **1990**, *169*, 101–122.

[24] M. D. Morse, M. E. Geusic, J. R. Heath, R. E. Smalley, Surface reactions of metal clusters. II. Reactivity surveys with D_2, N_2, and CO, *The Journal of Chemical Physics* **1985**, *83*, 2293–2304.

[25] G. Niedner-Schatteburg in *Cooperative Effects in Clusters and Oligonuclear Complexes of Transition Metals in Isolation*, Springer, **2016**, pp. 1–40.

[26] D. C. Parent, S. L. Anderson, Chemistry of metal and semimetal cluster ions, *Chemical reviews* **1992**, *92*, 1541–1565.

[27] H. S. Taylor, E. F. Armstrong, A theory of the catalytic surface, *Proceedings of the Royal Society of London. Series A Containing Papers of a Mathematical and Physical Character* **1925**, *108*, 105–111.

[28] P. Fayet, A. Kaldor, D. M. Cox, Palladium clusters: H_2, D_2, N_2, CH_4, CD_4, C_2H_4, and C_2H_6 reactivity and D_2 saturation studies, *The Journal of Chemical Physics* **1990**, *92*, 254–261.

[29] I. M. L. Billas, A. Châtelain, W. A. de Heer, Magnetism from the Atom to the Bulk in Iron, Cobalt, and Nickel Clusters, *Science* **1994**, *265*, 1682–1684.

[30] M. Niemeyer *et al.*, Spin Coupling and Orbital Angular Momentum Quenching in Free Iron Clusters, *Physical Review Letters* **2012**, *108*, 057201.

[31] H. Häkkinen, M. Moseler, O. Kostko, N. Morgner, M. A. Hoffmann, B. v. Issendorff, Symmetry and Electronic Structure of Noble-Metal Nanoparticles and the Role of Relativity, *Physical Review Letters* **2004**, *93*, 093401.

[32] S. Gilb, P. Weis, F. Furche, R. Ahlrichs, M. M. Kappes, Structures of small gold cluster cations (Au_n^+, n<14): Ion mobility measurements versus density functional calculations, *The Journal of Chemical Physics* **2002**, *116*, 4094–4101.

[33] D. Schooss, M. N. Blom, J. H. Parks, B. v. Issendorff, H. Haberland, M. M. Kappes, The Structures of Ag_{55}^+ and Ag_{55}^-: Trapped Ion Electron Diffraction and Density Functional Theory, *Nano Letters* **2005**, *5*, 1972–1977.

[34] B. Simard, S. Dénommée, D. M. Rayner, D. van Heijnsbergen, G. Meijer, G. von Helden, IR multiphoton depletion spectroscopy of metal cluster-ligand complexes, *Chemical Physics Letters* **2002**, *357*, 195–203.

[35] P. Bunker, P. Jensen, *Fundamentals of Molecular Symmetry*, CRC Press, **2004**.

[36] A. Sanov, Laboratory-Frame Photoelectron Angular Distributions in Anion Photodetachment: Insight into Electronic Structure and Inter-

molecular Interactions, *Annual Review of Physical Chemistry* **2014**, *65*, 341–363.

[37] D. Khuseynov, C. C. Blackstone, L. M. Culberson, A. Sanov, Photoelectron angular distributions for states of any mixed character: An experiment-friendly model for atomic, molecular, and cluster anions, *The Journal of Chemical Physics* **2014**, *141*, 124312.

[38] J. M. Hollas, *High Resolution Spectroscopy*, J. Wiley, New York, 2nd ed., **1998**.

[39] X.-B. Wang, L.-S. Wang, Experimental Observation of a Very High Second Electron Affinity for ZrF_6 from Photodetachment of Gaseous ZrF_6^{2-} Doubly Charged Anions, *The Journal of Physical Chemistry A* **2000**, *104*, 4429–4432.

[40] C.-G. Ning, P. D. Dau, L.-S. Wang, Guiding Electron Emissions by Excess Negative Charges in Multiply Charged Molecular Anions, *Physical Review Letters* **2010**, *105*, 263001.

[41] J. Simons in *Photoionization and Photodetachment* (Ed.: C.-Y. Ng), World Scientific, **2000**, pp. 958–1010.

[42] L. G. Christophorou, D. L. McCorkle, A. A. Christodoulides in *Electron-Molecule Interactions and their Applications* (Ed.: L. G. Christophorou), Academic Press, **1984**, pp. 477–617.

[43] C. R. Arumainayagam, H.-L. Lee, R. B. Nelson, D. R. Haines, R. P. Gunawardane, Low-energy electron-induced reactions in condensed matter, *Surface Science Reports* **2010**, *65*, 1–44.

[44] P. Grüne, PhD thesis, Technische Universität Berlin, **2009**.

[45] J. DeVine, PhD thesis, University of California, Berkeley, **2019**.

[46] M. Scheer, R. C. Bilodeau, J. Thaugersen, H. K. Haugen, Threshold photodetachment of Al^- : Electron affinity and fine structure, *Physical Review A* **1998**, *57*, R1493–R1496.

[47] D. Pegg in *Springer Handbook of Atomic, Molecular, and Optical Physics* (Ed.: G. Drake), Springer New York, New York, NY, **2006**, pp. 891–899.

[48] E. P. Wigner, On the Behavior of Cross Sections Near Thresholds, *Physical Review* **1948**, *73*, 1002–1009.

[49] G. Breit, E. Wigner, Capture of Slow Neutrons, *Physical Review* **1936**, *49*, 519–531.

[50] H. D. Cohen, U. Fano, Interference in the Photo-Ionization of Molecules, *Physical Review* **1966**, *150*, 30–33.

[51] J. E. Collin, Autoionization in atomic and molecular physics, *Endeavour* **1977**, *1*, 122–128.

[52] T. A. Patterson, H. Hotop, A. Kasdan, D. W. Norcross, W. C. Lineberger, Resonances in Alkali Negative-Ion Photodetachment and Electron Affinities of the Corresponding Neutrals, *Physical Review Letters* **1974**, *32*, 189–192.

[53] S. E. Novick, P. L. Jones, T. J. Mulloney, W. C. Lineberger, Resonances in photodetachment of sodium halide negative ions, *The Journal of Chemical Physics* **1979**, *70*, 2210–2214.

[54] M. N. Piancastelli, The neverending story of shape resonances, *Journal of Electron Spectroscopy and Related Phenomena* **1999**, *100*, 167–190.

[55] B. Ómarsson, PhD thesis, University of Iceland, **2014**.

[56] E. Illenberger, J. Momigny, *Gaseous Molecular Ions: An Introduction to Elementary Processes Induced by Ionization*, Steinkopff Verlag, **1992**.

[57] T. Sommerfeld, Dipole-bound states as doorways in (dissociative) electron attachment, *Journal of Physics: Conference Series* **2005**, *4*, 245–250.

[58] G. J. Schulz, Resonances in Electron Impact on Diatomic Molecules, *Reviews of Modern Physics* **1973**, *45*, 423–486.

[59] H. Hotop, M. W. Rul, I. I. Fabrikant, Resonance and Threshold Phenomena in Low-Energy Electron Collisions with Molecules and Clusters, *Physica Scripta* **2004**, *110*, 22.

[60] I. León, Z. Yang, L.-S. Wang, Resonant photoelectron spectroscopy of Au_2^- via a Feshbach state using high-resolution photoelectron imaging, *The Journal of Chemical Physics* **2013**, *139*, 194306.

[61] F. Gresteau, R. I. Hall, A. Huetz, D. Vichon, J. Mazeau, Decay of Feshbach resonances in NO. II. Dynamic coupling to Rydberg states, *Journal of Physics B: Atomic and Molecular Physics* **1979**, *12*, 2937–2945.

[62] F. Gresteau, R. I. Hall, A. Hetz, D. Vichon, J. Mazeau, Decay of Feshbach resonances in NO. I. Energy dependence of the electronic coupling to the ground state, *Journal of Physics B: Atomic and Molecular Physics* **1979**, *12*, 2925–2935.

[63] R. I. Hall, F. H. Read in *Molecular Spectroscopy by Electron Scattering* (Eds.: I. Shimamura, K. Takayanagi), Springer US, Boston, MA, **1984**, pp. 351–425.

[64] J. Mazeau, F. Gresteau, R. I. Hall, G. Joyez, J. Reinhardt, Electron impact excitation of N_2. I. Resonant phenomena associated with the $A^3\Sigma_u^+$ and $B^3\Pi_g$ valence states, *Journal of Physics B: Atomic and Molecular Physics* **1973**, *6*, 862–872.

[65] J. Mazeau, R. I. Hall, G. Joyez, M. Landau, J. Reinhardt, Electron excitation of N_2. II. Resonant phenomena associated with Rydberg states, *Journal of Physics B: Atomic and Molecular Physics* **1973**, *6*, 873–880.

[66] C. W. West, J. N. Bull, E. Antonkov, J. R. R. Verlet, Anion Resonances of para-Benzoquinone Probed by Frequency-Resolved Photoelectron Imaging, *The Journal of Physical Chemistry A* **2014**, *118*, 11346–11354.

[67] D. C. Clary, Photodetachment of electrons from dipolar anions, *The Journal of Physical Chemistry* **1988**, *92*, 3173–3181.

[68] J. Simons, Modified rotationally adiabatic model for rotational autoionization of dipole-bound molecular anions, *The Journal of Chemical Physics* **1989**, *91*, 6858–6865.

[69] H.-T. Liu, C.-G. Ning, D.-L. Huang, P. D. Dau, L.-S. Wang, Observation of Mode-Specific Vibrational Autodetachment from Dipole-Bound States of Cold Anions, *Angewandte Chemie International Edition* **2013**, *52*, 8976–8979.

[70] D. B. Dao, R. Mabbs, The effect of the dipole bound state on AgF^- vibrationally resolved photodetachment cross sections and photoelectron angular distributions, *The Journal of Chemical Physics* **2014**, *141*, 154304.

[71] T.-C. Jagau, D. B. Dao, N. S. Holtgrewe, A. I. Krylov, R. Mabbs, Same but Different: Dipole-Stabilized Shape Resonances in CuF^- and AgF^-, *The Journal of Physical Chemistry Letters* **2015**, *6*, 2786–2793.

[72] J. N. Bull, C. W. West, J. R. R. Verlet, Ultrafast dynamics of formation and autodetachment of a dipole-bound state in an open-shell π-stacked dimer anion, *Chemical Science* **2016**, *7*, 5352–5361.

[73] J. W. Cooper, Photoionization from Outer Atomic Subshells. A Model Study, *Physical Review* **1962**, *128*, 681–693.

[74] T. Koopmans, Über die Zuordnung von Wellenfunktionen und Eigenwerten zu den Einzelnen Elektronen Eines Atoms, *Physica* **1934**, *1*, 104–113.

[75] C. Bartels, PhD thesis, Albert-Ludwigs-Universität, Freiburg im Breisgau, **2008**.

[76] K. L. Reid, Photoelectron Angular Distributions, *Annual Review of Physical Chemistry* **2003**, *54*, 397–424.

[77] A. Sanov, R. Mabbs, Photoelectron imaging of negative ions, *International Reviews in Physical Chemistry* **2008**, *27*, 53–85.

[78] H. Bethe, F. Hund, N. F. Mott, W. Pauli, A. Rubinowicz, G. Wentzel, A. Smekal in *Quantenmechanik der Ein- und Zwei-Elektronenprobleme*, Springer Berlin Heidelberg, Berlin, Heidelberg, **1933**, pp. 273–560.

[79] J. Cooper, R. N. Zare, Angular Distribution of Photoelectrons, *Journal of Chemical Physics* **1968**, *48*, 942.

[80] U. Becker, Complete photoionisation experiments, *Journal of Electron Spectroscopy and Related Phenomena* **1998**, *96*, 105–115.

[81] M. Van Duzor *et al.*, Vibronic coupling in the superoxide anion: The vibrational dependence of the photoelectron angular distribution, *The Journal of Chemical Physics* **2010**, *133*, 174311.

[82] R. Mabbs, E. Surber, A. Sanov, Photoelectron anisotropy and channel branching ratios in the detachment of solvated iodide cluster anions, *The Journal of Chemical Physics* **2005**, *122*, 054308.

[83] R. Mabbs, F. Mbaiwa, J. Wei, M. Van Duzor, S. T. Gibson, S. J. Cavanagh, B. R. Lewis, Observation of vibration-dependent electron anisotropy in O_2^- photodetachment, *Physical Review A* **2010**, *82*, 011401.

[84] C. Oana, A. Krylov, Dyson orbitals for ionization from the ground and electronically excited states within equation-of-motion coupled-cluster formalism: Theory, implementation, and examples, *The Journal of chemical physics* **2007**, *127*, 234106.

[85] *https://winter.group.shef.ac.uk/orbitron/*, **2021-02-28**.

[86] K. J. Reed, A. H. Zimmerman, H. C. Andersen, J. I. Brauman, Cross sections for photodetachment of electrons from negative ions near threshold, *The Journal of Chemical Physics* **1976**, *64*, 1368–1375.

[87] F. A. Akin, L. K. Schirra, A. Sanov, Photoelectron Imaging Study of the Effect of Monohydration on O_2^- Photodetachment, *The Journal of Physical Chemistry A* **2006**, *110*, 8031–8036.

[88] A. Sanov, E. R. Grumbling, D. J. Goebbert, L. M. Culberson, Photodetachment anisotropy for mixed s-p states: 8/3 and other fractions, *The Journal of Chemical Physics* **2013**, *138*, 054311.

[89] E. R. Grumbling, A. Sanov, Photoelectron angular distributions in negative-ion photodetachment from mixed sp states, *The Journal of Chemical Physics* **2011**, *135*, 164302.

[90] E. R. Grumbling, PhD thesis, University of Arizona, **2010**.

[91] L. M. Culberson, PhD thesis, University of Arizona, **2013**.

[92] J. A. DeVine, M. C. Babin, K. Blackford, D. M. Neumark, High-resolution photoelectron spectroscopy of the pyridinide isomers, *The Journal of Chemical Physics* **2019**, *151*, 064302.

[93] D. Hanstorp, C. Bengtsson, D. J. Larson, Angular distributions in photodetachment from O^-, *Physical Review A* **1989**, *40*, 670–675.

[94] W. C. Wiley, I. H. McLaren, Time-of-Flight mass spectrometer with improved resolution, *Review of Scientific Instruments* **1955**, *26*, 1150–1157.

[95] A. Eppink, D. H. Parker, Velocity map imaging of ions and electrons using electrostatic lenses: Application in photoelectron and photofragment ion imaging of molecular oxygen, *Review of Scientific Instruments* **1997**, *68*, 3477–3484.

[96] T. G. Dietz, M. A. Duncan, D. E. Powers, R. E. Smalley, Laser production of supersonic metal cluster beams, *The Journal of Chemical Physics* **1981**, *74*, 6511–6512.

[97] D. E. Powers *et al.*, Supersonic metal cluster beams: laser photoionization studies of copper cluster (Cu_2), *The Journal of Physical Chemistry* **1982**, *86*, 2556–2560.

[98] D. E. Powers, S. G. Hansen, D. L. Geusic, M. E. Michalopoulos, R. E. Smalley, Supersonic copper clusters, *The Journal of Chemical Physics* **1983**, *78*, 2866–2881.

[99] G. von Helden, D. van Heijnsbergen, G. Meijer, Resonant Ionization Using IR Light: A New Tool To Study the Spectroscopy and Dynamics of Gas-Phase Molecules and Clusters, *The Journal of Physical Chemistry A* **2003**, *107*, 1671–1688.

[100] A. Fielicke, G. von Helden, G. Meijer, Far-Infrared spectroscopy of isolated transition metal clusters, *The European Physical Journal D - Atomic Molecular Optical and Plasma Physics* **2005**, *34*, 83–88.

[101] A. Y. Vorobyev, C. Guo, Reflection of femtosecond laser light in multipulse ablation of metals, *Journal of Applied Physics* **2011**, *110*, 043102.

[102] M. A. Duncan, Invited Review Article: Laser vaporization cluster sources, *Review of Scientific Instruments* **2012**, *83*, 041101.

[103] B. J. Whitaker, *Imaging in Molecular Dynamics: Technology and Applications*, Cambridge University Press, Cambridge, **2003**.

[104] A. Osterwalder, M. J. Nee, J. Zhou, D. M. Neumark, High resolution photodetachment spectroscopy of negative ions via slow photoelectron imaging, *The Journal of Chemical Physics* **2004**, *121*, 6317–6322.

[105] D. M. Neumark, Slow Electron Velocity-Map Imaging of Negative Ions: Applications to Spectroscopy and Dynamics, *Journal of Physical Chemistry A* **2008**, *112*, 13287–13301.

[106] A. Wituschek, *Versuchsanleitung/ Fortgeschrittenen Praktikum (Teil II)/ Velocity Map Imaging*, Institut für Mathematik und Physik: Albert-Ludwigs-Universität, Freiburg im Breisgau technical report, **2016**.

[107] G. M. Roberts, J. L. Nixon, J. Lecointre, E. Wrede, J. R. R. Verlet, Toward real-time charged-particle image reconstruction using polar onion-peeling, *Review of Scientific Instruments* **2009**, *80*, 053104.

[108] K. Zhao, T. Colvin, W. T. Hill III, G. Zhang, Deconvolving two-dimensional images of three-dimensional momentum trajectories, *Review of Scientific Instruments* **2002**, *73*, 3044–3050.

[109] P. F. Bernath, *Spectra of Atoms and Molecules*, Oxford University Press, New York, 3rd ed., **2016**.

[110] W. Demtröder, *Atoms, Molecules and Photons: An Introduction to Atomic- Molecular- and Quantum Physics*, Springer-Verlag Berlin Heidelberg, **2006**.

[111] G. Herzberg, *Molecular spectra and molecular structure. III. Electronic spectra and electronic structure of polyatomic molecules*, Van Nostrand, New York, **1966**.

[112] P. M. Morse, Diatomic Molecules According to the Wave Mechanics. II. Vibrational Levels, *Physical Review* **1929**, *34*, 57–64.

[113] *https* : *//en.wikipedia.org/wiki/Morsepotential*, **2021-02-28**.

[114] M. L. Weichman, PhD thesis, University of California, Berkeley, **2017**.

[115] A. O'Keefe, D. A. G. Deacon, Cavity ring-down optical spectrometer for absorption measurements using pulsed laser sources, *Review of Scientific Instruments* **1988**, *59*, 2544–2551.

[116] A. Terasaki, T. Majima, C. Kasai, T. Kondow, Photon-trap spectroscopy of size-selected free cluster ions: "direct" measurement of optical absorption of Ag_9^+, *The European Physical Journal D* **2009**, *52*, 43–46.

[117] J. B. Paul, R. A. Provencal, C. Chapo, K. Roth, R. Casaes, R. J. Saykally, Infrared Cavity Ringdown Spectroscopy of the Water Cluster Bending Vibrations, *The Journal of Physical Chemistry A* **1999**, *103*, 2972–2974.

[118] D. Gerlich in *Inhomogeneous RF Fields: A Versatile Tool for the Study of Processes with Slow Ions*, John Wiley & Sons, **1992**, pp. 1–176.

[119] C. Kerpal, D. J. Harding, G. Meijer, A. Fielicke, CO adsorption on neutral iridium clusters, *The European Physical Journal D* **2011**, *63*, 231–234.

[120] A. C. Hermes, S. M. Hamilton, G. A. Cooper, C. Kerpal, D. J. Harding, G. Meijer, A. Fielicke, S. R. Mackenzie, Infrared driven CO oxidation reactions on isolated platinum cluster oxides, $Pt_nO_m^+$, *Faraday Discussions* **2012**, *157*, 213–225.

[121] A. P. Woodham, G. Meijer, A. Fielicke, Activation of Molecular Oxygen by Anionic Gold Clusters, *Angewandte Chemie International Edition* **2012**, *51*, 4444–4447.

[122] A. P. Woodham, A. Fielicke, Superoxide Formation on Isolated Cationic Gold Clusters, *Angewandte Chemie International Edition* **2014**, *53*, 6554–6557.

[123] A. Yanagimachi, K. Koyasu, D. Valdivielso, S. Gewinner, W. Schöllkopf, A. Fielicke, T. Tsukuda, Size-Specific, Dissociative Activation of Carbon Dioxide by Cobalt Cluster Anions, *The Journal of Physical Chemistry C* **2016**, *120*, 14209–14215.

[124] W. J. C. Menezes, M. B. Knickelbein, Photodissociation spectroscopy of Nb_nAr_m complexes, *The Journal of Chemical Physics* **1993**, *98*, 1856–1866.

[125] P. Gruene, D. M. Rayner, B. Redlich, A. F. G. van der Meer, J. T. Lyon, G. Meijer, A. Fielicke, Structures of Neutral Au_7, Au_{19}, and Au_{20} Clusters in the Gas Phase, *Science* **2008**, *321*, 674–676.

[126] M. B. Knickelbein, Photodissociation spectroscopy of Cu_3, Cu_3Ar, and Cu_3Kr, *The Journal of Chemical Physics* **1994**, *100*, 4729–4737.

[127] J. G. Black, E. Yablonovitch, N. Bloembergen, S. Mukamel, Collisionless Multiphoton Dissociation of SF_6: A Statistical Thermodynamic Process, *Physical Review Letters* **1977**, *38*, 1131–1134.

[128] J. Oomens, A. G. G. M. Tielens, B. G. Sartakov, G. von Helden, G. Meijer, Laboratory Infrared Spectroscopy of Cationic Polycyclic Aromatic Hydrocarbon Molecules, *The Astrophysical Journal* **2003**, *591*, 968–985.

[129] A. A. Makarov, I. Y. Petrova, E. A. Ryabov, V. S. Letokhov, Statistical Inhomogeneous Broadening of Infrared and Raman Transitions in Highly Vibrationally Excited XY_6 Molecules, *The Journal of Physical Chemistry A* **1998**, *102*, 1438–1449.

[130] A. Bekkerman, E. Kolodney, G. von Helden, B. Sartakov, D. van Heijnsbergen, G. Meijer, Infrared multiphoton ionization of superhot C_{60}: Experiment and model calculations, *The Journal of Chemical Physics* **2006**, *124*, 184312.

[131] J. M. Bakker *et al.*, Intensity-resolved IR multiple photon ionization and fragmentation of C_{60}, *The Journal of Chemical Physics* **2010**, *132*, 074305.

[132] M. Mayer *et al.*, Rational design of an argon-binding superelectrophilic anion, *Proceedings of the National Academy of Sciences* **2019**, *116*, 8167.

[133] M. Räsänen, Argon out of thin air, *Nature Chemistry* **2014**, *6*, 82–82.

[134] P. Schilke *et al.*, Ubiquitous argonium (ArH^+) in the diffuse interstellar medium: A molecular tracer of almost purely atomic gas, *A&A* **2014**, *566*, A29.

[135] M. J. Barlow *et al.*, Detection of a Noble Gas Molecular Ion, $^{36}ArH^+$, in the Crab Nebula, *Science* **2013**, *342*, 1343–1345.

[136] R. Johnston, *Atomic Molecular Clusters*, CRC Press, **2002**.

[137] J. Jin, W. Li, Y. Liu, G. Wang, M. Zhou, Preparation and characterization of chemically bonded argon-boroxol ring cation complexes, *Chemical Science* **2017**, *8*, 6594–6600.

[138] L. Khriachtchev, M. Pettersson, N. Runeberg, J. Lundell, M. Räsänen, A stable argon compound, *Nature* **2000**, *406*, 874–876.

[139] N. Runeberg, M. Pettersson, L. Khriachtchev, J. Lundell, M. Räsänen, A theoretical study of HArF, a newly observed neutral argon compound, *The Journal of Chemical Physics* **2001**, *114*, 836–841.

[140] P. Y. Cheng, K. F. Willey, M. A. Duncan, Vibronic spectroscopy of Ag_2-Ar, *Chemical Physics Letters* **1989**, *163*, 469–474.

[141] A. M. Lyyra, W. P. Lapatovich, P. E. Moskowitz, M. D. Havey, R. Ahmad-Bitar, D. E. Pritchard, High resolution laser induced fluorescence spectroscopy of highly excited vibrational levels in NaAr: A $^2\Pi_r$ and B $^2\Sigma^+$, *AIP Conference Proceedings* **1986**, *146*, 469–471.

[142] D. Schwarzhans, D. Zimmermann, High resolution laser spectroscopy of NaAr: Improved interaction potential for the ground state, *The European Physical Journal D - Atomic Molecular Optical and Plasma Physics* **2003**, *22*, 193–198.

[143] M. Braune, H. Valipour, D. Zimmermann, High-resolution laser spectroscopy of the potassium-argon molecule: The B $^2\Sigma^+$ state, *Journal of Molecular Spectroscopy* **2006**, *235*, 84–92.

[144] J. Dhiflaoui, H. Berriche, M. Heaven, Electronic Absorption Spectra of the RbAr Van der Waals Complex, *AIP Conference Proceedings* **2011**, *1370*, 234–241.

[145] C. J. Evans, M. C. L. Gerry, The microwave spectra and structures of Ar-AgX (X=F,Cl,Br), *The Journal of Chemical Physics* **2000**, *112*, 1321–1329.

[146] X. Wang, L. Andrews, K. Willmann, F. Brosi, S. Riedel, Investigation of Gold Fluorides and Noble Gas Complexes by Matrix-Isolation Spectroscopy and Quantum-Chemical Calculations, *Angewandte Chemie International Edition* **2012**, *51*, 10628–10632.

[147] Y. Zhao, Y. Gong, M. Zhou, Matrix Isolation Infrared Spectroscopic and Theoretical Study of NgMO (Ng = Ar, Kr, Xe; M = Cr, Mn, Fe, Co, Ni) Complexes, *The Journal of Physical Chemistry A* **2006**, *110*, 10777–10782.

[148] D. C. Grills, M. W. George in *Advances in Inorganic Chemistry, Vol. 52*, Academic Press, **2001**, pp. 113–150.

[149] J. Demuynck, E. Kochanski, A. Veillard, Metal-rare gas interaction. A new bond?, *Journal of the American Chemical Society* **1979**, *101*, 3467–3472.

[150] A. W. Ehlers, G. Frenking, E. J. Baerends, Structure and Bonding of the Noble Gas-Metal Carbonyl Complexes $M(CO)_5$-Ng (M = Cr, Mo, W and Ng = Ar, Kr, Xe), *Organometallics* **1997**, *16*, 4896–4902.

[151] B. L. Hammond, W. A. Lester, M. Braga, C. A. Taft, Theoretical study of the interaction of ionized transition metals (Cr,Mn,Fe,Co,Ni,Cu) with argon, *Physical Review B* **1990**, *41*, 10447–10452.

[152] J. T. Koskinen, Novel Rare Gas Ions BXe^+, BKr^+, and BAr^+ Formed in a Halogen/Rare Gas Exchange Reaction, *The Journal of Physical Chemistry A* **1999**, *103*, 9565–9568.

[153] J. P. Wagner, D. C. McDonald 2nd, M. A. Duncan, An Argon-Oxygen Covalent Bond in the $ArOH^+$ Molecular Ion, *Angewandte Chemie International Edition* **2018**, *57*, 5081–5085.

[154] D. Ascenzi, P. Tosi, J. Roithová, C. L. Ricketts, D. Schröder, J. F. Lockyear, M. A. Parkes, S. D. Price, Generation of the organo-rare gas dications $HCCRg^{2+}$ (Rg = Ar and Kr) in the reaction of acetylene

dications with rare gases, *Physical Chemistry Chemical Physics* **2008**, *10*, 7121–7128.

[155] G. von Helden, P. R. Kemper, M. Hsu, M. T. Bowers, Determination of potential energy curves for ground and metastable excited state transition metal ions interacting with helium and neon using electronic state chromatography, *The Journal of Chemical Physics* **1992**, *96*, 6591–6605.

[156] D. Lessen, P. J. Brucat, Resonant photodissociation of $CoAr^+$ and $CoKr^+$ Analysis of vibrational structure, *Chemical Physics* **1989**, *90*, 6296–6305.

[157] T. Brupbacher, A. Bauder, Rotational spectrum and dipole moment of the benzene-argon van der Waals complex, *Chemical Physics Letters* **1990**, *173*, 435–438.

[158] K. C. Janda, L. S. Bernstein, J. M. Steed, S. E. Novick, W. Klemperer, Synthesis, microwave spectrum, and structure of $ArBF_3$, BF_3CO, and N_2BF_3, *Journal of the American Chemical Society* **1978**, *100*, 8074–8079.

[159] M. T. Bowers, W. E. Palke, K. Robins, C. Roehl, S. Walsh, On the structure and photodissociation dynamics of Ar_3^+, *Chemical Physics Letters* **1991**, *180*, 235–240.

[160] H. Motz, Applications of the Radiation from Fast Electron Beams, *Journal of Applied Physics* **1951**, *22*, 527–535.

[161] H. Motz, W. Thon, R. N. Whitehurst, Experiments on Radiation by Fast Electron Beams, *Journal of Applied Physics* **1953**, *24*, 826–833.

[162] D. Oepts, A. F. G. van der Meer, P. W. van Amersfoort, The Free-Electron-Laser user facility FELIX, *Infrared Physics & Technology* **1995**, *36*, 297–308.

[163] W. J. van der Zande, R. T. Jongma, L. van der Meer, B. Redlich, *38th International Conference on Infrared, Millimeter, and Terahertz Waves (IRMMW-THz)*, **2013**, pp. 1 – 2.

[164] W. Schöllkopf, S. Gewinner, H. Junkes, A. Paarmann, G. von Helden, H. P. Bluem, A. M. M. Todd, *Advances in X-ray Free-Electron Lasers Instrumentation III*, **2015**, pp. 238 – 250.

[165] *https://www.ru.nl/felix/about-felix/about-felix/fel-operating-principle/*, **2019-11-30**.

[166] *https://www.ru.nl/felix/about-felix/about-felix/felix-laboratory/*, **2019-11-30**.

[167] M. Härtelt, PhD thesis, Technische Universität Berlin, **2012**.

[168] V. Chernyy, PhD thesis, Radboud University Nijmegen, **2017**.

[169] C. F. Kerpal, PhD thesis, Fritz-Haber-Institut der Max-Planck-Gesselschaft, Berlin, **2013**.

[170] A. P. Woodham, PhD thesis, Fritz-Haber-Institut der Max-Planck-Gesselschaft, Berlin, **2014**.

[171] M. R. Fagiani, PhD thesis, Freie Universität, Berlin, **2017**.

[172] U. Boesl, R. Weinkauf, E. W. Schlag, Reflectron time-of-flight mass spectrometry and laser excitation for the analysis of neutrals, ionized molecules and secondary fragments, *International Journal of Mass Spectrometry and Ion Processes* **1992**, *112*, 121–166.

[173] A. Fielicke, G. von Helden, G. Meijer, D. B. Pedersen, B. Simard, D. M. Rayner, Size and charge effects on the binding of CO to late transition metal clusters, *The Journal of Chemical Physics* **2006**, *124*, 194305.

[174] W. Domcke, H. Köppel in *Conical intersections: theory, computation and experiment*, *Vol. 17* (Eds.: W. Domcke, D. Yarkony, H. Köppel), World Scientific, Singapore, **2011**, chapter 4, pp. 117–154.

[175] A. Weaver, D. W. Arnold, S. E. Bradforth, D. M. Neumark, Examination of the $^2A'_2$ and $^2E''$ states of NO_3 by ultraviolet photoelectron spectroscopy of NO_3^-, *Journal of Chemical Physics* **1991**, *94*, 1740–1751.

[176] E. P. Wigner, H. S. W. Massey, *Group Theory: And Its Application to the Quantum Mechanics of Atomic Spectra*, Elsevier Science, **2013**.

[177] H. A. Kramers, General theory of the paramagnetic rotation in crystals, *Proceedings of the Koninklijke Akademie Van Wetenschappen Te Amsterdam* **1930**, *33*, 959–972.

[178] H. A. Jahn, E. Teller, Stability of Polyatomic Molecules in Degenerate Electronic States. I. Orbital Degeneracy, *Proceedings of the Royal Society of London. Series A Mathematical and Physical Sciences* **1937**, *161*, 220–235.

[179] H. A. Jahn, W. H. Bragg, Stability of polyatomic molecules in degenerate electronic states II-Spin degeneracy, *Proceedings of the Royal Society of London. Series A - Mathematical and Physical Sciences* **1938**, *164*, 117–131.

[180] T. Azumi, K. Matsuzaki, WHAT DOES THE TERM "VIBRONIC COUPLING" MEAN?, *Photochemistry and Photobiology* **1977**, *25*, 315–326.

[181] M. Born, R. Oppenheimer, Zur Quantentheorie der Molekeln, *Annalen der Physik* **1927**, *389*, 457–484.

[182] I. B. Bersuker, V. Z. Polinger, *Vibronic Interactions in Molecules and Crystals*, Springer-Verlag, Berlin, Heidelberg, Bersuker, I.B. and Polinger, V. Z. ed., **1989**.

[183] I. B. Bersuker, *The Jahn-Teller Effect*, Cambridge University Press, Cambridge, **2006**.

[184] I. B. Bersuker, Pseudo-Jahn-Teller Effect-A Two-State Paradigm in Formation, Deformation, and Transformation of Molecular Systems and Solids, *Chemical Reviews* **2013**, *113*, 1351–1390.

[185] U. Öpik, M. H. L. Pryce, Studies of the Jahn-Teller effect. I. A survey of the static problem, *Proceedings of the Royal Society of London. Series A. Mathematical and Physical Sciences* **1957**, *238*, 425–447.

[186] I. B. Bersuker, Symmetry, instability, stereochemistry and phase transitions in coordination compounds, *Pure and Applied Chemistry* **1988**, *60*, 1167–1174.

[187] I. León, Z. Yang, L. S. Wang, High resolution photoelectron imaging of Au_2^-, *Journal of Chemical Physics* **2013**, *138*, 184304.

[188] K. M. Ervin, J. Ho, W. C. Lineberger, Electronic and vibrational structure of transition-metal trimers: Photoelectron Spectra of Ni_3^-, Pd_3^-, and Pt_3^-, *Journal of Chemical Physics* **1988**, *89*, 4514–4521.

[189] G. S. Icking-Konert, H. Handschuh, G. Gantefor, W. Eberhardt, Bonding of CO to metal particles: Photoelectron spectra of $Ni_n(CO)_m^-$ and $Pt_n(CO)_m^-$ clusters, *Physical Review Letters* **1996**, *76*, 1047–1050.

[190] G. Ganteför, G. S. Icking-Konert, H. Handschuh, W. Eberhardt, CO chemisorption on Ni_n^-, Pd_n^-, and Pt_n^- clusters, *International Journal of Mass Spectrometry* **1996**, *159*, 81–109.

[191] G. Ganteför, W. Eberhardt, H. Weidele, D. Kreisle, E. Recknagel, Energy dissipation in small clusters: Direct photoemission, dissociation, and thermionic emission, *Physical Review Letters* **1996**, *77*, 4524–4527.

[192] H. Handschuh, G. S. Icking-Konert, G. Gantefor, P. S. Bechthold, W. Eberhardt, The structure of reacted metal clusters: Photoelectron spectra of Pt_n^- clusters reacted with CO, *Surface Review and Letters* **1996**, *3*, 643–647.

[193] Z. L. Liu, H. Xie, Z. B. Qin, R. Cong, X. Wu, Z. C. Tang, X. Lu, J. He, Vibrationally resolved photoelectron imaging of platinum carbonyl anion $Pt(CO)_n^-$ (n=1-3): Experiment and theory, *Journal of Chemical Physics* **2012**, *137*, 204302.

[194] X. L. Ren, P. A. Hintz, K. M. Ervin, Chemisorption of carbon-monoxide on platinum cluster anions, *Journal of Chemical Physics* **1993**, *99*, 3575–3587.

[195] P. A. Hintz, K. M. Ervin, Chemisorption and oxidation reactions of nickel group cluster anions with N_2, O_2, CO_2 and NO_2, *Journal of Chemical Physics* **1995**, *103*, 7897–7906.

[196] C. Adlhart, E. Uggerud, Reactions of platinum clusters $Pt_n^{(+/-)}$, n=1-21, with CH_4: to react or not to react, *Chemical Communications* **2006**, *1*, 2581–2582.

[197] W. Eberhardt, P. Fayet, D. M. Cox, Z. Fu, A. Kaldor, R. Sherwood, D. Sondericker, Photoemission from mass-selected monodispersed Pt clusters, *Physical Review Letters* **1990**, *64*, 780–783.

[198] D. J. Harding, C. Kerpal, D. M. Rayner, A. Fielicke, Communication: The structures of small cationic gas-phase platinum clusters, *The Journal of Chemical Physics* **2012**, *136*, 211103.

[199] B. Bigot, C. Minot, Extended Huckel study fo the metallic growth of small platinum clusters: structure and energetics, *Journal of the American Chemical Society* **1984**, *106*, 6601–6615.

[200] A. Gavezzotti, G. F. Tantardini, H. Miessner, SCF-MO-pseudopotential and extended Hueckel calculations on the interaction of carbon monoxide with platinum clusters, *Journal of Physical Chemistry* **1988**, *92*, 872–878.

[201] H. Wang, E. A. Carter, Metal-Metal Bonding in Transition-Metal Clusters with Open d-Shells: Pt_3, *Journal of Physical Chemistry* **1992**, *96*, 1197–1204.

[202] J. Rubio, S. Zurita, J. C. Barthelat, F. Illas, Electronic and geometrical structures of Pt_3 and Pt_4: An ab initio one-electron proposal, *Chemical Physics Letters* **1994**, *217*, 283–287.

[203] S. H. Yang, D. A. Drabold, J. B. Adams, P. Ordejon, K. Glassford, Density functional studies of small platinum clusters, *Journal of Physics-Condensed Matter* **1997**, *9*, L39–L45.

[204] H. Grönbeck, W. Andreoni, Gold and platinum microclusters and their anions: comparison of structural and electronic properties, *Chemical Physics* **2000**, *262*, 1–14.

[205] T. Li, P. B. Balbuena, Computational studies of the interactions of oxygen with platinum clusters, *Journal of Physical Chemistry B* **2001**, *105*, 9943–9952.

[206] C. L. Heredia, V. Ferraresi-Curotto, M. B. Lopez, Characterization of Pt_n (n=2-12) clusters through global reactivity descriptors and vibrational spectroscopy, a theoretical study, *Computational Materials Science* **2012**, *53*, 18–24.

[207] A. Fortunelli, Density functional calculations on small platinum clusters: Pt_n^q (n=1-4, q=0,±1), *Journal of Molecular Structure-Theochem* **1999**, *493*, 233–240.

[208] L. Xiao, L. C. Wang, Structures of platinum clusters: Planar or spherical?, *Journal of Physical Chemistry A* **2004**, *108*, 8605–8614.

[209] Y. Xu, W. A. Shelton, W. F. Schneider, Effect of particle size on the oxidizability of platinum clusters, *Journal of Physical Chemistry A* **2006**, *110*, 5839–5846.

[210] A. H. Nie, J. P. Wu, C. G. Zhou, S. J. Yao, R. C. Forrey, H. S. Cheng, Structural evolution of subnano platinum clusters, *International Journal of Quantum Chemistry* **2007**, *107*, 219–224.

[211] M. N. Huda, M. K. Niranjan, B. R. Sahu, L. Kleinman, Effect of spin-orbit coupling on small platinum nanoclusters, *Physical Review A* **2006**, *73*, 053201.

[212] T. Futschek, J. Hafner, M. Marsman, Stable structural and magnetic isomers of small transition-metal clusters from the Ni group: an ab

initio density-functional study, *Journal of Physics: Condensed Matter* **2006**, *18*, 9703–9748.

[213] A. Sebetci, Z. B. Guvenc, Energetics and structures of small clusters: Pt_n, n=2-21, *Surface Science* **2003**, *525*, 66–84.

[214] A. Sebetci, A density functional study of bare and hydrogenated platinum clusters, *Chemical Physics* **2006**, *331*, 9–18.

[215] K. Bhattacharyya, C. Majumder, Growth pattern and bonding trends in Pt_n (n=2-13) clusters: Theoretical investigation based on first principle calculations, *Chemical Physics Letters* **2007**, *446*, 374–379.

[216] V. Kumar, Y. Kawazoe, Evolution of atomic and electronic structure of Pt clusters: Planar, layered, pyramidal, cage, cubic, and octahedral growth, *Physical Review B* **2008**, *77*, 205418.

[217] A. S. Chaves, G. G. Rondina, M. J. Piotrowski, P. Tereshchuk, J. L. F. Da Silva, The Role of Charge States in the Atomic Structure of Cu_n and Pt_n (n=2-14 atoms) Clusters: A DFT Investigation, *Journal of Physical Chemistry A* **2014**, *118*, 10813–10821.

[218] D. Majumdar, D. G. Dai, K. Balasubramanian, Theoretical study of the electronic states of platinum trimer (Pt_3^-), *Journal of Chemical Physics* **2000**, *113*, 7919–7927.

[219] L. Fernandez-Seivane, J. Ferrer, Magnetic anisotropies of late transition metal atomic clusters, *Physical Review Letters* **2007**, *99*, 183401.

[220] P. Blonski, S. Dennler, J. Hafner, Strong spin-orbit effects in small Pt clusters: Geometric structure, magnetic isomers and anisotropy, *Journal of Chemical Physics* **2011**, *134*, 034107.

[221] H. K. Yuan, H. Chen, A. L. Kuang, B. Wu, Spin-orbit effect and magnetic anisotropy in Pt clusters, *Journal of Magnetism and Magnetic Materials* **2013**, *331*, 7–16.

[222] K. Balasubramanian, K. K. Das, Excited electronic states of Au_3, *Chemical Physics Letters* **1991**, *186*, 577–582.

[223] A. Grushow, K. M. Ervin, Ligand and metal binding energies in platinum carbonyl cluster anions: Collision-induced dissociation of Pt_m^- and $Pt_m(CO)_n^-$, *Journal of Chemical Physics* **1997**, *106*, 9580–9593.

[224] U. Berzinsh, M. Gustafsson, D. Hanstorp, A. Klinkmueller, U. Ljungblad, A.-M. Pendrill, Isotope shift in the electron affinity of chlorine, *Physical Review A* **1995**, *51*, 231–238.

[225] A. C. J. Brouwer, E. J. J. Groenen, M. C. van Hemert, J. Schmidt, Isotope Shifts and Intersystem Crossing for Pentacene in p-Terphenyl. A Model System for Single-Molecule Dynamics, *The Journal of Physical Chemistry A* **1999**, *103*, 8959–8965.

[226] M. R. Godefroid, C. F. Fischer, Isotope shift in the oxygen electron affinity, *Physical Review A* **1999**, *60*, R2637–R2640.

[227] S. Bubin, J. Komasa, M. Stanke, L. Adamowicz, Isotope shift in the electron affinity of lithium, *The Journal of Chemical Physics* **2009**, *131*, 234112.

[228] T. Carette, C. Drag, O. Scharf, C. Blondel, C. Delsart, C. F. Fischer, M. Godefroid, Isotope shift in the sulfur electron affinity: Observation and theory, *Physical Review A* **2010**, *81*, 042522.

[229] D. Bresteau, C. Drag, C. Blondel, Isotope shift of the electron affinity of carbon measured by photodetachment microscopy, *Physical Review A* **2016**, *93*, 013414.

[230] X. Chen, C. Ning, Accurate electron affinity of Pb and isotope shifts of binding energies of Pb^-, *The Journal of Chemical Physics* **2016**, *145*, 084303.

[231] T. Carette, M. R. Godefroid, Isotope shift on the chlorine electron affinity revisited by an MCHF/CI approach, *Journal of Physics B: Atomic Molecular and Optical Physics* **2013**, *46*, 095003.

[232] C. M. Western, PGOPHER: A program for simulating rotational, vibrational and electronic spectra, *Journal of Quantitative Spectroscopy and Radiative Transfer* **2017**, *186*, 221–242.

[233] C. M. Western, B. E. Billinghurst, Automatic assignment and fitting of spectra with PGOPHER, *Physical Chemistry Chemical Physics* **2017**, *19*, 10222–10226.

[234] S. Winczewski, J. Rybicki, Structure of Small Platinum Clusters Revised, *Computational Methods in Science and Technology* **2011**, *17*, 75–85.

[235] R. Meiswinkel, H. Koppel, A pseudo-Jahn-Teller treatment of the pseudorotatioanl spectrum of Na_3, *Chemical Physics* **1990**, *144*, 117–128.

[236] E. Haller, H. Koppel, L. S. Cederbaum, W. Vonniessen, G. Bieri, Multimode Jahn-Teller and pseudo-Jahn-Teller effects in BF_3^+, *Journal of Chemical Physics* **1983**, *78*, 1359–1370.

[237] K. Kobe, H. Kuhling, S. Rutz, E. Schreiber, J. P. Wolf, L. Woste, M. Broyer, P. Dugourd, Time-resolved observation of molecular pseudorotation in Na_3, *Chemical Physics Letters* **1993**, *213*, 554–558.

[238] L. V. Poluyanov, W. Domcke, The ^{3}E x E, ^{4}E x E and ^{5}E x E Jahn-Teller Hamiltonians of trigonal systems, *Chemical Physics* **2008**, *352*, 125–134.

[239] C. C. Arnold, D. M. Neumark, Threshold photodetachment zero-electron kinetic energy spectroscopy of Si_3^-, *The Journal of Chemical Physics* **1994**, *100*, 1797–1804.

[240] M. S. Child, Anomalous spectroscopic properties accompanying a weak dynamical Jahn-Teller effect, *Journal of Molecular Spectroscopy* **1963**, *10*, 357–365.

[241] Y. Liu, I. B. Bersuker, W. Zou, J. E. Boggs, Pseudo Jahn-Teller versus Renner-Teller effects in the instability of linear molecules, *Chemical Physics* **2010**, *376*, 30–35.

[242] H. Köppel, W. Domcke, L. S. Cederbaum, Theory of vibronic coupling in linear molecules, *The Journal of Chemical Physics* **1981**, *74*, 2945–2968.

[243] S. Mishra, L. V. Poluyanov, W. Domcke, Spin-orbit vibronic coupling in π^3 states of linear triatomic molecules, *The Journal of Chemical Physics* **2007**, *126*, 134312.

[244] S. Mishra, V. Vallet, L. V. Poluyanov, W. Domcke, Spectroscopic effects of first-order relativistic vibronic coupling in linear triatomic molecules, *The Journal of Chemical Physics* **2005**, *123*, 124104.

[245] S. Mishra, W. Domcke, L. V. Poluyanov, Study of strong Σ-Π and spin-orbit vibronic coupling effects in linear triatomic molecules, *Chemical Physics* **2006**, *327*, 457–467.

[246] L. V. Poluyanov, W. Domcke, S. Mishra, Spin-orbit vibronic coupling in $^4\Pi$ states of linear triatomic molecules, *The Journal of Chemical Physics* **2019**, *151*, 134103.

[247] I. Sioutis, S. Mishra, L. V. Poluyanov, W. Domcke, Renner-Teller and spin-orbit vibronic coupling effects in linear triatomic molecules with a half-filled π shell, *The Journal of Chemical Physics* **2008**, *128*, 124318.

[248] I. León, Z. Yang, L.-S. Wang, Probing the electronic structure and Au-C chemical bonding in AuC_2^- and AuC_2 using high-resolution photoelectron spectroscopy, *The Journal of Chemical Physics* **2014**, *140*, 084303.

[249] T. Sommerfeld, Coupling between dipole-bound and valence states: the nitromethane anion, *Physical Chemistry Chemical Physics* **2002**, *4*, 2511–2516.

[250] R. N. Compton, H. S. Carman Jr., C. Desfrançois, H. Abdoul-Carime, J. P. Schermann, J. H. Hendricks, S. A. Lyapustina, K. H. Bowen, On the binding of electrons to nitromethane: Dipole and valence bound anions, *The Journal of Chemical Physics* **1996**, *105*, 3472–3478.

[251] O. Windelius, J. Welander, A. Aleman, D. J. Pegg, K. V. Jayaprasad, S. Ali, D. Hanstorp, Photoelectron angular distributions in photodetachment from P^-, *Physical Review A* **2021**, *103*, 033108.

[252] B. Zimmermann *et al.*, Localization and loss of coherence in molecular double-slit experiments, *Nature Physics* **2008**, *4*, 649–655.

[253] Y. Liu, C.-G. Ning, L.-S. Wang, Double- and multi-slit interference in photodetachment from nanometer organic molecular anions, *The Journal of Chemical Physics* **2019**, *150*, 244302.

[254] R. Mabbs, E. Surber, A. Sanov, An experimental manifestation of distinct electronic-structural properties of covalent dimer anions of CO_2 and CS_2, *Chemical Physics Letters* **2003**, *381*, 479–485.

[255] Q.-C. Ning, L.-Y. Peng, S.-N. Song, W.-C. Jiang, S. Nagele, R. Pazourek, J. Burgdörfer, Q. Gong, Attosecond streaking of Cohen-Fano interferences in the photoionization of H_2^+, *Physical Review A* **2014**, *90*, 013423.

[256] M. Kunitski *et al.*, Double-slit photoelectron interference in strong-field ionization of the neon dimer, *Nature Communications* **2019**, *10*, 1.

[257] S. E. Canton, E. Plésiat, J. D. Bozek, B. S. Rude, P. Decleva, F. Martín, Direct observation of Young's double-slit interferences in vibrationally resolved photoionization of diatomic molecules, *Proceedings of the National Academy of Sciences* **2011**, *108*, 7302–7306.

[258] D. Rolles *et al.*, Isotope-induced partial localization of core electrons in the homonuclear molecule N_2, *Nature* **2005**, *437*, 711–715.

[259] A. Afaq, M. Du, Interferences in Photodetachment of a Negative Molecular Ion Model, *Communications in Theoretical Physics* **2008**, *50*, 1401–1406.

[260] A. Afaq, I. Ahmad, M. A. Ahmad, A. Rashid, B. A. Tahir, M. T. Hussain, Interferences in photodetachment of a triatomic negative ion, *Applied Physics Letters* **2009**, *94*, 041125.

[261] Y. Bao-Chun, D. Mengli, Oscillations in Total Photodetachment Cross Sections of a Triatomic Anion, *Communications in Theoretical Physics* **2010**, *53*, 545–550.

[262] J. Xie, R. N. Zare, Selection rules for the photoionization of diatomic molecules, *The Journal of Chemical Physics* **1990**, *93*, 3033–3038.

[263] N. Pontius, P. S. Bechthold, M. Neeb, W. Eberhardt, Ultrafast Hot-Electron Dynamics Observed in Pt_3^- Using Time-Resolved Photoelectron Spectroscopy, *Physical Review Letters* **2000**, *84*, 1132–1135.

[264] J.-C. Hu, L.-L. Xu, H.-F. Li, D. Y. Valdivielso, A. Fielicke, S.-G. He, J.-B. Ma, Liberation of three dihydrogens from two ethene molecules as mediated by the tantalum nitride anion cluster $Ta_3N_2^-$ at room temperature, *Physical Chemistry Chemical Physics* **2017**, *19*, 3136–3142.

[265] Y. Zhao *et al.*, Dinitrogen Fixation and Reduction by $Ta_3N_3H_{0,1}^-$ Cluster Anions at Room Temperature: Hydrogen-Assisted Enhancement of Reactivity, *Journal of the American Chemical Society* **2019**, *141*, 12592–12600.

[266] M. D. Fryzuk, B. A. MacKay, B. O. Patrick, Hydrosilylation of a Dinuclear Tantalum Dinitrogen Complex: Cleavage of N_2 and Functionalization of Both Nitrogen Atoms, *Journal of the American Chemical Society* **2003**, *125*, 3234–3235.

[267] B. A. MacKay, B. O. Patrick, M. D. Fryzuk, Hydroalumination of a Dinuclear Tantalum Dinitrogen Complex: N-N Bond Cleavage and Ancillary Ligand Rearrangement, *Organometallics* **2005**, *24*, 3836–3841.

[268] P. Avenier *et al.*, Dinitrogen dissociation on an isolated surface tantalum atom, *Science* **2007**, *317*, 1056–60.

[269] J. Li, S. Li, Energetics and Mechanism of Dinitrogen Cleavage at a Mononuclear Surface Tantalum Center: A New Way of Dinitrogen

Reduction, *Angewandte Chemie International Edition* **2008**, *47*, 8040–8043.

[270] H.-P. Jia, E. A. Quadrelli, Mechanistic aspects of dinitrogen cleavage and hydrogenation to produce ammonia in catalysis and organometallic chemistry: relevance of metal hydride bonds and dihydrogen, *Chemical Society Reviews* **2014**, *43*, 547–564.

[271] J. Simons, Theoretical Study of Negative Molecular Ions, *Annual Review of Physical Chemistry* **2011**, *62*, 107–128.

[272] J. Simons, Molecular Anions, *The Journal of Physical Chemistry A* **2008**, *112*, 6401–6511.

[273] V. Flambaum, D. DeMille, M. Kozlov, Time-Reversal Symmetry Violation in Molecules Induced by Nuclear Magnetic Quadrupole Moments, *Physical Review Letters* **2014**, *113*, 103003.

[274] J. Baron *et al.*, Order of Magnitude Smaller Limit on the Electric Dipole Moment of the Electron, *Science* **2014**, *343*, 269.

[275] M. Pospelov, A. Ritz, Electric dipole moments as probes of new physics, *Annals of Physics* **2005**, *318*, 119–169.

[276] I. B. Khriplovich, S. K. Lamoreaux, *CP Violation Without Strangeness: Electric Dipole Moments of Particles, Atoms, and Molecules*, Springer-Verlag, Berlin Heidelberg, **1997**.

[277] J. K. Bates, D. M. Gruen, The electronic and vibrational absorption spectrum of tantalum nitride (TaN) isolated in an argon matrix, *The Journal of Chemical Physics* **1979**, *70*, 4428–4429.

[278] M. Zhou, L. Andrews, Reactions of Laser-Ablated Niobium, Tantalum, and Rhenium Atoms with Nitrogen Atoms and Molecules. Infrared Spectra and Density Functional Calculations of the Metal Nitride and Dinitride Molecules, *The Journal of Physical Chemistry A* **1998**, *102*, 9061–9071.

[279] R. S. Ram, J. Liévin, P. F. Bernath, Emission Spectroscopy and Ab Initio Calculations for TaN, *Journal of Molecular Spectroscopy* **2002**, *215*, 275–284.

[280] S. Mukund, S. Bhattacharyya, S. G. Nakhate, Jet-cooled laser-induced dispersed fluorescence spectroscopy of TaN: Observation of $a^3\Delta$ and $A^1\Delta$ states, *Chemical Physics Letters* **2016**, *655-656*, 51–54.

[281] J. L. Bouchard, T. Steimle, D. L. Kokkin, D. J. Sharfi, R. J. Mawhorter, Branching ratios, radiative lifetimes, and transition dipole moments for tantalum nitride, TaN, *Journal of Molecular Spectroscopy* **2016**, *325*, 1–6.

[282] T. Steimle, D. L. Kokkin, Y. Kim, R. J. Mawhorter, C. Linton, Characterization of the $[18.42]0^+$ - $X^1\Sigma^+$ (0,0) band of tantalum nitride, TaN, *Chemical Physics Letters* **2016**, *664*, 138–142.

[283] S. G. Nakhate, S. Mukund, S. Bhattacharyya, Laser-induced fluorescence spectroscopy of TaN in free-jet: Observation of high-lying excited electronic states, *Chemical Physics Letters* **2017**, *669*, 38–42.

[284] T. Steimle, D. L. Kokkin, C. Linton, L. Cheng, Characterization of the $[18.28]0^-$ - $a^3\Delta_1$ (0,0) band of tantalum nitride, TaN, *The Journal of Chemical Physics* **2017**, *147*, 154304.

[285] B. Hong, L. Cheng, M. Y. Wang, Z. J. Wu, Electronic structures and chemical bonding in 4d- and 5d-transition metal mononitrides, *Molecular Physics* **2010**, *108*, 25–33.

[286] L. V. Skripnikov, A. N. Petrov, N. S. Mosyagin, A. V. Titov, V. V. Flambaum, TaN molecule as a candidate for the search for a T,P-violating nuclear magnetic quadrupole moment, *Physical Review A* **2015**, *92*, 012521.

[287] T. Fleig, M. K. Nayak, M. G. Kozlov, TaN, a molecular system for probing $\mathcal{P},\mathcal{T}$-violating hadron physics, *Physical Review A* **2016**, *93*, 012505.

[288] P. Pyykkö, S. Riedel, M. Patzschke, Triple-bond covalent radii, *Chemistry - A European Journal* **2005**, *11*, 3511–20.

[289] W. Weltner Jr., D. McLeod Jr., Spectroscopy of TaO and TaO_2 in Neon and Argon Matrices at 4° and 20°K, *The Journal of Chemical Physics* **1965**, *42*, 882–891.

[290] W. Zheng, X. Li, S. Eustis, K. Bowen, Anion photoelectron spectroscopy of TaO_n^- (n=1-3), *Chemical Physics Letters* **2008**, *460*, 68–71.

[291] C. J. Cheetham, R. F. Barrow, Rotational analysis of electronic bands of gaseous TaO, *Transactions of the Faraday Society* **1967**, *63*, 1835–1845.

[292] G. Aravind, M. Nrisimhamurty, R. G. Mane, A. K. Gupta, E. Krishnakumar, Probing electronic states of TaC and observation of a stable excited state of TaC^- by anion-photoelectron spectroscopy, *Physical Review A* **2015**, *92*, 042503.

[293] S. Truppe *et al.*, Spectroscopic characterization of aluminum monofluoride with relevance to laser cooling and trapping, *Physical Review A* **2019**, *100*, 052513.

[294] R. N. Zare, A. L. Schmeltekopf, W. J. Harrop, D. L. Albritton, A direct approach for the reduction of diatomic spectra to molecular constants for the construction of RKR potentials, *Journal of Molecular Spectroscopy* **1973**, *46*, 37–66.

[295] E. Clementi, D. L. Raimondi, W. P. Reinhardt, Atomic Screening Constants from SCF Functions. II. Atoms with 37 to 86 Electrons, *The Journal of Chemical Physics* **1967**, *47*, 1300–1307.

[296] N. R. Walker, R. S. Walters, M. A. Duncan, Frontiers in the infrared spectroscopy of gas phase metal ion complexes, *New Journal of Chemistry* **2005**, *29*, 1495–1503.

[297] K. Müller-Dethlefs, P. Hobza, Noncovalent Interactions: A Challenge for Experiment and Theory, *Chemical Reviews* **2000**, *100*, 143–168.

[298] S. Seidel, K. Seppelt, Xenon as a complex ligand: The tetra xenono gold(II) cation in $AuXe_4{}^{2+}$ $(Sb_2F_{11}{}^-)_2$, *Science* **2000**, *290*, 117–118.

[299] G. Ganteför, H. R. Siekmann, H. O. Lutz, K. H. Meiwes-Broer, Pure metal and metal-doped rare-gas clusters grown in a pulsed ARC cluster ion source, *Chemical Physics Letters* **1990**, *165*, 293–296.

[300] M. Velegrakis, C. Lüder, Formation and stability of singly and doubly charged MgArN clusters, *Chemical Physics Letters* **1994**, *223*, 139–142.

[301] M. Beyer, C. Berg, G. Albert, U. Achatz, V. E. Bondybey, Coordinative saturation of cationic niobium- and rhodium-argon complexes, *Chemical Physics Letters* **1997**, *280*, 459–463.

[302] M. Velegrakis, G. E. Froudakis, S. C. Farantos, Stability and structure of Ni^+Ar_n and Pt^+Ar_n clusters, *The Journal of Chemical Physics* **1998**, *109*, 4687–4688.

[303] M. Velegrakis, G. Froudakis, S. Farantos, Coordination of Ti cation embedded in argon clusters, *Chemical Physics Letters* **1999**, *302*, 595–601.

[304] J. Opitz, B. Stegemann, B. Kaiser, K. Rademann in *Zinc and cadmium doped rare gas clusters cations*, WORLD SCIENTIFIC, **2000**, pp. 523–527.

[305] H. Odaka, M. Ichihashi, Production of cluster complexes by cluster-cluster collisions-incorporation of a size-selected cobalt dimer ion into a neutral argon cluster, *RSC Advances* **2015**, *5*, 78247–78252.

[306] P. R. Kemper, M. T. Hsu, M. T. Bowers, Transition-metal ion-rare gas clusters: bond strengths and molecular parameters for $Co^+(He/Ne)_n$, $Ni^+(He/Ne)_n$, and $Cr^+(He/Ne/Ar)$, *The Journal of Physical Chemistry* **1991**, *95*, 10600–10609.

[307] H. Partridge, C. W. Bauschlicher, S. R. Langhoff, Theoretical study of metal-ions bound to He, Ne and Ar, *Journal of Physical Chemistry* **1992**, *96*, 5350–5355.

[308] C. Heinemann, H. Schwarz, W. Koch, Ground-state potentials for Co^+/rare-gas interactions, *Molecular Physics* **1996**, *89*, 473–488.

[309] D. Lessen, P. J. Brucat, The unique stability of $CoAr_6^+$: Coordination complex or close-packed structure?, *Chemical Physics Letters* **1988**, *149*, 10–13.

[310] C. van der Linde, R. F. Höckendorf, O. P. Balaj, M. K. Beyer, Ion-molecule reactions of $CoAr_6^+$ with nitrogen oxides N_2, *Low Temperature Physics* **2010**, *36*, 411–416.

[311] R. F. Höckendorf, C. van der Linde, O. P. Balaj, I. Herber, M. K. Beyer, Ion-molecule reactions of $CoAr_6^+$ with di- and trifluorobenzenes probe absolute pressure in FT-ICR MS, *International Journal of Mass Spectrometry* **2011**, *300*, 44–49.

[312] L. Delgado-Callico, P. Ferrari, J. M. Bakker, F. Baletto, E. Janssens, Benchmarking density functional theory methods for modelling cationic metal-argon complexes, *Theoretical Chemistry Accounts* **2021**, *140*, 38.

[313] D. M. Kiawi, J. M. Bakker, J. Oomens, W. J. Buma, Z. Jamshidi, L. Visscher, L. B. F. M. Waters, Water Adsorption on Free Cobalt Cluster Cations, *The Journal of Physical Chemistry A* **2015**, *119*, 10828–10837.

[314] V. T. Ngan, E. Janssens, P. Claes, A. Fielicke, M. T. Nguyen, P. Lievens, Nature of the interaction between rare gas atoms and transition metal doped silicon clusters: the role of shielding effects, *Physical Chemistry Chemical Physics* **2015**, *17*, 17584–17591.

[315] R. Gehrke, P. Gruene, A. Fielicke, G. Meijer, K. Reuter, Nature of Ar bonding to small Co_n^+ clusters and its effect on the structure determination by far-infrared absorption spectroscopy, *The Journal of Chemical Physics* **2009**, *130*, 034306.

[316] A. Shayeghi, R. L. Johnston, D. M. Rayner, R. Schäfer, A. Fielicke, The Nature of Bonding between Argon and Mixed Gold-Silver Trimers,

Angewandte Chemie (International ed. in English) **2015**, *54*, 10675–10680.

[317] *TURBOMOLE V6.6 2014, a development of University of Karlsruhe and Forschungszentrum Karlsruhe GmbH, 1989-2007, TURBOMOLE GmbH, since 2007; available from* `http://www.turbomole.com`.

[318] J. Tao, J. P. Perdew, V. N. Staroverov, G. E. Scuseria, Climbing the Density Functional Ladder: Nonempirical Meta–Generalized Gradient Approximation Designed for Molecules and Solids, *Physical Review Letters* **2003**, *91*, 146401.

[319] S. Grimme, J. Antony, S. Ehrlich, H. Krieg, A consistent and accurate ab initio parametrization of density functional dispersion correction (DFT-D) for the 94 elements H-Pu, *The Journal of Chemical Physics* **2010**, *132*, 154104.

[320] R. M. Badger, A Relation Between Internuclear Distances and Bond Force Constants, *The Journal of Chemical Physics* **1934**, *2*, 128–131.

[321] E. Kraka, J. A. Larsson, D. Cremer in *Computational Spectroscopy: Methods, Experiments and Applications*, Wiley-VCH, **2010**, pp. 105–149.

[322] M. Kaupp, D. Danovich, S. Shaik, Chemistry is about energy and its changes: A critique of bond-length/bond-strength correlations, *Coordination Chemistry Reviews* **2017**, *344*, 355–362.

[323] X. Liu, G. Meijer, J. Pérez-Ríos, On the relationship between spectroscopic constants of diatomic molecules: a machine learning approach, *RSC Advances* **2021**, *11*, 14552–14561.

[324] D. Lessen, P. J. Brucat, Characterization of transition metal-rare-gas cations: VAr^+ and VKr^+, *The Journal of Chemical Physics* **1989**, *91*, 4522–4530.

[325] T. Ishii, S. Tsuboi, G. Sakane, M. Yamashita, B. K. Breedlove, Universal spectrochemical series of six-coordinate octahedral metal complexes for modifying the ligand field splitting, *Dalton Transactions* **2009**, 680–687.

[326] K. Seppelt, Metal-Xenon Complexes, *Zeitschrift für anorganische und allgemeine Chemie* **2003**, *629*, 2427–2430.

[327] E. Iglesia, Design, synthesis, and use of cobalt-based Fischer-Tropsch synthesis catalysts, *Applied Catalysis A: General* **1997**, *161*, 59–78.

[328] H. Schulz, Short history and present trends of Fischer-Tropsch synthesis, *Applied Catalysis A: General* **1999**, *186*, 3–12.

[329] M. Castro, C. Jamorski, D. R. Salahub, Structure, bonding, and magnetism of small Fe_n, Co_n, and Ni_n clusters, n$\leq$5, *Chemical Physics Letters* **1997**, *271*, 133–142.

[330] I. M. L. Billas, A. Châtelain, W. A. de Heer, Magnetism of Fe, Co and Ni clusters in molecular beams, *Journal of Magnetism and Magnetic Materials* **1997**, *168*, 64–84.

[331] X. Xu, S. Yin, R. Moro, W. A. de Heer, Magnetic Moments and Adiabatic Magnetization of Free Cobalt Clusters, *Physical Review Letters* **2005**, *95*, 237209.

[332] J. Meyer *et al.*, The spin and orbital contributions to the total magnetic moments of free Fe, Co, and Ni clusters, *The Journal of Chemical Physics* **2015**, *143*, 104302.

[333] S. Rives, A. Catherinot, F. Dumas-Bouchiat, C. Champeaux, A. Videcoq, R. Ferrando, Growth of Co isolated clusters in the gas phase: Experiment and molecular dynamics simulations, *Physical Review B* **2008**, *77*, 085407.

[334] J. Guevara, A. M. Llois, F. Aguilera-Granja, J. M. Montejano-Carrizales, Structural evolution of free Co cluster magnetism, *Solid State Communications* **1999**, *111*, 335–340.

[335] C. Jamorski, A. Martinez, M. Castro, D. R. Salahub, Structure and properties of cobalt clusters up to the tetramer: A density-functional study, *Physical Review B* **1997**, *55*, 10905–10921.

[336] S. Datta, M. Kabir, S. Ganguly, B. Sanyal, T. Saha-Dasgupta, A. Mookerjee, Structure, bonding, and magnetism of cobalt clusters from first-principles calculations, *Physical Review B* **2007**, *76*, 014429.

[337] S. Yang, M. B. Knickelbein, Photoionization studies of transition metal clusters: Ionization potentials for Fe_n and Co_n, *The Journal of Chemical Physics* **1990**, *93*, 1533–1539.

[338] H. Yoshida, A. Terasaki, K. Kobayashi, M. Tsukada, T. Kondow, Spin-polarized electronic structure of cobalt cluster anions studied by photoelectron spectroscopy, *The Journal of Chemical Physics* **1995**, *102*, 5960–5965.

[339] S.-R. Liu, H.-J. Zhai, L.-S. Wang, Electronic and structural evolution of Co_n^- clusters ($n = 1 - 108$) by photoelectron spectroscopy, *Physical Review B* **2001**, *64*, 153402.

[340] S. Minemoto, A. Terasaki, T. Kondow, Electronic structures of cobalt cluster cations: Photodissociation spectroscopy of Co_n^+Ar (n=3-5) in the visible to near-infrared range, *The Journal of Chemical Physics* **1996**, *104*, 5770–5775.

[341] D. A. Hales, C.-X. Su, L. Lian, P. B. Armentrout, Collision-induced dissociation of Co_n^+ (n=2-18) with Xe: Bond energies of cationic and neutral cobalt clusters, dissociation pathways, and structures, *The Journal of Chemical Physics* **1994**, *100*, 1049–1057.

[342] E. K. Parks, B. J. Winter, T. D. Klots, S. J. Riley, Evidence for polyicosahedral structure in ammoniated iron, cobalt, and nickel clusters, *The Journal of Chemical Physics* **1992**, *96*, 8267–8274.

[343] E. K. Parks, T. D. Klots, B. J. Winter, S. J. Riley, Reactions of cobalt clusters with water and ammonia: Implications for cluster structure, *The Journal of Chemical Physics* **1993**, *99*, 5831–5839.

[344] S. J. Riley, The atomic structure of transition metal clusters, *Journal of Non-Crystalline Solids* **1996**, *205-207*, 781–787.

[345] J. Ho, E. K. Parks, L. Zhu, S. J. Riley, Reactions of small cobalt clusters with N_2: implications for cluster structure, *Chemical Physics* **1995**, *201*, 245–261.

[346] D. Dieleman *et al.*, Orbit and spin resolved magnetic properties of size selected Co_nRh^+ and Co_nAu^+ nanoalloy clusters, *Physical Chemistry Chemical Physics* **2015**, *17*, 28372–28378.

[347] J. Lv, X. Bai, J.-F. Jia, X.-H. Xu, H.-S. Wu, Structural, electronic and magnetic properties of Co_nRh (n=1-8) clusters from density functional calculations, *Physica B: Condensed Matter* **2012**, *407*, 14–21.

[348] J. Wang, G. Wang, X. Chen, W. Lu, J. Zhao, Structure and magnetic properties of Co-Cu bimetallic clusters, *Physical Review B* **2002**, *66*, 014419.

[349] M.-Y. Jia, J. Tol, Y. J. Li, V. Chernyy, J. Bakker, L. N. Pham, M. Nguyen, E. Janssens, Structures and Magnetic Properties of Small Co_n^+ and $Co_{n-1}^+Cr^+$ (n=3-5) Clusters, *Journal of Physics: Condensed Matter* **2018**, *30*, 474002.

[350] H. Arslan, Structures and Energetic of Palladium-Cobalt Binary Clusters, *International Journal of Modern Physics C* **2008**, *19*, 1243–1255.

[351] Y. H. Chui, K.-Y. Chan, Structures and Energetics of Platinum-Cobalt Bimetallic Clusters, *Molecular Simulation* **2004**, *30*, 679–690.

[352] G. M. Koretsky, K. P. Kerns, G. C. Nieman, M. B. Knickelbein, S. J. Riley, Reactivity and Photoionization Studies of Bimetallic Cobalt-Manganese Clusters, *The Journal of Physical Chemistry A* **1999**, *103*, 1997–2006.

[353] A. Pramann, K. Koyasu, A. Nakajima, K. Kaya, Anion Photoelectron Spectroscopy of Vanadium-Doped Cobalt Clusters, *The Journal of Physical Chemistry A* **2002**, *106*, 2483–2488.

[354] K. Hoshino, T. Naganuma, K. Watanabe, Y. Konishi, A. Nakajima, K. Kaya, Ionization energies of cobalt-vanadium bimetallic clusters (Co_nV_m), *Chemical Physics Letters* **1995**, *239*, 369–372.

[355] S. Nonose, Y. Sone, K. Kaya, Reactivity and stability of bimetallic clusters, *Zeitschrift für Physik D Atoms Molecules and Clusters* **1991**, *19*, 357–359.

[356] A. Nakajima, T. Kishi, T. Sugioka, Y. Sone, K. Kaya, Structure and reactivity of bimetallic $Co_nV_m^+$ cluster ions, *The Journal of Physical Chemistry* **1991**, *95*, 6833–6835.

[357] S. Nonose, Y. Sone, K. Onodera, S. Sudo, K. Kaya, Structure and reactivity of bimetallic cobalt-vanadium (Co_nV_m) clusters, *The Journal of Physical Chemistry* **1990**, *94*, 2744–2746.

[358] N. Shen, J. Wang, L. Zhu, Ab initio study of magnetic properties of bimetallic $Co_{n-1}Mn$ and $Co_{n-1}V$ clusters, *Chemical Physics Letters* **2008**, *467*, 114–119.

[359] P. Wu, L.-F. Yuan, J. Yang, First-Principles Study of Electronic and Magnetic Properties of Co_nMn_m and Co_nV_m (m+n$\leq$ 6) Clusters, *The Journal of Physical Chemistry A* **2008**, *112*, 12320–12325.

[360] S. Ganguly, M. Kabir, S. Datta, B. Sanyal, A. Mookerjee, Magnetism in small bimetallic Mn-Co clusters, *Physical Review B* **2008**, *78*, 014402.

[361] M. B. Knickelbein, Magnetic moments of small bimetallic clusters: Co_nMn_m, *Physical Review B* **2007**, *75*, 014401.

[362] S. Yin, R. Moro, X. Xu, W. A. de Heer, Magnetic Enhancement in Cobalt-Manganese Alloy Clusters, *Physical Review Letters* **2007**, *98*, 113401.

[363] N. T. Tung, E. Janssens, P. Lievens, Dopant dependent stability of Co_nTM^+ (TM = Ti, V, Cr, and Mn) clusters, *Applied Physics B* **2014**, *114*, 497–502.

[364] M. J. Frisch *et al.*, *Gaussian 16 Revision C.01*, **2016**, Gaussian Inc. Wallingford CT.

[365] J. L. Rodríguez-López, F. Aguilera-Granja, K. Michaelian, A. Vega, Structure and magnetism of cobalt clusters, *Physical Review B* **2003**, *67*, 174413.

[366] Q.-M. Ma, Z. Xie, J. Wang, Y. Liu, Y.-C. Li, Structures, stabilities and magnetic properties of small Co clusters, *Physics Letters A* **2006**, *358*, 289.

[367] S. Peredkov, M. Neeb, W. Eberhardt, J. Meyer, M. Tombers, H. Kampschulte, G. Niedner-Schatteburg, Spin and Orbital Magnetic Moments of Free Nanoparticles, *Physical Review Letters* **2011**, *107*, 233401.

[368] A. Langenberg *et al.*, Spin and orbital magnetic moments of size-selected iron, cobalt, and nickel clusters, *Physical Review B* **2014**, *90*, 184420.

[369] M. B. Knickelbein, Magnetic ordering in manganese clusters, *Physical Review B* **2004**, *70*, 014424.

[370] M. B. Knickelbein, Experimental Observation of Superparamagnetism in Manganese Clusters, *Physical Review Letters* **2001**, *86*, 5255–5257.

[371] C. D. Dong, X. G. Gong, Magnetism enhanced layer-like structure of small cobalt clusters, *Physical Review B* **2008**, *78*, 020409.

[372] G. L. Gutsev, C. W. Weatherford, K. G. Belay, B. R. Ramachandran, P. Jena, An all-electron density functional theory study of the structure and properties of the neutral and singly charged M_{12} and M_{13} clusters: M=Sc-Zn, *The Journal of Chemical Physics* **2013**, *138*, 164303.

[373] F. Aguilera-Granja, A. Vega, L. C. Balbás, A new family of star-like icosahedral structures for small cobalt clusters, *Chemical Physics* **2013**, *415*, 106–111.

[374] C. J. H. Jacobsen *et al.*, Structure sensitivity of supported ruthenium catalysts for ammonia synthesis, *Journal of Molecular Catalysis A: Chemical* **2000**, *163*, 19–26.

[375] A. Logadottir, T. H. Rod, J. K. Norskov, B. Hammer, S. Dahl, C. J. H. Jacobsen, The Bronsted-Evans-Polanyi Relation and the Volcano Plot for Ammonia Synthesis over Transition Metal Catalysts, *Journal of Catalysis* **2001**, *197*, 229–231.

[376] F. R. García-García, A. Ruiz, I. Rodriguez-Ramos, Role of B5-Type Sites in Ru Catalysts used for the NH_3 Decomposition Reaction, *Topics in Catalysis* **2009**, *52*, 758–764.

[377] D. L. King, A Fischer-Tropsch study of supported ruthenium catalysts, *Journal of Catalysis* **1978**, *51*, 386–397.

[378] S. Shetty, A. P. J. Jansen, R. A. van Santen, Methane Formation on Corrugated Ru Surfaces, *The Journal of Physical Chemistry C* **2010**, *114*, 22630–22635.

[379] P. Liu, A. Logadottir, J. K. Norskov, Modeling the electro-oxidation of CO and H_2/CO on Pt, Ru, PtRu and Pt_3Sn, *Electrochimica Acta* **2003**, *48*, 3731–3742.

[380] Y. K. Kim, G. A. Morgan, J. T. Yates, Role of Atomic Step Defect Sites on the Catalytic Oxidation of Carbon Monoxide: Comparison between Ru(001) and Ru(109) Single-Crystal Surfaces, *The Journal of Physical Chemistry C* **2007**, *111*, 3366–3368.

[381] H. Pfnür, D. Menzel, F. M. Hoffmann, A. Ortega, A. M. Bradshaw, High resolution vibrational spectroscopy of CO on Ru(001): The importance of lateral interactions, *Surface Science* **1980**, *93*, 431–452.

[382] M. Bonn, C. Hess, W. G. Roeterdink, H. Ueba, M. Wolf, Dephasing of vibrationally excited molecules at surfaces: CO/Ru(001), *Chemical Physics Letters* **2004**, *388*, 269–273.

[383] P. Jakob, Dynamics of the C-O Stretch Overtone Vibration of CO/Ru(001), *Physical Review Letters* **1996**, *77*, 4229–4232.

[384] S.-i. Ishi, Y. Ohno, B. Viswanathan, An overview on the electronic and vibrational properties of adsorbed CO, *Surface Science* **1985**, *161*, 349–372.

[385] F. Abild-Pedersen, M. P. Andersson, CO adsorption energies on metals with correction for high coordination adsorption sites - A density functional study, *Surface Science* **2007**, *601*, 1747–1753.

[386] I. M. Ciobica, A. W. Kleyn, R. A. Van Santen, Adsorption and Coadsorption of CO and H on Ruthenium Surfaces, *The Journal of Physical Chemistry B* **2003**, *107*, 164–172.

[387] S. Shetty, R. A. van Santen, Hydrogen induced CO activation on open Ru and Co surfaces, *Physical Chemistry Chemical Physics* **2010**, *12*, 6330–6332.

[388] S. Shetty, R. A. van Santen, CO dissociation on Ru and Co surfaces: The initial step in the Fischer-Tropsch synthesis, *Catalysis Today* **2011**, *171*, 168–173.

[389] J. T. Lyon, P. Gruene, A. Fielicke, G. Meijer, D. M. Rayner, Probing C-O bond activation on gas-phase transition metal clusters: Infrared multiple photon dissociation spectroscopy of Fe, Ru, Re, and W cluster CO complexes, *The Journal of Chemical Physics* **2009**, *131*, 184706.

[390] H. Wang, Y. Liu, H. Haouari, R. Craig, J. R. Lombardi, D. M. Lindsay, Raman spectra of ruthenium dimers, *The Journal of Chemical Physics* **1997**, *106*, 6534–6537.

[391] L. Fang, X. Shen, X. Chen, J. R. Lombardi, Raman spectra of ruthenium and tantalum trimers in argon matrices, *Chemical Physics Letters* **2000**, *332*, 299–302.

[392] E. Waldt, R. Ahlrichs, M. M. Kappes, D. Schooss, Structures of Medium-Sized Ruthenium Clusters: The Octahedral Motif, *ChemPhysChem* **2014**, *15*, 862–865.

[393] C. Kerpal, D. J. Harding, D. M. Rayner, J. T. Lyon, A. Fielicke, Far-IR Spectra and Structures of Small Cationic Ruthenium Clusters: Evidence for Cubic Motifs, *The Journal of Physical Chemistry C* **2015**, *119*, 10869–10875.

[394] W. Zhang, H. Zhao, L. Wang, The Simple Cubic Structure of Ruthenium Clusters, *The Journal of Physical Chemistry B* **2004**, *108*, 2140–2147.

[395] S. Li, H. Li, J. Liu, X. Xue, Y. T. Tian, H. He, Structural and electronic properties of Ru_n clusters (n=2-14) studied by first-principles calculations, *Physical Review B* **2007**, *76*, 045410.

[396] L. L. Wang, D. D. Johnson, Removing Critical Errors for DFT Applications to Transition-Metal Nanoclusters: Correct Ground-State Structures of Ru Clusters, *The Journal of Physical Chemistry B* **2005**, *109*, 23113–23117.

[397] Y.-C. Bae, H. Osanai, V. Kumar, Y. Kawazoe, Atomic Structures and Magnetic Behavior of Small Ruthenium Clusters, *Materials Transactions* **2005**, *46*, 159–162.

[398] F. Aguilera-Granja, L. C. Balbás, A. Vega, Study of the Structural and Electronic Properties of Rh_n and Ru_n Clusters (n<20) within the Density Functional Theory, *The Journal of Physical Chemistry A* **2009**, *113*, 13483–13491.

[399] D. Kaiming, Y. Jinlong, X. Chuanyun, W. Kelin, Electronic properties and magnetism of ruthenium clusters, *Physical Review B* **1996**, *54*, 2191–2197.

[400] A. Fielicke, G. von Helden, G. Meijer, B. Simard, S. Dénommée, D. M. Rayner, Vibrational Spectroscopy of CO in Gas-Phase Rhodium Cluster-CO Complexes, *Journal of the American Chemical Society* **2003**, *125*, 11184–11185.

[401] P. Gruene, A. Fielicke, G. Meijer, D. M. Rayner, The adsorption of CO on group 10 (Ni, Pd, Pt) transition-metal clusters, *Physical Chemistry Chemical Physics* **2008**, *10*, 6144–6149.

[402] A. Fielicke, P. Gruene, G. Meijer, D. M. Rayner, The adsorption of CO on transition metal clusters: A case study of cluster surface chemistry, *Surface Science* **2009**, *603*, 1427–1433.

[403] M. Zhou, L. Andrews, Infrared Spectra and Density Functional Calculations of $RuCO^+$, $OsCO^+$, $Ru(CO)_x$, $Os(CO)_x$, $Ru(CO)_x^-$ and $Os(CO)_x^-$ (x = 1-4) in Solid Neon, *The Journal of Physical Chemistry A* **1999**, *103*, 6956–6968.

[404] S. Eckle, Y. Denkwitz, R. J. Behm, Activity, selectivity, and adsorbed reaction intermediates/reaction side products in the selective methanation of CO in reformate gases on supported Ru catalysts, *Journal of Catalysis* **2010**, *269*, 255–268.

[405] S. M. Lang, T. M. Bernhardt, M. Krstić, V. Bonacić-Koutecký, The Origin of the Selectivity and Activity of Ruthenium-Cluster Catalysts for Fuel-Cell Feed-Gas Purification: A Gas-Phase Approach, *Angewandte Chemie International Edition* **2014**, *53*, 5467–5471.

[406] J. E. Cyr, P. H. Rieger, Electrochemistry of ruthenium carbonyls, *Organometallics* **1991**, *10*, 2153–2159.

[407] S. M. Lang, S. U. Förtig, T. M. Bernhardt, M. Krstić, V. Bonacić-Koutecký, Gas-Phase Synthesis and Structure of Wade-Type Ruthenium Carbonyl and Hydrido Carbonyl Clusters, *The Journal of Physical Chemistry A* **2014**, *118*, 8356–8359.

[408] E. Hunstock, C. Mealli, M. J. Calhorda, J. Reinhold, Molecular Structures of $M_2(CO)_9$ and $M_3(CO)_{12}$ (M = Fe, Ru, Os): New Theoretical Insights, *Inorganic Chemistry* **1999**, *38*, 5053–5060.

[409] R. White, T. Bennett, V. Golovko, G. G. Andersson, G. F. Metha, A Systematic Density Functional Theory Study of the Complete Deligation of $M_3(CO)_{12}$, *Chemistry Select* **2016**, *1*, 1163–1167.

[410] E. A. Glascoe, M. F. Kling, J. E. Shanoski, C. B. Harris, Nature and Role of Bridged Carbonyl Intermediates in the Ultrafast Photoinduced Rearrangement of $M_3(CO)_{12}$, *Organometallics* **2006**, *25*, 775–784.

[411] Q. Kong, J. H. Lee, A. Plech, M. Wulff, H. Ihee, M. Koch, Ultrafast X-Ray Solution Scattering Reveals an Unknown Reaction Intermediate in the Photolysis of $M_3(CO)_{12}$, *Angewandte Chemie (International ed. in English)* **2008**, *47*, 5550–3.

[412] Q. Kong, J. H. Lee, K. H. Kim, J. Kim, M. Wulff, H. Ihee, M. H. J. Koch, Ultrafast X-ray Solution Scattering Reveals Different Reaction Pathways in the Photolysis of Triruthenium Dodecacarbonyl ($Ru_3(CO)_{12}$) after Ultraviolet and Visible Excitation, *Journal of the American Chemical Society* **2010**, *132*, 2600–2607.

[413] M. R. Harpham, A. B. Stickrath, X. Zhang, J. Huang, M. W. Mara, L. X. Chen, D.-J. Liu, Photodissociation Structural Dynamics of TrirutheniumDodecacarbonyl Investigated by X-ray Transient Absorption Spectroscopy, *The Journal of Physical Chemistry A* **2013**, *117*, 9807–9813.

[414] N. Liu, L. Guo, Z. Cao, W. Li, X. Zheng, Y. Shi, J. Guo, Y. Xi, Mechanisms of the Water-Gas Shift Reaction Catalyzed by Ruthenium Carbonyl Complexes, *The Journal of Physical Chemistry A* **2016**, *120*, 2408–2419.

[415] G. Critchley, P. J. Dyson, B. F. G. Johnson, J. S. McIndoe, R. K. O'Reilly, P. R. R. Langridge-Smith, Reactivity and Characterization of Transition-Metal Carbonyl Clusters Using UV Laser Desorption Mass Spectrometry, *Organometallics* **1999**, *18*, 4090–4097.

[416] J. S. McIndoe, Laser synthesis of transition metal clusters, *Transition Metal Chemistry* **2003**, *28*, 122–131.

[417] M. A. Henderson, S. Kwok, J. S. McIndoe, Gas-phase reactivity of ruthenium carbonyl cluster anions, *Journal of the American Society for Mass Spectrometry* **2009**, *20*, 658–666.

[418] I. Swart, F. M. F. de Groot, B. M. Weckhuysen, D. M. Rayner, G. Meijer, A. Fielicke, The Effect of Charge on CO Binding in Rhodium Carbonyls: From Bridging to Terminal CO, *Journal of the American Chemical Society* **2008**, *130*, 2126–2127.

[419] *TURBOMOLE V6.4 2012, a development of University of Karlsruhe and Forschungszentrum Karlsruhe GmbH, 1989-2007, TURBOMOLE GmbH, since 2007; available from* `http://www.turbomole.com`.

[420] P. J. Dyson, J. S. McIndoe, *Transition Metal Carbonyl Cluster Chemistry*, Taylor and Francis, **2000**.

[421] N. V. Sidgwick, The nature of the non-polar link, *Transactions of the Faraday Society* **1923**, *19*, 469–475.

[422] A. F. Holleman, N. Wiberg in *Kapitel XXXII. Überblick über wichtige Verbindungsklassen der Übergangsmetalle*, *Vol. 2*, De Gruyter, **2016**, pp. 2067–2224.

[423] G. Wang, J. Cui, C. Chi, X. Zhou, Z. H. Li, X. Xing, M. Zhou, Bonding in homoleptic iron carbonyl cluster cations: a combined infrared photodissociation spectroscopic and theoretical study, *Chemical Science* **2012**, *3*, 3272–3279.

[424] M. Zhou, L. Andrews, C. W. Bauschlicher, Spectroscopic and Theoretical Investigations of Vibrational Frequencies in Binary Unsaturated Transition-Metal Carbonyl Cations, Neutrals, and Anions, *Chemical Reviews* **2001**, *101*, 1931–1962.

[425] A. K. Hughes, K. Wade, Metal-metal and metal-ligand bond strengths in metal carbonyl clusters, *Coordination Chemistry Reviews* **2000**, *197*, 191–229.

[426] K. Wade, The structural significance of the number of skeletal bonding electron-pairs in carboranes, the higher boranes and borane anions, and various transition-metal carbonyl cluster compounds, *Journal of the Chemical Society D: Chemical Communications* **1971**, 792–793.

[427] R. Hoffmann, Building Bridges Between Inorganic and Organic Chemistry (Nobel Lecture), *Angewandte Chemie International Edition in English* **1982**, *21*, 711–724.

Publications

- A. Yanagimachi, K. Koyasu, D. Valdivielso, S. Gewinner, W. Schöllkopf, A. Fielicke, T. Tsukuda, Size-Specific, Dissociative Activation of Carbon Dioxide by Cobalt Cluster Anions, *The Journal of Physical Chemistry C* **2016**, *120*, 14209–14215.

- J.-C. Hu, L.-L. Xu, H.-F. Li, D. Y. Valdivielso, A. Fielicke, S.-G. He, J.-B. Ma, Liberation of three dihydrogens from two ethene molecules as mediated by the tantalum nitride anion cluster $Ta_3N_2^-$ at room temperature, *Physical Chemistry Chemical Physics* **2017**, *19*, 3136–3142.

Acknowledgements

- To those who scientifically made it possible:

  André Fielicke, Gerard Meijer, Gert von Helden, Otto Dopfer, Julius Jellinek, Aslihan Sumer, Alexander Paarman and Ines Bressel

- To the financing institutions:

  Deutsche Forschungsgemeinschaft and the Max Planck International Research School Berlin (IMPRS)

- To the people I met at the Technische Universität Berlin. Specially to:

  Pablo Nieto, Aude Bouchet, Alan Günther and Jenny Triptow

- To the people I met at the Fritz-Haber Institute. Specially to:

  Christian Schewe, Max Doppelbauer, Bruno Credidio, Mallikarjun Karra, Konrad Schatz and Sandra Eibenberger-Arias

- To other scientists who kindly offered their tips and help. Specially to:

  Andrei Sanov, Colin Western (developer of PGOPHER, RIP), Lai Sheng Wang and Phil Bunker

- To all those friends who brought me joy in Berlin and the pleasure for knowledge beyond the daily routine. Specially to:

  Susanne, Cacho, Carlos, Sergio, Bea and an endless etc

- **But mainly to my parents, MAXI and ISABEL, and to my girlfriend, PAULINE, who brought a new hope to my life: ALMA**